STUDYING THE ATMOSPHERES AND MAGNETIC FIELDS OF EXOPLANETS

Jake Daniel Turner
Walsenburg, CO

B.S. Astronomy & Physics, University of Arizona, 2011

M.S. Astronomy, University of Virginia, 2015

A Dissertation Presented to the Graduate
Faculty of the University of Virginia
in Candidacy for the Degree of
Doctor of Philosophy

Department of Astronomy

University of Virginia
June 2018

Committee Members:

Dr. Robert E. Johnson
Dr. Phil Arras
Dr. Arielle Moullet
Dr. Jean-Mathias Grießmeier
Dr. Charles Sackett

Abstract

Transits of exoplanets observed in the near-UV have been used to study the absorption properties of their atmospheres and possible star-planet interactions. In total, 25 transiting exoplanets were observed either in the near-UV or optical with the 1.5-m Kuiper Telescope to constrain their atmospheres and determine if asymmetries are visible in their light curves. I find that none of the near-UV transits exhibit any asymmetries. These observations suggest that asymmetries are not common in ground-based transits. With these observations I also conclude that 15 of the exoplanets have clouds, 5 have some type of scattering, and 3 may have TiO absorption in their atmospheres.

Next, I used the plasma photoionization code CLOUDY to explore whether there is a UV absorbing species in the stellar wind that can cause an early UV ingress in the transits of close-in exoplanets due to the presence of a bow shock compressing the coronal plasma. For all UV wavelengths, I find under realistic physical conditions for the corona that there are no species that can cause absorption with sufficient opacity. These conclusions suggest that UV asymmetry observations are not a suitable approach for exoplanet magnetic field detection. I also simulated escaping planetary gas in ionization and thermal equilibrium with the stellar radiation field with CLOUDY. From this model, I find species with strong absorption lines previously observed in exoplanet upper atmospheres but also make predictions for many species and lines not yet observed from X-rays to the radio domain.

Detection of radio emission from exoplanets can provide information on the star-planet system that is difficult to study otherwise, such as the planetary magnetic field, magnetosphere, rotation period, interior structure, atmospheric dynamics and escape, and star-planet interactions. Such a detection in the radio domain would open up a whole new field in the study of exoplanets. I created a pipeline for Low-Frequency Array (LOFAR)

beam-formed observations that mitigates radio frequency interference, calibrates the time-frequency response of the telescope, and searches for bursty planetary radio signals in the data. Next, I investigate the radio emission from Jupiter, scaled such that it mimics emission coming from an exoplanet, with low-frequency radio observations using the LOFAR. The goal is to determine up to what distance and with what strength radio emission from exoplanets can be detected using LOFAR. This is the first time that the sporadic nature of expected radio emission from exoplanets has been simulated. I find that radio bursts from an exoplanet located at 20 pc (encompassing tens of known exoplanets) could be detected if the flux is a million times stronger than the peak level of Jupiters radio emission. This finding is consistent with theoretical models that predict such strong radio emission can exist. The present study can be used as a guide to search for radio emission from exoplanets and to produce more reliable upper-limits for non-detections.

"If people sat outside and looked at the stars each night, I'll bet they'd live a lot differently." Bill Watterson

Acknowledgments

"If you think about it, your favorite memories, the most important moments in your life... were you alone?" Up in the Air (2009)

The journey to this day started on September 6, 2002 at 7:00pm (*I created a log, that's how I know*). On this day, I observed with my very own telescope for the first time and the first object was the planet Venus. The trek since then hasn't always followed a straight path but definitely has been made easier by the people along the way.

I will start by thanking my family for always being there for me and believing in me. I love you all very much! Dad, thank you for indulging in my Astronomy pursuits and helping me pursue my dreams. Chelsea, thanks for being my best sister (haha, see what I did there)! If it wasn't for you I wouldn't have known it was possible to escape Burg and pursue college and our dreams. Robert, thanks for also being the best brother and always being there even though I may be across the world somewhere! Grandma, you inspire me to be a better person everyday and to never take my family for granted! On this day, I can't help but think about my Grandpa (Bob Turner). During our last conversation, you said that you gave me the hardest job at TTT Construction so I would choose a different path and go to college. I love you Grandpa and today I've followed that path to a PhD (can you believe it)! I know if you were here you would be telling the best stories. To all my aunts and uncles, thank you for your help through it all! Thank you Uncle Jeff giving me my first telescope! Thank you Aunt Brenda for believing in me and helping me along my journey in many ways! Aunt Melinda thanks for the best hugs and hikes. To all my older cousins (Brandy, Colbie, Laree, Sarah, Kayt, Rob, Derik, Evan) I love you all! To all my younger cousins, I believe I'm graduating from 23rd grade and I love you too!

The first time I looked through any telescope was at a star party with the Southern

Colorado Astronomical Society (SCAS) at Lathrop State Park in the Summer of 2002. There is no doubt in my mind that I would not be here today without that initial spark. Thank you SCAS for expanding my mind and setting me on this course!

Another critical fork in my journey was attending the 2006 Advanced Teen Astronomy Camp at the University of Arizona the summer before my senior year of high school. At this camp, I observed my first exoplanet transit and from that moment on I was hooked. It was also here that I knew that I wanted to become an Astronomer. Thank you Don McCarthy for giving me this amazing opportunity! Thanks also for being there during undergraduate. During this camp, I for the first time meet other teenagers who loved astronomy. Some of these campers (Amy, Kelsey, Elizabeth, and Becky) I'm still good friends with until this day.

That brings me to Amy. Thank you for being the best friend anyone could ask for!! I know the path hasn't always been easy through it all. If it wasn't for you in undergraduate, I may not be here today. We've had many escapades, it is hard to pick just one to highlight (e.g. Astro Club adventures, dance performances, spoons, Mt. Graham cookie making). Can you believe that we have known each other for 12 years! I love you with all my heart and I can't wait to see what the next chapter brings in our friendship!

This moves me to my undergraduate days at the University of Arizona. Life at UofA was indeed a time to remember and shaped me both professionally and socially. EcoReps peeps (Tatiana, Brittany) thanks for always being there. You are definitely like family to me. RA friends (Ralphiee, Sean, Alyssa, Alan, Jackie, Paola, Steph, Jazmine, Christine) thanks for the amazing times!

Next, I would like to thank all my University of Arizona Astronomy friends. Astronomy club was home away from home. To all who went observing with me and reduced data, it was an adventure for sure! Kevin, I'm not sure how I would have made it this far without you. You have always been by my side and boy did we observe a lot! I can't believe we will be getting our PhD's one day apart (crazy!). Logan, thanks for being there for all the physics, life, and traveling adventures. I still remember the night when we got Sagan (he was so small). That trailer was pretty epic! I can't wait to see where our adventures take us next. Bri, thanks for your amazing friendship all these years! It has sure been an adventure and I can't wait to see what comes next.

Professionally, I have many people to recognize. To start, I would like to thank my first advisor Caitlin Griffith. Your guidance and support over these many years is greatly appreciated! You taught me more than I could have imagined. Thank you Robert Zellem and Johanna Teske for being amazing graduate student advisers to me in undergraduate and helping me grow as a researcher. Thank you Carl Schmidt and Duncan Christie for being great post-doc advisers! Thank you Philippe Zarka for your guidance as a mentor especially while in France!

I would especially like to thank my graduate advisers Robert (Bob) Johnson and Jean-Mathias Grießmeier for all your help and support over the years! Bob, thank you for believing in me and giving me the chance that no one else would. Your support over the past 5 years has been truly amazing and my graduate experience has been much greater for that reason. Jean-Mathias Grießmeier, thanks for giving me a shot to enter the exoplanetary radio field and helping me throughout my time in France.

As scientists we all build off and are inspired by the work that is done before us. I'm very glad to be build off the work of everyone before me. Two of my main inspirations have been Galileo Galilei and Stephen Hawking. Thank you for being part of the journey of science!

I think this leads into all my friends/colleagues made during graduate school. To my fellow UVA astro grads in my year (Andrew, Lauren, Trey, Patrick) and beyond (Sandy, Rachael, Bill, Tuck, Johanna) thank you for all your help and support over the years but especially that first year. Allision P.M. thanks for being there through it all (Arizona corner for life!)! To all the grads in the department, it sure has been an adventure going on this ride (aka grad school) with you! To my friends made during my time in Orleans, France, merci beaucoup! Zak, mon frère, I still remember when we meet the first day I was in Orleans. Who knew then that we would forever be best friends and brothers. Thanks for all your help and our grand Orleans/Paris adventures (the good and bad)! Thank you to the crew (Alba, Kévin, Dounia, Roberto, Sarah, Thomas, Rim, Allan) for all the great memories in Orleans! I hope we can all meet again somewhere in the world.

Also, thank you to the Cooperative Housing at the University of Virginia (CHÜVA) for an amazing two years! The friends I've made from living in CHÜVA will last forever. There is no doubt that living here has improved my mental health throughout graduate

school. Special thanks to Dale (El presidente), Andon, Vince, Liz, Kristin, Ariel Salvaro (my economist friend), Nitesh, Emma (the artist), and Jess for your friendship! I truly believe that communities like this bring light to the world. CHÜVA will always be home to me! #CHÜVA4Life

I would like to thank Veronica Fitzhugh (yes her, a real-life nazi-fighter, community activist, Sith-lord princess) for all your love and support these past 6 months! There is no doubt that you helped keep me more sane during the long post-doc job applications and thesis writhing process. I'm not sure what I would have done without you. Indeed, life is better with company.

Thank you to all the teachers I've had throughout my education! Specifically, thank you Mrs. Benine (my high school math, chemistry, and physics teacher) for setting the foundation of my STEM education! Thank you Mrs. Baker for being an amazing art teacher and mentor. At UofA, I would like to thank Shawn Jackson for being the most amazing (and very tough) physics teacher I've ever had. Thank you Albrecht Classen for the most amazing study abroad experience. Finally, thank you to everyone I've encountered along my path (personally or professionally) for being on this journey with me! The journey is the destination!

P.S. This was one of the hardest sections to write in my thesis.

Table of contents

List of Figures

List of Tables

Chapter 1

Introduction

"There are infinite worlds both like and unlike this world of ours." Epicurus (300 BCE)

1.1 Context

The study of exoplanets is ultimately derived from humanity's need to understand our place in the universe. Questions like "Are we alone?" or "Are there planets like Earth out there?" have been asked for thousands of years and only answered through philosophy or science fiction. It was only 26 years ago that the first exoplanet was discovered orbiting a pulsar (Wolszczan & Frail 1992) but the "offical" start of the field of exoplanets was not until 1995 after the discovery of the fist planet around a solar-like star (Mayor & Queloz 1995). Since then, the field of exoplanets has grown into one of the most vibrant and fast-paced in all of modern astronomy. Today, it is thought that every star has on average one planet orbiting around it (Cassan et al. 2012; Batalha 2014). We are now for the first time in human history starting to answer these age old questions and formulating new ones along the way.

There are currently over 4000 discovered exoplanets and many of these planets (ranging from super-Earths to hot Jupiters) are unlike those in our Solar System (NASA Exoplanet Archive; Akeson et al. 2013). An example of the diversity of planets can be seen by examining the mass- or radius-period distribution for known planets (Figure 1.1). Measuring exoplanet parameters provides insights into planet formation, the architecture of planetary systems, and even the possibility of planetary habitability (e.g. Howard et al. 2013). A va-

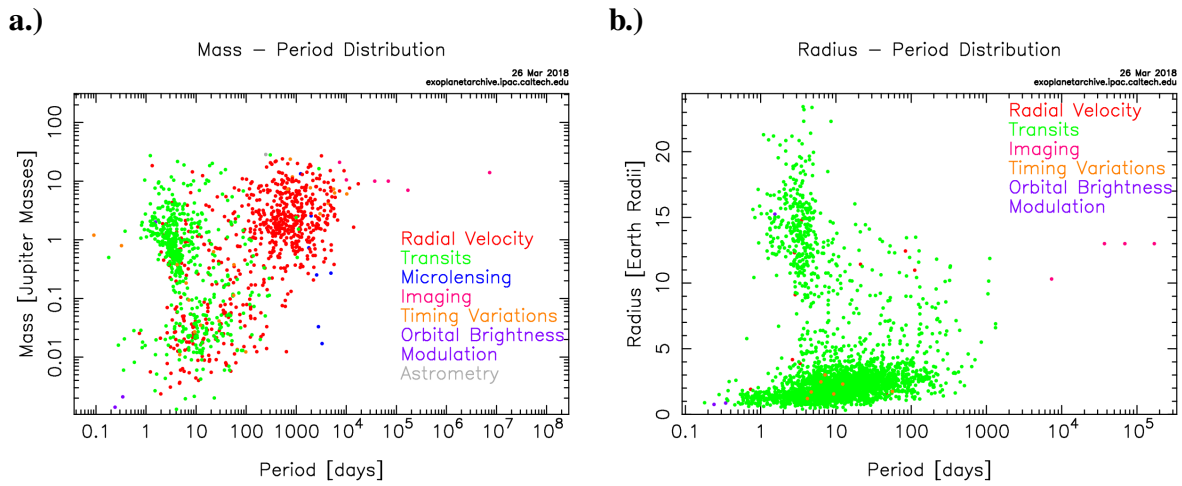

Figure 1.1: Mass-period (panel **a**) and radius-period (panel **b**) distribution for the confirmed exoplanets (as of 26 March 2018) in the Exoplanet Archive Database. The planets discovered by the various detection techniques are highlighted in different colors. Plots are taken from the Exoplanet Archive Database.

riety of techniques have been developed to detect and study the radii, masses, temperatures, orbital parameters, and atmospheric compositions of these exoplanets (e.g. Charbonneau et al. 2000). However, one of the most elusive goals in exoplanet science today is the detection of their magnetic fields (Zarka et al. 2015; Grießmeier et al. 2015).

1.2 Exoplanet Magnetic Fields

1.2.1 What can be learned from a measurement of the magnetic field of an exoplanet?

All of the planets in our Solar System, except Venus, have or used to have a magnetic field (Russell & Dougherty 2010) and interior structure models predict that many exoplanets should have them as well (Sánchez-Lavega 2004). Observations of an exoplanet's magnetic field would allow constraints on planetary properties difficult to study such as their interior structure (composition and thermal state), atmospheric dynamics and escape, and the physics of star-planet interactions (Hess & Zarka 2011; Zarka et al. 2015; Grießmeier

et al. 2015; Lazio et al. 2016). Historically, the first constraints on the interior structures of the Solar System gas giants came from the knowledge that they had magnetic fields. Additionally, magnetic drag could also be an important factor for solving the anomalous radii problem of hot Jupiters (Perna et al. 2010a,b; Koskinen et al. 2014). The presence of magnetic fields on gas giants also affects the understanding of their origins and evolution (Lovelace et al. 2008; Mordasini et al. 2012). For example, it was found that the migration timescale for gas giants is inversely proportional to the radius of the planetary magnetosphere and thus its magnetic field strength (Lovelace et al. 2008). Finally, the magnetic field of Earth is thought to help contribute to its sustained habitability by deflecting energetic stellar wind particles, cosmic rays, and UV radiation (Grießmeier et al. 2005, 2009, 2015; Lazio et al. 2010; Lammer et al. 2009; Kasting 2010; Lazio et al. 2016). Therefore, this characteristic may also be important for assessing the habitability of exoplanets.

1.3 Exoplanet Radio Emission

It has been suggested that an exoplanet's magnetic field can be detected through radio emission from the planet generated by the electron-cyclotron maser instability (CMI; Farrell et al. 1999). All the magnetized planets and moons in our Solar System emit in the radio by the CMI mechanism (Zarka 1998). Planetary CMI radio emission is caused by fast electrons from the stellar wind or coronal mass ejections interacting with the magnetosphere or by electron acceleration processes inside the magnetosphere (e.g., co-rotation breakdown in the Jupiter plasma torus; Cowley et al. 2003). CMI emission occurs at the cyclotron frequency (or gyrofrequency) in the source region, $f_g = 2.8\left[B_p/(1\ G)\right]$ MHz, up to a maximum frequency that corresponds to the strength of the magnetic field near the planetary surface above the magnetic pole (B_p). Observing emission over a range of frequencies could in principle be used to determine the exoplanet's radio spectrum and thus its magnetic field strength. As seen in Figure 1.2, the radio spectrum for the Solar System planets is complex below the maximum local gyrofrequency, which corresponds to the planet's polar magnetic field. For the magnetized planets in our Solar System it is known that CMI emission is not isotropic (Zarka 1998). For example, the decametric (3–40 MHz with wavelengths of 10–100 meters) emission from the Jovian auroral oval has a beaming

angle θ = 1.6 sr (Zarka et al. 2004). Simulations of the expected radio dynamic spectrum from hot Jupiters show that radio emission may only be detectable over a few percent of its orbital phase due to the beaming of CMI (Hess & Zarka 2011). Additionally, the CMI emission from Jupiter is intrinsically variable from millisecond to hour timescales (e.g. Lecacheux et al. 2004; Marques et al. 2017).

1.3.1 Can the radio emission from exoplanets be detected?

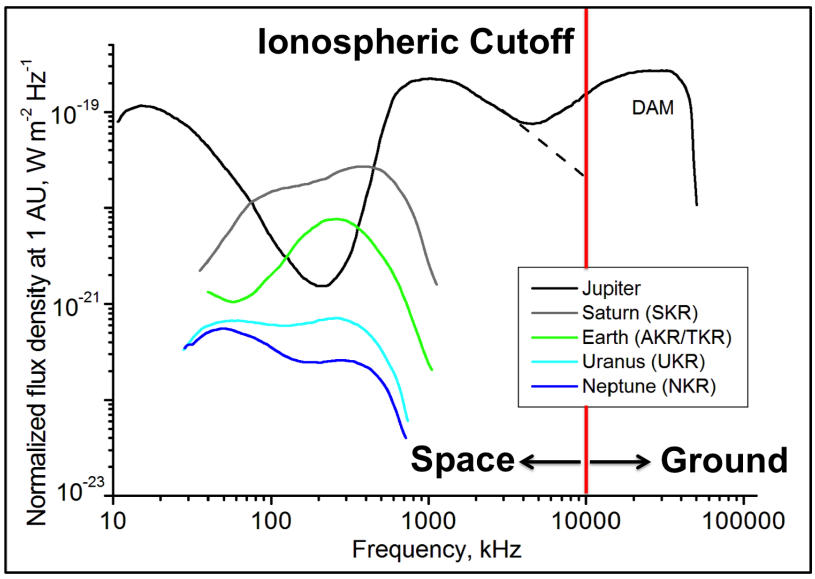

Figure 1.2: Comparative magnetospheric radio emission spectra for the planets in our Solar System. The ionospheric cutoff is at 10 MHz (red vertical line). Therefore, Jupiter's decametric radio emission (DAM) is the only emission observation from the ground. Plot taken from Zarka (2007).

Theoretical models can be used as a guide to determine whether radio emission from exoplanets can be observed with current ground-based radio telescopes. Of the Solar System planets, only Jupiter has a strong enough magnetic field to produce CMI emission at frequencies detectable from the ground (e.g., a planet must have a field stronger than 3 G to radiate at frequencies above the ionospheric cutoff of 10 MHz, shown in Figure 1.2). For the predicted magnetic field strengths of hot Jupiters (0.5 – 250 G; Sánchez-Lavega 2004; Reiners & Christensen 2010; Christensen 2010), the emission frequency overlaps with the

frequencies (10-400 MHz) observed by many ground-based low-frequency radio telescopes (e.g., LOFAR, MWA, GMRT, JVLA) (Grießmeier 2015). The magnetic field predictions for smaller planets would produce an emission frequency below 10 MHz (Zuluaga et al. 2013). Thus only hot Jupiters are predicted to be observable from the ground. However, the uncertainties in the magnetic field strength predictions can be about an order of magnitude depending on whether a rotational-independent (Christensen 2010) or rotational-dependent (Sánchez-Lavega 2004; Grießmeier et al. 2007) scaling-law is used. An overview all of all all scaling laws can be found in Christensen (2010) and Table 1.1. Additionally, a magnetic scaling law was found to exist between the emitted radio power of the magnetized Solar System planets/moons and the incident power from the solar wind (panel a in Figure 1.3). From this scaling law, hot Jupiters are estimated to have $10^3 - 10^6$ times greater radio power than that of Jupiter because a planet so close to the star experiences a much greater stellar wind flux. If we combine the estimate for magnetic field strengths and the radio power scaling law, we find that at least dozens of known exoplanets may emit at a frequency range and flux levels detectable by current telescopes (panel b in Figure 1.3). The systemic uncertainties on these scaling laws are large (Christensen 2010; Grießmeier 2015), therefore, observations are needed to confirm and refine these predictions.

Many ground-based studies conducted to find exoplanet radio emission have resulted in non-detections (Yantis et al. 1977; Winglee et al. 1986; Bastian et al. 2000; Lazio & Farrell 2007; Hallinan et al. 2013; Zarka et al. 2015; Grießmeier 2015). There are a few possible detections (Lecavelier des Etangs et al. 2013; Sirothia et al. 2014) but none have been confirmed by follow-up observations. The reasons for the non-detections are degenerate: (1) the observations were not sensitive enough, (2) the planetary magnetic field is not strong enough to emit at the observed frequencies, or (3) Earth was outside the beaming pattern of the radio emission (Hallinan et al. 2013; Zarka et al. 2015; Grießmeier 2015).

1.3.2 What can be learned from exoplanetary radio emissions?

The most important property obtained from radio emission observations of an exoplanet is the strength of the planetary magnetic field. Additionally, radio observations will allow constraints on the magnetosphere structure, planetary space environment (solar wind den-

Table 1.1: Proposed scaling laws for planetary magnetic fields in the literature. This table was reproduced from Christensen (2010).

#	Scaling Rule	Reference	Notes
1	$\mathrm{B}_p R_p^3 \propto \left(\rho_c \Omega R_p^5\right)^a$	1	Magnetic Bode Law
2	$\mathrm{B}^2 \propto \rho_c \Omega^2 R_c^2$	2	
3	$\mathrm{B}^2 \propto \rho_c \Omega \sigma^{-1}$	3	Elsasser number rule
4	$\mathrm{B}^2 \propto \rho_c R_c^3 q_c \sigma$	4	at low energy flux
5	$\mathrm{B}^2 \propto \rho_c \Omega R_c^{5/3} q_c^{1/3}$	5	mixing length theory
6	$\mathrm{B}^2 \propto \rho_c \Omega^{3/2} R_c \sigma^{-1/2}$	6	
7	$\mathrm{B}^2 \propto \rho_c \Omega^2 R_c$	7	
8	$\mathrm{B}^2 \propto \rho_c \Omega^{1/2} R_c^{3/2} q_c^{1/2}$	8	MAC balance
9	$\mathrm{B}^2 \propto \rho_c R_c^{4/3} q_c^{2/3}$	9	energy flux scaling

Symbols. — B_p: Planetary magnetic field strength at the surface; R_p: Planetary radius; ρ_c: Density of the planetary core; Ω: Planetary rotation rate; B: Magnetic field strength inside the dynamo; R_c: Radius of the electrically conducting fluid core of the planet; σ: Conductivity of the planetary core; q_c: Convected energy flux in the planetary core

References. — (1) Russell 1978; (2) Busse 1976; (3) Stevenson 1979; (4) Stevenson 1984; (5) Curtis & Ness 1986, modified; (6) Mizutani et al. 1992; (7) Sano 1993; (8) Starchenko & Jones 2002; (9) Christensen & Aubert 2006

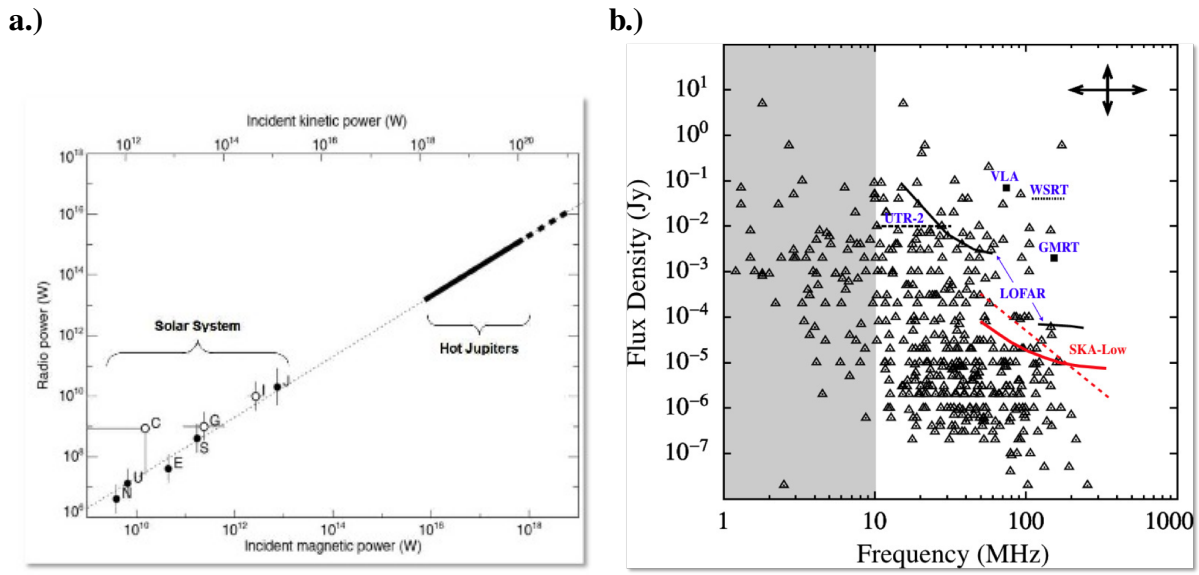

Figure 1.3: **(a)** Radio power scaling law comparing the average radio power from the Solar System planets/moons to the incident magnetic/kinetic power of the solar wind. For hot Jupiters, their radio power is predicted to be $10^4 - 10^6$ times greater than Jupiter's radio power. **(b)** Maximum predicted emission frequency and radio flux for known exoplanets as of 2011 (triangle symbols) using the magnetic scaling law and predicted magnetic field strengths (Grießmeier et al. 2007). The sensitivities for specific radio telescopes are labeled. Plots are taken from Zarka et al. (2015).

sity, etc.), orbital-inclination, the planetary rotation period, and the presence of extrasolar moons (Hess & Zarka 2011; Zarka et al. 2015). All of these parameters are extremely difficult to study otherwise. For non-transiting planets the planetary mass is not known exactly but there is an inclination ambiguity, therefore, observing radio emissions from these planets may allow for a more accurate determination of their masses.

1.4 Near-UV Light Curve Asymmetries

Aside from radio observations, the other main method proposed for studying exoplanet magnetic fields is near-UV light curve asymmetries. Two hot Jupiters have been found to show an earlier transit ingress in the UV than in the optical (Fossati et al. 2010; Ben-Jaffel & Ballester 2013). This observation has been tentatively explained by the presence of a bow shock on the leading edge of the planet formed by interactions between the planet's magnetosphere and the stellar coronal plasma (Vidotto et al. 2010a; Llama et al. 2011). If the shocked material in the magnetosheath is optically thick, it will absorb starlight and cause an early ingress in the near-UV light curve (Vidotto et al. 2011b, Figure 1.4). Thus the difference between ingress times in different wavelength bands can help constrain the properties of the planet's magnetic field. Vidotto et al. (2011a) predict that near-UV ingress asymmetries should be common in transiting exoplanets and tabulated a list of the 92 targets that should exhibit this effect. However, other studies suggest that the UV absorption is due to atmospheric escape (Lai et al. 2010; Bisikalo et al. 2013a) or exomoons (Ben-Jaffel & Ballester 2014; Kislyakova et al. 2016), which does not require the presence of a magnetic field.

1.5 Atmospheres of Transiting Exoplanets

Most of the planets discovered to date have been found using the transit method in large-scale transit surveys such as *Kepler*, *WASP*, and *CoRoT*. Transiting exoplanet systems (TEPs) are of great interest because their radius can be directly measured in relation to their star with photometric observations (Charbonneau et al. 2000). With the addition of spectroscopic and radial velocity measurements, many physical properties of TEP systems

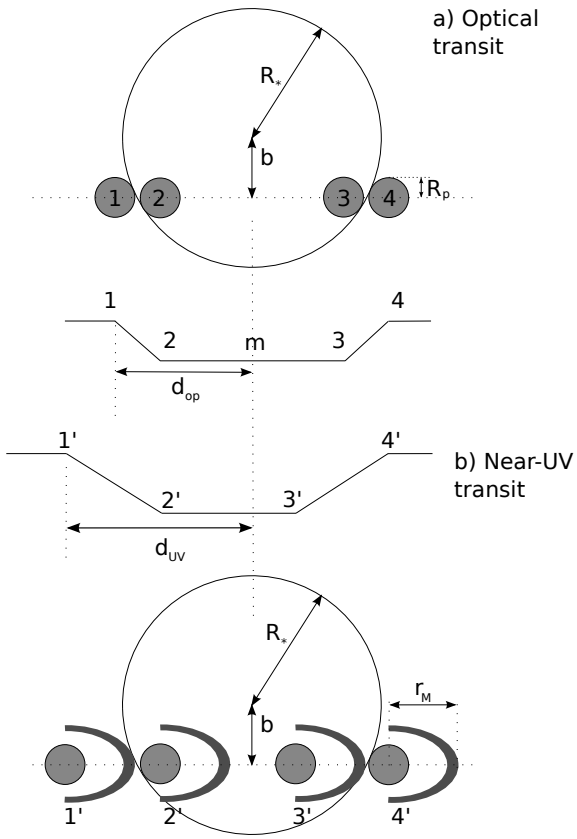

Figure 1.4: Diagram of transiting exoplanet light curves in the (a) optical and (b) near-UV, where the bow shock surrounding the planets magnetosphere is also able to absorb stellar radiation. Plot taken from Vidotto et al. (2011b).

(mass, radius, semi-major axis, gravity, temperature, eccentricity, orbital period) can be directly measured. Additionally, multiple-band photometry of a TEP system can be used to constrain the composition of an exoplanet's atmosphere (Seager & Sasselov 2000). The absorption properties of different species in a planetary atmosphere vary with wavelength, causing an observable variation in the planet's radius. Photometric light curve analysis can also be used to search for transit timing variations (TTVs). TTVs can indicate additional bodies in a TEP system (Miralda-Escudé 2002).

Exoplanet atmospheres in the optical can be dominated by hazes, absorption, and Mie or Rayleigh scattering (Seager & Sasselov 2000; Hubeny et al. 2003; Griffith 2014). Among the species that absorb in the optical wavelengths in exoplanetary atmospheres, titanium

oxide (TiO), sodium (Na), potassium (K), and water (H_2O) are expected to be the most abundant (Seager & Sasselov 2000). TiO is theoretically predicted to play an important role in the energy redistribution from the optical to the infrared and in generating temperature inversions in the atmosphere of the hottest hot Jupiters above 2000 K equilibrium temperature (Hubeny et al. 2003). Being generated in the lower thermosphere, the intensity of the H_2O bands indicates whether an additional source of opacity such as clouds or hazes is present in the atmosphere (Sing et al. 2016). Combining the complementary information on the presence of clouds by the H_2O and K spectral features will allow for a more complete picture of clouds and elemental abundances. Water has been repeatedly observed in the atmosphere of hot Jupiters both from space with *HST* and from the ground at high spectral resolution (e.g. Deming & Seager 2017). Na and K have also been observed in the atmospheres of hot gas giants (e.g. Sing et al. 2016). An example of a ground-based transmission spectra of the transiting hot Jupiter WASP-19b can be found in Figure 1.5. This spectra indicates the presence of H_2O, TiO, Na, and haze in the planet's atmosphere and is, to-date, among one of the best observations obtained from the ground.

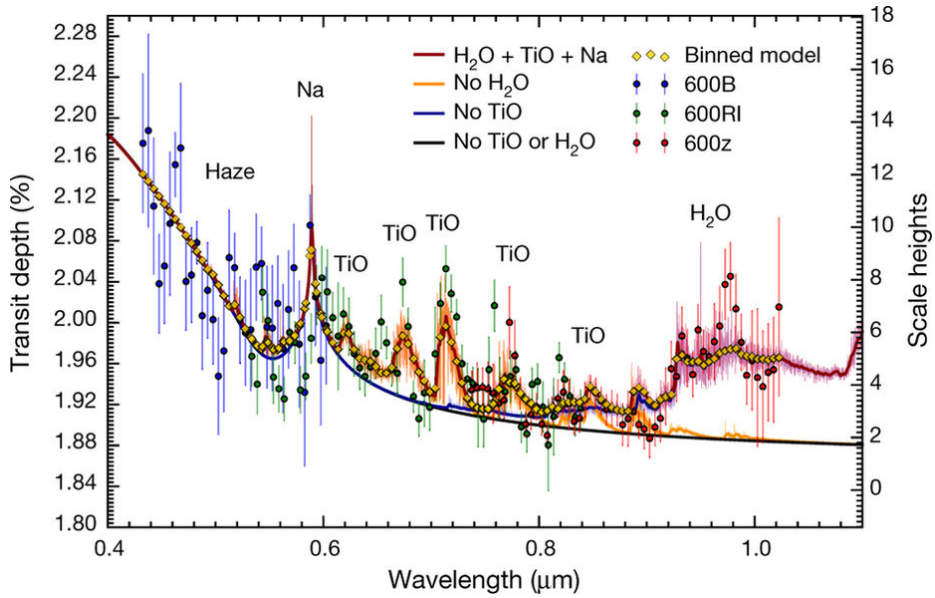

Figure 1.5: Transmission spectrum of the transiting hot Jupiter WASP-19b from Very Large Telescope observations (blue, green, red circles). The best-fitting spectrum (red-curve) includes opacity from H_2O, TiO, Na, and a global haze. Plot taken from Sedaghati et al. (2017).

Optical spectral observations also have the advantage of defining the slope of the transmission spectrum and thus the opacity source (Griffith 2014). If Mie scattering is observed it is a sign of aerosols in the planetary atmosphere and the sizes and distribution of the particles can be determined through the exact slope. Mie scattering is mainly wavelength independent and occurs when the particle sizes are larger than the observed wavelength. A Rayleigh scattering signature on the other hand would be an indication of scattering by the ambient gas. Rayleigh scattering is highly wavelength dependent ($\propto \lambda^4$) and occurs when the wavelength of light is smaller than the particle size. If Rayleigh scattering is observed, the mixing ratios of H_2O and methane in the atmospheres of hot Jupiters can be constrained within an order of magnitude (Griffith 2014). The H_2O and methane observations, taken alone, can not be used to constrain the composition precisely, because the derived mixing ratio depends strongly on the assumed radius at a specific pressure (usually at an altitude where the pressure if of the order of 10 bars). That is, it remains unclear whether it is the core of the planet or the opacity of the atmospheric gas that blocks out the stellar light. Finally, clouds and/or hazes have been found in nearly half of hot Jupiter atmospheres (Sing et al. 2016). Clouds reduce the strength of spectral features thus causing the optical transmission spectrum to be flat with wavelength (Seager & Sasselov 2000; Kreidberg et al. 2014).

1.6 Contents of the Thesis

In this thesis, I present detailed studies of the magnetic fields and atmospheres of close-in exoplanets using both observations (near-UV, optical, and radio) and theory.

In Chapter 2, I present the study of ground-based near-UV observations of 15 transiting exoplanets. The purpose of this chapter is to search for asymmetrical near-UV light curves that would be indicative of a bow shock and to constrain their planetary atmospheres if the transits do no exhibit asymmetries. This study was published in June 2016 in the *Monthly Notices of the Royal Astronomical Society*, 459, 789.

I investigate the environment around close-in transiting exoplanets using the CLOUDY plasma simulation code in Chapter 3. In this work, I show that under realistic physical conditions for the stellar corona there are not any species that can cause an absorption

with sufficient opacity to produce a detectable transit depth for any wavelength between X-ray and radio (including near-UV). Additionally, I simulate escaping planetary gas in ionization and thermal equilibrium with the stellar radiation field and promising sources of opacity from the X-ray to radio wavelengths are discussed, some of which are not yet observed. This work was published in June 2016 in the *Monthly Notices of the Royal Astronomical Society*, 458, 3880.

The physical properties and atmospheres of 11 transiting hot Jupiters observed with the 1.5-m Kuiper Telescope are studied in Chapter 4. This work was published in December 2017 in the *Monthly Notices of the Royal Astronomical Society*, 472, 3871 and was done in coordination with University of Virginia undergraduate student Robin Leiter.

In Chapter 5, I describe the data reduction pipeline created to analysis beam-formed LOFAR Low-band Antenna (14- 74 MHz) observations and the initial analysis of 4 hours of data on the exoplanetary system 55 Cnc. This study was published in October 2017 in *Planetary Radio Emissions VIII*, 301-303.

Finally, I investigate the radio emission from Jupiter, scaled such that it mimics emission coming from an exoplanet, with low-frequency beam-formed observations using LOFAR in Chapter 6. The goals are to define a set of observables that can be used as a guideline in the search for exoplanetary radio emission and to measure effectively the sensitivity limit for LOFAR beam-formed observations. This study was submitted for publication to *Astronomy & Astrophysics* in February 2018 and is currently undergoing review.

Chapter 2

Ground-based near-UV observations of 15 transiting exoplanets: Constraints on their atmospheres and no evidence for asymmetrical transits

"It's been said that astronomy is a humbling and, I might add, a character-building experience." Carl Sagan

The text in this chapter is reproduced primarily from Turner J.D., et al. 2016. Ground-based near-UV observations of 15 transiting exoplanets: Constraints on their atmospheres and no evidence for asymmetrical transits. MNRAS. 459. 789.

2.1 Introduction

Near-ultraviolet (near-UV) transits of short period exoplanets are a great tool to study star-planet interactions (e.g. tidal, gravitational, magnetic) and the scattering properties of their atmospheres (e.g. Fossati et al. 2015). The atmospheres of hot Jovian exoplanets in the near-UV (300 – 450 nm) can be dominated by Rayleigh scattering, other forms of scattering or absorption, or clouds/hazes (Seager & Sasselov 2000; Brown 2001; Benneke

& Seager 2013; Benneke & Seager 2012; Griffith 2014). Clouds reduce the strength of spectral features thus causing the transit depth from near-UV to optical to be constant (Seager & Sasselov 2000; Brown 2001; Gibson et al. 2013b; Kreidberg et al. 2014; Knutson et al. 2014a), and the Rayleigh scattering signature causes the transit depth to increase in the near-UV (Lecavelier Des Etangs et al. 2008; Tinetti et al. 2010; de Wit & Seager 2013; Griffith 2014). Additionally, near-UV transits may exhibit asymmetries in their light curves such as ingress/egress timing differences, asymmetric transit shapes, longer durations, or significantly deeper transit depths ($>\sim 1\%$) than the optical (e.g. Vidal-Madjar et al. 2003; Fossati et al. 2010; Ehrenreich et al. 2012; Kulow et al. 2014). The physical interpretations of these abnormalities vary, and include bow shocks, tidal interactions, star-planet magnetic interactions, a plasma torus originating from an active satellite, or escaping planetary atmospheres (e.g. Vidotto et al. 2010a; Lai et al. 2010; Ben-Jaffel & Ballester 2014; Matsakos et al. 2015).

There are 19 exoplanets with ground- or space-based observations in the UV (100–450 nm). These observations can be subdivided into two groups: asymmetric and symmetric light curves. There are 5 exoplanets (55 Cnc b, GJ 436b, HD 189733b, HD 209458b, WASP-12b) where asymmetries in their light curves are observed (Ehrenreich et al. 2012; Kulow et al. 2014; Ehrenreich et al. 2015;Ben-Jaffel & Ballester 2013; Vidal-Madjar et al. 2003; Ben-Jaffel 2007; Ben-Jaffel 2008, Vidal-Madjar et al. 2004; Vidal-Madjar et al. 2008; Vidal-Madjar et al. 2013; Ben-Jaffel & Ballester 2013; Fossati et al. 2010; Haswell et al. 2012; Nichols et al. 2015). For the symmetric transits, 9 hot Jupiters (HAT-P-1b, HAT-P-12b, HAT-P-16b, TrES-3b, WASP-12b, WASP-17b, WASP-19b, WASP-43b, WASP-39b) are observed to have a constant planetary radii from near-UV to optical wavelengths (Turner et al. 2013; Copperwheat et al. 2013; Pearson et al. 2014; Bento et al. 2014; Nikolov et al. 2014; Mallonn et al. 2015a; Ricci et al. 2015; Sing et al. 2016). Additionally, 11 exoplanets with symmetric light curves (GJ 3470b, HD 189733b, HD 209458b, HAT-P-5b, HATP-12b, WASP-6b, WASP-12b, WASP-17b, WASP-31b, WASP-39b, XO-2b) are observed to have a larger near-UV radii than optical wavelengths (Sing et al. 2008, Lecavelier Des Etangs et al. 2008; Sing et al. 2011; Southworth et al. 2012b, Sing et al. 2013; Nascimbeni et al. 2013; Sing et al. 2015; Zellem et al. 2015; Sing et al. 2016). There seems to be a wavelength distinction between asymmetric and symmetric light curves, where asymmetric transits

are only observed below 300 nm. However, recent observations of asymmetric transits at optical wavelengths (Rappaport et al. 2012; Rappaport et al. 2014; van Werkhoven et al. 2014; Cabrera et al. 2015; Cauley et al. 2015) hint that this dichotomy might not be the case.

In this study, we investigate whether ground-based near-UV observations exhibit asymmetries. Most notably, it was predicted that a transiting exoplanet can potentially show an earlier transit ingress in the UV than in the optical, while the transit egress times will be unaffected due to the early absorption of star light due to a bow shock (Vidotto et al. 2010a, 2011a,b; Vidotto et al. 2011c; Llama et al. 2011, 2013). Additionally, the near-UV transit will have a greater drop in flux than the optical transit and will no longer be symmetric about the mid-transit time (Vidotto et al. 2011b; Llama et al. 2011, 2013). This effect is explained by the presence of a bow shock on the leading edge of the planet formed by interactions between the planet's magnetosphere and the stellar coronal plasma. If the shocked material in the magnetosheath becomes sufficiently opaque, it will absorb starlight and cause an early ingress in the near-UV light curve (Vidotto et al. 2011b, see fig. 6). Vidotto et al. (2011a, hereafter VJH11a) predict that near-UV ingress asymmetries should be common in transiting exoplanets and tabulated a list of the 69 targets that should exhibit this effect.

Is it possible to observe near-UV asymmetries from the ground? Previous space-based observations of an early ingress on WASP-12b and HD 189733b observe a flux drop difference of about $\sim 1\%$ and a timing difference of $\geq$30 minutes between the near-UV and optical light curves (Fossati et al. 2010; Haswell et al. 2012; Ben-Jaffel & Ballester 2013; Nichols et al. 2015). Both these properties are well within reach for ground-based meter-sized telescopes (e.g. Copperwheat et al. 2013; Turner et al. 2013; Pearson et al. 2014), like the Steward Observatory 1.55-m Kuiper Telescope used for the near-UV observations in this study. Additionally, Nichols et al. 2015 find that summing over the entire NUV band (253.9–281.1 *nm*) on *Hubble Space Telescope* (*HST*) still resulted in an early ingress, which they attributed to a blend of thousands of lines of metals (e.g. Mg, Na, Fe, Al, Co, Al Mn). Therefore, ground-based broadband near-UV observations (303–417 nm) might also experience an early near-UV ingress by the blending of lots of lines from the same metal species that exist at *HST* wavelengths (e.g. Na I/II, Ca II/III, Na I, Mg I, Al I, Mn

I/II, Fe I/II, Co I/II; Morton 1991, 2000; Sansonetti 2005). Therefore, it is be feasible to observe near-UV asymmetries from the ground by taking all the factors discussed above into consideration.

However, recent studies by Ben-Jaffel & Ballester (2014) and Turner et al. (2016a) cast doubt on observing asymmetries in all ground- and space-based UV wavelengths using the VJH11a bow shock model. Ben-Jaffel & Ballester (2014) use simple recombination and ionization equilibrium calculations for realistic parameters of the stellar corona ($T \sim 10^6$K; Aschwanden 2005) to determine that only highly ionized stages of heavy elements can cause any detectable optical depth. Furthermore, Turner et al. (2016a) use the plasma photoionization and microphysics code `CLOUDY` (Ferland et al. 1998; Ferland et al. 2013) to investigate all opacity sources at UV and optical wavelengths that could cause an early ingress due to the presence of a bow shock compressing the coronal plasma. Turner et al. (2016a) also find that the optical depths in the compressed stellar wind ($T \sim 10^6$K; Aschwanden 2005, $n \sim 10^4$cm^{-3}; McKenzie et al. 1997) are orders of magnitude too small ($> 3 \times 10^{-7}$) to cause an observable absorption in space- and ground-based UV and optical observations (even for stellar wind densities 10^4 times higher than what is expected).

The goals of this paper are to study the atmospheres of 15 transiting exoplanet targets and to determine whether ground-based near-UV transit observations are sensitive to light curve asymmetries. Our data can be used to confirm the predictions by Ben-Jaffel & Ballester (2014) and Turner et al. (2016a) that an early ingress should not be present in ground- and space-based near-UV transits. Our sample is chosen to contain a wide variety of different system parameters to determine if any system parameters correlate with the existence of a bow shock (Table 2.1). We also perform follow-up ground-based near-UV observations of WASP-12b (Copperwheat et al. 2013) and HAT-P-16b (Pearson et al. 2014). Using our data set, we update the planetary system parameters (Section 2.4), present a new ephemeris to aid in future observations (Section 2.4.1), and search for a wavelength dependence in the planetary radii that can be used to constrain their atmospheric compositions (Section 2.6.2).

Table 2.1: Comparison of the planetary systems in this study[a]

Planet Name	M_p (M_{Jup})	R_p (R_{Jup})	a (AU)	P_p (d)	Spec. Type	M_* ($M_\odot$)	R_* ($R_\odot$)	$[Fe/H]$	$\log(R'_{hk})$[c]	λ[b] (°)
CoRoT-1b	1.03	1.49	0.025	1.51	G0V	0.95	1.11	-0.30	-5.132	77[d]
GJ346b	0.072	0.38	0.029	2.63	M2.5V	0.45	0.46	-0.32	-5.298	–
HAT-P-1b	0.53	1.24	0.055	4.47	G0V	1.13	1.14	0.13	-4.984	3.7[e]
HAT-P-13b	0.85	1.28	0.043	2.92	G4	1.22	1.56	0.43	-5.134	1.9[f]
HAT-P-16b	4.2	1.29	0.041	2.78	F8	1.22	1.24	0.17	-4.864	-10[g]
HAT-P-22b	2.15	1.08	0.041	3.21	G5	0.92	1.04	0.22	–	–
TrES-2b	1.19	1.22	0.036	2.47	G0V	0.98	1.0	-0.15	-4.949	-9[h]
TrES-4b	0.91	1.78	0.051	3.55	F	1.39	1.82	0.14	-5.104	6.3[i]
WASP-1b	1.03	1.49	0.025	1.51	F7V	0.95	1.11	-0.30	-5.114	-59[j]
WASP-12b	1.35	1.79	0.023	1.09	G0	1.28	1.63	0.30	-5.500	63[k]
WASP-33b	1.76	1.50	0.026	1.22	A5	1.5	1.44	0.1	–	251.6[l]
WASP-36b	2.26	1.27	0.026	1.54	G2	1.02	0.94	-0.31	–	–
WASP-44b	0.89	1.14	0.035	2.42	G8V	0.95	0.93	0.06	–	–
WASP-48b	0.97	1.67	0.034	2.14	G	1.19	1.75	-0.12	–	–
WASP-77Ab	1.76	1.21	0.024	1.36	G8V	1.0	0.96	0.1	–	–

[a] Information about the systems is obtained from the Exoplanet Data Explorer at exoplanets.org (Wright et al. 2011)

[b] λ is the angle between the sky projections of the planetary orbital axis and the stellar rotation axis

References. — (c) Knutson et al. (2010); (d) Pont et al. 2010; (e) Johnson et al. 2008; (f) Winn et al. 2010; (g) Moutou et al. 2011; (h) Winn et al. 2008a; (i) Narita et al. 2010; (j) Albrecht et al. 2011; (k) Albrecht et al. 2012; (l) Collier Cameron et al. 2010

2.2 Observations and Data Reduction

All of our observations were conducted at the University of Arizona's Steward Observatory 1.55-m (61") Kuiper Telescope on Mt. Bigelow near Tucson, Arizona, using the Mont4k CCD. The Mont4k CCD contains a 4096×4096 pixel sensor with a field of view of 9.7'×9.7'. We used 3×3 binning to achieve a resolution of 0.43"/pixel and shorten our readout time to ∼10 s. Our observations were taken with the Bessell U (303–417 nm), Harris B (360–500 nm), Harris V (473–686 nm), and Harris R (550–900 nm) photometric band filters. Specifically, the Bessell U filter is a near-UV filter and has a transmission peak of 70 per cent near 370 nm. To ensure accurate timing in these observations, the clocks were synchronized with an NTP time server every few seconds. In all the data sets, the average shift in the centroid of our targets is less than 1 pixel (0.43") due to excellent autoguiding (the max is 3 pixels), which minimizes our need to worry about intrapixel sensitivity. Seeing ranged from 0.86–4.12" throughout our complete set of observations. A summary of all our observations is displayed in Table 2.2.

To reduce the data we use the automated reduction pipeline `ExoDRPL`[1] which generates a series of `IRAF`[2] scripts that calibrate images using standard reduction procedures and perform aperture photometry (Pearson et al. 2014). Each of our images are bias-subtracted and flat-fielded. Turner et al. (2013) determined that using more than 10 flat-field images in the reduction of Kuiper/Mont4k data does not significantly reduce the noise in the resulting images. To optimize telescope time, we use 10 flat-field images and 10 bias frames in our all of our observations and reductions.

To produce the light curve for each observation we perform aperture photometry (using the task `phot` in the `IRAF DAOPHOT` package) by measuring the flux from our target star as well as the flux from up to eight different reference stars with 110 different circular aperture radii. We insure that each reference star is not a variable star by checking the Aladin Sky Atlas[3], the International Variable Star Index[4], and by examining their light curves divided

[1] https://sites.google.com/a/email.arizona.edu/kyle-pearson/exodrpl

[2] `IRAF` is distributed by the National Optical Astronomy Observatory, which is operated by the Association of Universities for Research in Astronomy, Inc., under cooperative agreement with the National Science Foundation.

[3] http://aladin.u-strasbg.fr/; Bonnarel et al. 2000

[4] http://www.aavso.org/vsx

by the average of the other reference stars. The aperture radii sizes we explore differ for every observation due to changes in seeing conditions. For the analysis we use a constant sky annulus for every night of observation of each target (a different sky annulus is used depending on the seeing for each date and the crowdedness of the field for each target). The sky analysis is chosen to be a radius greater than the target aperture so that no stray light from the target star is included. We also make sure that no other stars fall in the chosen sky annulus. A synthetic light curve is produced by averaging the light curves of the reference stars. Then, the final transit light curve of each date is normalized by dividing by this synthetic light curve to correct for systematics due to atmospheric variations and airmass differences throughout the observations. Every combination of reference stars and aperture radii are considered. We systematically choose the best reference stars and aperture by minimizing the scatter in the Out-of-Transit (OoT) data points. The 1σ error bars on the data points include the readout noise, the Poisson noise, and the flat-fielding errors. The final light curves are presented in Figs. 2.1–2.7. For all the transits, the OoT baselines have a photometric root-mean-squared (RMS) value between 1.23 and 6.22 millimagnitude (mmag), consistent with previous high S/N transit photometry using the Mont4k on the 1.55-m Kuiper telescope (Dittmann et al. 2009a,b, 2010, 2012; Scuderi et al. 2010; Turner et al. 2013; Teske et al. 2013; Pearson et al. 2014; Zellem et al. 2015; Turner et al. 2017b).

2.3 Light Curve Analysis

2.3.1 EXOplanet MOdeling Package (EXOMOP)

To find the best-fit to the light curves we develop a modeling package called the EXOplanet MOdeling Package (`EXOMOP`; Pearson et al. 2014)[5] that uses the analytic equations of Mandel & Agol (2002) to generate a model transit. The χ-fitting statistic for the model light curve is:

$$\chi^2 = \sum_{i=1}^{n} \left[\frac{f_i(\text{obs}) - f_i(\text{model})}{\sigma_i(\text{obs})} \right]^2, \tag{2.1}$$

[5] `EXOMOPv7.0` is used in the analysis and is available at https://sites.google.com/site/astrojaketurner/codes

where n is the total number of data points, f_i(obs) is the observed flux at time i, $\sigma_i(obs)$ is the error in the observed flux, and f_i(model) is the calculated model flux. The goal of the light curve modeling is to explore the solution-space effectively to determine the f_i(model) that minimizes χ^2.

The Bayesian Information Criterion (BIC; Schwarz 1978) is used to assess over-fitting of the data with `EXOMOP`. The BIC is defined as

$$BIC = \chi^2 + k \ln(n), \tag{2.2}$$

where χ^2 is the chi-squared calculated for the best-fitting model (equation 2.1), k is the number of free parameters in the model fit [f_i(model)], and n is the number of data points in the transit. The possible free parameters in the Mandel & Agol (2002) model are the planet-to-star radius (R_p/R_*), the normalized semi-major axis (a/R_*), orbital inclination (i), mid-transit time (T_c), linear limb darkening coefficient (μ_1), and quadratic limb darkening coefficient (μ_2). The power of the BIC is the penalty for a higher number of fitted model parameters, making it a robust way to compare different best-fit models. The preferred model is the one that produces the lowest BIC value. The BIC has been used extensively in many other exoplanet transit studies (e.g. Kipping et al. 2010; Croll et al. 2011; Sing et al. 2011; Gibson et al. 2010, 2013b; Demory et al. 2013; Crossfield et al. 2013; Rogers et al. 2013; Howard et al. 2013; Stevenson et al. 2014b; Murgas et al. 2014; Zellem et al. 2014).

We perform a Levenberg-Marquardt (LM) non-linear least squares minimization (`MPFIT`; Markwardt 2009; Press et al. 1992) to find a best-fit to the data and a bootstrap Monte Carlo technique (Press et al. 1992) to calculate robust errors of the LM fitted parameters. In addition, we perform a Differential Evolution Markov Chain Monte Carlo (DE-MCMC; Braak 2006; Eastman et al. 2013) analysis to find a best-fit to the data and associated errors. Both the LM and DE-MCMC methods take into account the photometric error bars on the data points.

Table 2.2: Journal of observations

Planet Name	Date (UT)	Filter[1]	Cadence (s)	OoT RMS[2] (mmag)	Res RMS[3] (mmag)	Seeing (”)	χ_r^{2a}
CoRoT-1b	2012 Dec. 06	U	70	3.59	3.95	1.46–2.95	0.49
GJ436b	2012 March 23	U	60	2.96	2.85	0.96–1.99	0.68
”	2012 April 07	U	61	2.83	2.70	1.22–2.10	1.37
HAT-P-1b	2012 Oct. 02	U	40	1.44	1.45	1.57–2.00	1.69
HAT-P-13b	2013 March 02	U	58	1.91	1.63	1.67–2.89	1.76
HAT-P-16b	2013 Nov. 02	U	55	2.50	2.50	1.40–3.98	1.23
HATP-22b	2013 Feb. 22	U	70	3.42	3.17	1.41–4.12	0.26
”	2013 March 22	U	71	2.07	2.12	1.34–2.26	1.16
TrES-2b	2012 Oct. 29	U	50	3.05	2.54	1.36–2.53	1.27
TrES-4b	2011 July 26	U	116	4.42	4.08	1.29–3.05	3.65
”	2011 July 26	R	116	5.54	3.93	1.29–3.05	2.09
WASP-1b	2013 Sept. 19	U	133	2.92	3.31	1.10–2.98	1.56
”	2013 Sept. 19	B	135	2.80	2.36	1.10–2.98	3.61
”	2013 Oct. 22	U	137	1.58	1.79	1.21–2.64	1.06
”	2013 Oct. 22	B	136	1.23	1.25	1.21–2.64	1.60
WASP-12b	2011 Nov. 15	R	126	1.40	1.47	1.72–2.10	2.14
”	2011 Nov. 15	U	126	1.67	1.62	1.72–2.10	0.92

Continued on next page

Table 2.2 – continued

Planet Name	Date (UT)	Filter[1]	Cadence (s)	OoT RMS[2] (mmag)	Res RMS[3] (mmag)	Seeing (”)	χ_r^{2a}
”	2012 March 22	U	61	2.54	2.23	1.33–2.15	0.47
”	2012 Oct. 02	U	61	2.53	2.11	2.07–3.18	0.79
”	2012 Nov. 30	U	55	3.30	3.61	1.45–3.24	0.94
WASP-33b	2012 Oct. 01	U	27	2.57	2.60	1.12–1.99	1.54
”	2012 Dec. 01	U	91	2.45	2.63	1.75–2.90	8.60
”	2012 Dec. 01	B	91	7.17	6.68	1.75–2.90	1.91
WASP-36b	2012 Dec. 29	R	31	1.90	2.50	1.92–2.80	1.44
”	2013 March 16	U	60	3.86	5.74	1.46–2.96	0.63
WASP-44b	2012 Oct. 13	U	68	6.22	5.64	1.77–2.58	1.08
”	2013 Oct. 19	B	116	2.33	2.50	1.07–1.95	1.19
”	2013 Oct. 19	V	120	2.04	2.25	1.07–1.95	1.85
WASP-48b	2012 Oct. 09	U	71	1.92	2.36	1.54–3.11	1.40
WASP-77Ab	2012 Dec. 06	U	68	1.58	1.53	2.31–2.95	2.87

[1] Filter: B is the Harris B (330–550 nm), R is the Harris R (550–900 nm), V is the Harris V (473–686 nm) and U is the Bessell U (303–417 nm)

[2] Out-of-Transit (OoT) root-mean-squared (RMS) relative flux

[3] Residual (res) RMS flux after subtracting the EXOplanet MOdeling Package (`EXOMOP`) best-fitting model from the data

[a] Reduced χ^2 calculated using the `EXOMOP` best-fitting model

The formal errors in the LM fit can underestimate the parameter uncertainties under strongly correlated parameters (Popper 1984; Maceroni & Rucinski 1997; Southworth et al. 2004a,b; Southworth 2008), which is the case for exoplanet transits (Carter & Winn 2009). Therefore, we determine a robust estimation of the uncertainties using the following Monte Carlo bootstrap procedure. (1) We obtain the best-fit light curves and parameters from the LM non-linear least squares algorithm. (2) We find new error bars, σ_n, by the following equation:

$$\sigma_n = \sigma_p N(\mu, \sigma^2), \tag{2.3}$$

where σ_p are the photometric (observational) error bars for each data point in the light curve, $N(\mu, \sigma^2)$ is a random Gaussian distributed variable (N) with a mean $\mu = 0$ and a standard deviation $\sigma = 1$. (3) We add σ_n to the flux measurements in the light curve. (4) Step (1) is repeated to find a new best-fit light curve (the original photometric error bars, σ_p, are used for the error on the flux measurements). This process is repeated at least 10000 times to avoid biasing the Gaussian fit due to small-number statistics. When all iterations are finished, each fit parameter from step (4) is subtracted from the original best-fit value and a Gaussian function is fit to the distribution. The standard deviations of the distributions are taken as the one sigma uncertainties in the fitted parameters.

We use the DE-MCMC analysis to find more robust parameter values because the solution is a global minimum in solution-space and χ^2. By default the DE-MCMC in `EXOMOP` uses 20 chains and 20^6 links. The Gelman-Rubin statistic (Gelman & Rubin 1992) is used to ensure chain convergence (Ford 2006). We use the DE-MCMC model from `EXOFAST` (exofast_demc; Eastman et al. 2013) in `EXOMOP`. `EXOMOP` uses the Metropolis-Hastings sampler and characterizes the uncertainties using a Bayesian inference that accounts for non-Gaussian errors and covariances between parameters (Eastman et al. 2013). The LM solution and errors are used as the seed for the DE-MCMC model.

`EXOMOP` is also capable of fitting a function to the OoT baseline to account for any residual curvature due to the atmospheric extinction. Either a linear or quadratic fit can be applied to both the LM and DE-MCMC models. The baseline function is fit to the transit simultaneously with the Mandel & Agol (2002) model. The BIC is also used to determine whether to include a baseline fit in the best-fit model.

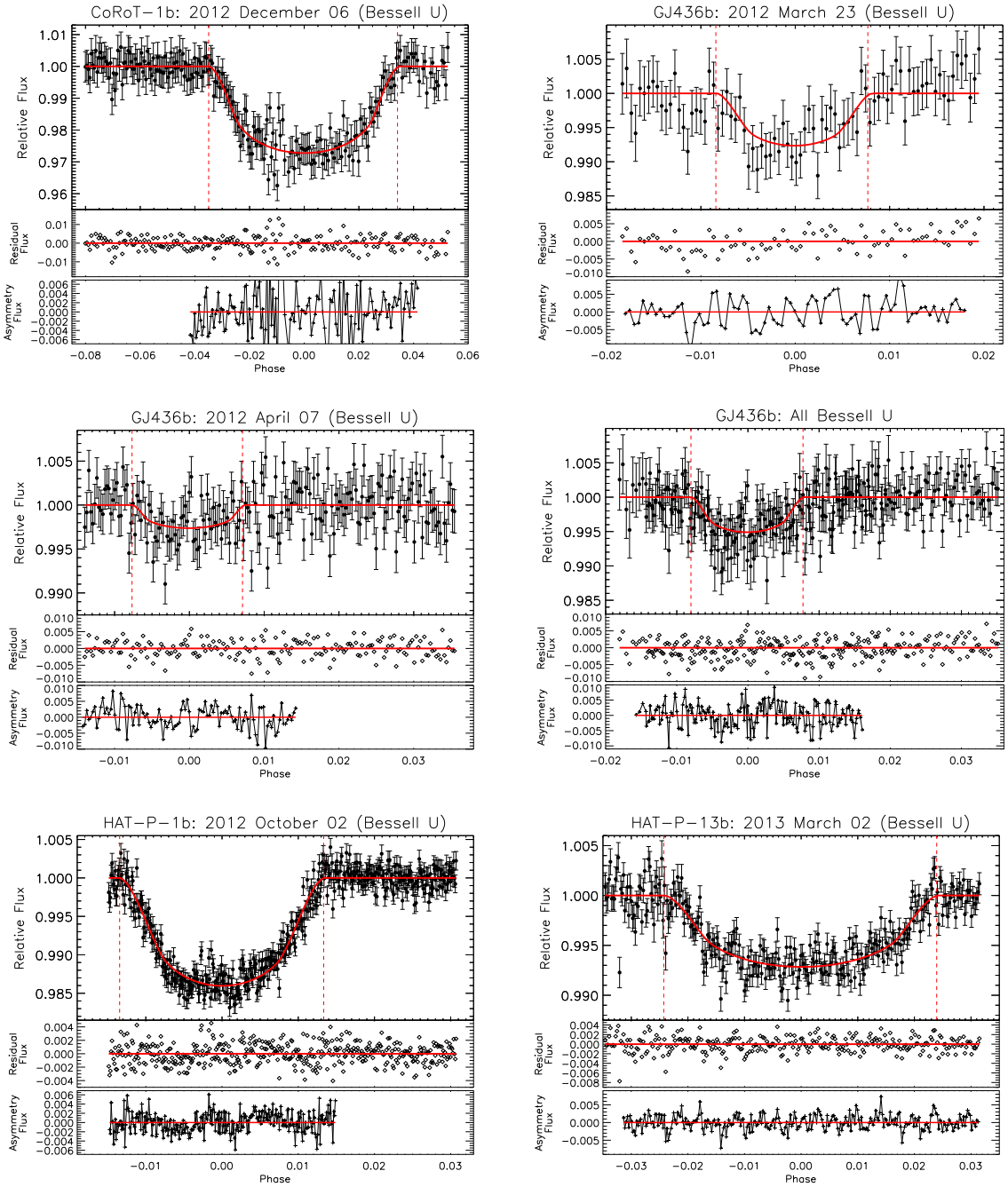

Figure 2.1: Light curves of CoRoT-1b, GJ436b, HAT-P-1b, and HAT-P-13b. The 1σ error bars include the readout noise, the Poisson noise, and the flat-fielding error. The best-fitting models obtained from the EXOplanet MOdeling Package (`EXOMOP`) are shown as a solid red line. The `EXOMOP` best-fitting model predicted ingress and egress points are shown as dashed red vertical lines. The residuals (Light Curve - `EXOMOP` Model) are shown in the second panel. The third panel shows the residuals of the transit subtracted by the mirror image of itself (Section 2.3.1). See Table 2.2 for the cadence, Out-of-Transit root-mean-squared (RMS) flux, and residual RMS flux for each light curve. We do not observe an early ingress or any asymmetries in any of the near-UV transits.

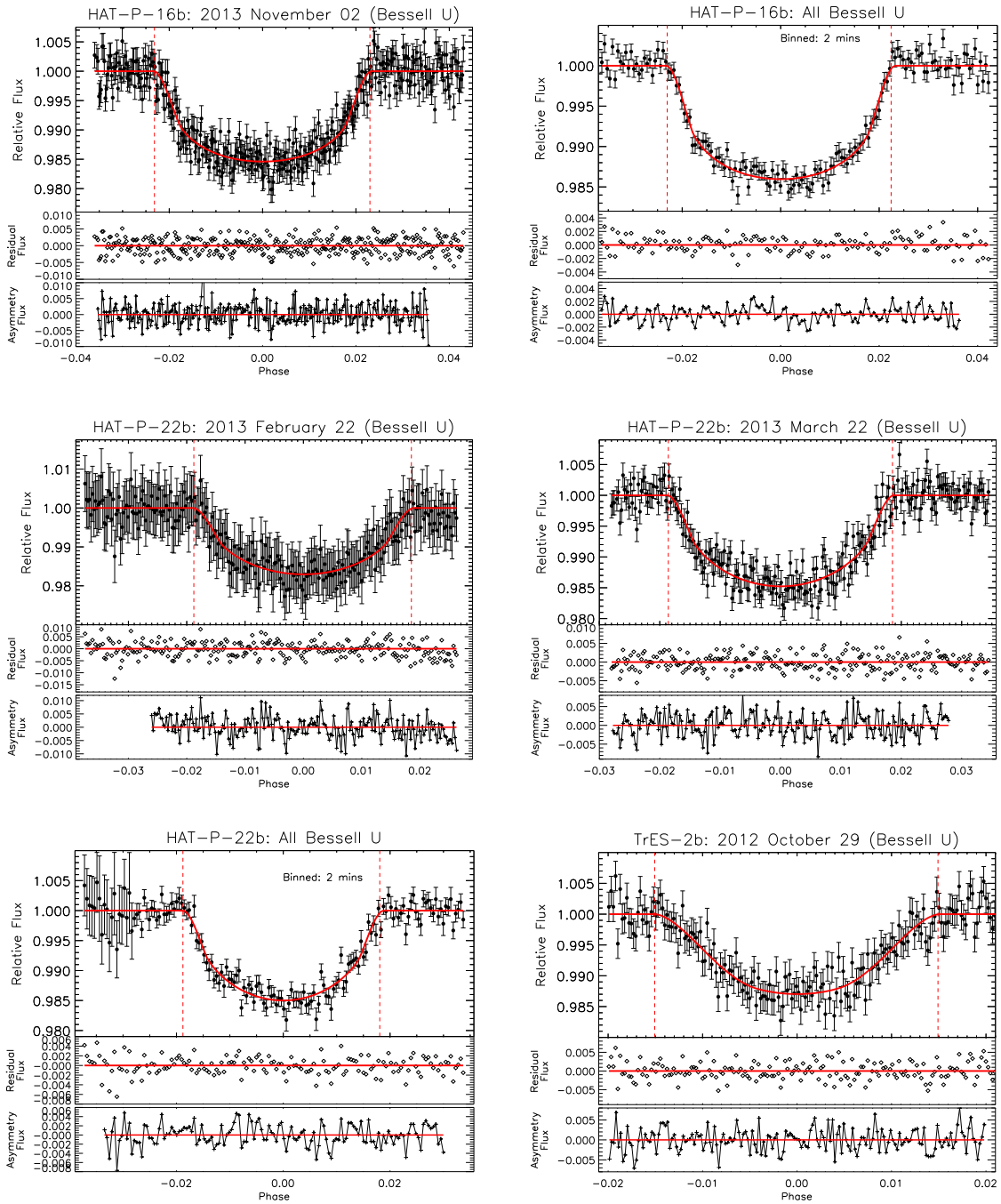

Figure 2.2: Light curves of HAT-P-16b, HAT-P22b, and TrES-2b. Other comments are the same as Fig. 2.1.

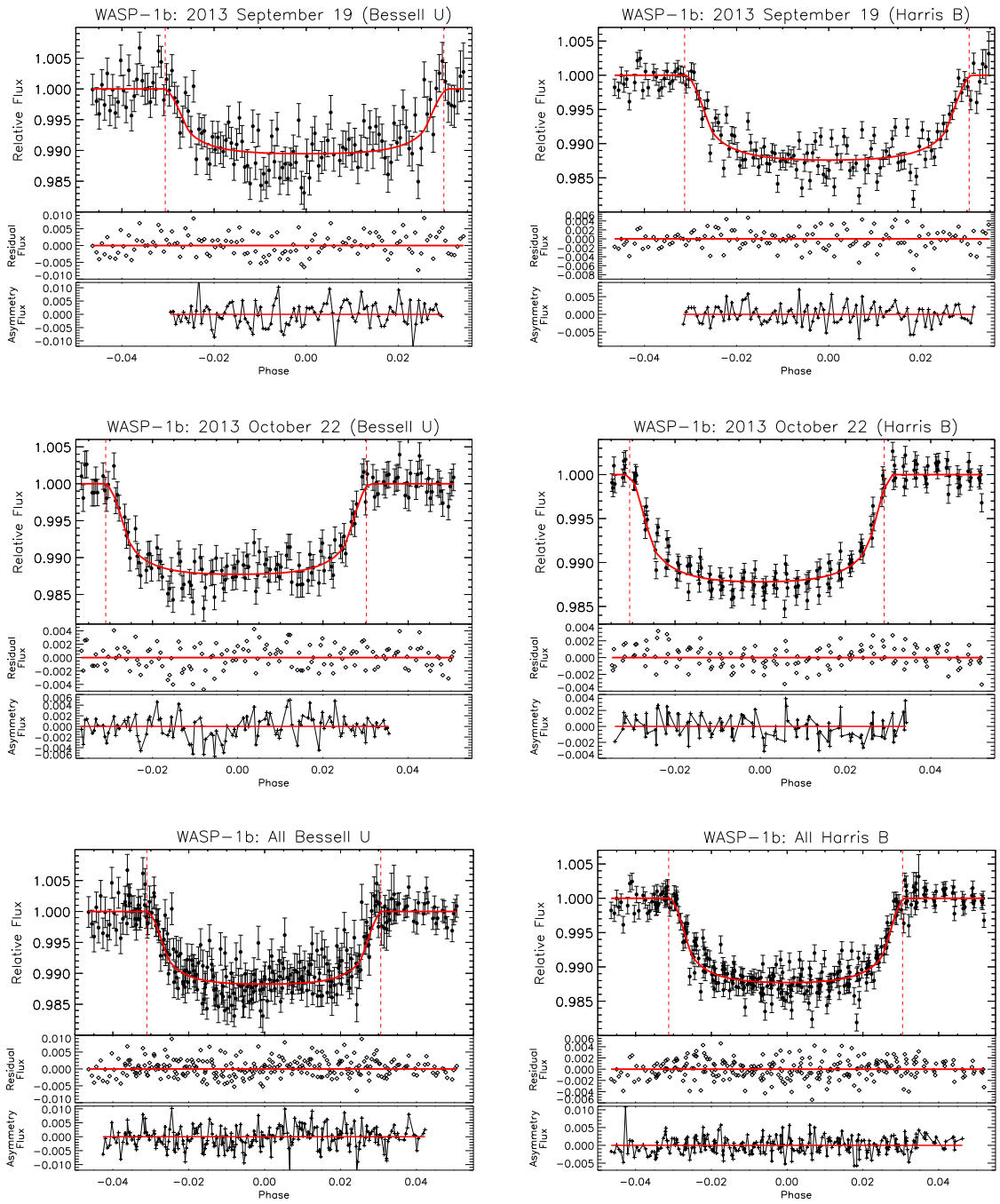

Figure 2.3: Light curves of WASP-1b. Other comments are the same as Fig. 2.1.

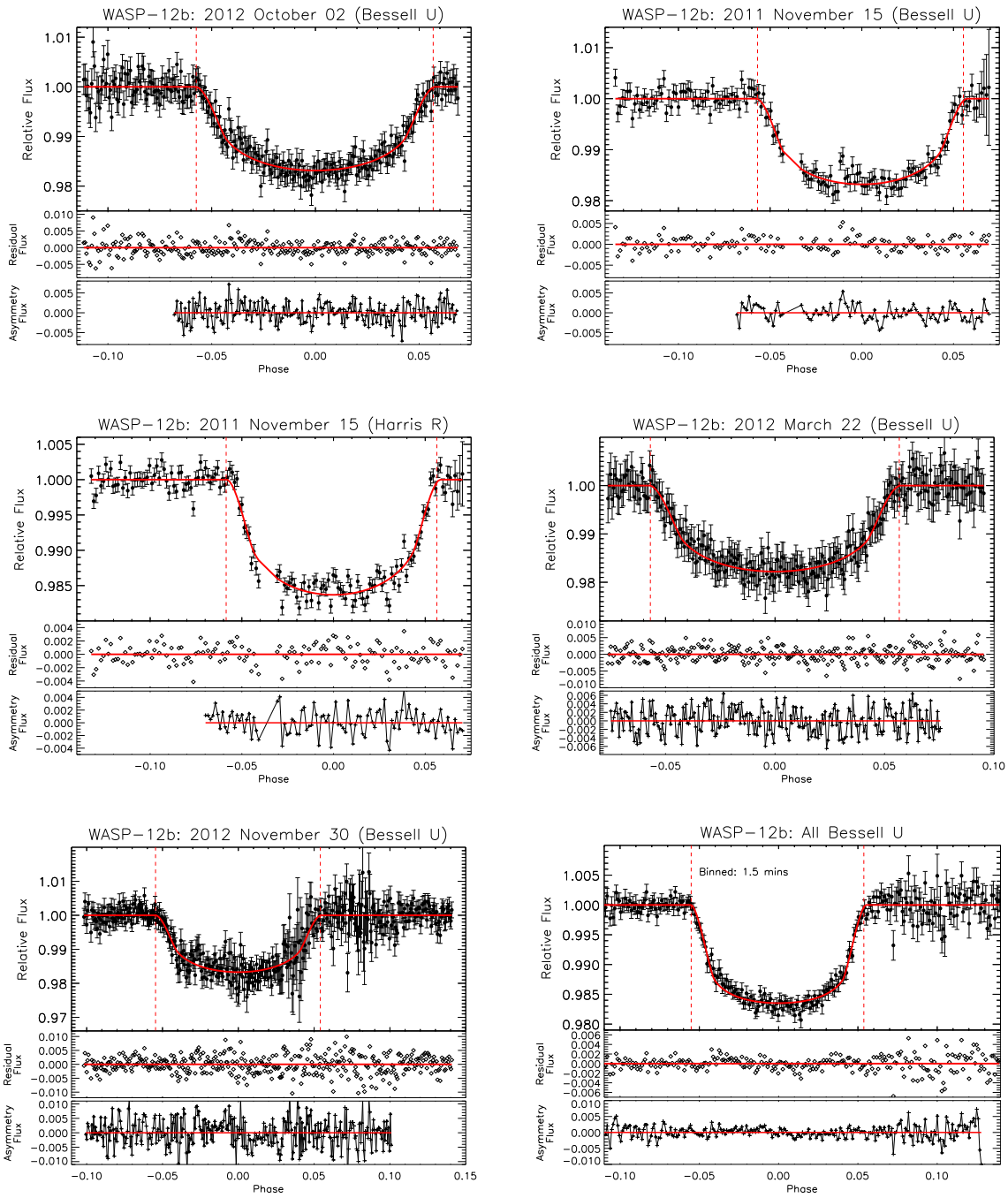

Figure 2.4: Light curves of WASP-12b. Other comments are the same as Fig. 2.1.

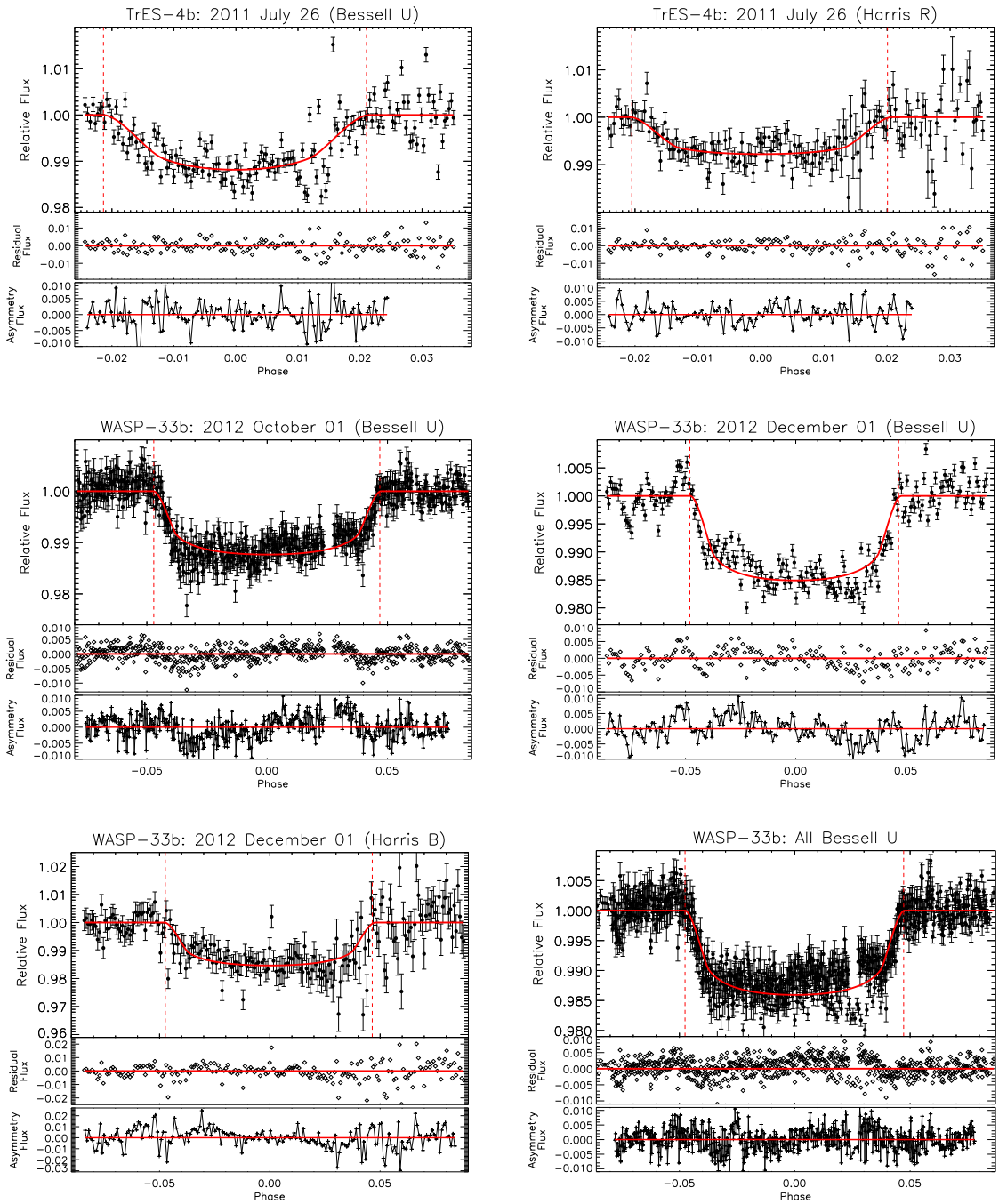

Figure 2.5: Light curves of TrES-4b and WASP-33b. Other comments are the same as Fig. 2.1.

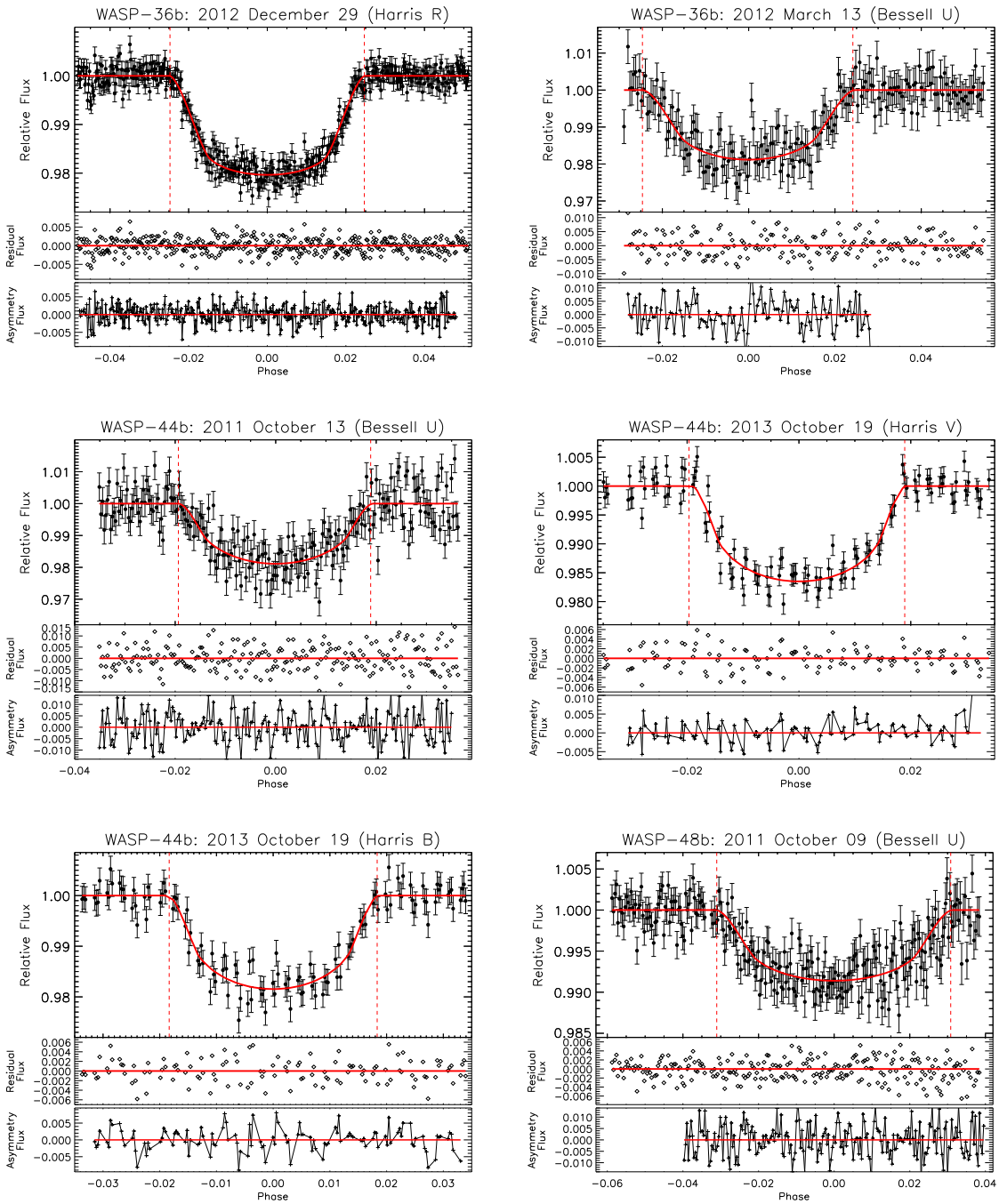

Figure 2.6: Light curves of WASP-36b, WASP-44b, and WASP-48b. Other comments are the same as Fig. 2.1.

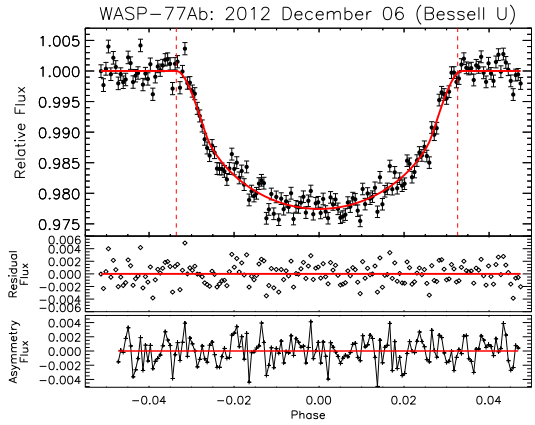

Figure 2.7: Light curve of WASP-77Ab. Other comments are the same as Fig. 2.1.

Red noise estimation

EXOMOP uses the residual permutation (rosary bead; Southworth 2008), time-averaging (Pont et al. 2006), and wavelet (Carter & Winn 2009) methods to access the importance of temporally-correlated (red) noise in both fitting methods. Red noise is accounted for in our analysis because the errors in the fitted parameter values can be underestimated if we don't account for red noise (Pont et al. 2006; Carter & Winn 2009). In order to be conservative, the red noise method that produces the largest β, the scaling factor of the red noise relative to the white noise errors, is used to inflate the errors in the fitted parameters (Section 2.3.1).

In the residual permutation method (Jenkins et al. 2002; Southworth 2008; Bean et al. 2008; Winn et al. 2008a) the best-fit model is subtracted from the data and the residuals are circularly shifted and then added to the data points. A new fit is found, and then the residuals are shifted again, with those at the end wrapped around to the start of the data. In this way, every new synthetic data set will have the same noise characteristics as the actual data but only translated in time. Usually this process continues until the residuals have cycled back to where they originated (e.g. Todorov et al. 2012). We perform two different residual permutation procedures to determine the effect of red noise in the precision of our derived parameters.

Our first residual permutation ($res1$) method uses a procedure very similar to Todorov et al. (2012) where the shifting process continues until the residuals have cycled back to

where they originated (one full circular permutation). The resulting parameter values may have non-Gaussian distributions if red noise is present. Consequently, we set the 1σ error bars of each parameter as half the range that covers 68% of the total number of the data points, centered on the best-fit value from either the DE-MCMC or LM analysis. For each fitted parameter we then define β_{res1} (the scaling factor of the errors relative to white noise using the $res1$ method) as σ_w/σ_{res1}, where σ_w are the error bars derived from the bootstrap Monte Carlo technique or the DE-MCMC technique and the σ_{res1} are the error bars derived from the first residual permutation method.

For the second residual permutation ($res2$) method we update this procedure by allowing for the error bars of the residuals to be taken into account. This is similar to step (2), (3), and (4) in the bootstrap procedure described above, however, in step (3) σ_n is added to the residuals and in step (4) the residuals are added to the data points and a new fit is found. We repeat this process 10000 times and on each step the residuals are circularly shifted. This procedure results in a distribution of fitted values for each parameter from which its uncertainty is estimated using the standard deviation of a Gaussian fit. For each fitted parameter we then define β_{res2} (the scaling factor of the errors relative to white noise using the $res2$ method) as σ_w/σ_{res2}, where σ_{res2} are the error bars derived from the second residual permutation method. The second residual permutation method is limited by the fact that we assume a Gaussian distribution for the errors.

The next red noise estimation we implement is the time-averaging method. This is done in a similar fashion to the procedure described by Winn et al. (2008a). For each light curve we find the best-fitting model and calculate the residuals between the observed and calculated fluxes. Next, the residuals are separated into bins of N points and we calculate the standard deviation, σ_N, of the binned residuals. In our analysis, N ranges from 1 to n, where n is the total number of data points in each respective transit. Using the set of σ_N and N values we then use a LM non-linear least squares minimization algorithm to find the RMS of red noise (σ_{red}) and the RMS of white noise (σ_{white}) using the following equation from Pont et al. 2006:

$$\sigma_N = \sqrt{\frac{\sigma_{white}^2}{N} + \sigma_{red}}. \tag{2.4}$$

Using σ_{white} and σ_{red} we estimate β_{time}, the scaling factor of the errors relative to white

noise using the time-averaging method, with the following equation from Carter & Winn (2009):

$$\beta_{time} = \sqrt{1 + \left(\frac{\sigma_{red}}{\sigma_{white}}\right)^2}. \tag{2.5}$$

Finally, we use the wavelet technique (solveredwv; Carter & Winn 2009) as a fourth check of the importance of red noise in the light curve fitting process. In this method the total noise of the transit is assumed to be formed as an additive combination of noise with power spectral density proportional to $1/f^{\alpha}$ (the red noise) and Gaussian white noise. A downhill simplex method (AMOEBA; Nelder & Mead 1965; Press et al. 1992) algorithm is used to maximize the likelihood that a function of σ_{red} and σ_{white} is related to the standard deviations of the $1/f^{\alpha}$ and white noise, respectively. A more thorough description of the wavelet model can be found in Carter & Winn (2009). Again, β_{wave}, the scaling factor of the errors relative to white noise using the wavelet technique, is estimated by using equation (2.5).

Final error bars on the fitted parameters

To get the final error bars for the fitted parameters we multiply σ_w by the largest β (β_{time}, β_{res1}, β_{res2}, or β_{wave}) from the residual permutation, time-averaging, and wavelet red noise calculations to account for underestimated error bars due to red noise (Winn et al. 2008a). To remain conservative this multiplication step is only done if the largest β is greater than one. Finally, in cases where the reduced chi-squared (χ^2_r) of the data (Table 2.2) for the best-fit model is greater than unity we multiply the error bars above by $\sqrt{\chi^2_r}$ to compensate for the underestimated observational errors (Bruntt et al. 2006; Southworth et al. 2007b; Southworth et al. 2007a; Southworth 2008; Barnes et al. 2013).

Additional features of EXOMOP

We calculate the transit duration, τ_t, of each of our transit model fits with the following equation (Carter et al. 2008):

$$\tau_t = t_{egress} - t_{ingress}, \tag{2.6}$$

where t_{egress} is the best-fitting model time of egress (4th contact), and $t_{ingress}$ is the best-fitting model time of ingress (1st contact). The error on τ_t is set to the $\sqrt{2}$ times the cadence of our observations (Carter & Winn 2009).

EXOMOP performs an asymmetry test on each transit. We subtract each light curve by the mirror image of itself about the calculated mid-transit time. This same technique is used in Turner et al. (2013) and Pearson et al. (2014) to search for asymmetries caused by a possible bow shock in TrES-3b and HAT-P-16b, respectively. This technique is useful for possible bow shock detection because bow shock models of WASP-12b (Llama et al. 2011) and HD 189733b (Llama et al. 2013) predict a distinct asymmetry between the two halves of the transit (Llama et al. 2011, see fig. 2; Llama et al. 2013, see fig. 3).

2.3.2 EXOMOP model comparison

Using artificial data, we perform several different comparison tests of EXOMOP with two different publicly-available modeling software packages: the Transit Analysis Package[6] (TAP; Mandel & Agol 2002; Carter & Winn 2009; Gazak et al. 2012; Eastman et al. 2013) and JKTEBOP[7] (Southworth et al. 2004a,b). We also test if the errors we calculate using EXOMOP are reliable by comparing the errors to analytic estimates.

We briefly discuss these two modeling packages below. TAP fits the transit light curves with a standard Mandel & Agol (2002) model using Markov Chain Monte Carlo techniques and the parameter uncertainties are found with a wavelet likelihood function (Carter & Winn 2009). JKTEBOP was adapted from the EBOP program written for eclipsing binary star systems (Popper & Etzel 1981) and implements the Nelson-Davis-Etzel eclipsing binary model (Nelson & Davis 1972). In addition, JKTEBOP uses a Monte Carlo simulation algorithm to compute errors (Southworth et al. 2004a,b; Southworth 2010; Hoyer et al. 2011).

We create a synthetic model transit using the analytic equations of Mandel & Agol (2002) with a planet-to-star radius (R_p/R_*) = 0.1173, the scaled semi-major axis (a/R_*) = 3.033, inclination (i) = 82.96°, period (P_p) = 1.0914209 d, the linear limb darkening coefficient (μ_1) = 0.61797203, the quadratic limb darkening coefficient (μ_2) = 0.20813438,

[6]http://ifa.hawaii.edu/users/zgazak/IfA/TAP.html
[7]http://www.astro.keele.ac.uk/jkt/codes/jktebop.html

eccentricity (e) = 0, and argument of periastron (ω) = 0°. These parameters are chosen because they match the parameters of WASP-12b observed in the near-UV. Next, three sets of different white and it does detect red noise parameters are added to the synthetic Mandel & Agol (2002) model to explore the effects of noise. The first set of models include only random Gaussian white noise with a standard deviation of 1, 2, 4, and 5 mmag. For the second and third set we create white noise and $1/f^{\alpha}$ red noise both with a standard deviation of 1 mmag where α is equal to 0.33 and 0.66, respectively. In total, we ran 6 models.

For the EXOMOP analysis we use 10000 iterations for the LM fit and 20 chains and 20^6 links for the DE-MCMC fit. With TAP, we model each transit individually using 5 chains with lengths of 10^5 links each. JKTEBOP is implemented using the Monte Carlo algorithm and residual permutation method described in Southworth (2008). During the analysis for each model, the time of mid-transit (T_c) and R_p/R_* are allowed to float. We only model these two parameters for the comparison tests because the errors on them are analytically tractable (see below; Carter et al. 2008). The i, e, ω, μ_1, μ_2, a/R_*, and the P_p of the planet are fixed. In addition, for TAP the white and red noise are left as free parameters. Since TAP does not automatically ensure chain convergence, we perform the Gelman-Rubin statistic (Gelman & Rubin 1992; Ford 2006) manually to ensure convergence. In addition, TAP does not take into account the individual error bars on each transit point, whereas both the EXOMOP and JKTEBOP models do take them into account.

The results of the white noise analysis can be found in Table 2.3 and the red noise analysis in Table 2.4. As expected, EXOMOP finds no red noise in the pure white noise tests and red noise in the red noise tests. In every case, the EXOMOP R_p/R_* values are within 1σ to the true R_p/R_*. We find that TAP overestimates the amount of red noise in every test we ran (by 2–14 σ) including the set of models with only white noise. Consequently, TAP is overestimating the error bars to their fitted parameters because of this excess red noise. Since both EXOMOP and TAP use the wavelet likelihood technique (Carter & Winn 2009) it is not clear why TAP is overestimating the amount of red noise in these tests. Using a variety of methods, our results confirm the need to account for red noise. Each of the methods used find red noise in the red noise tests but at slightly varying degrees. Turner et al. (2013) and Hoyer et al. (2012) both conclude that JKTEBOP may be underestimating the errors in its transit fits when compared to TAP. However, neither of these studies conduct a thorough

red and white noise test study. Therefore, we believe that TAP is overestimating the error bars in the fitted parameters compared to JKTEBOP and EXOMOP due its incorrect red noise calculation. The EXOMOP and JKTEBOP results are in very good agreement with each other.

To get an general idea if the error estimation in EXOMOP is behaving as expected, we compare our white noise tests (Table 2.3) to analytic estimations for the uncertainty in the flux drop, $\delta = (R_p/R_*)^2$, and mid-transit time. Carter et al. (2008) derive an analytic estimate for the 1σ uncertainty in δ (σ_δ) to be

$$\sigma_\delta = \frac{\sigma_g}{\sqrt{n}}, \tag{2.7}$$

where σ_g are the Gaussian errors in the relative flux (in our case the noise added) and n is the number of data points. Additionally, the analytic estimate of the 1σ uncertainty (σ_t) in the mid-transit time is (Carter et al. 2008):

$$\sigma_t = \frac{\sigma_g}{\sqrt{n}\delta}\,(\tau_t - \tau)\,\sqrt{\frac{\tau}{2(\tau_t - \tau)}}, \tag{2.8}$$

where τ is the ingress/egress duration. Limb darkening and red noise cause the error estimation in equations (2.7) and (2.8) to increase (Seager 2011). The error estimations we find using EXOMOP have the same behavior as the analytic estimates by Carter et al. (2008) exactly for both σ_δ and σ_t. For example, if the noise doubles in our white noise tests then the error estimates on R_p/R_* also double (Table 2.3). The JKTEBOP error bars also mimic this analytic behavior but the TAP error bars do not. Due to this result we believe the error estimation in EXOMOP is reliable.

2.3.3 EXOMOP analysis of the systems

Each individual transit is modeled with EXOMOP using 10000 iterations for the LM model and 20 chains and 20^6 links for the DE-MCMC model. During the analysis T_c and R_p/R_* are always left as free parameters for each transit. We systematically fit every combination with a/R_*, i, T_c, and R_p/R_* set as free parameters. The BIC is used to assess over-fitting of the data and the model that produces the lowest BIC value is always chosen. For every planet except HAT-P-13b, WASP-12b, WASP-44b, and WASP-77Ab the BIC is higher

Table 2.3: White Gaussian noise model tests with `EXOMOP`, `TAP`, and `JKTEBOP` using synthetic light curves

Model	Noise (mmag)	R_p/R_*	Mid-transit (HJD)	Red[1] (mmag)	White[1] (mmag)	β_{res2} R_p/R_*	β_{res1} R_p/R_*	β_{res2} Mid	β_{res1} Mid	Red[2] (mmag)	White[2] (mmag)
`TAP`	1	$0.11785^{+0.00065}_{-0.00068}$	$0.00000^{+0.00024}_{-0.00024}$	$2.8^{+1.7}_{-1.6}$	$0.94^{+0.03}_{-0.03}$	—	—	—	—	—	—
`TAP`	2	$0.1168^{+0.0012}_{-0.0012}$	$-0.00027^{+0.00045}_{-0.00044}$	$3.8^{+3.1}_{-2.5}$	$1.96^{+0.07}_{-0.06}$	—	—	—	—	—	—
`TAP`	4	$0.1170^{+0.0027}_{-0.0027}$	$-0.0007^{+0.0010}_{-0.0010}$	$11.4^{+7.0}_{-6.6}$	$3.79^{+0.13}_{-0.13}$	—	—	—	—	—	—
`TAP`	5	$0.1165^{+0.0036}_{-0.0034}$	$-0.0007^{+0.0012}_{-0.0012}$	$14.6^{+9.9}_{-8.8}$	$5.06^{+1.18}_{-0.18}$	—	—	—	—	—	—
`JKTEBOP`	1	$0.11775^{+0.00025}_{-0.00025}$	$0.00003^{+0.00013}_{-0.00013}$	—	— —		1.78	—	0.99	—	—
`JKTEBOP`	2	$0.11743^{+0.00052}_{-0.00052}$	$-0.00032^{+0.00028}_{-0.00028}$	—	— —		0.79	—	0.88	—	—
`JKTEBOP`	4	$0.1174^{+0.0010}_{-0.0010}$	$-0.00070^{+0.00053}_{-0.00053}$	—	— —		0.31	—	0.80	—	—
`JKTEBOP`	5	$0.1160^{+0.0013}_{-0.0013}$	$-0.00056^{+0.00069}_{-0.00069}$	—	— —		0.54	—	0.79	—	—
`EXOMOP`	1	$0.11769^{+0.00025}_{-0.00025}$	$0.00001^{+0.00013}_{-0.00013}$	0.0	0.94	0.97	0.58	0.96	0.85	0.00	$0.93^{+0.33}_{-0.33}$
`EXOMOP`	2	$0.11738^{+0.00051}_{-0.00050}$	$-0.00031^{+0.00028}_{-0.00028}$	0.0	1.84	0.45	0.90	0.84	0.88	0.00	$1.75^{+0.70}_{-0.70}$
`EXOMOP`	4	$0.1173^{+0.0011}_{-0.0011}$	$-0.00067^{+0.00059}_{-0.00057}$	0.0	3.84	0.91	0.72	0.93	0.74	0.00	$3.44^{+1.60}_{-1.60}$
`EXOMOP`	5	$0.1159^{+0.0013}_{-0.0013}$	$-0.00057^{+0.00062}_{-0.00062}$	0.0	5.12	0.89	0.65	0.89	0.76	0.00	$4.80^{+2.22}_{-2.22}$

[1] The red and white noise calculated using the wavelet likelihood technique (Carter & Winn 2009) described in Section 2.3.1.

[2] The red and white noise calculated using the Time-Averaging method (Pont et al. 2006) described in Section 2.3.1.

Table 2.4: Red noise model tests with `EXOMOP`, `TAP`, and `JKTEBOP` using synthetic light curves

Model	α Added	R_p/R_*	Mid-transit (HJD)	Red[1] (mmag)	White[1] (mmag)	β_{res2} R_p/R_*	β_{res1} R_p/R_*	β_{res2} Mid	β_{res1} Mid	Red[2] (mmag)	White[2] (mmag)
`TAP`	0.66	$0.1197^{+0.0022}_{-0.0023}$	$-0.00045^{+0.00061}_{-0.00062}$	$13.2^{+1.4}_{-1.4}$	$0.618^{+0.053}_{-0.059}$	—	—	—	—	—	—
`TAP`	0.33	$0.1176^{+0.0016}_{-0.0016}$	$-0.00054^{+0.00046}_{-0.00047}$	$9.1^{+1.5}_{-1.4}$	$0.856^{+0.043}_{-0.043}$	—	—	—	—	—	—
`JKTEBOP`	0.66	$0.11889^{+0.00067}_{-0.00067}$	$-0.000036^{+0.00028}_{-0.00028}$	—	—	2.59	—	—	2.18	—	—
`JKTEBOP`	0.33	$0.11693^{+0.00052}_{-0.00052}$	$-0.00038^{+0.00022}_{-0.00022}$	—	—	1.99	—	—	1.61	—	—
`EXOMOP`	0.66	$0.1177^{+0.0015}_{-0.0029}$	$-0.00004^{+0.00029}_{-0.00029}$	0.46	0.70	1.41	4.53	1.43	3.61	$0.55^{+0.19}_{-0.19}$	$1.41^{+0.65}_{-0.65}$
`EXOMOP`	0.33	$0.11817^{+0.00081}_{-0.00081}$	$-0.00018^{+0.00040}_{-0.00059}$	0.16	0.91	1.44	1.67	1.42	1.74	$0.07^{+0.34}_{-0.07}$	$1.53^{+0.46}_{-0.46}$

[1] The red and white noise calculated using the wavelet likelihood technique (Carter & Winn 2009) described in Section 2.3.1.

[2] The red and white noise calculated using the Time-Averaging method (Pont et al. 2006) described in Section 2.3.1.

when fitting for a/R_* and i. Therefore, for most transits these parameters are fixed. The a/R_*, i, e, ω, and P_p of each of the planets are fixed to their values listed in Table 2.5. The linear and quadratic limb darkening coefficients in each filter are taken from Claret & Bloemen (2011) and interpolated to the stellar parameters of the host stars (see Table 2.6) using the `EXOFAST` applet[8](Eastman et al. 2013). In addition, a linear or quadratic least squares fit is modeled to the OoT baseline simultaneously with the Mandel & Agol (2002) model. The BIC is used to determine whether to include a linear or quadratic OoT baseline fit in the best-fit model.

The fitted parameters from either the LM or DE-MCMC best-fitting model that produce the highest error bars are reported. In every case both models find results within 1σ of each other. The light curve parameters obtained from the `EXOMOP` analysis and the derived transit durations are summarized in Tables 2.7–2.9. The modeled light curves can be found in Figs. 2.1–2.7. The physical parameters for our targets are derived as outlined in Section 2.4 (Tables 2.10–2.11). A thorough description of the modeling and results of each system can be found in Section 2.5. We also perform the asymmetry test for each transit to search for any asymmetries.

2.4 Calculated Physical Properties of the Systems

We use the results of our light curve modeling with `EXOMOP` to calculate the planetary and geometrical parameters of our targets (mass, radius, density, surface gravity, equilibrium temperature, Safronov number, atmospheric scale height). The physical parameters of all our systems can be found in Tables 2.10–2.11. The planetary mass, M_p, can be calculated using the following equation (Winn 2010; Seager 2011):

$$M_p = \left(\frac{\sqrt{1-e^2}}{28.4329}\right)\left(\frac{K_*}{\sin i}\right)\left(\frac{P_b}{1yr}\right)^{1/3}\left(\frac{M_*}{M_\odot}\right)^{2/3} M_{jup}, \tag{2.9}$$

where K_* is the radial velocity amplitude of the host star and P_p is the orbital period of the planet. We adopt the formula by Southworth et al. (2007b) to calculate the surface

[8]http://astroutils.astronomy.ohio-state.edu/exofast/limbdark.shtml

Table 2.5: Parameters fixed for the light curve fitting using EXOMOP

Planet	Period	a/R_*	Inclination (°)	Eccentricity	Omega (°)	Source
CoRoT-1b	1.5089686	5.259	85.66	0.071	276.70	1
GJ436b	2.6438986	14.41	86.774	0.15	351	2
HAT-P-1b	4.46529976	9.853	85.634	0.00	0.00	3
HAT-P-13b	2.9162383	—	81.93	0.00	0.00	4
HAT-P-16b	2.7759690	7.17	86.6	0.034	214	5
HAT-P-22b	3.212220	8.55	86.90	0.016	156.00	6
TrES-2b	2.4706132	7.8957	83.8646	0.0002	143.13	7
TrES-4b	3.5539268	6.08	82.81	0.00	0.00	8
WASP-1b	2.5199449	5.64	88.65	0.00	0.00	9
WASP-12b	1.09142166	—	82.72	0.0447	274.44	10
WASP-33b	1.2198709	3.69	86.2	0.00	0.00	11
WASP-36b	1.5373653	5.977	83.61	0.00	0.00	12
WASP-44b	2.4238133	8.562	86.59	0.00	0.00	13
WASP-48b	2.143634	4.23	80.09	0.00	0.00	14
WASP-77Ab	1.3600309	—	89.4	0.00	0.00	15

References. — (1) Gillon et al. 2009; (2) Knutson et al. 2014a; (3) Nikolov et al. 2014; (4) Southworth et al. 2012a; (5) Pearson et al. 2014; (6) Bakos et al. 2011; (7) Esteves et al. 2013; (8) Chan et al. 2011; (9) Maciejewski et al. 2014; (10) Sing et al. 2013; (11) Kovács et al. 2013; (12) Smith et al. 2012; (13) Mancini et al. 2013; (14) Enoch et al. 2011; (15) Maxted et al. 2013

Table 2.6: Limb darkening coefficients for the light curve fitting using `EXOMOP`

Planet	Filter	Linear coefficient[1]	Quadratic coefficient[1]	T_{eff} [K]	[Fe/H]	log g [cgs]
CoRoT-1b[a]	Bessell U	0.66547	0.17302	5950	-0.30	4.25
GJ436b	Bessell U	0.926888	-0.120646	3350[b]	-0.15[c]	4.427[d]
HAT-P-1b[e]	Bessell U	0.73417	0.11238	5980	+0.130	4.382
HAT-P-13b[f]	Bessell U	0.89273	-0.02940	5653	+0.410	4.130
HAT-P-16b[g]	Bessell U	0.65720	0.17653	6158	+0.170	4.340
HAT-P-22b[h]	Bessell U	1.00392	-0.14338	5302	+0.24	4.36
TrES-2b[i]	Bessell U	0.74742	0.10232	5850	-0.15	4.427
TrES-4b[j]	Bessell U	0.61810	0.20952	6200	0.140	4.064
WASP-1b	Bessell U	0.151543	0.687788	6110[k]	0.26[d]	4.190[d]
”	Harris B	0.198846	0.599307	6110	0.26	4.190
WASP-12b[l]	Harris R	0.61797	0.20813	6300	0.30	4.38
”	Bessell U	0.30070	0.31983	6300	0.30	4.38
WASP-33b[m]	Bessell U	0.31668	0.38643	7430	+0.10	4.30
”	Harris B	0.37146	0.35168	7430	+0.10	4.30
WASP-36b[n]	Harris R	0.32106	0.30131	5880	-0.31	4.498
”	Bessell U	0.70503	0.13979	5880	-0.31	4.498
WASP-44b[o]	Bessell U	0.93916	-0.06561	5410	+0.06	4.481
”	Harris V	0.550120	0.199928	5410	+0.06	4.481
”	Harris B	0.758312	0.0728504	5410	+0.06	4.481
WASP-48b[p]	Bessell U	0.70217	0.14181	5920	-0.12	4.03
WASP-77Ab[q]	Bessell U	0.92696	-0.06241	5500	0.00	4.33

[1] The limb darkening coefficients are taken from Claret & Bloemen (2011) and interpolated to the stellar parameters of their host star

References. — (a) Barge et al. 2008; (b) Moses et al. 2013; (c) Bean et al. 2006; (d) Torres et al. 2008; (e) Torres et al. 2008; (f) Bakos et al. 2009; (g) Buchhave et al. 2010; (h) Bakos et al. 2011; (i) Torres et al. 2008; (j) Torres et al. 2008; (k) Simpson et al. 2011; (l) Hebb et al. 2009; (m) Collier Cameron et al. 2010; (n) Smith et al. 2012; (o) Anderson et al. 2012; (p) Enoch et al. 2011; (q) Maxted et al. 2013

gravitational acceleration, g_p:

$$g_p = \frac{2\pi}{P_p}\left(\frac{a}{R_p}\right)^2 \frac{\sqrt{1-e^2}}{\sin i} K_*. \tag{2.10}$$

The equilibrium temperature, T_{eq}, is derived using the relation (Southworth 2010):

$$T_{eq} = T_{eff}\left(\frac{1-A}{4F}\right)^{1/4}\left(\frac{R_*}{2a}\right)^{1/2}, \tag{2.11}$$

where T_{eff} is the effective temperature of the host star, A is the Bond albedo, and F is the heat redistribution factor. This formula is simplified by making the assumption, as done in Southworth (2010), that $A = 1 - 4F$; the resulting equation is the modified equilibrium temperature, T'_{eq}:

$$T'_{eq} = T_{eff}\left(\frac{R_*}{2a}\right)^{1/2}. \tag{2.12}$$

The Safronov number, Θ, is a measure of the ability of a planet to gravitationally scatter or capture other bodies in nearby orbits (Safronov 1972). We calculate Θ using the equation from Southworth (2010):

$$\Theta = \frac{M_p a}{M_* R_p}. \tag{2.13}$$

Differences between Safronov numbers could point to differences in migration or stopping mechanisms (Seager 2011). As defined by Hansen & Barman (2007), Class I hot Jupiters have $\Theta = 0.07 \pm 0.01$ and Class II have $\Theta = 0.04 \pm 0.01$. However, Southworth (2012) find that this devision of hot Jupiters into two classes is not evident when using a greater sample of planets. The atmospheric scale height, H, is calculated using (de Wit & Seager 2013)

$$H = \frac{k_B T'_{eq}}{\mu g_b}, \tag{2.14}$$

where k_B is Boltzmann's constant and μ is the mean molecular weight in the planet's atmosphere (set to 2.3; de Wit & Seager 2013).

Table 2.7: Parameters derived in this study for the CoRoT-1b, GJ436b, HAT-P-1b, HAT-P-16b, HAT-P-22b, TrES-2b, TrES-4b, and WASP-1b light curves using EXOMOP

Planet	CoRoT-1b	GJ436b	GJ436b	GJ436b	HAT-P-1b
Date	2012 Dec. 06	2012 March 23	2012 April 07	All	2012 Oct. 02
Filter[1]	U	U	U	U	U
T_c (HJD-2450000)	$6268.98963^{+0.00070}_{-0.0013}$	$6009.8889^{+0.0019}_{-0.0020}$	$6025.7322^{+0.0073}_{-0.0068}$	—	$6203.64907^{+0.00084}_{-0.00095}$
R_p/R_*	$0.1439^{+0.0020}_{-0.0018}$	$0.0930^{+0.0083}_{-0.0048}$	$0.0703^{+0.0099}_{-0.0071}$	$0.0758^{+0.0086}_{-0.0075}$	$0.1189^{+0.0010}_{-0.0014}$
Duration (min)	$149.9^{+1.9}_{-1.9}$	$59.6^{+2.5}_{-2.5}$	$58.30^{+1.45}_{-1.45}$	$59.55^{+1.07}_{-1.07}$	$172.12^{+0.95}_{-0.95}$
$\beta_{res2}{}^a$ (R_p/R_*)	0.74	0.79	1.17	1.14	1.35
$\beta_{res2}{}^a$ (T_c)	0.74	0.75	1.15	—	1.30
$\beta_{res1}{}^b$ (R_p/R)	+1.04 − 0.70	+1.92 − 0.59	+2.35 − 1.67	+2.64 − 2.28	+1.33 − 1.94
$\beta_{res1}{}^b$ (T_c)	+0.70 − 2.02	+1.16 − 1.48	+2.15 − 2.00	—	+2.13 -2.43
$\beta_{time}{}^c$	1.00	1.00	1.03	1.01	1.03
White Noise^d (mmag)	$2.47^{+1.04}_{-1.04}$	$1.87^{+0.66}_{-0.66}$	$2.52^{+1.41}_{-1.41}$	$2.86^{+1.38}_{-1.38}$	$1.50^{+0.64}_{-0.64}$
Red Noise^d (mmag)	0.00	0.00	$0.66^{+1.05}_{-0.66}$	$0.40^{+0.75}_{-0.40}$	$0.35^{+0.29}_{-0.29}$
$\beta_{wavelet}{}^e$	1.01	1.004	1.03	1.01	1.02
White Noise^f (mmag)	3.47	2.19	2.08	1.95	1.28
Red Noise^f (mmag)	0.00	0.20	0.49	0.32	0.25
OoT Baseline Function	None	None	None	—	None

Continued on next page

Table 2.7 – continued

Planet	HAT-P-16b	HAT-P-16b	HAT-P-22b	HAT-P-22b	HAT-P-22b
Date	2013 Nov. 02	All	2013 Feb. 22	2013 March 22	All
Filter[1]	U	U	U	U	U
T_c (HJD-2450000)	$6598.79110^{+0.00060}_{-0.00059}$	—	$6346.8144^{+0.0013}_{-0.0014}$	$6738.70864^{+0.00061}_{-0.00063}$	—
R_p/R_*	$0.1115^{+0.0011}_{-0.0011}$	$0.10645^{+0.00067}_{-0.00067}$	$0.1151^{+0.0021}_{-0.0022}$	$0.1072^{+0.0013}_{-0.0012}$	$0.10797^{+0.00086}_{-0.00094}$
Duration (min)	$185.44^{+1.28}_{-1.28}$	$181.78^{+3.06}_{-3.06}$	$172.46^{+1.66}_{-1.66}$	$172.89^{+2.38}_{-2.38}$	$170.50^{+3.05}_{-3.05}$
$\beta_{res2}{}^a$ (R_p/R_*)	0.67	1.08	0.50	0.71	1.18
$\beta_{res2}{}^a$ (T_c)	0.88	—	0.51	0.83	—
$\beta_{res1}{}^b$ (R_p/R)	+0.16 − 0.24	+0.29 − 0.38	0.10 -0.70	0.23 -0.15	0.53 -0.56
$\beta_{res1}{}^b$ (T_c)	+0.75 − 0.54	—	0.59 -0.53	0.53 -0.32	—
$\beta_{time}{}^c$	1.00	1.00	1.00	1.00	1.00
White Noise^d (mmag)	$1.23^{+0.61}_{-0.61}$	$0.97^{+0.25}_{-0.25}$	$2.23^{+0.65}_{-0.65}$	$1.11^{+0.52}_{-0.52}$	$1.19^{+0.36}_{-0.36}$
Red Noise^d (mmag)	0.00	0.00	0.00	0.00	0.00
$\beta_{wavelet}{}^e$	1.00	1.00	1.00	1.00	1.00
White Noise^f (mmag)	2.07	0.86	3.06	2.07	1.42
Red Noise^f (mmag)	0.00	0.00	0.20	0.00	0.00
OoT Baseline Function	Linear	—	None	Linear	—

Continued on next page

Table 2.7 – continued

Planet	TrES-2b	TrES-4	TrES-4b	WASP-1b	WASP-1b
Date	2012 Oct. 29	2011 July 26	2011 July 26	2013 Sept. 19	2013 Sept. 19
Filter[1]	U	R	U	U	B
T_c (HJD-2450000)	$6230.5980^{+0.00059}_{-0.00060}$	$5769.7536^{+0.0040}_{-0.0040}$	$5769.7532^{+0.0036}_{-0.0037}$	$6555.9381^{+0.0038}_{-0.0025}$	$6555.9393^{+0.0027}_{-0.0027}$
R_p/R_*	$0.1243^{+0.0022}_{-0.0024}$	$0.0880^{+0.0055}_{-0.0055}$	$0.1094^{+0.0052}_{-0.0052}$	$0.0938^{+0.0023}_{-0.0023}$	$0.1018^{+0.0040}_{-0.0040}$
Duration (min)	$106.68^{+1.19}_{-1.19}$	$205.35^{+2.73}_{-2.73}$	$216.96^{2.64}_{2.64}$	$219.49^{+3.15}_{-3.15}$	$224.17^{+3.18}_{-3.18}$
$\beta_{res2}{}^a$ (R_p/R_*)	0.72	1.6	2.23	1.28	1.89
$\beta_{res2}{}^a$ (T_c)	0.97	1.46	2.25	1.19	1.68
$\beta_{res1}{}^b$ (R_p/R)	+0.26 -0.27	+0.54 -0.85	+0.67 -0.74	+0.43 -0.58	+0.45 -0.67
$\beta_{res1}{}^b$ (T_c)	+0.32 -0.86	+1.30 -1.24	+1.14 -1.15	+1.96 -1.28	+1.03 -1.10
$\beta_{time}{}^c$	1.00	1.00	1.00	1.01	1.00
White Noise[d] (mmag)	$1.67^{+0.53}_{-0.53}$	$1.78^{+1.05}_{-1.05}$	$3.79^{+1.40}_{-1.40}$	$3.12^{+1.76}_{-1.76}$	$2.09^{+0.90}_{-0.90}$
Red Noise[d] (mmag)	0.00	0.00	0.00	$0.32^{+0.32}_{-0.32}$	0.00
$\beta_{wavelet}{}^e$	1.00	1.00	1.00	1.00	1.00
White Noise[f] (mmag)	2.23	3.08	3.32	2.37	1.69
Red Noise[f] (mmag)	0.00	0.001	0.001	0.00	0.00
OoT Baseline Function	Linear	Quad	Linear	Linear	Linear

Continued on next page

Table 2.7 – continued

Planet	WASP-1b	WASP-1b	WASP-1b	WASP-1b	WASP-33b
Date	2013 Oct. 22	2013 Oct. 22	All	All	2012 Dec. 01
Filter[1]	U	B	U	B	U
T_c (HJD-2450000)	$6588.69666^{+0.00090}_{-0.00082}$	$6588.6961^{+0.0008}_{-0.0012}$	—	—	$6263.8434^{+0.0022}_{-0.0029}$
R_p/R_*	$0.09630^{+0.00092}_{-0.00092}$	$0.10096^{+0.00097}_{-0.00097}$	$0.0964^{+0.0010}_{-0.00010}$	$0.1013^{+0.0018}_{-0.0018}$	$0.1125^{+0.0047}_{-0.0097}$
Duration (min)	$222.01^{+3.22}_{-3.22}$	$213.71^{+3.22}_{-3.22}$	$223^{+1.83}_{-1.83}$	$224.17^{+1.83}_{-1.83}$	$164.77^{+2.15}_{-2.15}$
$\beta_{res2}{}^a$ (R_p/R_*)	1.03	1.26	1.41	1.73	2.81
$\beta_{res2}{}^a$ (T_c)	1	1.2	—	–	2.7
$\beta_{res1}{}^b$ (R_p/R)	+0.69 -0.81	+0.81 -0.30	+0.64 -0.57	+1.63 -0.73	+3.88 -8.40
$\beta_{res1}{}^b$ (T_c)	+1.53 -1.40	+1.50 -2.20	—	—	+3.60 -4.55
$\beta_{time}{}^c$	1.03	1.06	1.002	1.01	1.1
White Noise[d] (mmag)	$1.71^{+0.96}_{-0.96}$	$1.12^{+0.70}_{-0.70}$	$1.28^{+0.72}_{-0.72}$	$1.81^{+0.94}_{-0.94}$	$2.73^{+1.31}_{-1.31}$
Red Noise[d] (mmag)	$0.39^{+0.62}_{-0.39}$	$0.41^{+0.30}_{-0.30}$	$0.17^{+0.90}_{-0.17}$	$0.29^{+0.33}_{-0.29}$	$1.23^{+2.82}_{-1.23}$
$\beta_{wave}{}^e$	1	1.04	1.004	1	1.54
Wavelet White Noise[f] (mmag)	1.32	0.79	1.91	1.36	1.28
Wavelet Red Noise[f] (mmag)	0	0.22	0.18	0	1.52
OoT Baseline Function	None	Linear	—	—	Linear

Continued on next page

Table 2.7 – continued

Planet	WASP-33b	WASP-33b	WASP-33b	WASP-36b	WASP-48b
Date	2012 Dec. 01	2012 Oct. 01	All	2012 Dec. 29	2011 October 09
Filter[1]	B	U	U	R	U
T_c (HJD-2450000)	$6263.8419^{+0.0036}_{-0.0076}$	$6202.84778^{+0.00067}_{-0.00069}$	—	$6290.86129^{+0.00034}_{-0.00026}$	$5844.7249^{+0.0019}_{-0.0017}$
R_p/R_*	$0.1127^{+0.0054}_{-0.0056}$	$0.1017^{+0.0027}_{-0.0027}$	$0.1086^{+0.0022}_{-0.0007}$	$0.13850^{+0.00071}_{-0.00082}$	$0.0916^{+0.0017}_{-0.0017}$
Duration (min)	$167.31^{+2.15}_{-2.15}$	$165.50^{+0.71}_{-0.71}$	$166.94^{+0.55}_{-0.55}$	$109.46^{+0.72}_{-0.72}$	$192.20^{+1.73}_{-1.73}$
$\beta_{res2}{}^a$ (R_p/R_*)	1.44	1.21	2.33	1.24	1.16
$\beta_{res2}{}^a$ (T_c)	1.197	1.16	—	1.18	1.19
$\beta_{res1}{}^b$ (R_p/R)	+0.85 -1.67	2.34 -2.70	+6.95 -3.68	+0.95 -0.41	+0.11 -0.98
$\beta_{res1}{}^b$ (T_c)	+3.31 -3.33	+4.11 -2.70	—	+1.59 -0.50	+1.35 -1.24
$\beta_{time}{}^c$	1.05	1.01	1.02	1.002	1
White Noise[d] (mmag)	$6.45^{+3.50}_{-3.50}$	$3.03^{+1.31}_{-1.31}$	$3.21^{+1.35}_{-1.35}$	$1.99^{+0.86}_{-0.86}$	$2.16^{+0.96}_{-0.96}$
Red Noise[d] (mmag)	$1.96^{+1.71}_{-1.71}$	$0.28^{+0.28}_{-0.28}$	$0.67^{+0.24}_{-0.24}$	$0.13^{+0.68}_{-0.13}$	0
$\beta_{wave}{}^e$	1.05	1.39	1.14	1	1
White Noise[f] (mmag)	5.13	1.18	1.84	1.8	2.22
Red Noise[f] (mmag)	1.58	1.13	1	0.01	0.02
OoT Baseline Function	None	Quadratic	—	Linear	None

Continued on next page

Table 2.7 – continued

[1] Filter: B is the Harris B (330–550 nm), R is the Harris R (550–900 nm), V is the Harris V (473–686 nm) and U is the Bessell U (303–417 nm)

[a] β_{res2} is found by using the second residual permeation method (Section 2.3.1)

[b] β_{res1} is found by using the first residual permeation method (Section 2.3.1)

[c] β_{time} is the scaling factor for the Time-Averaging method (Pont et al. 2006) (Section 2.3.1)

[d] The red and white noise calculated using the Time-Averaging method (Pont et al. 2006) (Section 2.3.1)

[e] β_{wave} is the scaling factor for the wavelet likelihood technique (Carter & Winn 2009) (Section 2.3.1)

[f] The red and white noise calculated using the wavelet likelihood technique (Carter & Winn 2009) (Section 2.3.1)

Table 2.8: Parameters derived in this study for the HAT-P-13b, WASP-12b, and WASP-44b light curves using `EXOMOP`

Parameter	Value	Value	Value	Value
Planet	HAT-P-13b	WASP-12b	WASP-12b	WASP-12b
Date	2013 March 02	2011 Nov. 15	2011 Nov. 15	2012 March 22
Filter[1]	U	U	R	U
T_c (HJD-2450000)	$6354.6974^{+0.0014}_{-0.0014}$	$5881.98375^{+0.00047}_{-0.00078}$	$5881.98229^{+0.00080}_{-0.00080}$	$6009.67929^{+0.00060}_{-0.00057}$
R_p/R_*	$0.0850^{+0.0022}_{-0.0014}$	$0.11963^{+0.00082}_{-0.00082}$	$0.1153^{+0.0016}_{-0.0016}$	$0.12313^{+0.00087}_{-0.00087}$
a/R_*	$5.280^{+0.065}_{-0.065}$	$3.189^{+0.021}_{-0.021}$	$3.057^{+0.052}_{-0.051}$	$3.202^{+0.025}_{-0.036}$
Duration (min)	$202.44^{+1.38}_{-1.38}$	$176.44^{+3.08}_{-3.08}$	$180.57^{+3.08}_{-3.08}$	$179.58^{+1.39}_{-1.39}$
$\beta_{res2}{}^a$ (R_p/R_*)	1.48	0.99	1.50	0.70
$\beta_{res2}{}^a$ (T_c)	1.35	0.91	1.46	0.70
$\beta_{res2}{}^a$ (a/R_*)	1.348	0.91	1.47	0.73
$\beta_{res1}{}^b$ (R_p/R)	+1.55 -0.63	+0.49 − 1.01	+1.20 − 1.26	+0.31 − 0.71
$\beta_{res1}{}^b$ (T_c)	+0.98 -1.35	+0.64 − 1.70	+1.23 − 1.99	+0.23 − 0.89
$\beta_{res1}{}^a$ (a/R_*)	+0.87 -0.99	+1.29 − 0.80	+1.75 − 2.01	+1.30 − 0.78
$\beta_{time}{}^c$	1.00	1.00	1.00	1.00
White Noise^d (mmag)	$1.67^{+0.46}_{-0.46}$	$1.59^{+0.74}_{-0.74}$	$1.42^{+0.65}_{-0.65}$	$2.31^{+0.65}_{-0.65}$
Red Noise^d (mmag)	0.00	0.00	0.00	0.00
$\beta_{wave}{}^e$	1.00	1.00	1.00	1.00

Continued on next page

Table 2.8 – continued

White Noise[f] (mmag)	1.20	1.22	1.11	1.62
Red Noise[f] (mmag)	0.00	0.00	0.00	0.00
OoT Baseline Function	None	Linear	Linear	Linear
Planet	WASP-12b	WASP-12b	WASP-12b	WASP-44b
Date	2012 Oct. 02	2012 Nov. 30	All	2011 Oct. 13
Filter[1]	U	U	U	U
T_c (HJD-2450000)	$6202.95339^{+0.00045}_{-0.00055}$	$6262.88831^{+0.00068}_{-0.00068}$	—	$5848.8477^{+0.0013}_{-0.0013}$
R_p/R_*	$0.11660^{+0.00077}_{-0.00077}$	$0.1193^{+0.0014}_{-0.0014}$	$0.12016^{+0.00076}_{-0.00065}$	$0.1228^{+0.0028}_{-0.0028}$
a/R_*	$3.096^{+0.023}_{-0.046}$	$3.313^{+0.046}_{-0.051}$	$3.217^{+0.038}_{-0.026}$	$8.31^{+0.30}_{-+0.30}$
Duration (min)	$179.43^{+1.43}_{-1.43}$	$170.78^{+1.31}_{-1.31}$	$171.26^{+2.17}_{-2.17}$	$135.81^{+1.60}_{-1.60}$
$\beta_{res2}{}^a$ (R_p/R_*)	0.97	1.14	1.87	1.15
$\beta_{res2}{}^a$ (T_c)	0.92	1.02	—	1.07
$\beta_{res2}{}^a$ (a/R_*)	0.92	1.02	1.27	1.25
$\beta_{res1}{}^b$ (R_p/R)	+0.77 − 0.41	+1.01 − 1.00	+1.00 − 1.40	+0.25 -0.28
$\beta_{res1}{}^b$ (T_c)	+0.92 − 1.23	+0.95 − 0.91	—	0.86 -0.72
$\beta_{res1}{}^a$ (a/R_*)	+0.56 − 1.97	+1.15 − 1.16	+2.03 − 1.61	0.87 -0.53
$\beta_{time}{}^c$	1.02	1.00	1.00	1.00
White Noise[d] (mmag)	$2.07^{+0.91}_{-0.91}$	$3.35^{+1.32}_{-1.32}$	$2.51\ ^{+1.31}_{-1.31}$	$5.05^{+1.70}_{-1.70}$
Red Noise[d] (mmag)	$0.15^{+0.15}_{-0.15}$	0.00	0.00	0.00

Continued on next page

Table 2.8 – continued

β_{wave}[e]	1.00	1.00	1.00	1.00
Wavelet White Noise[f] (mmag)	1.56	3.23	2.06	5.25
Wavelet Red Noise[f] (mmag)	0.001	0.00	0.00	0.00
OoT Baseline Function	Linear	Linear	—	Linear

[1] Filter: B is the Harris B (330–550 nm), R is the Harris R (550–900 nm), V is the Harris V (473–686 nm) and U is the Bessell U (303–417 nm)

[a] β_{res2} is found by using the second residual permeation method (Section 2.3.1)

[b] β_{res1} is found by using the first residual permeation method (Section 2.3.1)

[c] β_{time} is the scaling factor for the Time-Averaging method (Pont et al. 2006) (Section 2.3.1)

[d] The red and white noise calculated using the Time-Averaging method (Pont et al. 2006) (Section 2.3.1)

[e] β_{wave} is the scaling factor for the wavelet likelihood technique (Carter & Winn 2009) (Section 2.3.1)

[f] The red and white noise calculated using the wavelet likelihood technique (Carter & Winn 2009) (Section 2.3.1)

Table 2.9: Parameters derived in this study for the WASP-44b and WASP-77Ab light curves using EXOMOP

Parameter	Value	Value	Value
Planet	WASP-44b	WASP-44b	WASP-77Ab
Date	2013 Oct. 19	2013 Oct. 09	2012 Dec. 06
Filter[1]	B	V	U
T_c (HJD-2450000)	$6585.68580^{+0.00063}_{-0.00063}$	$6585.68618^{+0.00077}_{-0.00053}$	$6271.65804^{+0.00032}_{-0.00035}$
R_p/R_*	$0.1236^{+0.0018}_{-0.0019}$	$0.1164^{+0.0017}_{-0.0017}$	$0.12612^{+0.00098}_{-0.00094}$
a/R_*	$8.59^{+0.11}_{-+0.12}$	$8.33^{+0.09}_{-+0.14}$	$5.396^{+0.054}_{-0.054}$
Duration (min)	$126.21^{+2.73}_{-2.73}$	$129.10^{+2.84}_{-2.84}$	$129.67^{+1.61}_{-1.61}$
$\beta_{res2}{}^a$ (R_p/R_*)	1.04	1.23	1.69
$\beta_{res2}{}^a$ (T_c)	1.04	1.26	1.55
$\beta_{res2}{}^a$ (a/R_*)	1.01	1.21	1.47
$\beta_{res1}{}^b$ (R_p/R)	+0.11 -0.14	+0.92 -0.75	0.36 -0.53
$\beta_{res1}{}^b$ (T_c)	+0.58 -0.49	+1.62 -1.03	1.07 -0.87
$\beta_{res1}{}^a$ (a/R_*)	+0.44 -0.32	+0.96 -1.77	1.00 -1.33
$\beta_{time}{}^c$	1.00	1.00	1.00
White Noise^d (mmag)	$2.18^{+1.06}_{-1.06}$	$2.04^{+1.02}_{-1.02}$	$1.53^{+0.51}_{-0.51}$
Red Noise^d (mmag)	0.00	0.00	0.00
$\beta_{wave}{}^e$	1.00	1.00	1.00
White Noise^f (mmag)	2.45	2.18	1.34
Red Noise^f (mmag)	0.00	0.00	0.00
OoT Baseline Function	Linear	Linear	Linear

[1] Filter: B is the Harris B (330–550 nm), R is the Harris R (550–900 nm), V is the Harris V (473–686 nm) and U is the Bessell U (303–417 nm)

[a] β_{res2} is found by using the second residual permeation method (Section 2.3.1) using the first residual permeation method (Section 2.3.1)

[c] β_{time} is the scaling factor for the Time-Averaging method (Pont et al. 2006) (Section 2.3.1)

[d] The red and white noise are calculated using the Time-Averaging method (Pont et al. 2006) (Section 2.3.1)

[e] β_{wave} is the scaling factor for the wavelet likelihood technique (Carter & Winn 2009) (Section 2.3.1)

[f] The red and white noise are calculated using the wavelet likelihood technique (Carter & Winn 2009) (Section 2.3.1)

Table 2.10: Physical Properties of CoRoT-1b, GJ436b, HAT-P-1b, HAT-P-13b, HAT-P-22b, TrES-2b, TrES-4b, WASP-1b, WASP-12b, WASP-33b, WASP-36b, WASP-44b, and WASP-48b derived from the light curve modeling

Parameter (units)	Value	Source	Value	Source
Planet	CoRoT-1b	–	GJ436b	—
M_b (M_{Jup})	1.07±0.17	1	0.0728±0.0024	1
Near-UV R_p/R_*	$0.1439^{+0.0020}_{-0.0018}$	1	$0.0758^{+0.0086}_{-0.0075}$	1
Optical R_p/R_*	$0.1381^{+0.0007}_{-0.0015}$	2	0.08310±0.00027	3
Near-UV R_b (R_{Jup})	1.48±0.13	1	0.342±0.041	1
Optical R_b (R_{Jup})	1.42±0.24	2	0.3739±0.0097	3
ρ_b (ρ_{Jup})	0.33±0.10	1	1.30±0.11	1
log g_b (cgs)	3.12±0.20	1	3.180±0.032	1
T'_{eq} (K)	1834±46	2	686 ±10	3
H (km)	705±320	1	230 ±17	1
Θ	0.039±0.013	1	0.0267±0.0015	1
Orbital inclination (°)	$85.66^{+0.62}_{-0.48}$	2	86.774± 0.030	3
Orbital eccentricity	$0.071^{+0.62}_{-0.48}$	2	0.150±0.012	3
a (AU)	$0.0259^{+0.0011}_{-0.0020}$	2	0.03109±0.00074	3
Period (d)	1.508976552±0.000000097	1	2.64389788±0.00000010	1
$T_c(0)$ (BJD)	2454138.303971±0.000036	1	2454238.479958±0.000039	1

Continued on next page

Table 2.10 – continued

Planet	HAT-P-1b	–	HAT-P-13b	—
M_b (M_{Jup})	0.529±0.020	1	0.906±0.023	1
Near-UV R_p/R_*	$0.1189^{+0.0010}_{-0.0015}$	1	$0.0850^{+0.0022}_{-0.0014}$	1
Optical R_p/R_*	0.11802±0.00018	4	0.0870498±0.0024	5
Near-UV R_b (R_{Jup})	1.358±0.036	1	1.452±0.052	1
Optical R_b (R_{Jup})	1.319±0.019	4	1.487±0.038	5
ρ_b (ρ_{Jup})	0.269±0.040	1	0.272±0.021	1
$\log g_b$ (cgs)	2.912±0.048	1	3.008±0.032	1
T'_{eq} (K)	1322±15	4	1740±27	1
H (km)	1008±73	1	863±65	1
Θ	0.0403±0.0032	1	0.0405±0.0023	1
Orbital inclination (°)	85.634±0.056	4	81.93±0.26	5
Orbital eccentricity	0.00	4	0.0133±0.0041	6
a (AU)	0.05561±0.00083	4	0.0431±0.0012	1
Period (d)	4.4652968±0.0000018	1	2.9162382±0.0000016	1
$T_c(0)$ (BJD)	2453979.93165±0.00025	1	2455176.53864±0.00023	1

Continued on next page

Table 2.10 – continued

Planet	HAT-P-16b	—	HAT-P-22b	–
M_b (M_{Jup})	4.189±0.092	1	2.148±0.062	1
Near-UV R_p/R_*	0.10645±0.00067	1	0.1079±0.00094	1
Optical R_p/R_*	0.1071±0.0014	7	0.1065±0.0017	9
Near-UV R_b (R_{Jup})	1.28±0.056	1	1.092±0.047	1
Optical R_b (R_{Jup})	1.190±0.035	7	1.080±0.058	9
ρ_b (ρ_{Jup})	1.86±0.24	1	1.61±0.21	1
$\log g_b$ (cgs)	3.858±0.053	1	3.691±0.063	1
T'_{eq} (K)	1571±21	7	1463±19	9
H (km)	109±13	1	150±22	1
Θ	0.237±0.017	1	0.186±0.017	1
Orbital inclination (°)	87.74±0.59	7	$86.9^{+0.6}_{-0.5}$	9
Orbital eccentricity	0.034±0.003.	8	0.016±0.009	9
a (AU)	0.04130±0.00047	7	0.0414±0.0005	9
Period (d)	2.775970244±0.00000066	1	3.2122312±0.0000012	1
$T_c(0)$ (BJD)	2455027.592939±0.00019	1	2454930.22296±0.00025	1

Continued on next page

Table 2.10 – continued

Planet	TrES-2b	—	TrES-4b	—
M_b (M_{Jup})	1.44±0.21	10	0.917±0.070	1
Near-UV R_p/R_*	0.1243±0.0024	1	$0.1094^{+0.0052}_{-0.0052}$	1
Optical R_p/R_*	$0.125358^{+0.000019}_{-0.000024}$	10	0.09745±0.00076	11
Near-UV R_b (R_{Jup})	1.215±0.049	1	1.91±0.11	1
Optical R_b (R_{Jup})	$1.245^{+0.045}_{-0.041}$	10	1.706±0.056	11
ρ_b (ρ_{Jup})	1.82±0.23	10	0.173±0.022	1
log g_b (cgs)	3.798±0.046	10	2.89±0.055	1
T'_{eq} (K)	1472±12	10	1778±22	11
H (km)	118±12	1	1373±167	1
Θ	0.216±0.020	10	0.0393±0.0038	1
a (AU)	$0.0367^{+0.0013}_{-0.0012}$	10	0.05084±0.00050	11
Orbital inclination (°)	$83.8646^{+0.0041}_{-0.0036}$	10	82.81±0.37	11
Orbital eccentricity	0 $0.0002^{+0.0010}_{-0.0002}$	10	0	11
Period (d)	2.4706132±0.0000001	10	3.5539246±0.0000014	1
$T_c(0)$ (BJD)	2454969.39661±0.0048	10	2454223.79850±0.00032	1

Continued on next page

Table 2.10 – continued

Planet	WASP-1b	—	WASP-12b	—
M_b (M_{Jup})	0.846±0.054	1	2.01±0.14	1
Near-UV R_p/R_*	$0.0964^{+0.0010}_{-0.00010}$	1	$0.12016^{+0.00076}_{-0.00065}$	1
Optical R_p/R_*	0.1013±0.0018	1	0.1173±0.0005	14
Near-UV R_b (R_{Jup})	1.379±0.033	1	1.835±0.08	1
Optical R_b (R_{Jup})	1.449±0.041	1	1.860±0.090	14
ρ_b (ρ_{Jup})	0.26022±0.028	1	0.326± 0.049	1
log g_b (cgs)	2.998±0.039	1	3.210±0.057	1
T'_{eq} (K)	1812±14	1	2483±79	1
H (km)	920±82	1	773±103	1
Θ	0.0366±0.0034	1	0.0389±0.0055	1
a (AU)	$0.03889^{+0.00053}_{-0.00073}$	12	0.0235±0.0011	1
Orbital inclination (°)	88.65±0.55	13	$82.96^{+0.50}_{-0.44}$	14
Orbital eccentricity	0	13	0.0447±0.0043	14
Period (d)	2.51994529±0.00000056	1	1.09142119±0.00000021	1
$T_c(0)$ (BJD)	2453912.51504 ±0.00035	1	2455147.45820±0.00013	1

Continued on next page

Table 2.10 – continued

Planet	WASP-33b	—	WASP-36b	—
M_b (M_{Jup})	3.28±0.73	1	2.286±0.066	1
Near-UV R_p/R_*	$0.1086^{+0.0022}_{-0.0007}$	1	$0.1316^{+0.0018}_{-0.0018}$	1
Optical R_p/R_*	0.1143±0.0002	15	$0.13850^{+0.00071}_{-0.00082}$	1
Near-UV R_b (R_{Jup})	$1.594^{+0.043}_{-0.043}$	1	1.218±0.028	1
Optical R_b (R_{Jup})	$1.679^{+0.019}_{-0.030}$	15	1.281±0.026	1
ρ_b (ρ_{Jup})	0.65±0.14	1	1.017±0.068	1
log g_b (cgs)	3.459±0.098	1	3.538±0.028	1
T'_{eq} (K)	2723±37	16	1724±39	17
H (km)	477±108	1	252±17	1
Θ	0.065±0.015	1	0.0905±0.0047	1
a (AU)	$0.0259^{+0.0005}_{-0.0005}$	3	0.02643±0.00026	17
Orbital inclination (°)	86.2±0.2	15	83.61±0.21	17
Orbital eccentricity	0	15	0	17
Period (d)	1.21987016±0.00014	1	1.53736423±0.00000057	1
$T_c(0)$ (BJD)	2452984.82964±0.00030	1	2455569.83817±0.00010	1

Continued on next page

Table 2.10 – continued

Planet	WASP-44b	—	WASP-48b	—
M_b (M_{Jup})	0.867±0.064	1	0.984±0.085	1
Near-UV R_p/R_*	0.1228±0.0028	1	0.0916±0.0017	1
Optical R_p/R_*	0.1164±0.0017	1	0.0980±0.0010	19
Near-UV R_b (R_{Jup})	1.03±0.038	1	1.560±0.088	1
Optical R_b (R_{Jup})	0.98±0.032	1	1.67±0.10	19
ρ_b (ρ_{Jup})	0.86±0.11	1	0.198±0.039	1
$\log g_b$ (cgs)	3.35±0.05	1	2.941±0.092	1
T'_{eq} (K)	1304±36	18	2035±52	19
H (km)	292±32	1	1178±415	1
Θ	0.0664±0.0068	1	0.0340±0.0046	1
a (AU)	0.03443±0.00099	18	0.0344±0.0026	18
Orbital inclination (°)	86.59	18	80.09±0.55	19
Orbital eccentricity	0	18	0	19
Period (d)	2.4238120±0.0000012	1	2.14363592±0.0000046	1
$T_c(0)$ (BJD)	2455434.37655±0.00020	1	2455364.55217±0.00020	1

References. — (1) Our Study; (2) Gillon et al. 2009; (3) Knutson et al. 2014a; (4) Nikolov et al. 2014; (5) Southworth et al. 2012a; (6) Winn et al. 2010; (7) Ciceri et al. 2013; (8) Husnoo et al. 2012; (9) Bakos et al. 2011; (10) Barclay et al. 2012; (11) Chan et al. 2011; (12) Maciejewski et al. 2014; (13) Stempels et al. 2007; (14) Maciejewski et al. 2013; (15) Kovács et al. 2013; (16) Collier Cameron et al. 2010; (17) Smith et al. 2011; (18) Anderson et al. 2012; (19) Enoch et al. 2011;

Table 2.11: Physical Properties of WASP-77Ab derived from the light curve modeling

Parameter (units)	Value	Source
Planet	WASP-77Ab	–
M_b (M_{Jup})	1.76±0.057	1
Near-UV R_p/R_*	$0.1305^{+0.0010}_{-0.0010}$	1^a
Optical R_p/R_*	0.13012±0.00065	2
Near-UV R_b (R_{Jup})	1.21±0.02	1
Optical R_b (R_{Jup})	1.21±0.02	2
ρ_b (ρ_{Jup})	0.928±0.055	1
$\log g_b$ (cgs)	3.471±0.022	1
T'_{eq} (K)	1674±24	1
H (km)	286±59	1
Θ	0.0694±0.0043	1
a (AU)	0.02396±0.00043	1
Orbital inclination (°)	89.40±0.7	2
Orbital eccentricity	0	2
Period (d)	1.3600306±0.0000012	1
$T_c(0)$ (BJD)	2455870.44977±0.00014	1

References. — (1) Our Study; (2) Maxted et al. 2013

(a) The near-UV R_p/R_* of WASP-77Ab is corrected for the dilution of the companion stars (Section 2.5.15)

2.4.1 Period Determination

By combining our EXOMOP derived mid-transit times with previously published mid-transit times, we refine the orbital period of our targets. When necessary, the mid-transit times are transformed from Heliocentric Julian Date (HJD), which is based on Coordinated Universal Time (UTC) time, into Barycentric Julian Date (BJD), which is based on Barycentric Dynamical Time (TDB), using the online converter[9] by Eastman et al. (2010). We derive an

[9]http://astroutils.astronomy.ohio-state.edu/time/hjd2bjd.html

improved ephemeris for each target by performing a weighted linear least-squares analysis using the following equation:

$$T_c = T_c(0) + P_p \times E, \tag{2.15}$$

where $T_c(0)$ is the mid-transit time at the discovery epoch in BJD, P_p is the orbital period of the target, and E is the integer number of cycles after their discovery paper. See Tables 2.10–2.11 for an updated $T_c(0)$ and P_p for each system.

2.5 Individual Systems

2.5.1 CoRoT-1b

CoRoT-1b is the first transiting exoplanet discovered by the CoRoT satellite (Baglin 2003; Barge et al. 2008). Several follow-up primary transit photometry studies of the system find no signs of a changing period (Bean 2009; Gillon et al. 2009; Csizmadia et al. 2010; Rauer et al. 2010; Southworth 2011; Sada et al. 2012; Ranjan et al. 2014). CoRoT-1b's atmosphere may have a temperature inversion (Snellen et al. 2009; Alonso et al. 2009; Rogers et al. 2009; Gillon et al. 2009; Zhao et al. 2012) or an isothermal profile (Deming et al. 2011). Infrared transmission spectroscopy observations by Schlawin et al. (2014) disfavor a TiO/VO-rich spectrum for CoRoT-1b, suggesting the temperature inversion is caused by another absorber in the atmosphere or that flat spectrum is due to clouds or a haze layer. Pont et al. (2010) observed the Rossiter-McLaughlin effect (Winn 2011) for this planet and found that the projected spin-orbit angle is not aligned with the stellar spin axis with $\lambda = 77° \pm 11°$. The Rossiter-McLaughlin effect is important because planets that are not coplanar with their host stars may exhibit bow shock variability (see Section 2.6.2, Vidotto et al. 2011c; Llama et al. 2013).

We observed CoRoT-1b on 2012 December 07 using the U filter (Table 2.2), which is the first published near-UV light curve of this planet (Fig. 2.1). Our derived physical parameters (Table 2.10) agree with previous studies and reduce the uncertainty on the period by a factor of 5 compared to Gillon et al. (2009). We also find a near- UV $R_p/R_* = 0.1439^{+0.0020}_{-0.0018}$ which is 2.3σ larger that its optical $R_p/R_* = 0.1381^{+0.0007}_{-0.0015}$ (Gillon et al. 2009). An early near-UV or any asymmetries are not seen in this transit of CoRoT-1b.

2.5.2 GJ436b

GJ436b, a hot Neptune, was discovered through radial velocity measurements (Butler et al. 2004) and later confirmed to be a transiting exoplanet (Gillon et al. 2007). There have been extensive ground-based and space-based photometry and spectral studies of the GJ436b (e.g. Maness et al. 2007; Deming et al. 2007; Ballard et al. 2010; Gibson et al. 2010; Knutson et al. 2014a). The host star is found to be inactive (e.g. Wright et al. 2007; Torres 2007; Madhusudhan & Winn 2009; Ballerini et al. 2012;) and there are two other transiting planets in the system (Ribas et al. 2008; Ballard et al. 2010; Stevenson et al. 2012; Knutson et al. 2014b). The host star being inactive reduces the possibility of bow shock variability in our near-UV observations (Vidotto et al. 2011c; Llama et al. 2013). In our sample, GJ436b has the lowest planetary mass, is the only hot Neptune, and the only planet orbiting an M-dwarf.

We observed the first near-UV light curve of GJ436b on 2012 March 23 and subsequently on 2012 April 07 (Table 2.2, Fig. 2.1). The light curves obtained for this object are noisy because the observations are reaching the precision limit ($\sim 2\times$ the photon limit) for the 1.55-m Kuiper telescope due to the small transit depth and the faintness of the M-dwarf in the near-UV. However, there are no asymmetries in the near-UV light-curves of GJ436b. Our physical parameters (Table 2.10) and light curve solution (Table 2.7) are consistent with previous studies. We find a near-UV $R_p/R_* = 0.0758^{+0.0086}_{-0.0075}$ which is consistent within 1σ of its optical $R_p/R_* = 0.08310\pm0.00027$ (Knutson et al. 2014a).

2.5.3 HAT-P-1b

HAT-P-1b is the first planet discovered by the HATNet project (Bakos et al. 2002; Bakos et al. 2007) and the planet orbits one of the stars in a visual binary (Bakos et al. 2007; Liu et al. 2014). There have been many follow-up transit observations of HAT-P-1b (e.g. Winn et al. 2007; Johnson et al. 2008; Todorov et al. 2010; Sada et al. 2012; Wilson et al. 2015). Secondary eclipse measurements by Béky et al. (2013) found a 2σ upper limit of 0.64 for HAT-P-1b's geometric albedo between 577 and 947 nm. Nikolov et al. (2014) report a conclusive detection of both sodium and water in the transmission spectra using the Space Telescope Imaging Spectrograph onboard the *HST*. Rossiter-McLaughlin effect

measurements of the system found that HAT-P-1b is aligned (3.7°±2.1°) with the host star's equator (Johnson et al. 2008). HAT-P-1b has the longest orbital period (P_p = 4.5 days) of all the planets in our study.

The first near-UV light curve of HAT-P-1b was observed on 2012 October 02 (Table 2.2, Fig. 2.1). The binary companion of the planet host star was used as the main reference star in our light curve analysis since the two stars are nearly identical in their stellar parameters (Bakos et al. 2007; Liu et al. 2014) and will experience similar variations due to the atmosphere (the stars are only separated by 11"). Our light curve solution (Table 2.7) and derived planetary parameters (Table 2.10) agree with previous studies. We find a near-UV $R_p/R_* = 0.1189^{+0.0010}_{-0.0015}$ which is within 1σ of the optical $R_p/R_* = 0.11802 \pm 0.00018$ (Nikolov et al. 2014). We do not observe an early ingress or any asymmetries in the light curve of HAT-P-1b.

2.5.4 HAT-P-13b

HAT-P-13b, is an inflated hot Jupiter in a nearly circular orbit (Bakos et al. 2009) and the system also has a massive outer planet ($M_{p,c} \sin i_c = 14.3\ M_{Jup}$; Winn et al. 2010; Knutson et al. 2014b), on a highly eccentric orbit (Bakos et al. 2009). Follow-up photometry studies have refined the planetary parameters of HAT-P-13b and searched for possible transit timing variations (Winn et al. 2010; Szabó et al. 2010; Pál et al. 2011; Nascimbeni et al. 2011; Fulton et al. 2011; Southworth et al. 2012a; Sada & Ramón-Fox 2016). In addition, Winn et al. (2010) performed Rossiter-McLaughlin effect measurements of the system and found that HAT-P-13b is likely aligned (1.9° ± 8.6°) with its host star's equator. HAT-P-13 has the highest metallicity of all the host stars in our sample (Fe/H = 0.43).

We observed the first near-UV transit of HAT-P-13b on 2013 March 02 (Table 2.2, Fig. 2.1). Our light curve (Table 2.8) and physical parameters (Table 2.10) agree with previous studies and the error on our period is improved by a factor of 1.6 over the error found by Southworth et al. (2012a). We find a near-UV $R_p/R_* = 0.0850^{+0.0022}_{-0.0014}$, which is consistent with its optical $R_p/R_* = 0.0871 \pm 0.0024$ (Southworth et al. 2012a). Turner et al. (2013) suggest that their non-detection of a bow shock around TrES-3b could have been caused by the low metallicity of the host star (Fe/H = -0.19). Therefore, HAT-P-13b is an

important target to test this suggestion since it has a high metallicity. Despite HAT-P-13 having a high metallicity, we do not observe an early near-UV ingress.

2.5.5 HAT-P-16b

HAT-P-16b is a hot Jupiter with a radius of 1.289±0.066 R_{Jup} and an abnormally large mass of 4.193±0.094 M_{Jup} (Buchhave et al. 2010). Spectroscopic and photometric studies have confirmed and improved upon the discovery values (Husnoo et al. 2012; Ciceri et al. 2013; Pearson et al. 2014; Sada & Ramón-Fox 2016). It was found through Rossiter-McLaughlin observations (Moutou et al. 2011) that HAT-P-16b's projected spin-orbit angle of $\lambda = -10^{\circ} \pm 16^{\circ}$ is aligned with the stellar spin axis. HAT-P-16b has the highest planetary mass in our sample.

We observed the second near-UV transit of HAT-P-16b on 2013 November 02 using the near-UV filter (Table 2.2, Fig. 2.2). This near-UV transit is observed to follow-up the observations done by Pearson et al. (2014). We perform a combined analysis with our near-UV transit and the near-UV transit presented by Pearson et al. (2014) since they used the same telescope/filter and the data reduction pipeline (`ExoDRPL`) as we do in this study. This combined light curve is binned by 2 min to minimize the contribution of red noise. Our light curve solution (Table 2.7) and derived planetary parameters (Table 2.10) agree with previous studies. The error on our period improved by a factor of 2 over that presented by Pearson et al. (2014). We also find a near-UV radius of $R_p/R_* = 0.10645 \pm 0.00067$, which is consistent within 1σ of its optical radius $R_p/R_* = 0.1071 \pm 0.0014$ (Ciceri et al. 2013). The near-UV light curves used in this study are stable (the R_p/R_* values are constant) over the ~1 year time period observed.

A very extended planetary magnetosphere (Vidotto et al. 2011b, see fig. 9) or a clumpy magnetosheath could cause a double transit if the material absorbing the near-UV radiation is concentrated in a small area. Specifically, if the absorbing material does not fill the entire planetary magnetosphere then there will be a gap between the absorbing material and the planetary radius (thus causing a double transit). The early ingress scenario described in the introduction assumes a filled planetary magnetosphere (constant absorption from the planet to the bow-shock) resulting in a blended absorption light curve. Pearson et al. (2014)

suggest they may have observed a double transit in their 2012 December 29 near-UV data of HAT-P-16b at a phase of -0.0305 or ∼26 minutes before the start of ingress (see their fig. 1). These authors cautioned that this 2σ feature requires follow-up observations. Our observations of HAT-P-16b do not reproduce this characteristic. Therefore, we believe the feature seen by Pearson et al. (2014) may have been an unknown systematic in their dataset or it is time-variable.

2.5.6 HAT-P-22b

HAT-P-22b, a hot Jupiter, was discovered by Bakos et al. (2011) around a G5 star that is part of a binary system with a distant M-dwarf companion (Bakos et al. 2011; Knutson et al. 2014b). This planet is a pL class exoplanet as defined by the Fortney et al. (2008) due to a low incoming flux impinging on its atmosphere. The host star of HAT-P-22b has the lowest mass of the hot Jupiter hosting stars in our sample.

We observed the first follow-up light curves of HAT-P-22b on 2013 February 22 and 2013 March 22 using the U filter (Table 2.2, Fig. 2.2). We combined the near-UV data and binned it by 2 mins (this time was chosen to minimize the contribution of red noise). The derived planetary parameters agree with the discovery values and the error on the period is improved by a factor of 7.5 (Table 2.10). We also find a near-UV radius of R_p/R_*= 0.1079±0.00094, which is consistent with its optical R_p/R_* = 0.1065±0.0017 (Bakos et al. 2011). We do not see asymmetries in our data.

2.5.7 TrES-2b

The hot Jupiter TrES-2b was the first transiting planet discovered in the Kepler field (O'Donovan et al. 2006). Follow-up transit observations have confirmed and refined the planetary parameters of this system (Holman et al. 2007; Colón et al. 2010; Mislis et al. 2010; Gilliland et al. 2010; Croll et al. 2010; O'Donovan et al. 2010; Scuderi et al. 2010; Southworth 2011;Kipping & Bakos 2011; Kipping & Spiegel 2011; Christiansen et al. 2011; Schröter et al. 2012; Barclay et al. 2012; Esteves et al. 2013; Ranjan et al. 2014). In addition, Rossiter-McLaughlin effect measurements of the system found that TrES-2b is aligned with its host star's equator (-9° ± 12°) and orbits in a prograde orbit (Winn et al. 2008b). TrES-2b

has the lowest albedo of any exoplanet currently known (Kipping & Spiegel 2011).

We observed the first near-UV light curve of TrES-2b on 2012 October 29 (Table 2.2, Fig. 2.2). There is no clear evidence for any asymmetries in the near-UV transit of TrES-2b. The TrES-2 system parameters were measured by Esteves et al. (2013) using 3 years of observations by the *Kepler* spacecraft. Due to their extensive analysis, we choose to only derive the near-UV radius of the planet (Table 2.10). We find a near-UV $R_p/R_* = 0.1243 \pm 0.0024$, which is consistent with its optical $R_p/R_* = 0.125358^{+0.000019}_{-0.000024}$ (Esteves et al. 2013).

2.5.8 TrES-4b

The hot Jupiter TrES-4b has a very low density and is one of the most highly inflated transiting giant planets known to date (Mandushev et al. 2007). Primary transit follow-up studies have refined these planetary parameters and searched for transit timing variations (Torres et al. 2008; Sozzetti et al. 2009; Southworth 2010; Chan et al. 2011; Sada et al. 2012; Ranjan et al. 2014; Sozzetti et al. 2015). TrES-4b was found to be aligned ($6.3° \pm 4.7°$) with its host star's equator using measurements of the Rossiter-McLaughlin effect (Narita et al. 2010). This system has the largest planetary radius and largest host star mass and radius in our sample.

Our observations of TrES-4b were conducted on 2011 July 26 using the Bessell U and Harris R filters (Table 2.2). We present the only published near-UV light curve of TrES-4b (Fig. 2.5, Table 2.7). Our planetary parameters agree with the discovery values and improve the error on the period by a factor of 2.3 (Table 2.10). We also find a near-UV $R_p/R_* = 0.1094^{+0.0052}_{-0.0052}$, which is larger by 2σ of its optical $R_p/R_* = 0.09745 \pm 0.00076$ (Chan et al. 2011). We do not observe any asymmetries in our data due to the presence of an optically thick bow shock.

2.5.9 WASP-1b

WASP-1b is the first exoplanet discovered by the SuperWASP survey (Pollacco et al. 2006; Collier Cameron et al. 2007). Several follow-up photometry studies that have refined these planetary parameters and searched for transit timing variations (Charbonneau et al. 2007b;

Shporer et al. 2007; Southworth 2008; Szabó et al. 2010; Southworth 2012; Sada et al. 2012; Maciejewski et al. 2014; Granata et al. 2014). Wheatley et al. (2010) observed the secondary transit of WASP-1b and found a strong temperature inversion in its atmosphere and ineffective day-night energy redistribution. Rossiter-McLaughlin effect measurements found WASP-1b to be misaligned (λ = -59 °) with the equator of its host star (Stempels et al. 2007; Albrecht et al. 2011; Simpson et al. 2011). WASP-1 is the only F star (F7V) in our sample.

Here we present the first near-UV light curves of WASP-1b (Table 2.2; Fig. 2.3, Table 2.7, Table 2.7). The light curve solution (Table 2.7, Table 2.7) and the derived planetary parameters (Table 2.10) are in agreement with previous studies. We also find a near-UV radius of R_p/R_* = 0.0964±0.0010, which is smaller by 3.5 σ than its optical radius of R_p/R_* = 0.1048±0.0014 (Granata et al. 2014). We do not see an early ingress or any asymmetries in our near-UV transits. Our near-UV light curves are stable over the 1 month time period observed.

2.5.10 WASP-12b

WASP-12b is a hot Jupiter orbiting a G0 star with a short orbital period (Hebb et al. 2009). There have been extensive photometric and spectroscopic studies of WASP-12b (e.g. López-Morales et al. 2010; Maciejewski et al. 2011, 2013; Swain et al. 2013; Teske et al. 2014; Stevenson et al. 2014b; Stevenson et al. 2014a; Kreidberg et al. 2015). WASP-12 is a triple star system with a binary M dwarf system in orbit around the G0 star (Crossfield et al. 2012; Bergfors et al. 2013; Bechter et al. 2014). Previous studies by Fossati et al. 2010, Haswell et al. (2012), and (Nichols et al. 2015) observed an early near-UV ingress with *HST* using the Cosmic Origins Spectrograph. However, these studies have a low number of data points and therefore follow-up near-UV studies are needed. Ground-based near-UV observations (Copperwheat et al. 2013) and additional space-based UV observations of WASP-12b using the Space Telescope Imaging Spectrograph instrument on *HST* (Sing et al. 2013) all do not observe any asymmetries in their near-UV light curves. Finally, WASP-12b has the closest orbital distance and largest planetary radius in our study and is the top candidate predicted by VJH11a to exhibit an early near-UV ingress.

Our observations were conducted from 2011 November to 2012 November (Table 2.2, Table 2.8; Fig. 2.4). These observations were performed to follow-up the previous near-UV observations and to confirm the detection of an early ingress. We didn't account for the M-dwarf companions in the our analysis, because they contribute a negligible amount of flux at the wavelengths observed (Copperwheat et al. 2013). We combined all the near-UV transits and binned the light curve by 90 s (this time was chosen to minimize the dominance of red noise). The derived planetary parameters (Table 2.10) are in agreement to previous studies. Our near-UV radius is within 1σ of that found by Copperwheat et al. (2013) and Sing et al. (2013). We also find a near-UV $R_p/R_* = 0.12016^{+0.00076}_{-0.00065}$, which is 2.5σ larger than optical radius of $R_p/R_* = 0.1173 \pm 0.0005$ (Maciejewski et al. 2013). The larger near-UV radius is consistent with Rayleigh scattering (Section 2.6.2). We do not observe an early ingress in any of our near-UV light curves. Our near-UV light curves are stable over the ~1 year time period observed.

2.5.11 WASP-33b

WASP-33b is a hot Jupiter (Collier Cameron et al. 2010) that orbits a bright (V-mag = 8.3) δ Scuti variable host star (Herrero et al. 2011). It is the first planet discovered to orbit an A-type star (Herrero et al. 2011). This system has been extensively studied with photometry and spectroscopy (Herrero et al. 2011; Moya et al. 2011; Smith et al. 2011; Deming et al. 2012; Sada et al. 2012; (de Mooij et al. 2013); von Essen et al. 2014; Haynes et al. 2015; Johnson et al. 2015; von Essen et al. 2015; Hardy et al. 2015). Secondary eclipse measurements indicate that WASP-33b has a low albedo (de Mooij et al. 2013) and inefficient heat-transport from the day-side to the night-side (Smith et al. 2011; Deming et al. 2012; Madhusudhan 2012; de Mooij et al. 2013; Haynes et al. 2015). In our study, WASP-33b has the highest planetary equilibrium temperature and is the only planet around an A star.

We observed the first near-UV light curve of WASP-33b on 2012 October 01 and subsequently in the B and U bands on 2012 December 01 (Table 2.2, Fig. 2.5). We did not take into account the pulsations in our modeling because it was found by von Essen et al. 2014 that taking them into account did not change their final parameter results. We see the

variability of the host star in our transits, residuals, and asymmetry test very clearly. The light curve solution (Table 2.7) and derived physical parameters (Table 2.10) are consistent with previous studies (e.g. Collier Cameron et al. 2010; Kovács et al. 2013; von Essen et al. 2014). We find a near-UV $R_p/R_* = 0.1086^{+0.0022}_{-0.0007}$, which is consistent with its optical R_p/R_* = 0.1066±0.0009 (Collier Cameron et al. 2010). There are asymmetries in our light curves (Fig. 2.5), however, the amplitude and shape of the variability in the residuals are due to host star's variability. Our near-UV transits are stable over the several months observed.

2.5.12 WASP-36b

The hot Jupiter WASP-36b was discovered around a G2 dwarf (Smith et al. 2012). The host star shows low levels of stellar activity and has undergone little or no tidal spin-up due to the planet (Smith et al. 2012). WASP-36 has the lowest metallicity of all the hot Jupiter host stars in our sample.

We observed the first near-UV light curve of WASP-36b on 2012 December 29 and an additional R band transit on 2013 March 15 (Table 2.2, Table 2.7, Fig. 2.6). The derived physical parameters (Table 2.10) agree with the discovery values and the error on the period is improved by a factor of 4.7. We also find a near-UV radius of $R_p/R_* = 0.1316^{+0.0018}_{-0.0018}$ which is 2.6σ smaller than the optical radius of $\mathrm{R}_p/\mathrm{R}_* = 0.13850^{+0.00071}_{-0.00082}$.

2.5.13 WASP-44b

The hot Jupiter WASP-44b is a highly inflated planet in orbit around a G8V star (Anderson et al. 2012). The host star, WASP-44, is found to be inactive based on observations of weak Ca II H&K emission and no rotational modulation (Anderson et al. 2012). The first follow-up light curve of WASP-44b (Mancini et al. 2013) indicates a constant radius from the optical to NIR wavelengths. This system has the smallest host star radius of all hot Jupiter systems in our study.

We observed the first near-UV light curve of WASP-44b on 2012 October 13 using the U filter and subsequently on 2013 October 19 with the B and V filter (Table 2.2, Table 2.8, Table 2.9, Fig. 2.6). The light curve solution (Table 2.7) and planetary parameters (Table 2.10) are consistent with the discovery value and the error on the period is im-

proved by a factor of 1.2 (Mancini et al. 2013). We also find a near-UV radius of $R_p/R_* = 0.1228 \pm 0.0028$, which is larger by 1.4σ with its optical radius of $R_p/R_* = 0.1164 \pm 0.0017$. An early near-UV or any asymmetries are not observed in the data.

2.5.14 WASP-48b

WASP-48b is a typical inflated hot Jupiter orbiting a slightly evolved F star (Enoch et al. 2011). These parameters were confirmed by follow-up J-band primary transit observations by Sada et al. (2012). Secondary eclipse measurements indicate that WASP-48b has a weak temperature inversion and moderate day/night recirculation (O'Rourke et al. 2014). Ciceri et al. (2015) find that the spectrum of WASP-48b is flat from the optical to near-IR, which suggests that the atmosphere is not affected by strong Rayleigh scattering. WASP-48 is the oldest system in our study with an age of $7.9^{2.0}_{-1.6}$ Gyr and may have undergone synchronization of its stellar rotation with the planetary orbital period due to interactions with WASP-48b (Enoch et al. 2011).

We observed WASP-48b on 2012 October 9 using the U filter (Table 2.2, Table 2.7, Fig. 2.6). The derived planetary parameters (Table 2.10) agree with the discovery values. We find a near-UV $R_p/R_* = 0.0916 \pm 0.0017$ which is 2.4σ smaller than its optical $R_p/R_* = 0.0980 \pm 0.0010$ (Enoch et al. 2011). We do not observe an early ingress in our near-UV transit.

2.5.15 WASP-77Ab

WASP-77Ab is a hot Jupiter orbiting a G8 star in a double-star system (Maxted et al. 2013). The host star exhibits moderate chromospheric activity determined by emission in the cores of the Ca II H & K lines and rotational modulation with a period of 15.3 days (Maxted et al. 2013). WASP-77 is the only multi-star system in our sample where both companions are solar-like stars (G8 and K).

On 2012 December 06 using the U filter we observed the first follow-up light curve of WASP-77Ab (Table 2.2, Fig. 2.7). The light curve solution is shown in Table 2.9.

We make sure to correct for the dilution due to the companion star being in our aperture using the procedure described below. The separation of the stars is 3.3" (our seeing

was 2.31–6.93") and the magnitude differences between the components of the binary in the near-UV are $\Delta m_u = 2.961 \pm 0.015$ (Maxted et al. 2013). WASP-77Ab orbits around the brighter companion (WASP-77A). We perform the procedure described below to find the corrected R_p/R_* value and error. (1) We model the light curve with `EXOMOP` and find $\left(R_p/R_*\right)_{uncor} = 0.12612^{+0.00098}_{-0.00094}$ for the uncorrected case. (2) We then calculate the flux of WASP-77B (F_2) using the following equation:

$$m_1 - m_2 = \Delta m_u = 2.5 \log\left(\frac{F_1}{F_2}\right), \tag{2.16}$$

where m_1 is the magnitude of WASP-77A, m_2 is the magnitude of WASP-77B, F_2 is the flux measured in the aperture for WASP-77A ($F_2 = 1\ erg\ s^{-1}\ cm^{-2}\ \text{Å}^{-1}$), and F_1 is the flux of WASP-77B (found to be $0.0654034 F_2$). (3) We then find the corrected $\left(R_p/R_*\right)_{cor}$ value using the equations

$$\left(\frac{R_p}{R_*}\right)_{cor} = \sqrt{\frac{\Delta F}{F_{cor}}} \tag{2.17}$$

$$\left(\frac{R_p}{R_*}\right)_{cor} = \sqrt{\frac{\Delta F}{F_2 - F_1}} \tag{2.18}$$

where ΔF is the change in flux during the transit and is equal to $\left(R_p/R_*\right)^2_{uncor}$ and F_{cor} is the corrected flux for WASP-77A. (4) We propagate all the errors (including Δm_u and the error from `EXOMOP` modeling) to find the new error on the $\left(R_p/R_*\right)_{cor}$. Performing this procedure, we find a near-UV radius of $\left(R_p/R_*\right)_{cor} = 0.1305 \pm 0.0010$.

We agree with the discovery values for our planetary parameters and the error on the period is improved by a factor of 1.7 (Table 2.11). The near-UV radius of WASP-77Ab of $\left(R_p/R_*\right)_{cor} = 0.1305 \pm 0.0010$ is consistent with its optical $R_p/R_* = 0.13012 \pm 0.00065$ (Maxted et al. 2013).

2.6 Discussion

2.6.1 Asymmetric Transits

A large early ingress (Figs. 2.1–2.7) or significant (>0.5%) R_p/R_* difference (Tables 2.7–2.9) is not observed in any of our near-UV light curves. To investigate whether the transit shapes are symmetrical, we perform an asymmetry test where we subtract the mirror image of the transit with itself (See Section 2.3.1). Asymmetries do not appear in any of these tests with the exception of WASP-33b, which is potentially the result of its host star's variability (Herrero et al. 2011; Smith et al. 2011; Kovács et al. 2013). Therefore, within the precision (1.23 – 5.54 mmag) and timing resolution (61 - 137 s) of our observations no asymmetries are observed. Our results are consistent with the previous non-detections of an early ingress in the ground-based near-UV light curves of HAT-P-5b (Southworth et al. 2012b), HAT-P-16b (Pearson et al. 2014), TrES-3b (Turner et al. 2013), WASP-12b (Copperwheat et al. 2013), WASP-17b (Bento et al. 2014), and XO-2b (Zellem et al. 2015).

Additionally, the non-detection of asymmetrical transits confirms and expands upon the theoretical modeling done by Ben-Jaffel & Ballester 2014 and Turner et al. 2016a. These theoretical studies concentrated on modeling the corona around solar-like stars. Therefore, since the targets in this study are deliberately chosen to have a variety of planetary and host star parameters (Table 2.1), based on the work in this paper we do not expect to observe near-UV asymmetries caused by an opacity source in the stellar corona in any system regardless of its spectral type.

Variability in the bow shock

Assuming that the bow shock is sufficiently optically thick to absorb light from the host star during transit, then we need to assess whether shock variability is a key factor in the non-detections. It is predicted that bow shock variations would be common for planets that are not circularized, not in the corotation radius of their host star, or orbiting around active stars (Vidotto et al. 2011c; Llama et al. 2013). Rossiter-McLaughlin effect (McLaughlin 1924; Rossiter 1924; Winn 2011) measurements and activity indicators can assess whether any of the systems would be prone to bow shock variability.

Measurements of the Rossiter-McLaughlin effect can be used to determine whether our systems are coplanar with their hosts stars. If the coronal material is axisymmetric and if a planet's orbital plane and the stellar equator are coplanar then the planet will move through coronal material of constant density and temperature during transit. In our sample, we have 4 planets (CoRoT-1b, WASP-1b, WASP-12b, WASP-33b) that are not aligned with their stars, 5 planets (HAT-P-1b, HAT-P-13b, HAT-P-16b, TrES-2b, TrES-4b) that are aligned with their stars, and 6 planets (GJ 436b, HAT-P-22b, WASP-36b, WASP-44b, WASP-48b, WASP-77Ab) that are in need of Rossiter-McLaughlin measurements (See Table 2.1). Therefore, it is possible that members of our sample may exhibit shock variability due to the planet moving through coronal material with different densities. However, this phenomenon does not explain all our non-detections since the planets that are aligned with their host stars are moving through coronal material with a similar density and through an environment with a constant stellar magnetic field.

Furthermore, if the host stars are active then fluctuations in the stellar wind, flaring, or coronal mass ejections could cause inhomogeneity in the coronal outflow. The $R^{'}_{HK}$ index, the ratio between chromospheric activity to the total bolometric emission of the star, can be used to gauge the amount of stellar activity of a star (Noyes et al. 1984) and more active stars exhibit higher $R^{'}_{HK}$ indices. In our sample, there are 6 planets (CoRoT-1b, GJ436b, HAT-P-13b, TrES-4b, WASP-1b, WASP-12b) with a $R^{'}_{HK}$ index lower than the Sun ($R^{'}_{HK,\odot}$ = -4.96), 1 planet (HAT-P-16b) with a $R^{'}_{HK} > R^{'}_{HK,\odot}$, 2 planets (HAT-P-1b, TrES-2b) with a $R^{'}_{HK} \sim R^{'}_{HK,\odot}$, and 6 planets (HAT-P-22b, WASP-33b, WASP-36b, WASP-44b, WASP-48b, WASP-77Ab) that do not have a $R^{'}_{HK}$ index measured (Table 2.1). Therefore, some of the non-detections of the bow shocks of planets around the active stars could be caused by their orbits moving through inhomogeneous coronal material. Also, stellar flares can raise the coronal temperature above the maximum temperature allowed for shock formation (VJH11a). HAT-P-16b (the only planet in our sample known to orbit an active host star) is observed more than once and all the observations result in non-detections despite six months between successive observations. Additionally, WASP-12b, WASP-1b, and GJ436b (planets known to orbit non-active host stars) are observed more than once and also result in non-detections. Therefore, variability of the coronal plasma may be causing some of our non-detections but not all of them.

However, the interpretation of variability causing some of our non-detections changes significantly if we now consider the theoretical study by Turner et al. (2016a). An extensive parameter study was conducted by Turner et al. (2016a) to determine if temperature ($3 \times 10^4 - 2 \times 10^6$K) or density ($10^4 - 10^8$cm^{-4}) changes in the coronal outflow would cause variation in the absorption due to the bow shock. They find that under all realistic conditions for a steady state or varying stellar corona, no absorption occurred in the bow shock. Therefore, we did not observe any asymmetries in our observations because bow shocks do not actually cause any absorption in the first place.

2.6.2 Wavelength dependence on the planetary radius

Observing the primary transit of an exoplanet at multiple wavelengths allows for an investigation into the composition and structure of its atmosphere. The measured R_p/R_* depends on the opacity of the planetary atmosphere and thus allows for useful insights into the atmosphere's spectral features and composition. If the opacity in our near-UV band is dominated by Rayleigh scattering of molecular hydrogen, it may be possible to place strong upper limits on the planet's 10 bar radius (Tinetti et al. 2010; Benneke & Seager 2013; Benneke & Seager 2012; Griffith 2014). Such constraints can break the degeneracy between an exoplanet's physical radius and atmospheric composition in radiative transfer retrievals (e.g. Lecavelier Des Etangs et al. 2008; Tinetti et al. 2010; Benneke & Seager 2012; Griffith 2014).

The R_p/R_* of 10 exoplanets (GJ436b, HAT-P-1b, HAT-P-13b, HAT-P-16b, HAT-P-22b, TrES-2b, WASP-33b, WASP-44b, WASP-48b, WASP-77Ab) are consistent to within 1σ of their optical R_p/R_* (Tables 2.10–2.11). Clouds in the upper atmospheres of these planets are consistent with these observations because clouds reduce the strength of spectral features (e.g. Seager & Sasselov 2000; Brown 2001; Gibson et al. 2013b; Kreidberg et al. 2014). Also, day-side spectral features may be absent due to an isothermal pressure-temperature profile (Fortney et al. 2006). These planets are consistent with other transiting exoplanet observations with flat spectra in optical wavelengths on TrES-3b (Turner et al. 2013), GJ 3470b (a hot Uranus; Biddle et al. 2014), GJ 1214b (Bean et al. 2011; Kreidberg et al. 2014), WASP-29b (Gibson et al. 2013a), and HAT-P-32b (Gibson et al. 2013b).

We also find that some of our targets do not exhibit a flat spectrum. The R_p/R_* in the near-UV of CoRoT-1b, TrES-4b, and WASP-12b are larger than their optical R_p/R_* by 2.3, 2, and 2.5σ, respectively (Table 2.10). This variation corresponds to a difference in the radius of 6 scale heights (H) for both CoRoT-1b and TrES-4b and 3H for WASP-12b. This is consistent with the 6H variation observed in HD 189733b (Sing et al. 2011). A larger near-UV radius may indicate non-uniform clouds (Griffith 2014) or Rayleigh scattering in the planetary atmospheres (Tinetti et al. 2010; Benneke & Seager 2013; Benneke & Seager 2012; Griffith 2014). Additionally, the near-UV R_p/R_* of WASP-1b and WASP-36b are smaller than their optical R_p/R_* by 3.6 and 2.6σ (Tables 2.10), respectively. To our knowledge, this is the first time a hot Jupiter has been observed to have a smaller near-UV transit depth than that measured in the optical. Additionally, the near-UV transit depths of WASP-1b and WASP-36b are smaller than any transit depth measurement made for the planets. A smaller transit depth could be caused by absorption of TiO (Evans et al. 2016), however, more work is needed to investigate possible opacity sources. The variation corresponds to a difference of 7 and 20H for WASP-1b and WASP-36b, respectively. The large scale height variations are similar with the 13H variation found for WASP-103b (Southworth et al. 2015). These results are consistent with other exoplanets not having flat spectrum (HD 209458b, Sing et al. 2008; HAT-P-5b, Southworth et al. 2012b; GJ 3470b, Nascimbeni et al. 2013; Qatar-2, Mancini et al. 2014).

For illustration, we compare the observed R_p/R_* with wavelength for each target to theoretical predictions by Fortney & Nettelmann (2010) for a model planetary atmosphere (Figures 2.8–2.10). The models used were estimated for planets with a 1 M_{Jup}, $g_p = 25m/s$, base radius of 1.25 R_{Jup} at 10 bars, solar metallicity, and T_{eq} closest to the measured value for each exoplanet (with model choices of 500, 750, 1000, 1250, 1500, 1750, 2000, 2500 K). Additionally, TiO and VO opacity were not included in the synthetic model. A vertical offset was added to the model to provide the best fit to the spectral changes. This comparison is illustrative of the size of variation of the observations compared to what the models predict. However, in-depth radiative transfer models calculated for all the exoplanets are still needed to fully understand their transmission spectra.

Next, we apply the MassSpec concept (Lecavelier Des Etangs et al. 2008, de Wit & Seager 2013) to the spectral slope to determine if the observed radius variations are con-

sistent with Rayleigh scattering. This approximation assumes a well-mixed, isothermal atmosphere in chemical equilibrium, and an effective atmospheric opacity source with an extinction cross section which follows a power-law index, α, $\sigma = \sigma_0(\lambda/\lambda_0)^\alpha$. The slope of the spectrum is related to α by using the scale height (Lecavelier Des Etangs et al. 2008)

$$\alpha H = \frac{d\,[R_p/R_*](\lambda)}{d\ln\lambda}, \tag{2.19}$$

where λ is the wavelength. A value of $\alpha = -4$ would be consistent with Rayleigh scattering (Lecavelier Des Etangs et al. 2008). In order to calculate α, we use our near-UV R_p/R_* values and the literature values of the nearest wavelength. In some cases, the nearest literature wavelength are not in the blue part of the spectra. This lack of measurement can cause a problem in the interpretation of α because the U and B bands are the only bands where strong spectral features are not present (Tinetti et al. 2010; Benneke & Seager 2012; Benneke & Seager 2013; Griffith 2014). The calculation of α also assumes that only a single species is dominant in the atmosphere, an assumption that may not always hold. We find a value of α of -17.3±7.9, -19.1±2.4 , and -5.9±0.9 for CoRoT-1b, TrES-4b, and WASP-12b, respectively. The spectral index calculated for WASP-12b (see also Sing et al. 2013) and CoRoT-1b are within 2σ of Rayleigh scattering. Follow-up observations are needed to confirm this result. It is possible that the index of TrES-4b is caused by scattering from aerosols (Sing et al. 2013) but this suggestion needs to be explored in greater detail. Additionally, values of α of +11.6±1.1 and +34.8±2.7 are found for WASP-1b and WASP-36b, respectively. This is the first time a positive α has been estimated for any exoplanet and more theoretical modeling is needed to identify possible opacity sources.

Variability due to the host stars

Our interpretation that the observed wavelength variations are due to the planetary atmosphere assumes that the host stars do not vary significantly due to stellar activity. The presence of stellar activity and star spots on the stellar surface can produce variations in the observed transit depth when measured at different times (e.g. Czesla et al. 2009; Oshagh et al. 2013; Oshagh et al. 2014; Zellem et al. 2015). This effect is particularly stronger in the near-UV than in the optical and can mimic a Rayleigh scattering signature (e.g. Oshagh

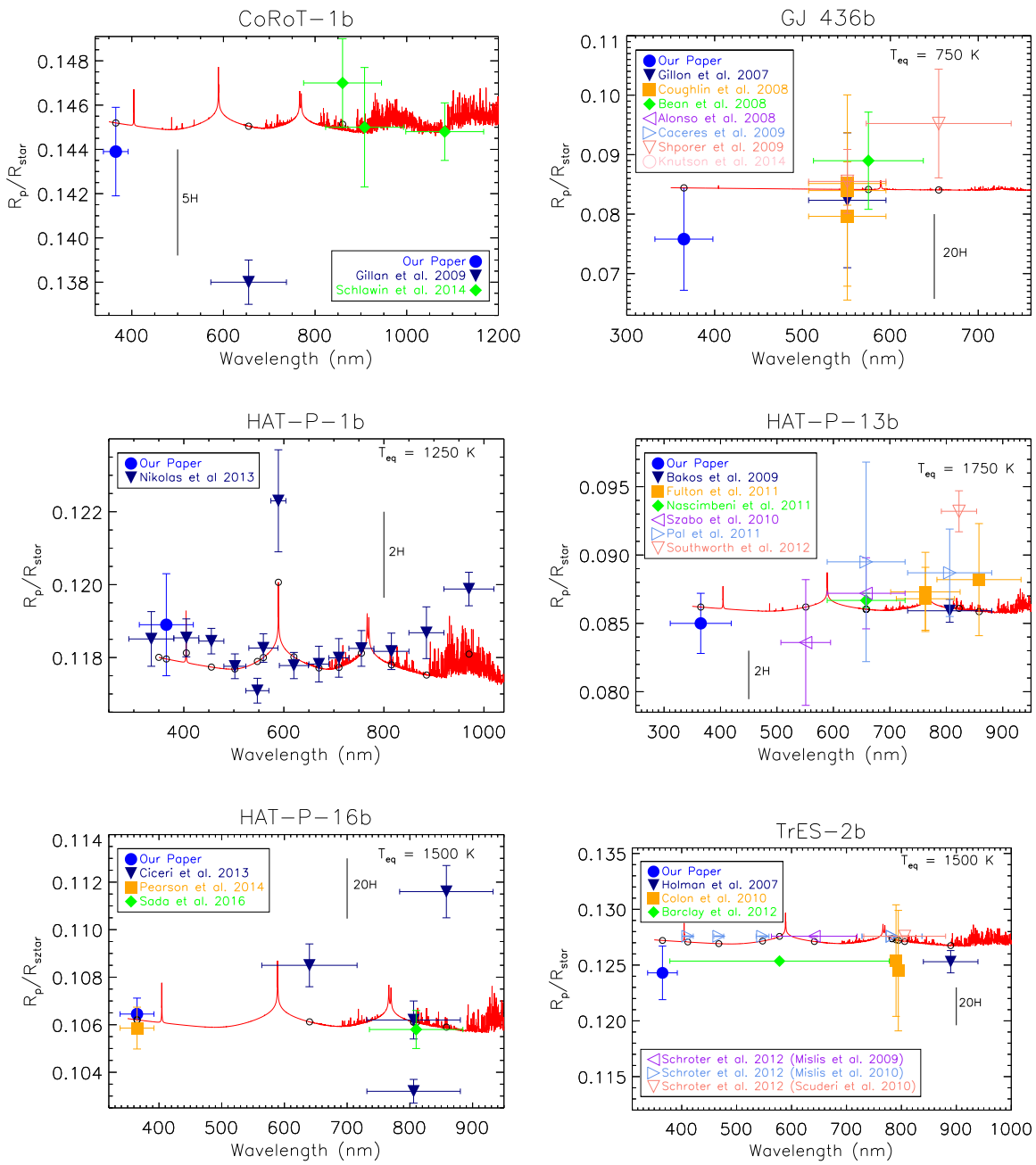

Figure 2.8: Variation of R_p/R_* vs. wavelength for CoRoT-1b, GJ 436b, HAT-P-1b, HAT-P-13b, HAT-P-16b, and TrES-2b. Over-plotted in red are atmospheric models by Fortney & Nettelmann (2010) for planets with a 1 M_{Jup}, $g_p = 25m/s$, base radius of 1.25 R_{Jup} at 10 bar, and T_{eq} (specified on plot). The scale height of the planet is also shown on each plot for reference.

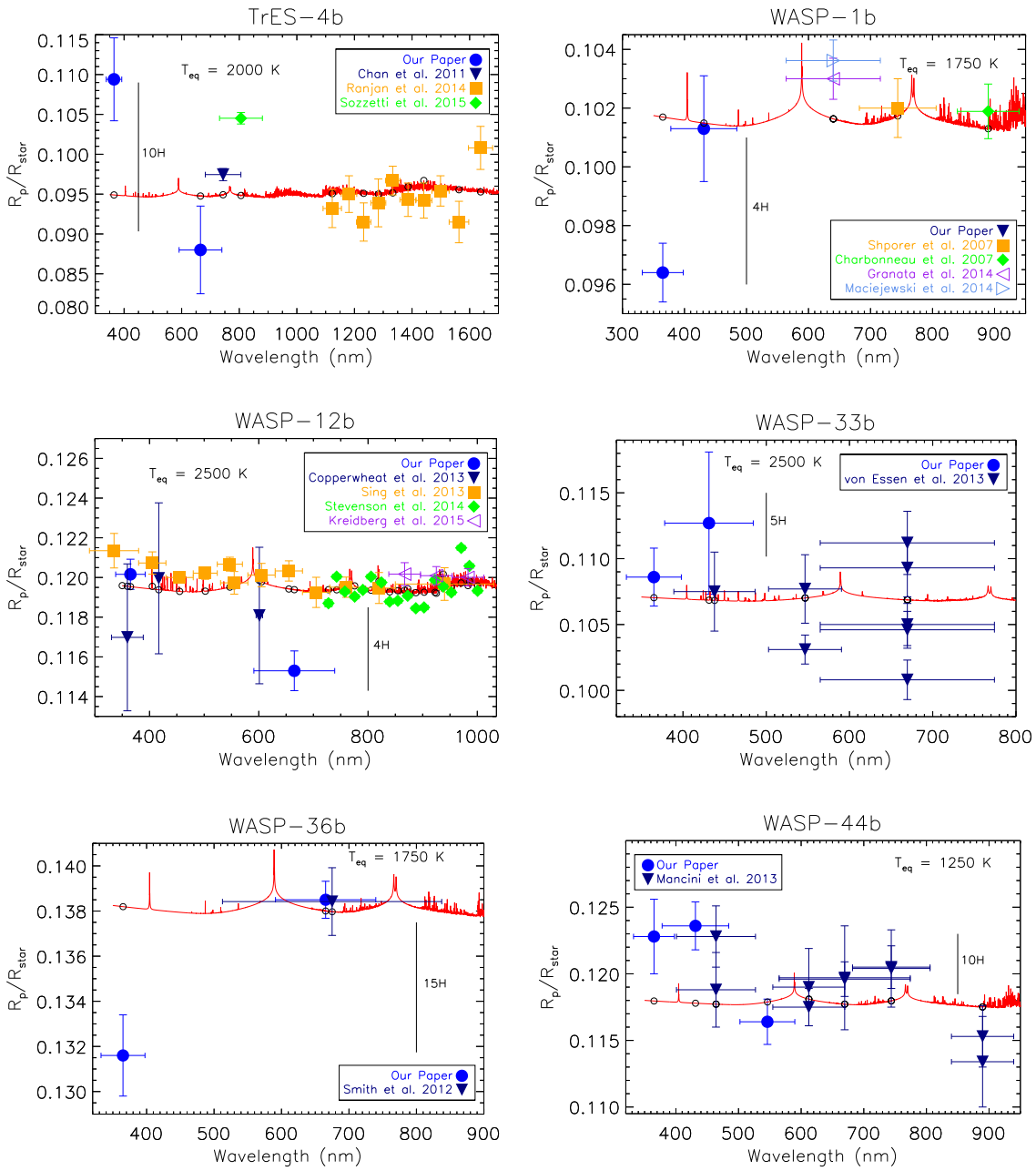

Figure 2.9: Variation of R_p/R_* vs. wavelength for TrES-4b, WASP-1b, WASP-12b, WASP-33b, WASP-36, and WASP-44b. The observation of a smaller near-UV than the optical radius on WASP-1b and WASP-36b are the first of such a detection on a hot Jupiter. Other comments are the same as Fig. 2.8.

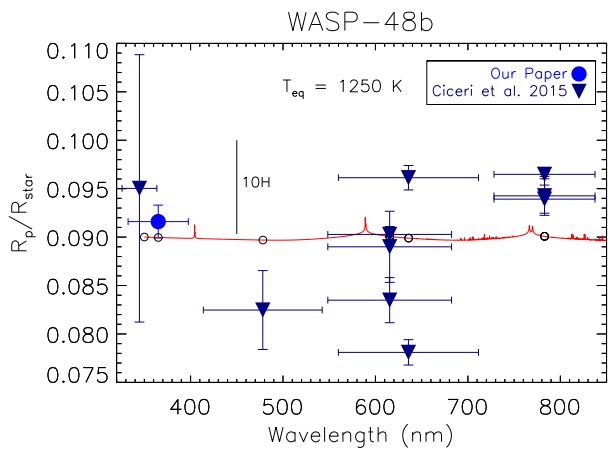

Figure 2.10: Variation of R_p/R_* vs. wavelength for WASP-48b. Other comments are the same as Fig. 2.8.

et al. 2014; McCullough et al. 2014). As described in section 2.6.1, for the planets with measured R'_{HK} indices only one (HAT-P-16b) in our sample is known to orbit an active star (Table 2.1). Additionally, no obvious star spot crossing is seen for any planet in our data (Figs. 2.1-2.7). The WASP-1b and WASP-36b near-UV and optical observations were done at the same time, thus the influence of stellar activity on the smaller near-UV transit depth result should be minimal.

Next, we estimate how much the transit depth changes due to unocculted spots using the formalization presented by Sing et al. (2011). The three main assumptions of this method are that the emission spectrum of the spots are treated as a stellar spectrum but with a lower effective temperature, the surface brightness outside the spots does not change, and no facule are present. These assumptions lead to an overall dimming of the star and increase in the transit depth. Sing et al. (2011) calculate that the change in transit depth due to unocculted spots, $\Delta(R_p/R_*)$, is

$$\Delta\left(\frac{R_p}{R_*}\right) = \frac{1}{2}\frac{\Delta d}{d}\frac{R_p}{R_*}, \tag{2.20}$$

where

$$\frac{\Delta d}{d} = \Delta f(\lambda_0, t)\left(1 - \frac{F_\lambda^{T_{spot}}}{F_\lambda^{T_{star}}}\right)\Big/\left(1 - \frac{F_{\lambda_0}^{T_{spot}}}{F_{\lambda_0}^{T_{star}}}\right), \tag{2.21}$$

$\Delta f(\lambda_0, t)$ is the total dimming at the reference wavelength (λ_0) over some time scale (t), and F_λ^T is the surface brightness of the stellar models at the temperature of the star (T_{star})

and the spot (T_{spot}). An exact value for $\Delta(R_p/R_*)$ is beyond that scope of this paper since the $\Delta f(\lambda_0, t)$ and T_{spot} are unknown for all targets. Sing et al. (2011) find for HD 189733b that $\Delta\left(R_p/R_*\right) = 2.08 \times 10^{-3}/2\left(R_p/R_*\right)$ between 375–400 nm assuming $T_{spot} = 4250$K, $T_{star} = 5000$K, $\Delta f(\lambda_0) = 1\%$, and $\lambda_0 = 400$nm. Therefore, unocculted spots have minimal influence (assuming the stars we are observing have spots similar to HD 189733b) on the observed transit depth variations since the influence of these spots are about 10 times smaller (e.g. $\Delta\left[R_p/R_*\right] = 0.00014$ for WASP-36b) than our final error bars (Tables 2.10-2.11). This result is also consistent with the recent study by Llama & Shkolnik (2015) who find that stellar activity similar to that of the Sun has minimal effect on the transit depth in the wavelengths explored in our study. Nonetheless, follow-up observations and host star monitoring are encouraged to monitor the effect of stellar activity on the transit depth variations we observe.

2.7 Conclusions

We investigate the primary transits of the 15 exoplanets (CoRoT-1b, GJ436b, HAT-P-1b, HAT-P-13b, HAT-P-16, HAT-P-22b, TrES-2b, TrES-4b, WASP-1b, WASP-12b, WASP-33b, WASP-36b, WASP-44b, WASP-48b, WASP-77Ab) using ground-based near-UV and optical filters to study their atmospheres (Section 2.6.2; Figure 2.8–2.10). A constant R_p/R_* from near-UV to optical wavelengths is found for 10 targets (GJ436b, HAT-P-1b, HAT-P-13b, HAT-P-16b, HAT-P-22b, TrES-2b, WASP-33b, WASP-44b, WASP-48b, WASP-77Ab), suggestive of clouds in their atmospheres. Additionally, the near-UV R_p/R_* of 3 targets (CoRoT-1b, TrES-4b, WASP-12b) are larger and 2 targets (WASP-1b, WASP-36b) are smaller by at least 2σ from their optical R_p/R_*. The atmospheric implications of the transit depth variations are explored (Section 2.6.2) and we find that the spectral slope of WASP-12b and CoRoT-1b are consistent with Rayleigh scattering. To our knowledge this is the first time a hot Jupiter has been observed to have a smaller near-UV transit depth than optical and a possible opacity source that can cause such a radius variation is currently unknown. The WASP-1b and WASP-36b near-UV and optical observations were done at the same time, thus limiting the influence of stellar activity on the transit depth variations. Follow-up observations are encouraged to confirm all our results but especially

the observation of a smaller near-UV transit depth.

Additionally, we do not detect any near-UV light curve asymmetries in any of the 15 targets within the precision (1.23 – 6.22 mmag) and timing resolution (27 – 137 s) of our observations (Table 2.2; Section 2.6.1). All the non-detections in this study confirm and expand upon the theoretical modeling done by Ben-Jaffel & Ballester (2014) and Turner et al. 2016a that near-UV asymmetries cannot be seen from the ground. These findings are consistent with the previous ground-based non-detection of asymmetries in HAT-P-16b (Pearson et al. 2014) and WASP-12b (Copperwheat et al. 2013) and 4 (HAT-P-5b, TrES-3b, WASP-17b, XO-2b) other exoplanets (Southworth et al. 2012b; Turner et al. 2013; Bento et al. 2014; Zellem et al. 2015).

Finally, for each target we derive a new set of planetary system parameters and the orbital period and ephemeris are updated to help with follow-up observations (Tables 2.10–2.11). Our data includes the first published ground-based near-UV light curves of 12 of the targets (CoRoT-1b, GJ436b, HAT-P-1b, HAT-P-13b, HAT-P-22b, TrES-2b, TrES-4b, WASP-1b, WASP-33b, WASP-36b, WASP-48b, WASP-77Ab) and greatly expands the number of near-UV light curves in the literature.

Acknowledgments

J. Turner, K. Pearson, R. Zellem, J. Teske, and C. Griffith were partially supported by the NASA's Planetary Atmospheres program. J. Turner was also partially funded by the Virginia Space Grant Consortium Graduate Research Fellowship Program and by the National Science Foundation Graduate Research Fellowship under Grant No. DGE-1315231.

We sincerely thank the University of Arizona Astronomy Club, the Steward Observatory TAC, the Steward Observatory telescope day crew, John Bieging, Elizabeth Green, Don McCarthy, Maria Schuchardt, the Lunar and Planetary Laboratory, and the Associated Students of the University of Arizona for supporting this research.

We also thank John Southworth, Jason Eastman, Ian Crossfield, Josh Carter, and John Johnson for their helpful comments on `JKTEBOP`, `EXOFAST`, `TAP`, and `EXOMOP`. We also thank Joe Llama for the discussion on his bow shock models and Aline Vidotto, Moira Jardine, and Christiane Helling on the useful discussion of their UV bow shock predictions.

Finally, we would like to thank Michael Cushing, Jon Bjorkman, Robert Johnson, Carl Schmidt, Phil Arras, and Andrew Collier Cameron for their insightful comments on this research.

This research has made use of the Exoplanet Orbit Database (Wright et al. 2011), Exoplanet Data Explorer at exoplanets.org, Exoplanet Transit Database, Extrasolar Planet Transit Finder, NASA's Astrophysics Data System Bibliographic Services, and the International Variable Star Index (VSX) database, operated at AAVSO, Cambridge, Massachusetts, USA.

We would also like to thank the anonymous referee for their insightful comments during the publication process. This manuscript is much improved thanks to their comments.

Chapter 3

Investigation of the environment around close-in transiting exoplanets using CLOUDY

"I have not failed. I've just found 10,000 ways that won't work." Thomas A. Edison

The text in this chapter is reproduced primarily from Turner J.D., Christie D., Arras P., Johnson R. 2016a. Investigation of the environment around close-in transiting exoplanets using CLOUDY. MNRAS. 458. 3880.

3.1 Introduction

Exoplanet transits observed at broadband optical wavelengths probe relatively dense gas in the planet's atmosphere (e.g. Charbonneau et al. 2002; Charbonneau et al. 2007a). By contrast, radiative transitions for abundant species and with large cross sections may probe more rarefied regions at much larger radii (e.g. Vidal-Madjar et al. 2003). Absorption well before or after the broadband optical transit implies optically thick absorbing gas at large distances from the planet (e.g. Llama et al. 2011; Lai et al. 2010). Recent observations of asymmetry in transit lightcurves (e.g. Fossati et al. 2010; Haswell et al. 2012; Ben-Jaffel & Ballester 2013), specifically an early ingress, have been interpreted as an enhanced density of absorbers on the leading side of the planet.

There are several space-based observations of transit light curves exhibiting an early UV ingress. An early UV ingress on WASP-12b was observed based on 5 data points from the Cosmic Origins Spectrograph (*COS*) onboard the *Hubble Space Telescope* (HST) in the NUVA (253.9–258.0 nm) near-UV wavelength region (Fossati et al. 2010). Additionally, Haswell et al. (2012) observed an early ingress on WASP-12b in the NUVC (278.9 – 282.9 nm) near-UV wavelength region caused by Mg II and the NUVA region using an additional 5 data points from *COS* on *HST*. Sequential *HST COS* observations of WASP-12b by Nichols et al. (2015) combined the data from the NUVA, NUVB (265.5 – 271.1 nm), and NUVC wavelength regions and also found an early ingress. The data from Haswell et al. (2012) and Nichols et al. (2015), however, are noisy. They observed absorption before the start of the optical transit but never observed a pre-transit baseline. Interpretation of the observations become more difficult if you include all the data points and do not exclude certain data points (see fig 5 in Haswell et al. 2012). Follow-up observations of WASP-12b using the Space Telescope Imaging Spectrograph instrument (wavelength range from 290.0–570.0 nm) on *HST* (Sing et al. 2013) resulted in a non-detection of an early ingress. There was also a reported early ingress on HD 189733b in the C II 133.5 nm line using *COS* on *HST* (Ben-Jaffel & Ballester 2013). However, these authors call for additional observations and caution that the detection could have been caused by unknown systematics.

There are two main models for explaining the origin of an early ingress – magnetic (Vidotto et al. 2010a, 2011a,b; Vidotto et al. 2011c; Llama et al. 2011, 2013) and non-magnetic (Lai et al. 2010; Bisikalo et al. 2013a; Bisikalo et al. 2013b) – which we will now describe. A planet traveling supersonically through the ambient coronal medium will form a bow shock. An early ingress can result if the bow shock is leading the planet and the compressed post-shock material in the magnetosheath becomes sufficiently opaque, absorbing the background starlight. The transit depth will then become a function of the geometry of the post-shock layer and the chemistry therein (Llama et al. 2011, 2013). Ignoring thermal and ram pressure, the approximate location of the magnetopause[1] is found assuming

[1]The approximate location of the magnetopause (r_m) can be found using the following equation $r_m = R_p \left(\frac{B_p}{B_*}\right)^{1/3} \frac{a}{R_*}$, where R_p is the radius of the planet, B_p is the planetary magnetic field strength at the surface of the planet, B_* is the host star's magnetic field strength at the surface of the star, a is the semi-major axis of the planet, and R_* is the radius of the star (Vidotto et al. 2011a). Both the star and the planet magnetic field geometry are approximated as dipolar.

pressure balance between the planetary magnetic field and the stellar wind magnetic field (Vidotto et al. 2011a). This type of bow shock will be referred as a magnetic bow shock in the rest of the chapter. Thus, assuming that the stellar magnetic field is known, that the thermal and ram pressures are negligible, and that the stellar wind gas is opaque enough to cause detectable absorption, constraints on the planet's magnetic field can in principle be made by observing differences between ingress times in different wavelengths. The reason this effect is thought to occur in the UV is not entirely understood and is one area of investigation for this chapter. Vidotto et al. (2011a, hereafter VJH11a) presented a magnetic bow shock model that they applied to all transiting exoplanets and predicted that UV ingress asymmetries should be common in transiting exoplanets and tabulated a list of the 92 targets that should exhibit this effect.

A model ignoring magnetic fields has recently been proposed to explain the WASP-12b *HST* observations (Bisikalo et al. 2013a; Bisikalo et al. 2013b; see also Lai et al. 2010). These authors perform hydrodynamic simulations in 3-D and modeled the interaction between the stellar wind and the escaping planetary atmosphere. In order to find the stand off distance from the planet, the stellar wind ram pressure was balanced by pressure from the planetary gas assuming negligible contribution from the planetary and the stellar wind magnetic field (Bisikalo et al. 2013a). This type of bow shock will be referred to as a non-magnetic shock in the chapter. Gas leaving the L1 point is bent forward in the orbit by the Coriolis force, leading to a distribution of gas leading the planet. As with the VJH11a model, the exact absorbing species in the non-magnetic bow shock that can cause an early ingress is unknown and is also investigated in this chapter.

While both the magnetic bow shock theory and initial observations focused on the UV, a recent study by Cauley et al. (2015) opens up the possibility of applying the VJH11a magnetic bow shock model to other wavelengths. Cauley et al. (2015) observe an asymmetric transit in HD 189733b using *HiRES* on *Keck I* in the hydrogen Balmer lines. These authors apply the magnetic bow shock model to their observations by balancing the planetary magnetic field pressure with the stellar wind pressure assuming negligible contribution from the stellar magnetic field.

Furthermore, there are extensive near-UV observations from the ground looking for asymmetries due to bow shocks. Absorption is thought to be observable in ground-based

observations because the spectral region covered by the ground-based near-UV observations and at least one of the *HST* NUVA, NUVB, or NUVC filters include strong resonance lines (e.g. Ne I, Na I, Mg I, Al I, Mn I, Fe I, Co I, Ni I, Cu I; Morton 1991, 2000; Sansonetti 2005) and a large number of lines from ionised abundant elements (e.g. Ne III, Na II, Cl II, Ca II, Ca III, Sc II, V II, Cr II, Mn II, Fe II, Co II, Ni I, Cu II, Cu III; Morton 1991, 2000; Sansonetti 2005). However, near-UV ground-based broad-band (303–415 nm) photometry observations of 19 exoplanets (including WASP-12b) have all resulted in non-detections (Southworth et al. 2012b; Pearson et al. 2014; Turner et al. 2013; Bento et al. 2014; Copperwheat et al. 2013; Zellem et al. 2015; Turner et al. 2016b) despite the prediction by Copperwheat et al. (2013) that an early ingress could be seen in these filters. The ground-based broad-band photometry non-detections might imply that the coronal material does not absorb sufficiently strongly at the observed wavelengths, the absorption of specific spectral lines being diluted by using broad-band filters, or one of the requirements presented by VJH11a for a stable bow shock detection not being satisfied (Turner et al. 2013; Pearson et al. 2014; Vidotto et al. 2015; Turner et al. 2016b). Our study will shed light onto the correct interpretation of the ground-based observations.

In this study we investigate all known UV opacity sources by performing a detailed radiative transfer, chemical, and ionization analysis of the coronal plasma environment in the bow shocks around close-in exoplanets using the plasma simulation code `CLOUDY` (Ferland et al. 2013). Our simulations will test the basic assumption of VJH11a that the stellar wind is sufficiently opaque to cause the early transit ingress. We do not, however, consider the opacity from a population of energetic atoms which arise due to charge exchange reactions between "cold" atoms from the planet and "hot" stellar wind protons (Holmström et al. 2008; Tremblin & Chiang 2013). Additionally, we model with `CLOUDY` the planetary gas in thermal and ionization equilibrium with the stellar radiation field to determine what species may be observable. The overview of the `CLOUDY` modeling can be found in § 3.2 and the results and discussion for the coronal gas and planetary gas can be found in § 3.3 and § 3.4, respectively.

3.2 Overview of CLOUDY

CLOUDY is a widely-used plasma simulation code designed to simulate the ionization, chemical, and thermal state of an astronomical plasma exposed to an external radiation field and to predict its emission and absorption spectra (Ferland et al. 2013; Ferland et al. 1998). It accounts for the entire electromagnetic spectrum from hard X-rays to the radio and includes the 30 lightest elements in its calculations. By default, the abundances of these elements are assumed to be solar but this can be changed. CLOUDY self-consistently balances all ionization, excitation, and microphysical (e.g. inner shell ionization and charge exchange) rates for all constituents (Badnell et al. 2003; Bryans et al. 2006). For the ionic and molecular emission data, CLOUDY uses the CHIANTI database (version 7: Dere et al. 1997; Landi et al. 2012), the LAMDA database (Schöier et al. 2005), and its own Atomic and Molecular Database (STOUT; Lykins et al. 2015). All known spectral lines are taken into account from these three databases and level energies are from NIST when available (Kramida et al. 2014). A thorough description of STOUT can be found in Lykins et al. (2015). The program has been thoroughly tested and can be used for number densities up to 10^{15} cm^{-3} and temperatures from 3 K to 10^{10} K (Ferland et al. 2013). All CLOUDY modeling performed in this study is done in 1-D.

The two main choices for the equilibrium condition enforced by CLOUDY are thermal and coronal equilibrium. In coronal equilibrium, the temperature is fixed and the collisional ionization rate is set by the gas temperature and ionization potentials of all the constituents. Photoionization also occurs in coronal equilibrium if an external radiation field is specified. Heating and cooling are not necessarily in equilibrium for the coronal case. The level populations are then determined by balancing all the relevant processes. In thermal equilibrium, the temperature of the slab of gas (cloud) is determined by the balance of cooling and heating of the gas.

3.3 Modeling of the coronal gas with CLOUDY

For the CLOUDY modeling, we simulate the output spectrum and transit depth in the conditions of the shocked stellar coronal gas in the magnetosheath. The spectrum used is the net

transmitted spectrum by summing the attenuated incident and diffuse continua and lines[2].

A brief description of the geometry of the bow shock (Figure 3.1) and the simplified geometry used for the CLOUDY modeling (Figure 3.2) can be found below. A bow shock will form if the relative velocity between the planetary and the stellar coronal material is supersonic and will lead the exoplanet if the star's rotational period is greater than planet's orbital period (as is the case for most close-in exoplanets; VJ11a). The upstream region is composed of three regions of interest: the bow shock, the magnetosheath, and the magnetopause. In this chapter we adopt magnetospheric terminology for the shock geometry; however, this geometry applies generally to any planet with a bow shock not just magnetic ones. The magnetosheath is the area of compressed coronal material and has a width of Δr_m. The magnetopause is the boundary between the magnetosphere and surrounding plasma from the stellar wind. Inside the magnetopause, the plasma is assumed to be composed predominantly of material from the planet (See §3.4.2). The stand-off distance, r_M, is determined by balancing the planetary magnetic field pressure with the ram pressure of the stellar wind. For the CLOUDY modeling, we model the magnetosheath as a cloud with a width of $2\Delta r_m$ and a covering factor equal to $\Omega/4\pi$ (Figure 3.2). This approximation to the cloud width is chosen as a simplification of the 3-D structure of the bow shock since photons along the line of sight go through the magnetosheath twice. The covering factor is the fraction of 4π sr covered by the cloud, as viewed from the star (the central source of radiation) and represents the fraction of the radiation field emitted by the star that strikes nebular gas. The line luminosities and intensities are the main characteristics that depend on the covering factor. The solid angle of the cloud as viewed from the central star is

$$\Omega = \pi \frac{(r_m + \Delta r_m)^2}{2a^2}, \tag{3.1}$$

where r_m is the magnetospheric radius. Using Equation (3.1), we find a covering factor of 0.0011 for $r_m = 4.4$ R_p, assuming a planetary magnetic field (B_p) of 4 G, and 0.0034 for $r_m = 8.0$ R_p, assuming a B_p of 30 G (Lai et al. 2010). Since the strength of the planetary magnetic fields are not known, we use a covering factor of 0.0034 in order to be conservative in testing whether the total absorption is substantial enough to explain the observations.

[2]This spectrum is from column 5 in the continuum command in CLOUDY

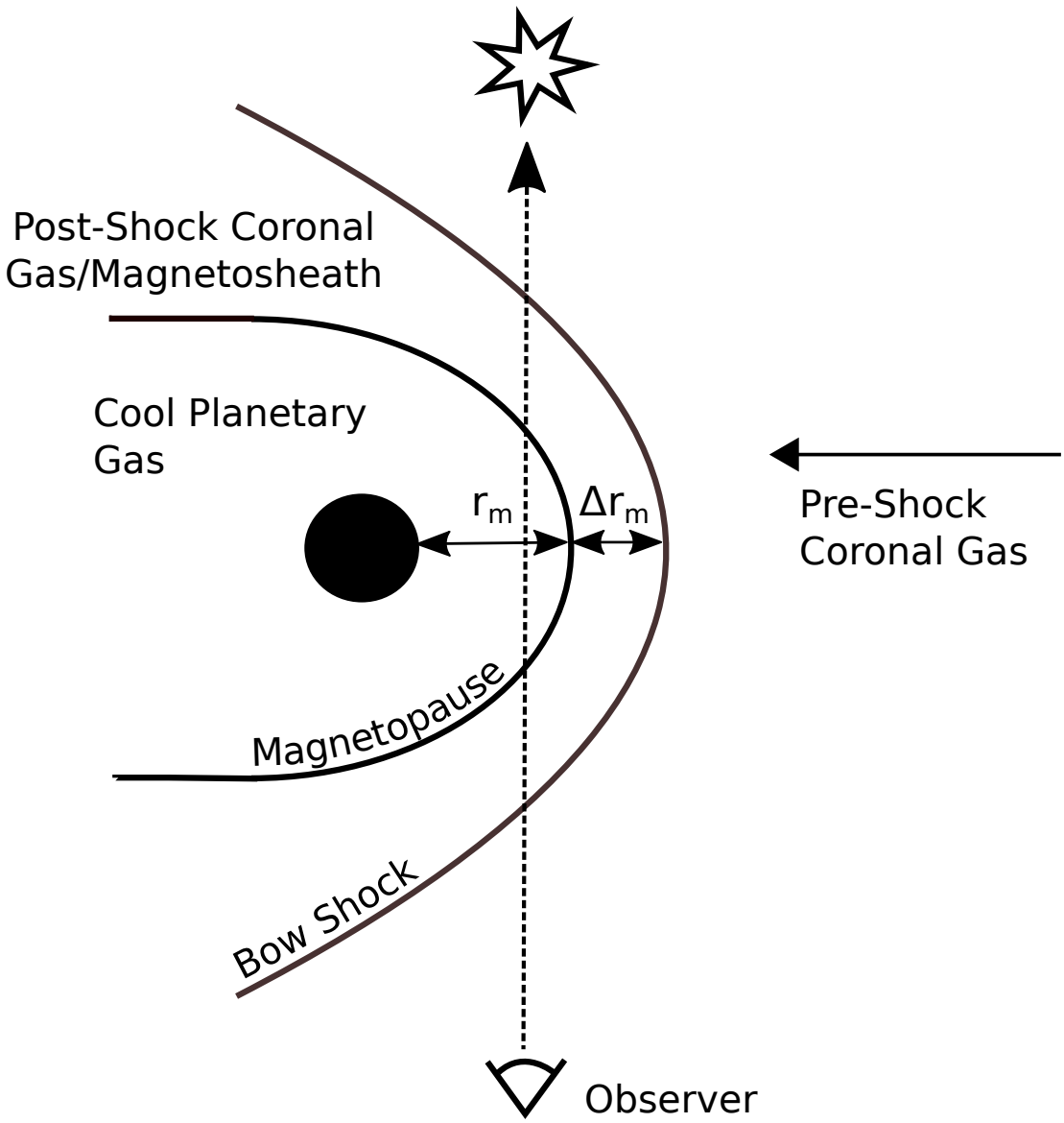

Figure 3.1: Schematic of the magnetic bow shock geometry (not to scale). The stand-off distance, r_M, is determined by balancing the planetary magnetic field pressure with the ram pressure from the stellar wind. Δr_M is the region of compressed stellar coronal material. This geometry also applies to non-magnetic bow shocks.

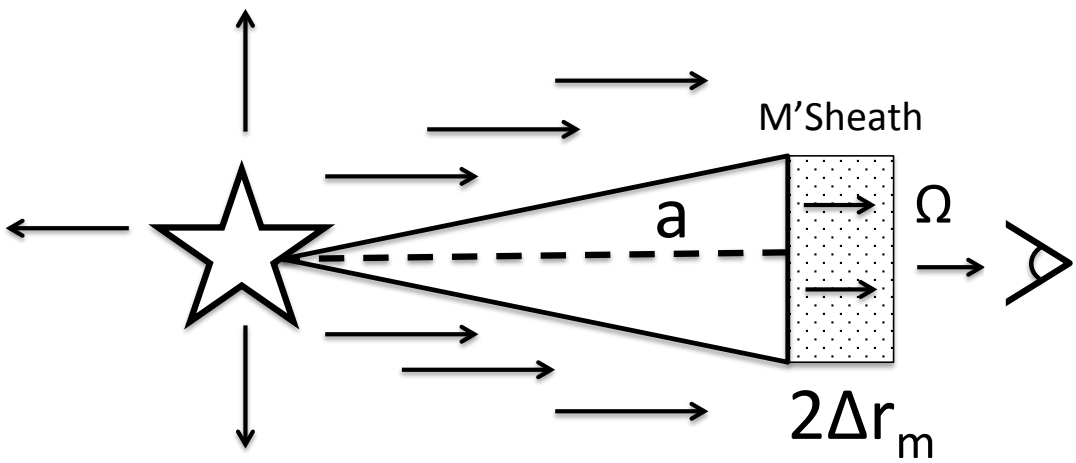

Figure 3.2: Schematic of the CLOUDY input model (not drawn to scale). The magnetosheath is modeled as a cloud with a width of $2\Delta r_m$ and a covering factor equal to $\Omega/4\pi$. See § 3.3 for more details. The incident radiation strikes the cloud at a normal illumination.

We ran CLOUDY[3] in an open geometry and in coronal equilibrium assuming a constant temperature of 1×10^6 K (see description below about why this is a good assumption), a nominal magnetosheath width (Δr_m) of 0.24 R_{Jup} (Llama et al. 2011), an orbital distance (a) of 0.023 AU (the orbital distance of WASP-12b; Hebb et al. 2009), and a solar metallicity ($[Fe/H]$) for the cloud (Table 3.1). The external radiation field was a solar spectrum taken from stitching together data from the TIMED-SEE (Woods et al. 2000) and SORCE (Anderson & Cahalan 2005) satellites (Figure 3.3). We then varied the hydrogen density (n_H) in the cloud between $10^4 - 10^8$ cm^{-3} and calculated the output spectrum. In order to correctly interpret the CLOUDY results it is important to note that n_H is the density of hydrogen nuclei, irrespective of their form (protons, bound atoms, molecules). All the elements are scaled relative to n_H based on their solar abundances.

We explain below our choice of the parameter range explored for the hydrogen densities. The expected stellar wind density at the planet may be estimated as $n_{\rm H} = 10^4$ cm^{-3} $(0.03\ {\rm AU}/a)^2$ by scaling the density of the solar wind as measured near Earth as $1/a^2$ with separation a from the star (this profile is an approximation to the actual stellar wind profile measured for the Sun; McKenzie et al. 1997). Hence the lower limit of the density

[3]Calculations were performed with version 13.00 of CLOUDY (Ferland et al. 2013)

Table 3.1: CLOUDY model parameters

Parameter	Magnetosheath
Hydrogen Density (cm^{-3})	$10^4 - 10^8$
Stellar Luminosity ($L_\odot$)	1
Orbital Distance (AU)	0.023
Magnetosheath Width (cm)	0.24 R_{Jup}
Shock Temperature (K)	1×10^6
Metallicity	Solar
Covering Factor ($\Omega/4\pi$)	0.0034

range explored is thought to be the actual value around a solar-type star. The upper limit $n_{\rm H} \simeq 10^8$ cm^{-3} is an estimate of the density at the base of the solar corona (Withbroe 1988), the highest density expected for coronal gas. Since the base of the corona is at $a \sim 1.001 R_\star$, and the planets considered here orbit at $a \sim 3 - 9\ R_\star$, the planets are expected to be orbiting in an environment with density much smaller than the coronal base density. These densities are consistent with those estimated by Vidotto et al. (2010a) and VJH11a for an hydrostatic isothermal corona (see table 1 in VJH11a). The actual stellar wind density at WASP-12b and HD189733b are not known but should be within the limits explored in this study. Assuming the Rankine-Hugoniot conditions for a $\gamma = 5/3$ gas, we only expect a maximum increase of 4 in the plasma density across the bow shock between the stellar wind and magnetosheath.

The temperature of the shock is one of the most important parameters in our modeling, therefore, we discuss our choice of shock temperature and the assumptions we use in greater detail below. A shock temperature is adopted that is comparable to that of the solar coronal gas ($T = 10^6$K; Aschwanden 2005) and subsequently we vary the specific choice of temperature in a parameter study (Section 3.3.1). Previous works have posited that the post-shock gas, while initially hotter due to compression (increased by the square of the Mach number), undergoes radiative cooling to reach temperatures in the range of 10^4 to 10^5 K (Lai et al. 2010; Vidotto et al. 2010a). No attempts are made, however, to estimate whether this degree of cooling is realistic. To determine whether our adopted shock temperature is a reasonable assumption we compare the cooling rate of the gas to the dynamical time. Sutherland & Dopita (1993) find that for gas with temperatures on the order

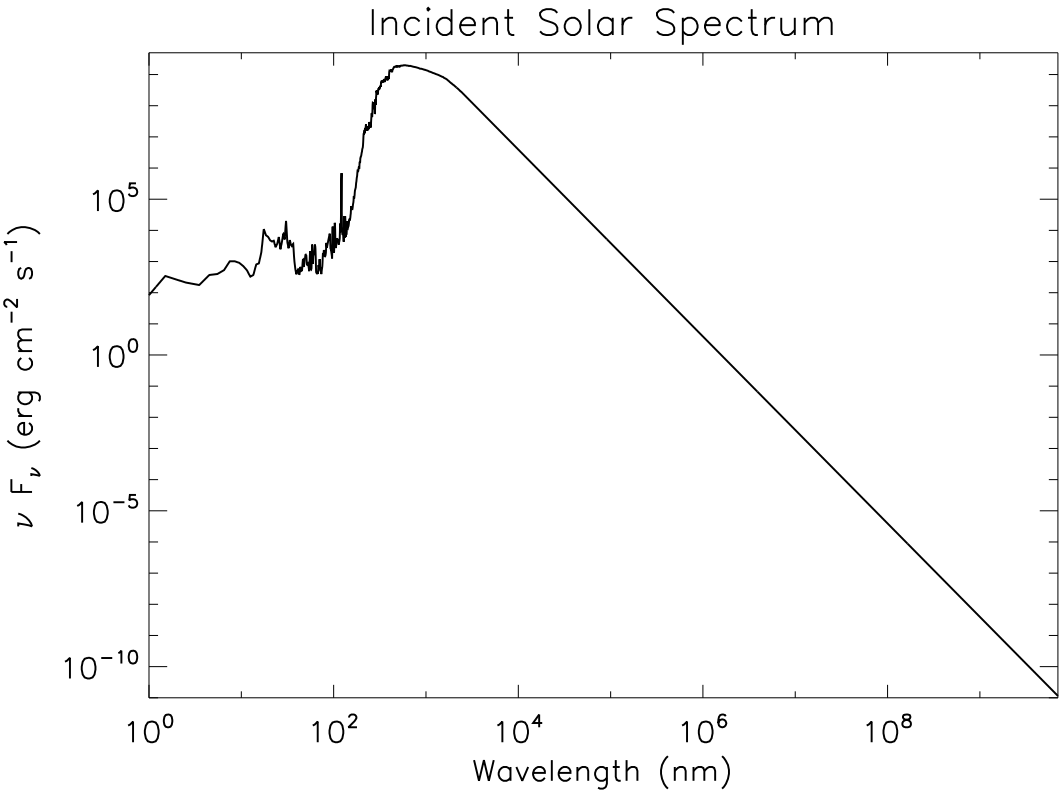

Figure 3.3: Solar spectrum input into CLOUDY as the external radiation field incident on the cloud. The spectrum was taken from stitching together data from the TIMED-SEE (Woods et al. 2000) and SORCE (Anderson & Cahalan 2005) satellites.

of $10^6 - 10^7$ K, the cooling rate is approximately $10^{-22} n_e n \,\mathrm{erg\,cm^3\,s^{-1}}$ where n is the total density of nuclei and n_e is the number density of electrons. The characteristic cooling time $t_{\rm cool}$ for gas with energy density E and a cooling rate $\dot{E}$ is then

$$t_{\rm cool} \sim \frac{E}{\dot{E}} \sim \frac{nkT}{(10^{-22}\,\mathrm{erg\,cm^3\,s^{-1}})\, n_{\rm e} n} \tag{3.2}$$

$$\sim 10^8 \left(\frac{T}{10^6\,\mathrm{K}}\right)\left(\frac{10^4\,\mathrm{cm^{-3}}}{n_{\rm e}}\right)\ \mathrm{s}\ . \tag{3.3}$$

Adopting a thickness of the post-shock gas of 10^{10} cm, comparable to $R_{\rm p}$, and a characteristic velocity of $100\,\mathrm{km\,s^{-1}}$ we find a dynamical time $t_{\rm dyn}$ of

$$t_{\rm dyn} \sim \frac{10^{10}\,\mathrm{cm}}{100\,\mathrm{km\,s^{-1}}} = 10^3\ \mathrm{s}\ . \tag{3.4}$$

The cooling time is thus much longer than the dynamical time, and the post-shock gas leading the planet should not be expected to cool significantly. Therefore, post-shock temperatures comparable to the coronal temperatures are reasonable within the context of the model being examined.

3.3.1 Results

The net transmitted spectrum of the shocked material is shown in Figure 3.4 for all wavelengths and the UV wavelengths probed by *HST* and the ground-based observations. Next, we calculate the transit depth, δ_F, due to the magnetosheath being in front of the star during the transit assuming the magnetosheath is half of a spherical shell (see Figure 3.1),

$$\delta_F = \frac{F_{bow}(\lambda) - F_{Star}(\lambda)}{F_{Star}(\lambda)} \min\left(\frac{1}{2}\frac{(r_m + \Delta r_m)^2}{R_\odot^2}, 1\right) \tag{3.5}$$

where F_{bow} is the flux from the bow shock calculated from the output of `CLOUDY`, F_{star} is the flux from the star (the input solar spectrum), r_m is the magnetospheric radius (set as $8R_{Jup}$ to be conservative to produce the largest δ_F; Lai et al. 2010), and Δr_m is the width of the magnetosheath. The left term in Equation 3.5 is essentially the opacity of the cloud. The geometric factor (equal to $\frac{1}{2}\frac{(r_m+\Delta r_m)^2}{R_\odot^2} = 0.336 = 33.6\%$ for the nominal model) is applied

(a)

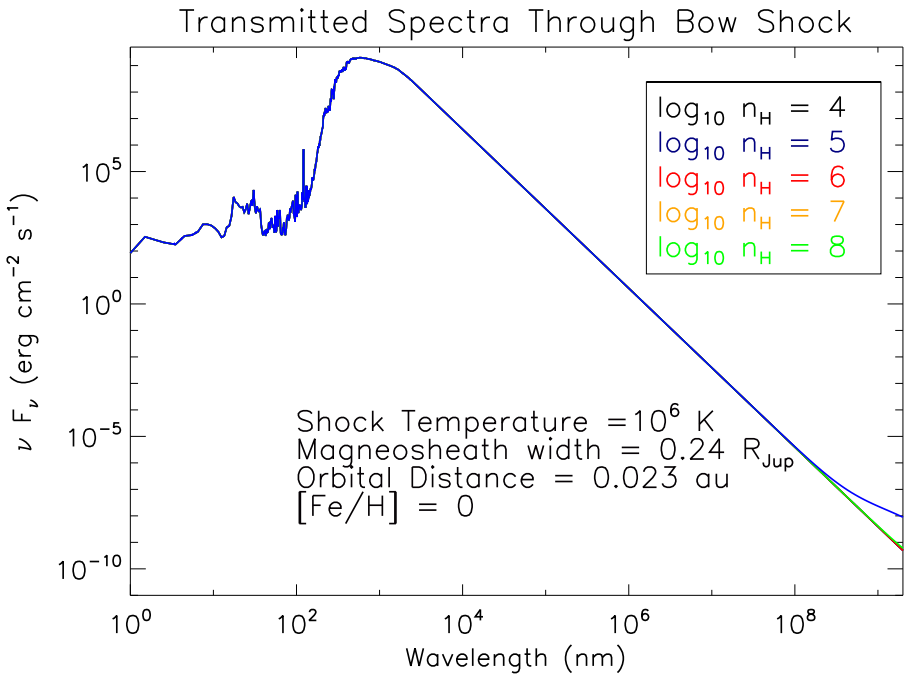

(b)

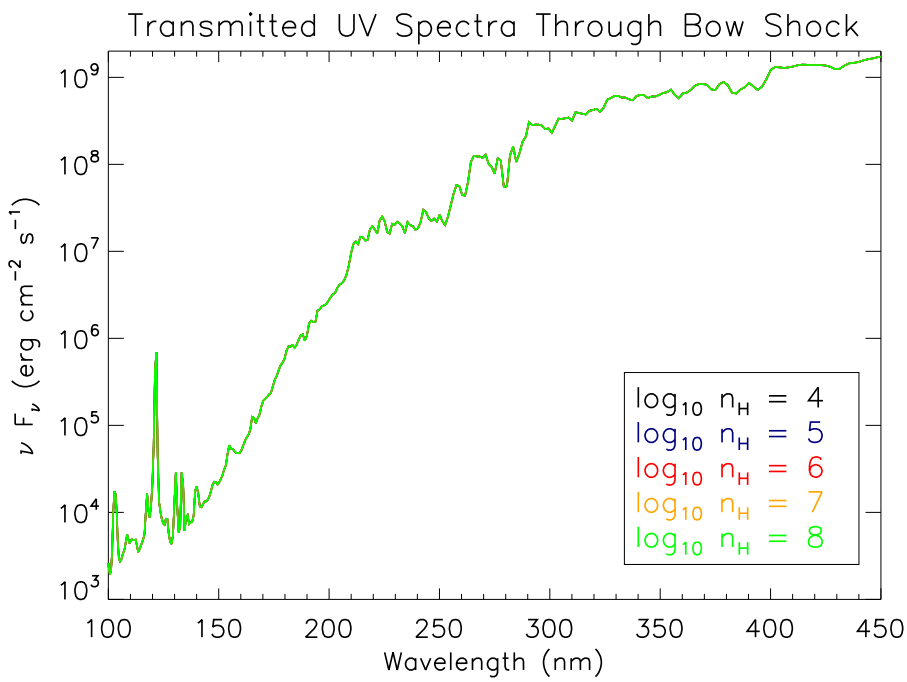

Figure 3.4: Output CLOUDY spectra of the magnetosheath with varying hydrogen densities (n_H) in the stellar corona for all (**a**) and UV (**b**) wavelengths. The output spectra are all identical to each other for the entire UV wavelength range.

since the output spectrum from CLOUDY does not account for the size of the magnetosheath or the star[4]. In models of the bow shock incorporating more geometric sophistication (e.g., Llama et al. 2011), the absorption due to the bow shock occurs primarily in a thin sliver at the leading edge of the shock (see fig. 2 in Llama et al. 2011). Our assumption, that the occulting area is that of the entire half circle, is an overestimation; however, this is preferable as the resulting transit depths can be viewed as upper limits with geometric constraints producing smaller values of δ_F. In order to be compared to observations δ_F would need to be convolved with the filter bandpass or spectral resolution.

The results of determining the transit depth due to the bow shock are in Figure 3.5 for UV wavelengths. For the expected value $n_{\rm H} \simeq 10^4$ cm^{-3} of the coronal density, and indeed even for $n_{\rm H}$ larger than the expected value by a factor of 10^3, the transit depths are orders of magnitude too small to be observable. At the unphysically large density $n_{\rm H} = 10^8$ cm^{-3} expected at the base of the corona (10^{-3} $R_\star$) above the photosphere, a hydrogen Lyman-alpha absorption feature and a C VI *emission* feature are apparent. Both are still a factor $\sim 10^3$ too small to be measurable by *HST*. Note that the emission feature from highly ionized C VI is in emission as the slab is brighter than the background star at such unphysically large columns for C VI in the slab.

In order to further interpret our results, we can estimate the optical depth of spectral lines. The optical depth of a spectral line would be

$$\tau = \int_0^x \sigma n(x)\, dx \tag{3.6}$$

where σ is the cross section, n is the number density of that species, and x is the width of the cloud. The cross section at line-center is equal to

$$\sigma = \frac{\sqrt{\pi} e^2}{m_e c} \frac{f \lambda_0}{v_t} \tag{3.7}$$

where e is the electric charge of an electron, m_e is the mass of an electron, c is the speed of light, λ_0 is the wavelength at line center, $v_t = \sqrt{2kT/m_H}$ is the thermal velocity, and f is

[4]The min function is used in Equation 3.5 because the bow shock in principle (depending on the value of r_m) can be larger than the star and the maximum δ_F is -100% (the whole star is blocked out when the bow shock is completely optically thick).

the oscillator strength. For illustration, the optical depth of Lyman-alpha at line-center is

$$\tau_{Ly\alpha} = \frac{\sqrt{\pi}e^2}{m_e c}\frac{f\lambda_0}{v_t}n_{1s}x \tag{3.8}$$

$$\tau_{Ly\alpha} = 1.0\left(\frac{n_H}{1.98\times10^{11}\ \mathrm{cm}^{-3}}\right), \tag{3.9}$$

where n_H is the density of hydrogen nuclei (protons or atoms or molecules) and in our model the density of hydrogen in the 1s state is $n_{1s} = 10^{-6.589}n_H$ cm^{-3} (Table 3.2). To determine the pre-factor in Equation 3.9, the values of the variables we use in Equation (3.8) are λ_0 = 121.56701 nm, T = 10^6 K, f = 0.4164 (Kramida et al. 2014), and x = $2\Delta r_m$ (Table 3.1). Therefore, for a $n_H = 10^8$ cm^{-3} we find τ = 0.0005 which is consistent with the value found from `CLOUDY` of 0.0001 and the transit depth in Figure 3.5. Lyman-alpha is very optically thin, which is why we see little absorption and no absorption for n_H below 10^8 cm^{-3}.

The cloud optical depth is used from the `CLOUDY` modeling to determine if absorption occurs. The optical depth of the cloud is calculated to be between $\sim 2.664\times10^{-11}$ and 2.663×10^{-8} for all UV and optical wavelengths for densities between $10^4 - 10^7$cm^{-3}, respectively. For a density of 10^8cm^{-3} the optical depths are calculated to be 2.663×10^{-7} across the UV and optical except for the Lyman-alpha and C VI line. All of these optical depths are too small to cause any detectable absorption (Figures 3.4 and 3.5).

Additionally, we perform a thorough parameter search with `CLOUDY` to determine what conditions can cause absorption in the UV and to check the robustness and biases of the nominal parameters (Table 3.1). The following cloud parameters are explored:

1. Temperature from 2,000 to 2×10^6 K
2. $[Fe/H]$ from 0 (solar) to +1
3. Δr_m from 0.24 R_{Jup} to 3 R_{Jup}
4. n_{H} values from 10^4 cm^{-3} to 10^{12} cm^{-3}
5. Stellar luminosity from 1 to 5 $L_\odot$

The results are presented in Figure 3.6. The top panel shows the result of scaling the coronal density up to levels a factor $\sim 10^8$ above that expected at the orbital radius of the planet, and a factor of 10^4 higher than that expected at the base of the corona. Even at such high densities, transit depths over the range $300 - 450$nm are still at the $< 0.1\%$ level. The middle panel of Figure 3.6 shows the result of using an unphysically low value for the shock temperature (10^4 K) of the coronal gas. In this case, absorption lines for H I, Si II, and C II exhibit transit depths between $\sim 0.2 - 0.7\%$ at very high densities $10^7 - 10^8$ cm^{-3}. Lastly, the bottom panel of Figure 3.6 again shows transit depths for a shock temperature 10^4 K, now in the NUV (NUVA, NUVB, NUVC) bands. Again at unphysically high densities there is now absorption by He II, Mn II, Mg I, and Mg II. The results of the bottom panel are at odds with the detection of Mg I but no Mg II absorption in HD 209458b, a typical hot Jupiter (Vidal-Madjar et al. 2013). For Mg II and Mg I the mean ionization fraction averaged over the width of the cloud with a T=10^4 K is $10^{-13.092}$ and $10^{-9.181}$, respectively. Therefore, this result suggests that the temperature of the planetary gas producing the Mg I absorption in HD 209458b is at a lower temperature, consistent with the temperature upper limits found by Vidal-Madjar et al. (2013).

3.3.2 Discussion

We find that using realistic parameters (Table 3.1) for the shocked coronal plasma in the `CLOUDY` modeling clearly indicates there is no species present that can absorb in the UV with any detectable optical depth (Figures 3.4 and 3.5). This is also true for all other wavelengths examined (including optical). The mean ionization fractions of H, He, C, Ne, Na, Mg, Al, Cl, Ca Sc, Cr, Mn, Fe, Co, Ni, Nu, and Cu found using `CLOUDY` indicate that there aren't any spectral lines observable in the UV (e.g. Na I, Al I, Sc II, Mn II, Fe I, Co I, Mg I, Mg II) because the atoms are highly ionized (Table 3.2). The results from our `CLOUDY` models appear to be at odds with the previous investigations of an early UV ingress (Vidotto et al. 2010a, 2011a,b,c; Llama et al. 2011, 2013). The models in these chapters suppose the source of opacity is Mg II; however, at temperatures characteristic of the corona, magnesium is highly ionized with very little Mg II remaining (see Table 3.2, also Ben-Jaffel & Ballester 2014). While much of the literature focuses on Mg II,

Table 3.2: Mean ionization fractions for the coronal gas for the ionization states of interest for H, He, C, Ne, Na, Mg, Al, Cl, Ca Sc, Cr, Mn, Fe, Co, Ni, Nu, and Cu calculated from the CLOUDY modeling

State	Fraction (10^X)	State	Fraction (10^X)
H I	-6.589	H II	-1.119×10^{-7}
He II	-4.535	He III	-1.267×10^{-5}
C I	-16.531	C II	-11.258
C VI	-0.243	Ne I	19.103
Ne II	-14.348	Ne III	-10.478
Ne IX	-0.036	Na I	-20.064
Na II	13.898	Na X	-0.175
Mg I	-19.528	Mg II	-14.041
Mg IX	-0.483	Al I	-19.849
Al II	-14.529	Al VIII	-0.399
Cl I	-23.207	Cl II	-17.431
Cl III	-12.58	Cl VIII	-0.346
Ca I	-24.387	Ca II	-17.916
Ca III	-13.829	Ca XI	-0.064
Sc II	-19.240	Sc XII	-0.149
Cr I	-27.072	Cr II	-20.507
Cr X	-0.336	Mn I	-27.606
Mn II	-21.056	Mn X	-0.328
Fe I	-25.168	Fe II	19.027
Fe III	-14.267	Fe IX	-0.395
Co I	-28.678	Co II	-22.135
Co X	-0.659	Ni I	-27.872
Ni II	-21.656	Ni XI	-0.374
Cu I	-27.100	Cu II	-21.052
Cu III	-15.717	Cu X	-21.052

Note. — The values in this table were taken for the nominal model presented in Table 3.1 with a hydrogen density of 10^8 cm^{-3}. Every CLOUDY model produced very similar trends. The ionization fractions presented are averaged over the width of the cloud.

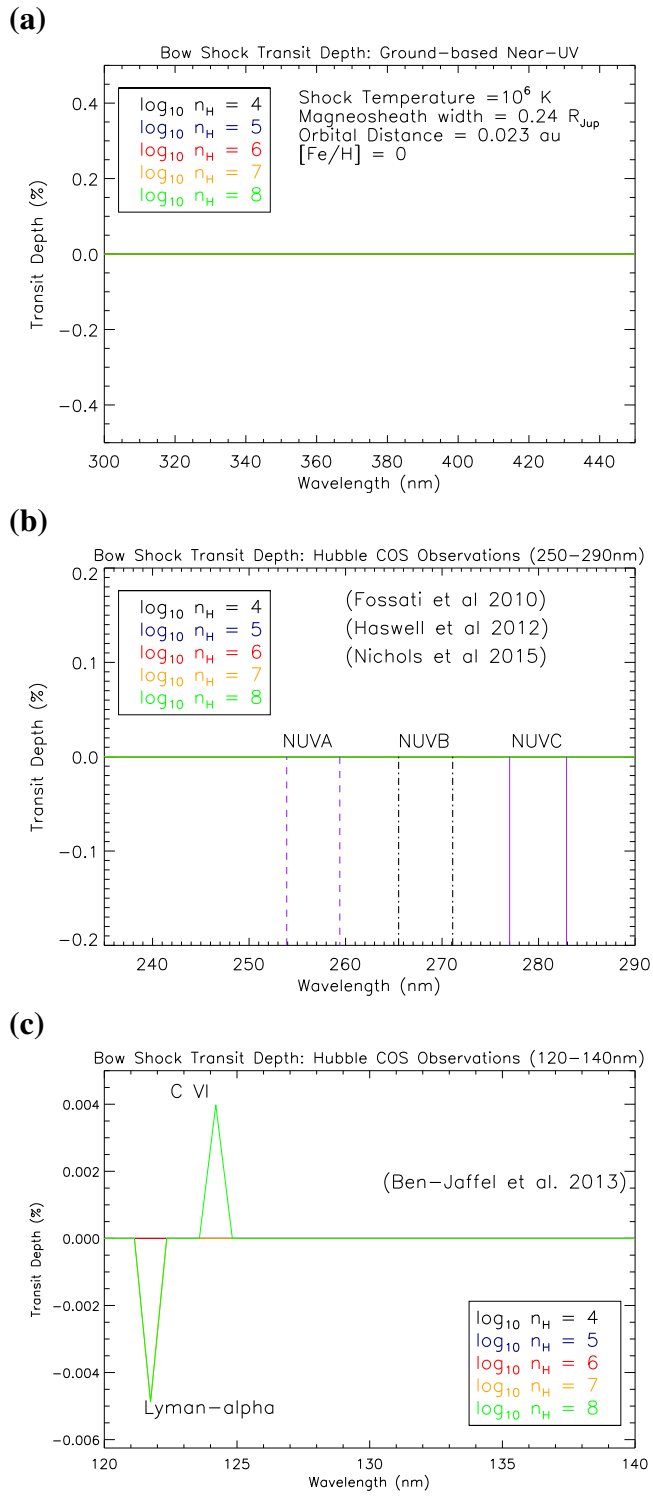

Figure 3.5: Transit depths due to the magnetosheath for the nominal model (Table 3.1) at varying hydrogen densities (n_H) for ground-based (**a**) and *Hubble Space Telescope* (panels **b** and **c**) UV wavelengths. We do not detect any UV absorbing species under realistic conditions for the shocked coronal plasma that could cause an early UV ingress.

this applies more broadly: coronal gas, either pre- or post-shock, will consist primarily of highly-ionized species with no expectation of opacity from neutral or singly-ionized species. For example, one should not expect Lyman or Balmer absorption from neutral hydrogen within the post-shock coronal gas or lines from lower energy levels such as Mg I and Fe I (Haswell et al. 2012; Bourrier et al. 2013).

Interactions between the post-shock stellar wind gas and the planetary gas can result in a hot population of neutral hydrogen through charge-exchange reactions which is potentially observable (e.g., Tremblin & Chiang 2013); however, this is not an observation of the shocked stellar wind gas, as the hot population is generated downstream at the interaction layer (contact discontinuity) between the post-shocked gas and the planetary gas (e.g. Kislyakova et al. 2014). For a more detailed discussion, see §3.4.2.

From the parameter search, we determine the robustness of our results and under what conditions UV absorption can actually occur. We find for reasonable shock temperatures between $8 \times 10^5 - 2 \times 10^6$ K (consistent with the coronal temperatures measured for F-, G-, K-, and M-stars: Aschwanden 2005; Vaiana et al. 1981) that the absence of an UV absorbing species did not change. Additionally, changing the $[Fe/H]$, Δr_m, and the stellar luminosity for the nominal model (Table 3.1) did not help with detectability. Therefore, our result of not finding any UV absorbing species is robust. In order for the C II 133.5 nm line to appear (as in the Ben-Jaffel & Ballester 2013 HD 189733b observations) we need a plasma temperature between 2,000-100,000 K (Figure 3.6) suggesting that this absorption is not coming from the stellar corona but likely from a gas with a much lower temperature such as an escaping planetary atmosphere. We find that no lines or continuum absorption sources appear in the NUV (NUVA, NUVB, NUVC filters) space-based wavelengths unless the cloud temperatures are below 10,000 K (Figure 3.6). This suggests that whatever caused the early ingress in WASP-12b (Fossati et al. 2010; Haswell et al. 2012; Nichols et al. 2015) was not from shocked stellar wind gas but is more likely planetary gas as has been previously suggested (Lanza 2009; Lai et al. 2010; Bisikalo et al. 2013a; Bisikalo et al. 2013b; Cherenkov et al. 2014; Lanza 2015). An escaping atmosphere of WASP-12b would also explain the variability in the complete set of near-UV observations (Fossati et al. 2010; Haswell et al. 2012; Sing et al. 2013; Nichols et al. 2015). For the case of a hot ($T \sim 10^6$ K) gas, we find that significant opacity (mainly metal lines) only appears for the ground-based

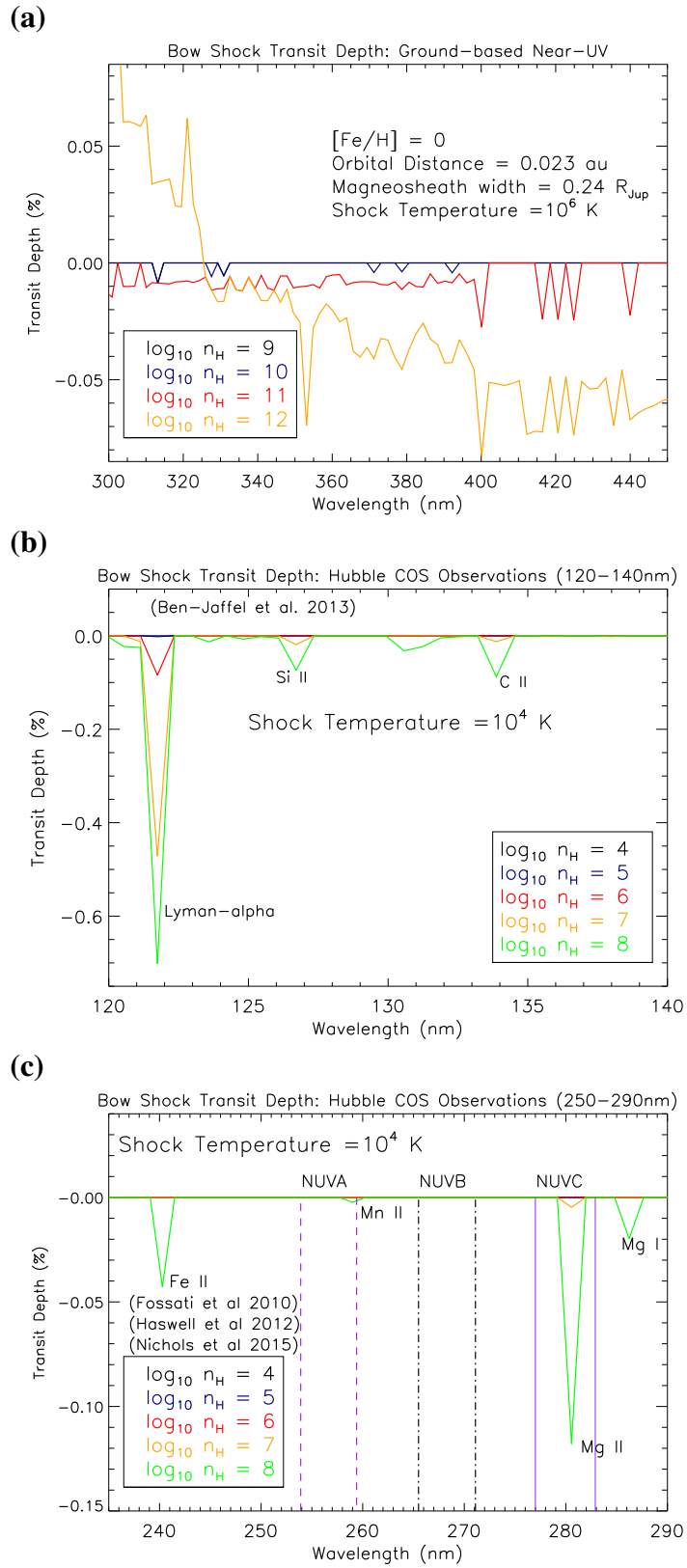

Figure 3.6: Transit depths due to the magnetosheath for **(a)** ground-based near-UV wavelengths for above $n_H = 10^{10}$ cm^{-3}, panels **(b)** and **(c)** HST UV wavelengths with the nominal model except the cloud temperature is 10,000 K.

near-UV wavelengths under *unrealistic* conditions of a n_H above 10^{10} cm^{-3} for the nominal model (Figure 3.6). Also, our modeling shows that for a density of 10^{12} cm^{-3} the cloud actually becomes brighter than the star at wavelengths lower than 320 nm.

Due to our results, any interpretation of UV absorption which relies on shocked coronal gas as the source of opacity (Vidotto et al. 2010a; Turner et al. 2013; Pearson et al. 2014; Turner et al. 2016b) may need to be re-evaluated. This result also applies more broadly to all wavelengths, including interpreting optical asymmetry observations with magnetic bow shocks models. We believe this result is robust due to the fact that we covered the likely parameter space and found no effect. Our conclusions add to a body of theoretical work suggesting that UV asymmetry observations are not suitable approach for exoplanet magnetic field detection (Ben-Jaffel & Ballester 2014; Grießmeier 2015; Alexander et al. 2015). Additionally, our modeling of lower temperature clouds suggests that the UV and optical observations are likely caused by gas from the planetary atmosphere (Lai et al. 2010; Bisikalo et al. 2013a; Bisikalo et al. 2013b; Cherenkov et al. 2014). Therefore, any future models attempting to explain the early UV observation need to include planetary gas in their simulations. The modeling described here does not provide any additional constraints on whether a bow shock exists around close-in exoplanets (see Saur et al. 2013 and VJH11a for conflicting arguments) but does show that the bow shock does not produce any observable signature in the UV and optical.

We, however, acknowledge that improvements to our modeling could be considered, such as using a more realistic density structure in the magnetosheath and stellar wind profile, including (magneto-) hydrodynamics (e.g. `TPCI`; Salz et al. 2015), and 3-D simulations (using `pyCloudy`; Morisset 2013). Given the broad range of parameters tested here, we do not expect such improvements to change our conclusions.

3.4 Modeling of planetary gas with `CLOUDY`

Next, we simulate planetary gas in thermal and ionization equilibrium with the radiation field. The `CLOUDY` model transmission spectra presented in this chapter for the planetary gas allow for a comprehensive study of 30 atomic elements and many molecules in ionization and thermal equilibrium with the stellar and diffuse radiation field. Since `CLOUDY` balances

all the radiative and collisional rates self-consistently, the present study is able to make predictions for a number of transitions which have not yet been observed for any exoplanet.

We ran CLOUDY with the same exact geometry setup as in § 3.3 (Figures 3.2), a width of 1 R_{Jup}, a covering factor of 0.0041, geometric factor in Equation 3.5 of 0.401 (40.1%), an orbital distance of 0.023 AU, and solar metallicity for the cloud. The external radiation field was the same as used in § 3.3 (Figure 3.3). The hydrogen density (n_H) in the cloud is set to 10^7 and 10^9 cm^{-3}. The former choice is representative of the planetary gas found a few planetary radii from the planet (e.g. Koskinen et al. 2014). The latter choice is where the gas becomes opaque to Lyman continuum photons (Murray-Clay et al. 2009) and could be caused by escaping gas in a thick column (e.g. Roche lobe overflow; Lai et al. 2010). The gas kinetic temperature for this model is set by balancing the heating and cooling in the gas and the temperatures calculated by CLOUDY for the 10^7 and 10^9 cm^{-3} clouds are approximately 8725 and 12859 K, respectively.

A brief discussion on the limitations of our modeling for the escaping planetary gas is as follows. We assume solar metallicity for both models; however, this is a source of uncertainty. Atomic species which reach the atomic layer will be carried along with the EUV-driven wind; however, the degree to which these atmospheres remain well mixed up to 1 μbar pressures where the gas transitions from molecular to atomic is unknown (Koskinen et al. 2014). Since the mixing of the atmosphere is beyond the scope of this chapter and the goal is only to find potential sources of opacity, we view the assumption of solar metallicity to be sufficient. The use of the static slab geometry will introduce uncertainties in the amount of absorption as it fails to capture the density and velocity structures. The denser parts of the atmosphere are likely not well characterized. This exercise does, however, still offer potential opacity sources to look for during future transit observations.

3.4.1 Results and Discussion

The output transit depths of the planetary gas are shown in Figure 3.7 for X-ray, UV (space and ground), and optical and in Figure 3.8 for radio wavelengths. The mean ionization fractions of H, He, C, N, Ni, O, Na, Mg, Al, Si, S, P, Ca, Ti, Mn, Fe, and Co found using CLOUDY are given in Table 3.3. The most interesting results found for the planetary gas

(Figure 3.7) are discussed below. The X-ray results (top-left) for a density $n_{\rm H} = 10^9$ cm^{-3} are consistent with the 8% transit depth observed on HD 189733b at X-ray wavelengths using Chandra (Poppenhaeger et al. 2013). The main source of opacity for the X-rays is bound-free absorption from hydrogen and helium and the spectral lines are blended metal lines. The space-based UV wavelengths from 113-290 nm are shown (top-right, middle-left, middle-right). The most interesting lines that are potentially observable (this limit is anything with a transit depth greater than 0.10%) in this wavelength regime (113-290 nm) are H I, C I, C II, N I, Ni II, Mg I, Mg II, Al II, Si II, S I, Mn II, Fe II, and Co II. We find that the Lyman-alpha line now has an optical depth of 124 (very optically thick), as compared to the optically thin (0.0001) case for the coronal equilibrium. In the ground-based near-UV (bottom-left) the most promising observable lines are Ca II, He I, and Ti II (all not yet observed). In the optical regime (bottom-right), H-alpha, He I, and Ca II are the most promising lines. The detection of H-alpha in our modeling is consistent with the observations of H-alpha in the atmospheres of HD 189733b (Jensen et al. 2012) and HD 209458b (Astudillo-Defru & Rojo 2013). For the ALMA wavelength range (Figure 3.7), binning bands 3-5 together results in a predicted transit depth of 0.27 %. While this transit depth is possibly observable (see also Selhorst et al. 2013), the problem with these bands is the fact that the hosts stars are very faint. The main source of opacity for frequencies lower than 200 GHz is free-free absorption and between 200-400 GHz overlapping molecular lines are the dominate source.

There are approximately 20 species (H I, C II, O I, Na I, Mg I, Mg II, Al I, Al III, Si III, K I, Ca I, Sc II, V II, Mn I, Mn II, Fe I, Fe II, Co I, Sn I, Eu III, Yb II) with lines currently observed in exoplanet upper atmospheres (e.g. Charbonneau et al. 2002; Vidal-Madjar et al. 2003; Vidal-Madjar et al. 2004; Sing et al. 2008; Fossati et al. 2010; Linsky et al. 2010, Sing et al. 2011; Haswell et al. 2012; Jensen et al. 2012; Ben-Jaffel & Ballester 2013; Astudillo-Defru & Rojo 2013; Vidal-Madjar et al. 2013; Bourrier et al. 2013). Many of these same species are found in the `CLOUDY` modeling but we also find species (e.g. He I, C I, Al II, Si I/II, S II, Ca II, Ti II, Ni II, Mn II) and lines (e.g. Al III, Fe II, Mn I) that have not yet been observed. A comprehensive list of all the lines predicted can be found in Table 3.4. Future observations are encouraged to search for these lines but more detailed theoretical models are still needed to shed light into opacity sources in escaping

Table 3.3: Mean ionization fractions for the planetary gas for the ionization states of interest for H, He, C, N, Ni, O, Na, Mg, Al, Si, S, P, Ca, Ti, Mn, Fe, and Co calculated from the CLOUDY modeling

State	Fraction (10^X)	State	Fraction (10^X)
H I	-0.083	H II	-0.761
He I	-0.206	He II	-0.433
C I	-0.868	C II	-0.072
C III	-1.76	N I	-0.115
N II	-0.632	Ni I	-0.115
Ni II	-0.632	O I	-0.069
O II	-0.836	Na I	-2.868
Na II	-0.11	Mg I	-1.585
Mg II	-0.086	Mg III	-0.811
Al I	-3.943	Al II	-0.014
Al III	-1.711	Al IV	-1.906
Si II	-0.001	Si III	-2.657
S I	-1.423	S II	-0.038
P I	-3.856	P II	-0.028
Ca I	-3.543	Ca II	-0.087
Ca III	-0.741	Ti I	-4.049
Ti II	-0.033	Mn I	-3.981
Mn II	-0.011	Mn III	-1.599
Fe I	-4.177	Fe II	-0.005
Fe III	-1.937	Fe IV	-5.469
Co I	-1.135	Co II	-0.033

Note. — The values in this table were from the model with a hydrogen density of 10^9 cm^{-3}. The ionization fractions presented are averaged over the width of the cloud. The gas kinetic temperature calculated by CLOUDY was ~12859 K (§3.4).

atmospheres of exoplanets.

Table 3.4: Spectral lines predicted for the planetary gas by CLOUDY.

Vacuum (Air) λ [nm]	Species	Transit Depth [%]	Previously Detected	Vacuum λ [nm]	Species	Transit Depth [%]	Previously Detected
1083.3306 (1083.303)	He I	0.28	N	167.079	Al II	0.26 (blend)	N
866.452 (866.214)	Ca II	0.052	N	166.217	S I	0.26 (blend)	N
854.444 (854.209)	Ca II	0.026	N	165.7	C I	0.36	N
656.4614 (656.28)	H-alpha	0.021	Y (1)	157.591	Co II	0.03	N
396.959 (396.847)	Ca II	0.16	N	156.133	C I	0.314	N
393.477 (393.366)	Ca II	0.19	N	153.1	Si II	0.24	N
388.9750 (388.865)	He I	0.019	N	150	Fe II	0.015	N
336.571 (336.474)	Ti II	0.044	N	147.274	Ni II	0.0535	N
323.8078 (323.714)	Ti II	0.036	N	140.037	Ni II	0.049	N
318.8667 (318.775)	He I	0.01	N	137.573	Ni II	0.083	N
285.2965 (285.213)	Mg I	0.24	Y (2)	135.605	S I	0.065	N
280.3531 (280.271)	Mg II	0.623	Y (3)	133.5	C II	0.44	Y (4)
258.9746 (258.897)	Mn II	0.11	N	132.4117	Ni II	0.294 (blend)	N
251.8226 (2517.47)	Si I	0.01	N	131.477	C I	0.215 (blend)	N
239.9997 (2399.27)	Fe II	0.217	N	130.766	Si II	0.362 (blend)	N
233.5123 (233.441)	S IV	0.0192 (blend)	N	126.332	Si II	0.381	N
233.5321 (233.46)	S IV	0.0192 (blend)	N	125.6	S II	0.162	N

Continued on next page

Table 3.4 – continued

221.500 (221.431)	Si I	0.025	N	125.068	C I	0.223	N
206.156 (206.09)	Co II	0.095	N	124.75	C I	0.33	N
202.6477 (202.582)	Mg I	0.84	N	123.329	C I	0.31	N
186.2789	Al III	0.03 (blend)	N	121.567	Lyman-alpha	12.4 (blend)	Y (5)
185.4716	Al III	0.03 (blend)	N	120.651	Si III	0.58 (blend)	Y (6)
185.3047	Si 1	0.03 (blend)	N	117.959	Si II	0.38	N
181.399	Si II	0.2 (blend)	N	116.681	C I	0.42 (blend)	N
181.7313	Mg I	0.08 (blend)	N	116.598	C I	0.42 (blend)	N
1786	Fe II	0.28	N	116.236	C I	0.42 (blend)	N
176.793	Si I	0.0843 (blend)	N	113.206	C I	0.64 (blend)	N
175.1823	C I	0.15 (blend)	N	113.112	N I	0.64 (blend)	N
174.424	Ni II	0.318 (blend)	N	113.046	C I	0.64 (blend)	N

Note. — The model used has a hydrogen density of 10^9 cm^{-3} and the gas kinetic temperature calculated by `CLOUDY` was ~12859 K (§3.4). Additionally, the default resolution model was not used to search for spectral lines due to many spectral lines overlapping each other. We used the line labels command (creates a list of all emission lines transported in the code) in `CLOUDY` to determine the species responsible for each spectral line in Figure 3.7.

References. — (1) Jensen et al. 2012; (2) Vidal-Madjar et al. 2013; (3) Haswell et al. 2012; (4) Linsky et al. 2010; (5) Vidal-Madjar et al. 2003; (6) Bourrier et al. 2013

3.4.2 Planetary gas interacting with the stellar wind

The gas modeled in § 3.4.1 is assumed to reside in the planet's upper atmosphere. While interaction with the stellar radiation field was included, collisions between particles in the planetary gas and the stellar wind were ignored. However, there are models for the hydrogen Lyman-alpha absorption during transit for HD 209458b that invoke charge exchange of atoms from the planet with solar wind protons to create fast moving neutral atoms (Holmström et al. 2008; Tremblin & Chiang 2013; Christie et al. 2016). In the limit of short mean free paths for the atoms in the stellar wind gas, the energetic atoms occupy a hydrodynamic mixing layer created by eddies at the interface of the two gases (Tremblin & Chiang 2013). For finite mean free paths (Holmström et al. 2008), as long as the mean free path of the planetary atoms is not much larger than the magnetosheath width, some atoms can collide with the stellar wind protons and be entrained with the magnetosheath flow around the planet.

While we have argued that stellar wind gas near the bow shock region cannot provide enough opacity to cause observable transit depths, atoms *originating from the planet*, and entrained with the stellar wind flow through the magnetosheath could provide this source of opacity, as long as they are not ionized too quickly by the hot stellar wind gas. Hence the geometry assumed in the magnetic or non-magnetic bow shock models may indeed be valid, although a sufficient source of atoms from the planet must always be considered. As movement of charged particles through the planetary magnetosphere may only occur along field lines, movement of neutral particles across field lines is subject to strong ion-neutral drag forces (Yelle 2004; Trammell et al. 2011). Open field lines carrying an outflow from the polar regions of the planet are another possible source of neutrals (Trammell et al. 2014).

It is important to distinguish between absorbing atoms originating in the planet, as is assumed here, and in the stellar wind, as is assumed in VJH11a. The source matters even if the geometry is the same. The key point is that the distribution of planetary neutrals decreases with distance from the planet and there would be a far greater number of absorbing species toward the planet. Hence for planetary neutrals one might expect absorption not only near the bow shock, but also all along the line from the bow shock to the planet. This

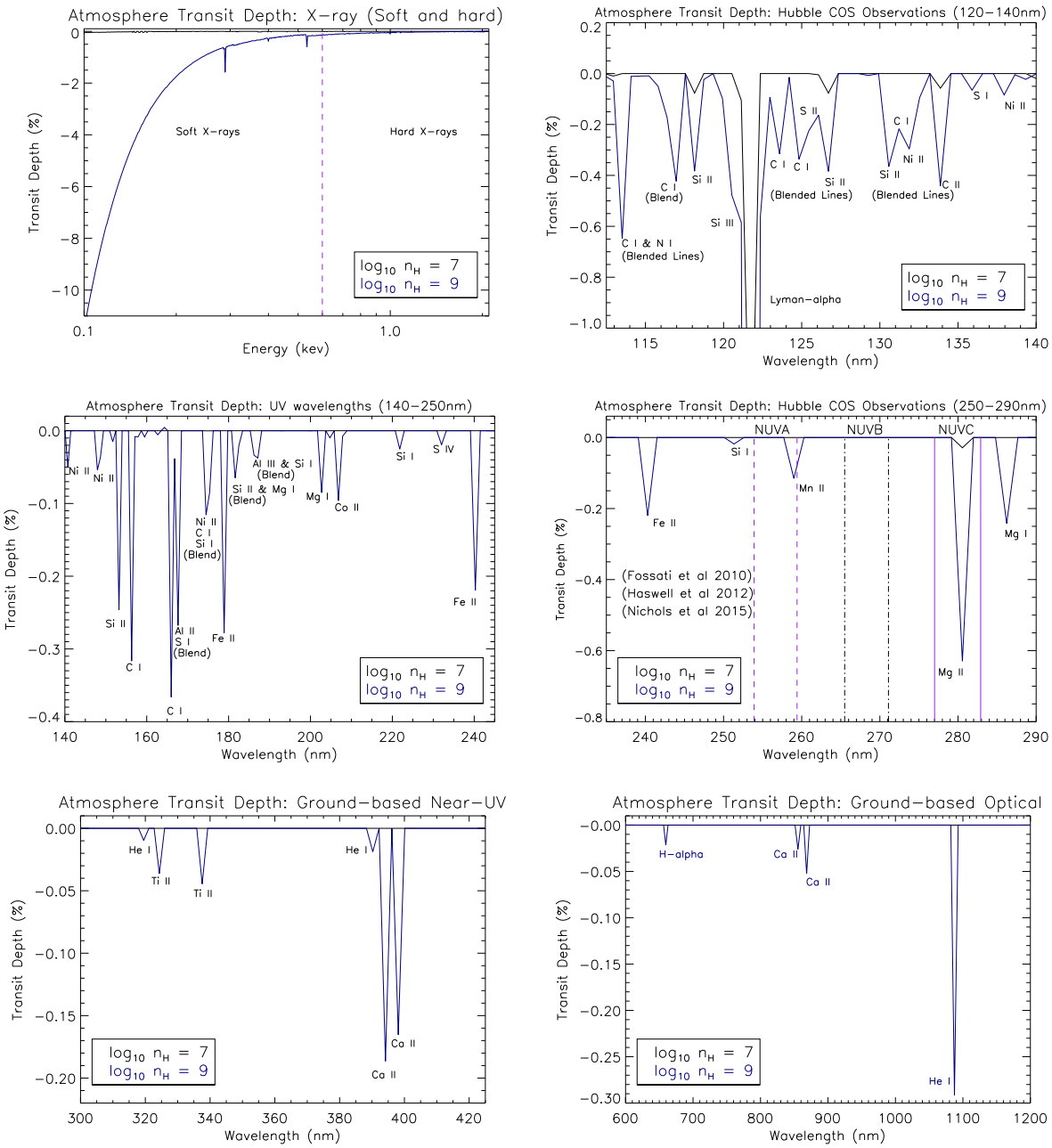

Figure 3.7: Transit depths for the CLOUDY modeling of the escaped planetary gas in thermal equilibrium with the radiation field. We show the transit depth from X-rays to ground-based optical wavelengths. In the top-right plot, Lyman-alpha extends down to 12 %. A complete list of all the lines predicted can be found in Table 3.4.

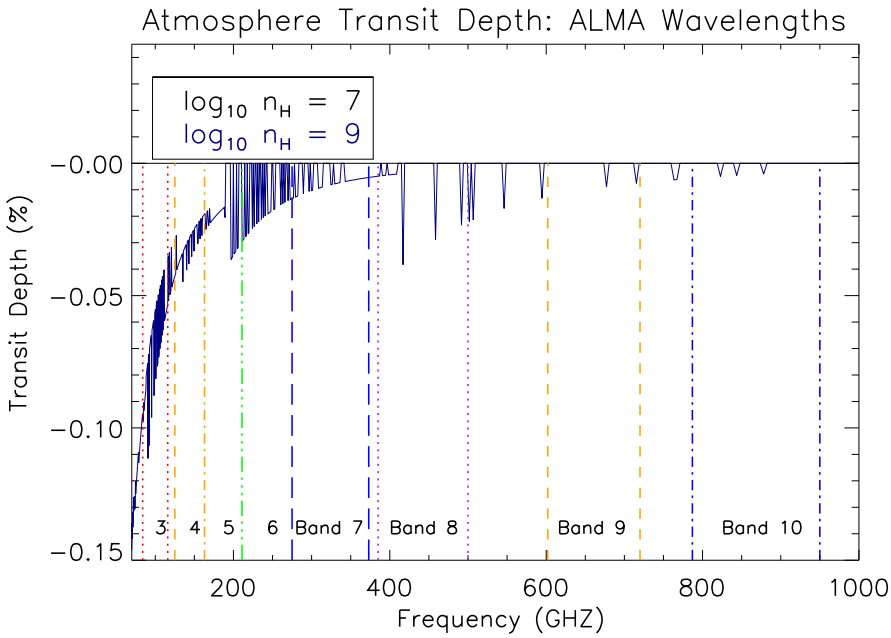

Figure 3.8: Transit depth for radio wavelengths for the CLOUDY modeling of the escaped planetary gas in thermal equilibrium with the radiation field.

would be a significant change to the model used to interpret the observations as compared to assuming the absorption is solely from the stellar wind gas.

3.5 Conclusions

Using the plasma photoionization and microphysics code CLOUDY (Ferland et al. 1998; Ferland et al. 2013) we explore whether there is a UV absorbing species in the stellar wind that can cause an early UV ingress in the transits of close-in exoplanets due to the presence of a magnetic (Vidotto et al. 2011a) or non-magnetic (Lai et al. 2010; Bisikalo et al. 2013a; Bisikalo et al. 2013b) bow shock compressing the coronal plasma. We find under realistic physical conditions for the corona (Table 3.1; § 3.3) that there aren't any species that can cause an absorption with sufficient opacity all wavelengths between X-ray and radio (Figures 3.4 and 3.5). A thorough parameter search with CLOUDY is performed to check the robustness and biases of the nominal parameters and we find that our conclusions are robust (§ 3.3.1). Therefore models cannot posit a distribution of neutrals only out in

the stellar wind, but rather if absorbers are mixed into the stellar wind, there must be an even larger population toward the planet which may cause absorption all the way between the planet and the bow shock. In other words, the bow shock geometry model which has been used to infer planetary magnetic fields is an incomplete model as it does not confront the likely existence of absorbers between the bow shock and the planet. Previous detections of an early ingress in WASP-12b (Fossati et al. 2010; Haswell et al. 2012) and HD 189733b (Ben-Jaffel & Ballester 2013; Cauley et al. 2015) are likely caused by the planetary upper atmosphere or a mixture of planetary and stellar wind material as suggested by our modeling of clouds with lower temperatures (§3.3.2; Figure 3.6). Our conclusions are consistent with other studies suggesting that UV asymmetry observations are not a suitable approach for detecting exoplanet magnetic fields (Ben-Jaffel & Ballester 2014; Grießmeier 2015; Alexander et al. 2015) and that suggest an escaping atmosphere (Lai et al. 2010; Bisikalo et al. 2013a; Bisikalo et al. 2013b; Cherenkov et al. 2014) is the cause of the UV observations.

We also simulate escaping planetary gas in ionization and thermal equilibrium with the stellar radiation field with `CLOUDY` (§ 3.4). From this modeling, we find species with strong absorption lines (Figure 3.7 and 3.8; Table 3.4) previously observed in exoplanet upper atmospheres (e.g. Charbonneau et al. 2002; Vidal-Madjar et al. 2003; Vidal-Madjar et al. 2004; Sing et al. 2008; Fossati et al. 2010; Linsky et al. 2010, Sing et al. 2011; Haswell et al. 2012; Jensen et al. 2012; Ben-Jaffel & Ballester 2013; Astudillo-Defru & Rojo 2013; Vidal-Madjar et al. 2013; Bourrier et al. 2013) but also make predictions for many species and lines that have not been observed (Table 3.4; He I, C I, Al II, Si I/II, S II, Ca II, Ti II, Ni II, Mn II). Therefore, the `CLOUDY` modeling in this chapter is a motivation for more detailed studies of possible absorbing species which may be observable in the transmission spectra of close-in exoplanets (see also, Salz et al. 2015, 2016).

Acknowledgments

J. Turner and R. Johnson were partially supported by the NASA's Planetary Atmospheres program. J. Turner was also partially funded by the Virginia Space Grant Consortium Graduate Research Fellowship Program and by the National Science Foundation Gradu-

ate Research Fellowship under Grant No. DGE-1315231. P. Arras and D. Christie were supported by NASA Origins of Solar Systems Grants NNX14AE16G and NNX10AH29G

We would like to thank Aline Vidotto, Moira Jardine, Christiane Helling, Joe Llama, and Andrew Collier Cameron for their insightful comments on this research. We thank Greg Ferland on his help with the `CLOUDY` modeling. `CHIANTI` was used in this research and is a collaborative project involving George Mason University, the University of Michigan (USA) and the University of Cambridge (UK).

We would like to thank the anonymous referee for their useful comments which have led to considerable improvements in this chapter.

Chapter 4

Investigating the physical properties of transiting hot Jupiters with the 1.5-m Kuiper Telescope

"Remember to look up at the stars and not down at your feet. Try to make sense of what you see and wonder about what makes the universe exist. Be curious." Stephen Hawking

The text in this chapter is reproduced primarily from Turner J.D., Leiter R.M., et al. 2017. Investigating the physical properties of transiting hot Jupiters with the 1.5-m Kuiper Telescope. MNRAS. 472. 3871.

4.1 Introduction

To date, over 3400 exoplanets have been discovered (NASA Exoplanet Archive; Akeson et al. 2013) and most of these planets have been found using the transit method (e.g. Charbonneau et al. 2000; Henry et al. 2000) in large-scale transit surveys such as *Kepler* (Borucki et al. 2010), *K2* (Howell et al. 2014), *WASP* (Pollacco et al. 2006; Collier Cameron et al. 2007) and *CoRoT* (Baglin 2003; Moutou et al. 2013). Transiting exoplanet systems (TEPs) are of great interest because their radius can be directly measured in relation to their

star with photometric observations (Charbonneau et al. 2000; Henry et al. 2000). With the addition of spectroscopic and radial velocity measurements, many physical properties of TEP systems (mass, radius, semi-major axis, gravity, temperature, eccentricity, orbital period) can be directly inferred (e.g., Charbonneau et al. 2007a). Additionally, multiple-band photometry of a TEP system can be used to constrain the composition of an exoplanet's atmosphere (Seager & Sasselov 2000; Brown 2001; Hubbard et al. 2001; Charbonneau et al. 2002). The absorption properties of different species in a planetary atmosphere vary with wavelength, causing an observable variation in the planet's radius. Photometric light curve analysis can also be used to search for transit timing variations (TTVs). TTVs can indicate additional bodies in a TEP system or an unstable orbit caused by tidal forces from the star (e.g., Miralda-Escudé 2002; Holman & Murray 2005; Holman et al. 2010).

In this work, we present new ground-based photometric data of 11 confirmed transiting hot Jupiter exoplanets. We describe and perform TEP modeling techniques (Section 4.2–4.3) to determine the orbital and physical parameters of each system, and compare our results with previous published results to confirm and improve the planetary parameters (Section 4.4–4.5). For each system, we combine our results with previous work to search for a variation in planetary radius with wavelength (Section 4.6), which could indicate Rayleigh scattering, the presence of an absorptive atmosphere, or clouds. Finally, we combine our mid-transit data with previous observations to recalculate each system's orbital period and search for TTVs.

4.2 Observations and Data Reduction

All the observations were performed at the University of Arizona's Steward Observatory 1.55-m Kuiper Telescope on Mt. Bigelow near Tucson, Arizona. The Mont4k CCD has a field of view of 9.7'×9.7' and contains a 4096×4096 pixel sensor. The CCD is binned 3×3 to achieve a resolution of 0.43"/pixel and binning reduces the read-out time to ~10 s. Our observations were taken with the Bessell U (303–417 nm), Harris B (360–500 nm), and Harris R (550–900 nm) photometric band filters. To ensure accurate timing in these observations, the clocks were synchronized with a GPS every few seconds. In all the data sets, the average shift in the centroid of our targets is less than 0.6 pixels (0.26") due to excel-

lent autoguiding (the maximum is 3.4 pixels). This telescope has been used extensively in exoplanet transit studies (Dittmann et al. 2009a,b, 2010, 2012; Scuderi et al. 2010; Turner et al. 2013; Teske et al. 2013; Pearson et al. 2014; Biddle et al. 2014; Zellem et al. 2015; Turner et al. 2016b). A summary of all our observations is displayed in Table 4.1.

To reduce the data and create the light curves we use the reduction pipeline `ExoDRPL`[1] (Pearson et al. 2014). Each of our images are bias-subtracted and flat-fielded with 10 biases and flats. To produce the light curve for each observation we perform aperture photometry (using `phot` in the `IRAF`[2] `DAOPHOT` package) by measuring the flux from our target star as well as the flux from 8 different reference stars with 110 different circular aperture radii. The aperture radii sizes we explore are different for every observation due to changes in seeing conditions. For the analysis, a constant sky annulus for every night of observation of each target is chosen (a different sky annulus is used depending on the seeing and the crowdedness of the target field) to measure the brightness of the sky during the observations. We reduce the risk of contamination by making sure no stray light from the target star or other nearby stars falls in the chosen aperture. A synthetic reference light curve is produced by averaging the light curves from our reference stars. The final light curve of each date is normalized by dividing by this synthetic light curve to correct for any systematic differences from atmospheric variations (i.e. airmass) throughout the night. Every combination of reference stars and aperture radii are considered and we systematically choose the best aperture and reference stars by minimizing the scatter in the Out-of-Transit (OoT) data points. The 1σ error bars on the data points include the readout noise, flat-fielding errors, and Poisson noise. The final light curves are presented in Figs. 4.1–4.3. For all the transits, the OoT baselines have a photometric root-mean-squared (RMS) value between 1.13 and 7.76 millimagnitude (mmag).

[1] https://sites.google.com/a/email.arizona.edu/kyle-pearson/exodrpl

[2] `IRAF` is distributed by the National Optical Astronomy Observatory, which is operated by the Association of Universities for Research in Astronomy, Inc., under cooperative agreement with the National Science Foundation.

Table 4.1: Journal of observations

Planet Name	Date (UT)	Filter[1]	Cadence (s)	N_{pts}	OoT RMS[2] (mmag)	Res RMS[3] (mmag)	Seeing (")	k[a]	$\chi_r^{2\ b}$
CoRoT-12b	2013 Feb. 15	R	60.39	265	6.06	4.99	1.96-4.06	4	1.32
HAT-P-5b	2015 June 6	U	80.64	191	3.02	2.84	1.36-2.17	4	0.97
HAT-P-12b	2014 Jan. 19	B	188.25	89	1.13	1.27	2.22-2.96	7	1.99
HAT-P-33b	2012 April 6	R	24.29	706	3.65	4.15	1.01-2.68	4	7.84
HAT-P-37b	2015 July 1	B	115.51	128	2.37	2.88	0.98-2.45	4	1.10
HAT-P-37b	2015 July 1	R	115.51	129	2.33	2.30	0.98-2.45	4	1.33
WASP-2b	2014 June 14	B	59.31	230	2.41	2.28	1.43-2.68	7	3.55
WASP-24b	2012 March 23	R	24.95	531	2.41	2.55	1.03-2.12	7	4.06
WASP-24b	2012 April 6	R	26.77	434	5.14	5.73	1.01-2.72	6	2.04
WASP-60b	2012 Dec. 1	B	20.46	751	5.30	4.65	0.83-6.82	4	1.21
WASP-80b	2014 June 16	U	93.50	160	7.76	7.20	1.54-2.92	7	1.15
WASP-103b	2015 June 3	U	65.05	363	3.66	3.62	1.37-2.56	6	1.29
XO-3b	2012 Nov. 30	B	40.63	418	2.04	2.20	1.44-2.23	4	1.96

[1] Filter: B is the Harris B (330–550 nm), R is the Harris R (550–900 nm) and U is the Bessell U (303–417 nm)

[2] Out-of-Transit (OoT) root-mean-squared (RMS) relative flux

[3] Residual (res) RMS flux after subtracting the EXOplanet Modeling Package (`EXOMOP`) best-fitting model from the data

[a] k is the degrees of freedom used in the `EXOMOP` best-fitting model

[b] Reduced χ^2 (χ_r^2) calculated using the `EXOMOP` best-fitting model, N_{pts}, and k.

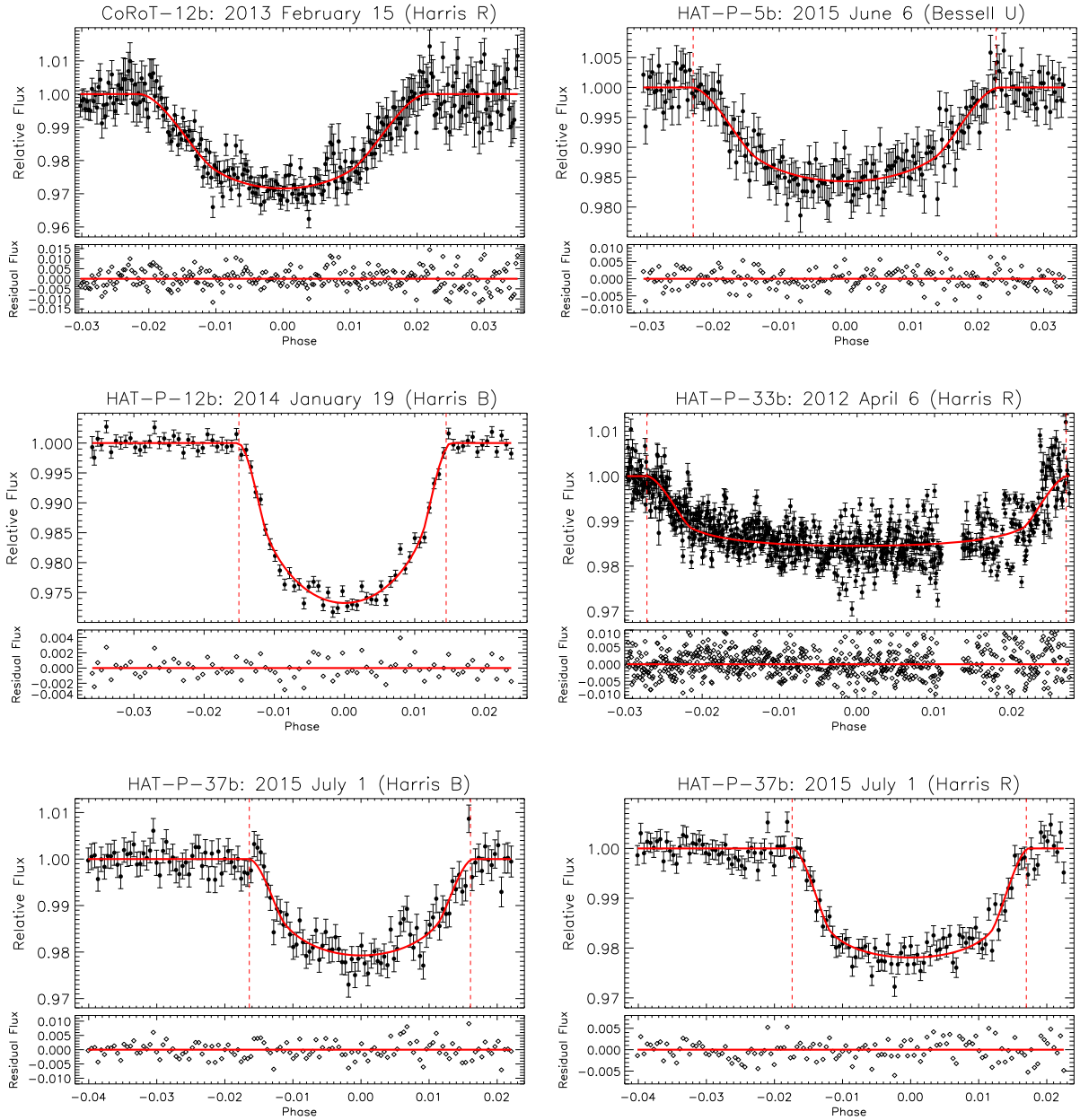

Figure 4.1: Light curves of CoRoT-12b, HAT-P-5b, HAT-P-12b, HAT-P-33b, and HAT-P-37b. The 1σ error bars include the readout noise, the Poisson noise, and the flat-fielding error. The best-fitting models obtained from the EXOplanet MOdeling Package (`EXOMOP`) are shown as a solid red line. The model predicted ingress and egress points from `EXOMOP` are shown as dashed red vertical lines. The residuals (Light Curve - `EXOMOP` Model) are shown in the second panel. See Table 4.1 for the cadence, Out-of-Transit root-mean-squared (RMS) flux, and residual RMS flux for each light curve.

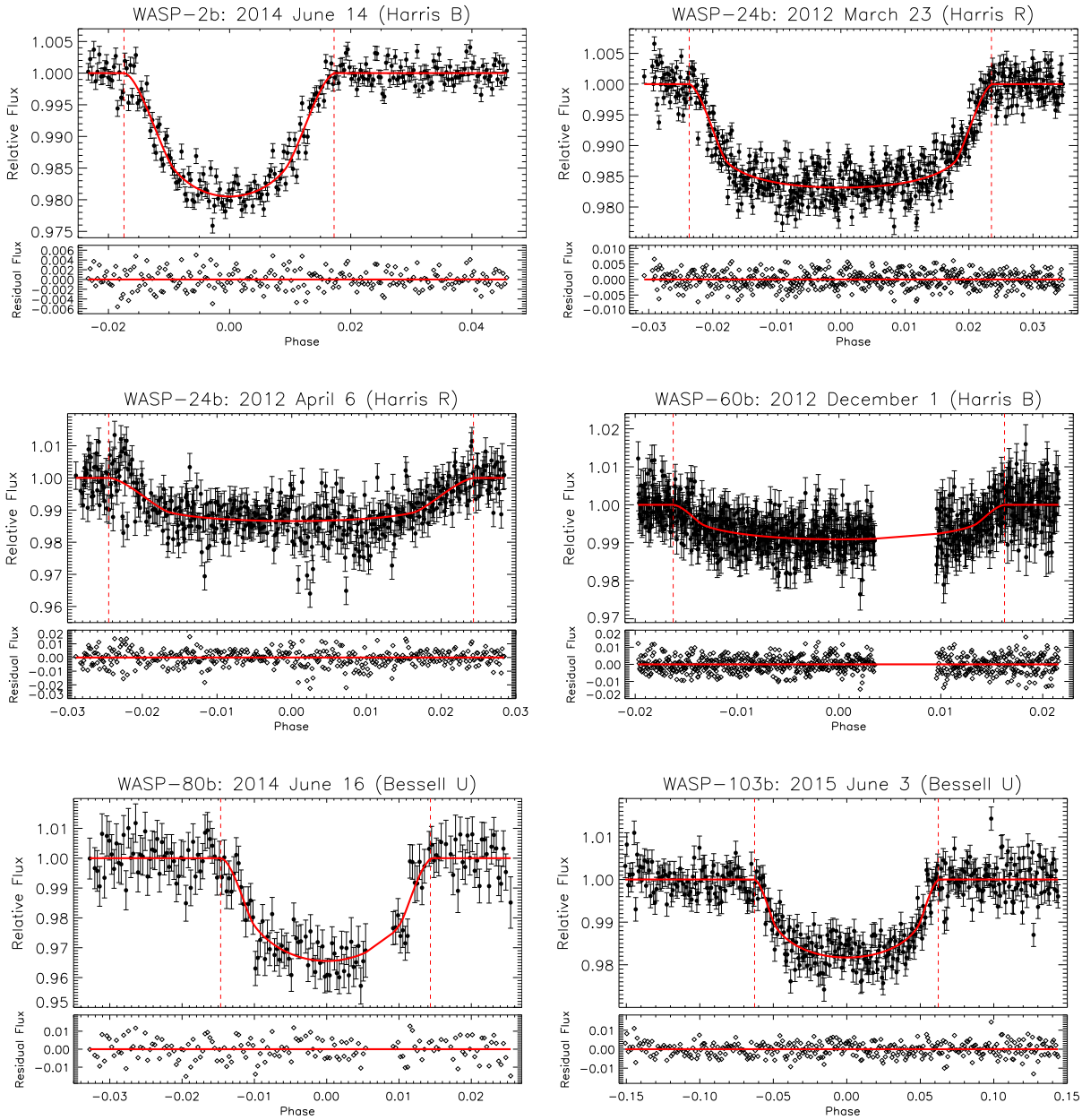

Figure 4.2: Light curves of WASP-2b, WASP-24b, WASP-60b, WASP-80b, and WASP-103b. Other comments are the same as Fig. 4.1.

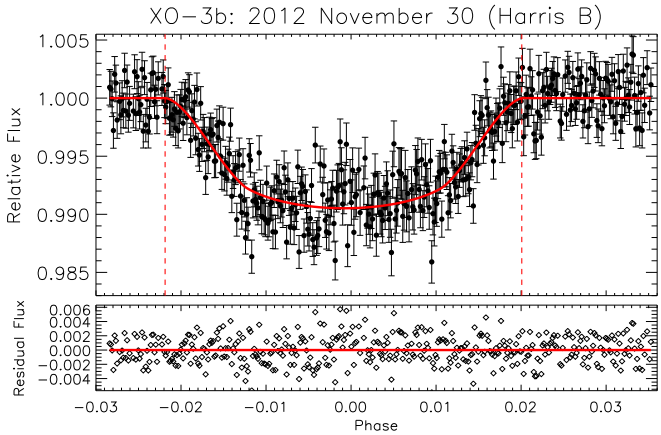

Figure 4.3: Light curve of XO-3b. Other comments are the same as Fig. 4.1.

4.3 Light Curve Analysis

To find the best-fit to the light curves we use the EXOplanet MOdeling Package (`EXOMOP`; Pearson et al. 2014; Turner et al. 2016b)[3], which utilizes the analytic equations of Mandel & Agol (2002) to generate a model transit. For a complete description of `EXOMOP` see Pearson et al. (2014) and Turner et al. (2016b). The χ^2-fitting statistic for the model light curve used in `EXOMOP` is:

$$\chi^2 = \sum_{i=1}^{N_{pts}} \left[\frac{f_i(\text{obs}) - f_i(\text{model})}{\sigma_i(\text{obs})} \right]^2 \tag{4.1}$$

where N_{pts} is the total number of data points (Table 4.1), f_i(obs) is the observed flux at time i, σ_i(obs) is the error in the observed flux, and f_i(model) is the calculated model flux.

`EXOMOP` uses the following procedure to find a best-fit to the data. A Levenberg-Marquardt (LM) non-linear least squares minimization (`MPFIT`; Markwardt 2009; Press et al. 1992) is performed on the data and a bootstrap Monte Carlo technique (Press et al. 1992) is used to calculate robust errors of the LM fitted parameters. Additionally, a Differential Evolution Markov Chain Monte Carlo (DE-MCMC; Braak 2006; Eastman et al. 2013) analysis is used to model the data. The fitted parameters that have the highest error bars from either the LM or DE-MCMC best-fitting model are used in the analysis. In every

[3] `EXOMOPv7.0` is used in the analysis and is available on Github at https://github.com/astrojake/EXOMOP

case both models find results within 1σ of each other. Additionally, EXOMOP uses the residual permutation (rosary bead; Southworth 2008), time-averaging (Pont et al. 2006), and wavelet (Carter & Winn 2009) methods to assess the importance of red noise in both fitting methods. Not accounting for red noise in the data underestimates the fitted parameters (Pont et al. 2006; Carter & Winn 2009). In order to be conservative, the red noise method that produces the largest errors is used to inflate the errors in the fitted parameters. Finally, in order to compensate for underestimated observational errors we multiply the error bars of the fitted parameters by $\sqrt{\chi_r^2}$ when the reduced chi-squared (χ_r^2) of the data (Table 4.1) is greater than unity (e.g. Bruntt et al. 2006; Southworth et al. 2007b; Southworth et al. 2007a; Southworth 2008; Barnes et al. 2013; Turner et al. 2016b).

EXOMOP uses the Bayesian Information Criterion (BIC; Schwarz 1978) to assess overfitting of the data. The BIC is defined as

$$BIC = \chi^2 + k \ln (N_{pts}), \tag{4.2}$$

where χ^2 is calculated for the best-fitting model (equation 4.1) and k is the number of free parameters (Table 4.1) in the model fit [f_i(model)]. The power of the BIC is the penalty for a higher number of fitted model parameters, making it a robust way to compare different best-fit models. The preferred model is the one that produces the lowest BIC value.

Each transit is modeled with EXOMOP using 10000 iterations for the LM model and 20 chains and 20^6 links for the DE-MCMC model. The Gelman-Rubin statistic (Gelman & Rubin 1992) is used to ensure chain convergence (Ford 2006) in the MCMC model. During the analysis of each transit the mid-transit time (T_c), planet-to-star radius (R_p/R_*), scaled semi-major axis (a/R_*), and inclination (i) are set as free parameters. The previously published values for a/R_*, i, and a/R_* are used as priors for the LM model (Table 4.2). The results of the LM fit are used as the prior for the DE-MCMC. The eccentricity (e), argument of periastron (ω), and period (P_p) of each of the planets are fixed (see Table 4.2 for their values) in the analysis because these parameters have minimal effect on the overall shape of the light curve. The linear and quadratic limb darkening coefficients in each filter are taken from Claret & Bloemen (2011) and interpolated to the stellar parameters of the host stars

(see Table 4.3) using the EXOFAST applet[4](Eastman et al. 2013). In addition, a linear or quadratic least squares fit is modeled to the OoT baseline simultaneously with the Mandel & Agol (2002) model. The BIC is used to determine whether to include any baseline fit in the best-fit model and the baseline with the lowest BIC value is always chosen.

The light curve parameters obtained from the EXOMOP analysis and the derived transit durations are summarized in Table 4.4. The modeled light curves can be found in Figs. 4.1–4.3 and the physical parameters for our targets are derived as outlined in Section 4.4 (Tables 4.5–4.6). A thorough description of the modeling and results of each system can be found in Section 4.5.

Table 4.4: Light curve parameters derived in this study using EXOMOP

Planet	CoRoT-12b	HAT-P-5b	HAT-P-12b
Date	2013 Feb. 15	2015 June 6	2014 Jan. 19
Filter[1]	R	U	B
T_c (BJD$_{TDB}$-2.45×10^6)	$6338.67097^{+0.00074}_{-0.00074}$	$7180.82658^{+0.00076}_{-0.00076}$	$6677.97482^{+0.00047}_{-0.00047}$
R$_p$/R$_*$	$0.1645^{+0.0038}_{-0.0040}$	0.1225±0.0051	$0.1386^{+0.0013}_{-0.0014}$
a/R_*	$6.59^{+0.31}_{-0.29}$	6.05±0.44	11.86±0.57
Inclination (°)	83.54±0.71	83.31±1.11	90.98±1.09
Duration (mins)	174.0±1.4	184.1±1.9	139.8±4.4
Red noise (mmag)	0.0001	1.6	0.21
OoT baseline function	None	None	Quadratic
Planet	HAT-P-33b	HAT-P-37b	HAT-P-37b
Date	2012 April 6	2015 July 1	2015 July 1
Filter[1]	R	B	R
T_c (BJD$_{TDB}$-2.45×10^6)	$6024.71746^{+0.0012}_{-0.0012}$	$7205.91376^{+0.00054}_{-0.00054}$	$7205.91325^{+0.00056}_{-0.00056}$
R$_p$/R$_*$	0.1152±0.0017	0.1253±0.0021	0.1361±0.0028
a/R_*	5.67±0.13	10.82±0.91	9.14±0.63
Inclination (°)	90.08±3.43	89.991.83	86.73±0.93
Duration (mins)	270.45±0.48	132.8 ± 2.7	140.5 ± 2.7

Continued on next page

[4]http://astroutils.astronomy.ohio-state.edu/exofast/limbdark.shtml

Table 4.4 – continued

Red noise (mmag)	0.78	0.0001	0.34
OoT baseline function	None	None	None
Planet	HAT-P-37b	WASP-2b	WASP-24b
Date	Weight. Avg.	2014 June 14	2012 March 23
Filter[1]	—	B	R
T_c (BJD$_{TDB}$-2.45×10^6)	—	$6823.83839^{+0.00055}_{-0.00055}$	$6010.8437^{+0.0017}_{-0.0017}$
R$_p$/R$_*$	0.1291±0.0017	0.1383±0.0049	0.1139±0.0015
a/R_*	9.68±0.52	8.05±1.21	7.42±0.15
Inclination (°)	87.4±0.82	84.86±1.61	90.0±5.4
Duration (mins)	136.6±1.9	108.4±1.4	159.5±0.6
Red noise (mmag)	—	0	0.27
OoT baseline function	—	Quadratic	Quadratic
Planet	WASP-24b	WASP-24b	WASP-60b
Date	2012 April 6	Weight. Avg.	2012 Dec. 1
Filter[1]	R	R	B
T_c (BJD$_{TDB}$-2.45×10^6)	$6024.8910^{+0.0015}_{-0.0015}$	—	$6263.6330^{+0.0012}_{-0.0012}$
R$_p$/R$_*$	0.1113±0.0043	0.1136±0.0014	0.0852±0.0036
a/R_*	6.06±0.73	7.36±0.15	9.49±1.81
Inclination (°)	83.95±2.74	85.19±2.44	87.48±2.83
Duration (mins)	165.0±0.6	162.1±0.4	201.9±0.3
Red noise (mmag)	0.6	—	0
OoT baseline function	Linear	—	None
Planet	WASP-80b	WASP-103b	XO-3b
Date	2014 June 16	2015 June 3	2012 Nov. 30
Filter[1]	U	U	B
T_c (BJD$_{TDB}$-2.45×10^6)	$6824.88661^{+0.00091}_{-0.00091}$	$7177.8222^{+0.0015}_{-0.0009}$	$6262.6566^{+0.0015}_{-0.0015}$
R$_p$/R$_*$	0.1615±0.0033	0.1181±0.0016	0.0968±0.0023
a/R_*	12.85±0.42	2.90±0.05	5.68±0.51

Continued on next page

Table 4.4 – continued

Inclination (°)	90.0±1.8	90.00±0.18	81.75±0.77
Duration (mins)	126.7 ±2.2	167.6 ±1.5	185.4 ±0.9
Red noise (mmag)	0.01	0.001	0.001
OoT baseline function	Quadratic	Linear	None

1 Filter: U is the Bessell U (303–417 nm), B is the Harris B (330–550 nm), and R is the Harris R (550–900 nm)

4.4 Physical Properties of the Systems

We use the results of our light curve modeling with `EXOMOP` combined with other measurements in the literature to calculate the planetary mass (e.g. Winn 2010; Seager 2011), radius, density, surface gravity (e.g. Southworth et al. 2007b), modified equilibrium temperature (e.g. Southworth 2010), Safronov number (e.g. Safronov 1972; Southworth 2010), and atmospheric scale height (e.g. Seager 2011; de Wit & Seager 2013). An updated period and ephemeris is also calculated and is described in detail in Section 4.4.1. To calculate the physical parameters we use the values from the modeling (P_p, R_p/R_*, i, a/R_*) and for the orbital (e) and host star parameters (radial velocity amplitude, mass, radius, equilibrium temperature) we use the values found in the literature. When calculating the scale height, the mean molecular weight in the planet's atmosphere was set to 2.3 assuming a H/He-dominated atmosphere (de Wit & Seager 2013). The physical parameters of all our systems can be found in Tables 4.5–4.6.

4.4.1 Period Determination

By combining our mid-transit times found using `EXOMOP` with previously published mid-transit times, we can refine the orbital period of the targets. When necessary, the mid-transit times were transformed from Heliocentric Julian Date (HJD), which is based on Coordinated Universal Time (UTC) time, into Barycentric Julian Date (BJD), which is

Table 4.2: Parameters fixed for the light curve fitting using `EXOMOP`

Planet	Period (P_p) (days)	a/R_*^a	Inclination (i)^a (°)	Eccentricity (e)	Omega (ω) (°)	Source
CoRoT-12b	2.828042	7.7402	85.48	0.070	105	1
HAT-P-5b	2.788491	7.5	86.75	0	0	2
HAT-P-12b	3.213089	11.7371	89.915	0	0	3
HAT-P-33b	3.474474	6.56	87.2	0.148	96	4
HAT-P-37b	2.797436	9.32	86.9	0.058	164	5
WASP-2b	2.15221812	8.06	84.89	0	0	6
WASP-24b	2.341213	5.98	83.64	0	0	7
WASP-60b	4.3050011	10	87.9	0	0	8
WASP-80b	3.06785	12.989	89.92	0.07	0	9
WASP-103b	0.925542	2.978	86.3	0	0	10
XO-3b	3.191524	7.07	84.2	0.26	345.8	11

a These parameter values were not fixed but were used as priors for the MCMC.

References. — (1) Gillon et al. 2010; (2) Bakos et al. 2007; (3) Lee et al. 2012; (4) Hartman et al. 2011; (5) Bakos et al. 2012; (6) Becker et al. 2013; (7) Street et al. 2010; (8) Hébrard et al. 2013; (9) Triaud et al. 2013; (10) Gillon et al. 2014; (11) Winn et al. 2008a

Table 4.3: Limb darkening coefficients for the light curve fitting using EXOMOP

Planet	Filter	Linear coefficient[1]	Quadratic coefficient[1]	T_{eff} [K]	[Fe/H]	log g [cgs]	Source
CoRoT-12b	R	0.39440901	0.26682249	5675	0.160	4.375	1
HAT-P-5b	U	0.75552025	0.093484300	5960	0.240	4.368	2
HAT-P-12b	B	0.93774724	-0.083432883	4650	-0.290	4.610	3
HAT-P-33b	R	0.27628872	0.32295169	6401	0.05	4.15	4
HAT-P-37b	B	0.72832760	0.097543998	5500	0.03	4.52	5
HAT-P-37b	R	0.41967640	0.25020840	5500	0.03	4.52	5
WASP-2b	B	0.82272126	0.018632333	5200	0.100	4.537	2
WASP-24b	R	0.31410756	0.30624587	6080	-0.002	4.26	6
WASP-60b	B	0.61455358	0.18477201	5900	-0.040	4.20	7
WASP-80b	U	0.82663825	-0.029831771	4150	-0.140	4.60	8
WASP-103b	U	0.65536932	0.17875591	6110	0.060	4.22	9
XO-3b	B	0.50449954	0.25897027	6429	-0.177	3.950	10

1The limb darkening coefficients are taken from Claret & Bloemen (2011) and interpolated to the stellar parameters of their host star using EXOFAST

References. — (1) Gillon et al. 2010; (2) Torres et al. 2008; (3) Hartman et al. 2009; (4) Hartman et al. 2011; (5) Bakos et al. 2012; (6) Street et al. 2010; (7) Hébrard et al. 2013; (8) Triaud et al. 2013; (9); Gillon et al. 2014; (10) Johns-Krull et al. 2008

based on Barycentric Dynamical Time (TDB), using the online converter[5] by Eastman et al. (2010). A refined ephemeris for each target is found by performing a weighted linear least-squares analysis using the following equation:

$$T_c = T_c(0) + P_p \times E, \tag{4.3}$$

where $T_c(0)$ is the mid-transit time at the discovery epoch measured in BJD, P_p is the orbital period of the target and E is the integer number of cycles after their discovery paper. See Tables 4.5-4.6 for an updated T_c and P_b for each system.

For every system, we also made observation minus calculation mid-transit time (O-C) plots in order to search for any TTVs due to other bodies in the system. We used the derived period and ephemeris found in Tables 4.5-4.6 and Equation 4.3 for the calculated mid-transit times. The O-C plots can be found in Figs 4.4–4.5. We do not observe any significant TTVs in our data with the exception of a 3.8σ deviation for WASP-80b for our observed transit. Since the possible TTV is only one data point and may be caused by an unknown systematic error, more observations of WASP-80b are needed to confirm this result.

4.5 Individual Systems

4.5.1 CoRoT-12b

CoRoT-12b was discovered by the CoRoT satellite (Carone et al. 2012) and was confirmed by follow-up photometry and radial-velocity measurements (Gillon et al. 2010). CoRoT-12b is an inflated hot Jupiter with a low density that is well predicted by standard models (Fortney et al. 2007) for irradiated planets (Gillon et al. 2010).

We observed a transit of CoRoT-12b on 2013 February 15 with the Harris R filter (Fig. 4.1). We find a R_p/R_* value 4.6σ greater than the discovery value. Our derived physical parameters are in good agreement with Gillon et al. (2010). We find a planetary radius within 1.3σ of the previously calculated value and a planetary mass within 1σ (Tables 4.4 and 4.5).

[5]http://astroutils.astronomy.ohio-state.edu/time/hjd2bjd.html

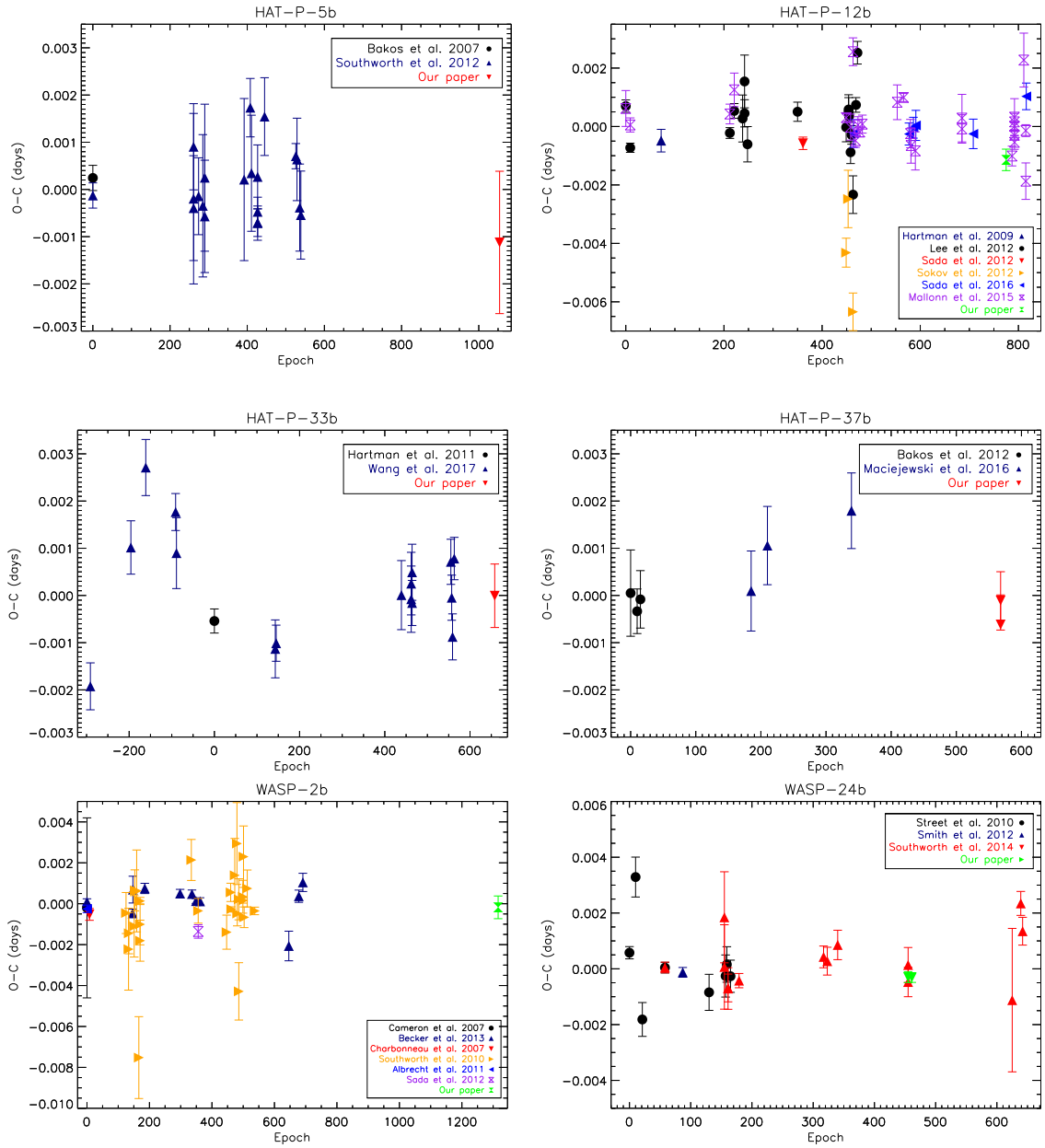

Figure 4.4: Observation minus calculation mid-transit time (O-C) plots of HAT-P-5b, HAT-P-12b, HAT-P-33b, WASP-2b, and WASP-24b from this paper and previous literature. We do not see any evidence for TTVs.

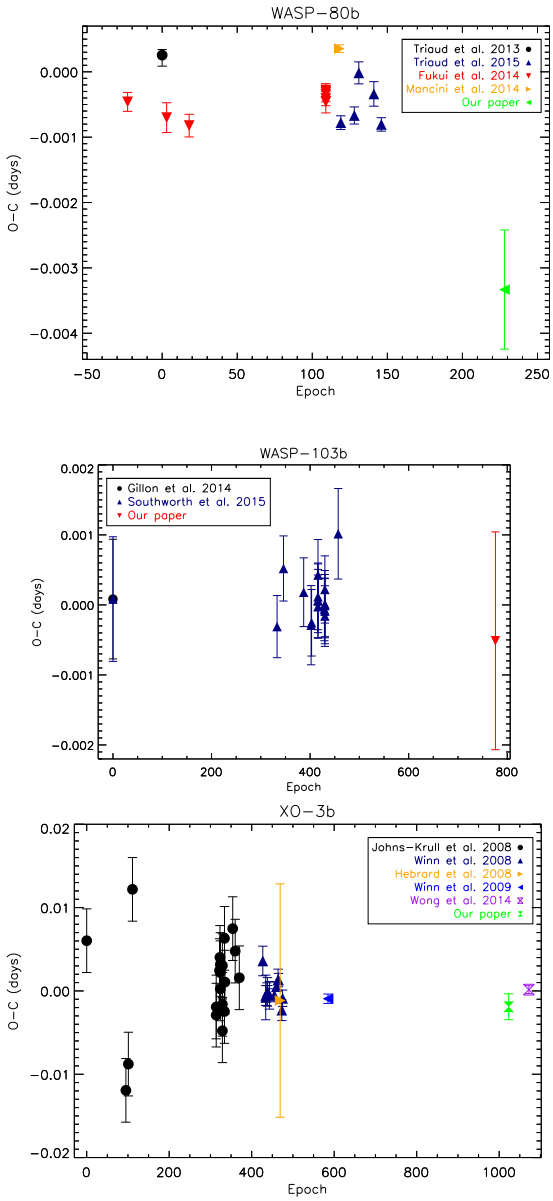

Figure 4.5: O-C plot of WASP-80b, XO-3b, and WASP-103b from this paper and previous literature. We do not see any TTVs with the exception of WASP-80b but there are large uncertainties in our measurement, so we recommend follow-up observations to verify this claim.

Table 4.5: Physical parameters derived in this study for CoRoT-12b, HAT-P-5b, HAT-P-12b,HAT-P-33b, HAT-P-37b, WASP-2b, WASP-24b, WASP-60b, and WASP-80b.

Planet	CoRoT-12b	HAT-P-5b	HAT-P-12b
Date	2013 Feb. 15	2015 June 6	2014 Jan. 19
Period (Days)	2.828051 ±0.000080	2.78847280 ±0.00000039	3.21305761 ±0.00000020
$T_c(0)$ (BJD-2.45×10^6)	4398.628 ±0.055	4241.77716 ±0.00015	4187.85623 ±0.00013
M_b (M_{Jup})	0.922 ± 0.072	1.06 ± 0.12	0.211±0.012
Our R_b (R_{Jup})	1.79 ± 0.15	1.36 ± 0.057	0.949±0.017
Reference R_b (R_{Jup})	1.44 ± 0.13 (a)	1.26 ± 0.05 (b)	0.959±0.029 (c)
ρ_b (cgs)	0.200 ± 0.054	0.531 ± 0.088	0.306±0.023
$\log g_b$ (cgs)	2.72 ± 0.12	2.946 ± 0.085	2.77±0.052
T'_{eq} (K)	1563 ± 22	1713 ± 29	954±12
Θ	0.0327 ± 0.0054	0.0431 ± 0.0064	0.0235±0.0019
a (AU)	0.0342 ± 0.0032	0.0320 ± 0.0023	0.0386±0.0019
H (km)	1521 ± 402	979 ± 193	822 ± 98
Planet	HAT-P-33b	HAT-P-37b	WASP-2b
Date	2012 April 6	2015 July 1	2014 June 14
Period (Days)	3.4744750±0.00000037	2.79744149 ±0.00000083	2.15222114 ±0.00000019
$T_c(0)$ (BJD-2.45×10^6)	5110.92726±0.00012	5616.96710± 0.00028	3991.515553 ±0.000074
M_b (M_{Jup})	1.26±0.23	1.17 ± 0.10	0.880 ± 0.087

Continued on next page

Table 4.5 – continued

Our R_b (R_{Jup})	1.99±0.32	1.16 ± 0.06	1.12 ± 0.13
Reference R_b (R_{Jup})	1.827±0.290 (d)	1.178 ± 0.077 (e)	1.043 ± 0.033 (f)
ρ_b (cgs)	0.20±0.10	0.93 ± 0.17	0.77 ± 0.28
$\log g_b$ (cgs)	2.83±0.21	3.369 ± 0.088	3.25 ± 0.18
T'_{eq} (K)	1901±26	1250 ± 22	1284 ± 20
Θ	0.042 ± 0.013	0.085 ± 0.012	0.058 ± 0.016
a (AU)	0.0468 ± 0.0075	0.0394 ± 0.0029	0.0312 ± 0.0056
H (km)	1408±679	270 ± 54	364 ± 155
Planet	WASP-24b	WASP-60b	WASP-80b
Date	Combined	2012 Dec. 1	2014 June 16
Period (Days)	2.34121877 ±0.00000030	4.305022 ±0.000021	3.06785925 ±0.00000047
$T_c(0)$ (BJD-2.45×10^6)	4945.589444 ±0.000090	5747.0302±0.0022	6125.418034±0.000052
M_b (M_{Jup})	1.032 ± 0.037	0.512± 0.034	0.551± 0.036
Our R_b (R_{Jup})	1.27 ± 0.055	0.94± 0.12	0.99± 0.24
Reference R_b (R_{Jup})	1.303 ± 0.047 (g)	0.86± 0.12 (h)	0.999± 0.031 (i)
ρ_b (cgs)	0.628 ± 0.085	0.75± 0.27	0.71± 0.51
$\log g_b$ (cgs)	3.279 ± 0.057	3.11± 0.22	3.22± 0.29
T'_{eq} (K)	1583 ± 27	1354± 23	817± 20
Θ	0.0566 ± 0.0043	0.051± 0.013	0.072± 0.025

Continued on next page

Table 4.5 – continued

a (AU)	0.0392 ± 0.0018	0.050± 0.011	0.0376 ± 0.0090
H (km)	421 ± 55	536 ± 274	248 ± 168

References. — (a) Gillon et al. 2010; (b) Bakos et al. 2007; (c) Hartman et al. 2009; (d) Hartman et al. 2011; (e) Bakos et al. 2012; (f) Southworth et al. 2010; (g) Southworth et al. 2014; (h) Hébrard et al. 2013; (i) Triaud et al. 2015

Table 4.6: Physical parameters derived in this study for WASP-103b and XO-3b

Planet	WASP-103b	XO-3b
Date	2015 June 3	2012 Nov. 30
Period (days)	0.9255454±0.0000010	3.19153125±0.00000053
$T_c(0)$ (BJD-2.45×10^6)	6459.59948 ±0.00041	2997.72200 ±0.00040
M_b (M_{Jup})	1.484 ± 0.082	13.07± 0.66
Our R_b (R_{Jup})	1.640 ± 0.066	1.403± 0.093
Previous R_b (R_{Jup})	1.528 ± 0.073 (a)	1.217± 0.073 (b)
ρ_b (cgs)	0.417 ± 0.055	5.87± 1.20
$\log g_b$ (cgs)	3.114 ± 0.055	4.05± 0.11
T'_{eq} (K)	2537 ± 42	2011± 13
Θ	0.0286 ± 0.0023	0.519± 0.075
a (AU)	0.09361 ± 0.00078	0.0393± 0.0041
H (km)	986 ± 125	90 ± 22

References. — (a) Gillon et al. 2014; (b) Winn et al. 2008a

4.5.2 HAT-P-5b

HAT-P-5b is a hot Jupiter discovered by the HATNet project that orbits a slightly metal-rich star (Bakos et al. 2007). Follow-up multi-color transit observations of HAT-P-5b by Southworth et al. (2012b) confirmed the existence of the planet and searched for a variation in planetary radius with wavelength. A significantly larger radius was found in the U-band than expected from Rayleigh scattering alone, which the authors suggest may be due to an unknown systematic error.

We observed a transit of HAT-P-5b on 2015 June 6 with the Bessell U filter (Fig. 4.1). Our derived physical parameters are in agreement with previous literature (Tables 4.4 and 4.5). We derive a U-band radius consistent with a weighted average of radii taken from 350-733 nm within 1σ (Fig 4.6). The error on our U-band observation is too large to determine if the observation by Southworth et al. (2012b) in the same band may have an unknown systematic error (as suggested by them). Our calculated period is in good agreement with the value found by Southworth et al. (2012b) with a similar uncertainty.

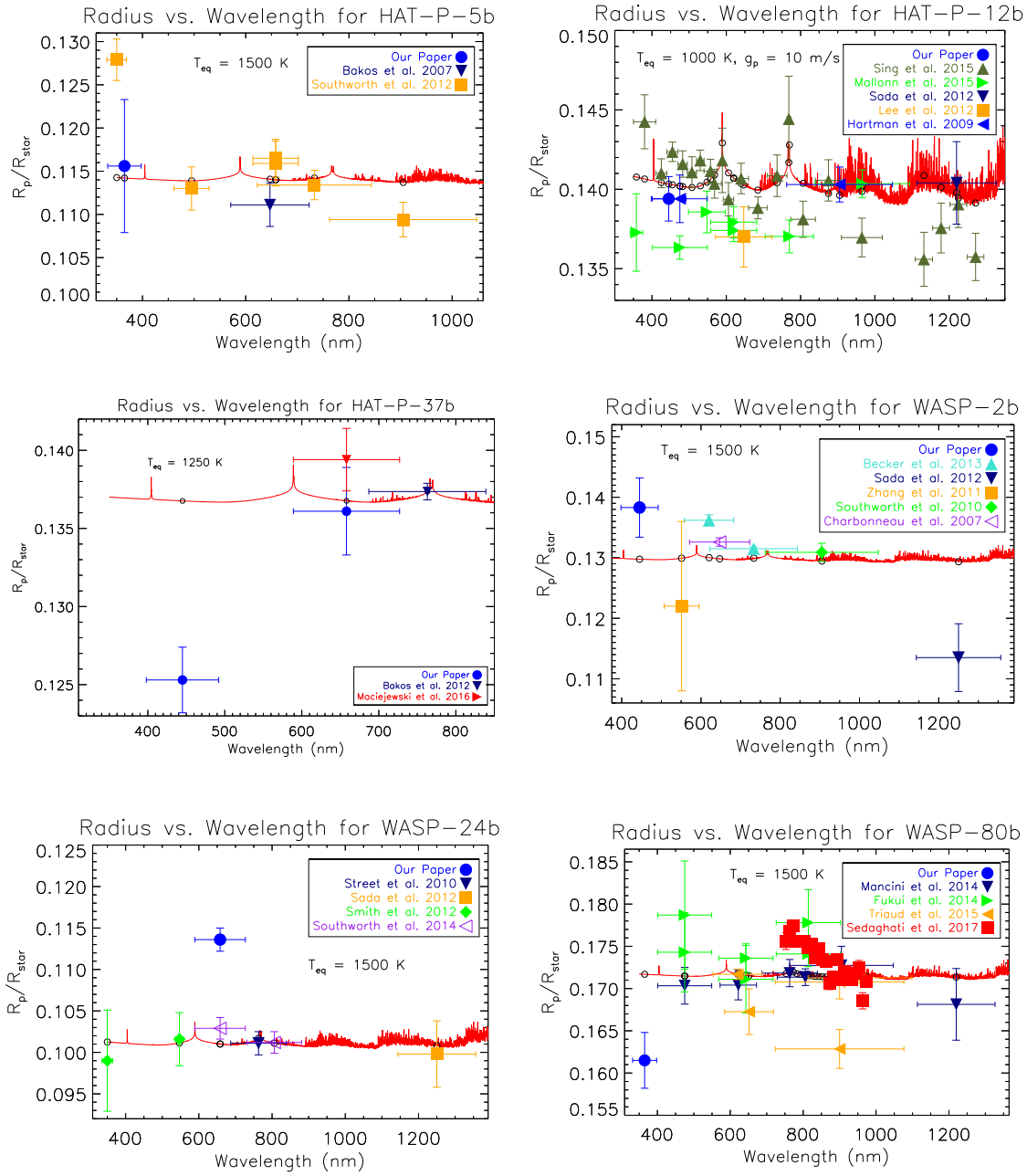

Figure 4.6: Plot of R_p/R_* against wavelength for HAT-P-5b, HAT-P-12b, HAT-P-37b, WASP-2b, WASP-24b, and WASP-80b from this paper and previous literature. Our data are shown as blue circles. Over-plotted in red are atmospheric models by Fortney & Nettelmann (2010) for planets with a 1 M_{Jup}, $g_p = 25m\ s^{-1}$ (unless specified on plot), T_{eq} (specified on plot), and a base radius of 1.25 R_{Jup} at 10 bar. We find that HAT-P-5b, HAT-P-12b, WASP-2b, and WASP-80b have flat spectra that could indicate the presence of clouds. The transit depth variation of HAT-P-37b could be due to absorption of TiO/VO (Evans et al. 2016).

4.5.3 HAT-P-12b

HAT-P-12b is a low density, sub-Saturn mass planet discovered by the HAT survey (Hartman et al. 2009). Multiple photometric studies have further refined the system's parameters and searched for TTVs (Sada et al. 2012; Sokov et al. 2012; Lee et al. 2012; Line et al. 2013; Mallonn et al. 2015a; Sing et al. 2016; Sada & Ramón-Fox 2016). Sing et al. (2016) find a strong optical scattering slope from blue to near-IR wavelengths using *Hubble Space Telescope* and *Spitzer Space Telescope* transmission spectrum data.

We observed a transit of HAT-P-12b on 2014 January 19 using the Harris B filter (Fig. 4.1). We derive an optical R_p/R_* within 1σ of previously derived radii at optical wavelengths (Fig 4.6). These results are consistent with the planet having high clouds in its atmosphere (e.g. Seager & Sasselov 2000; Kreidberg et al. 2014) and the finding by Line et al. (2013) that HAT-P-12b has a cloudy atmosphere. We also find a period similar to Mallonn et al. (2015a).

4.5.4 HAT-P-33b

HAT-P-33b is an inflated hot Jupiter orbiting a high radial velocity jitter star (Hartman et al. 2011). The high-jitter is believed to be caused by convective inhomogeneities in the host star (Saar et al. 1998; Hartman et al. 2011). The planetary radius and mass, which both depend on eccentricity, and the stellar parameters are not well constrained due to the large jitter (20 m s^{-1}). HAT-P-33b's radius is either 1.7 or 1.8 R_{Jup} assuming a circular or eccentric orbit, respectively. The first follow-up observations by the Transiting Exoplanet Monitoring Project (TEMP) of HAT-P-33b confirmed the discovery parameters and detected no signs of TTVs (Wang et al. 2017).

We observed one transit of HAT-P-33b on 2012 April 6 with the Harris R filter (Fig. 4.1). We find a R-band R_p/R_* value that is larger by 3.4σ from the discovery R_p/R_*. Follow-up observations are need to determine the cause of this discrepancy.

4.5.5 HAT-P-37b

HAT-P-37b was identified by the HATNet survey and was confirmed by high-resolution spectroscopy and further photometric observations (Bakos et al. 2012). HAT-P-37b is a hot Jupiter with a planetary mass of 1.169±0.103 M_{Jup}, a radius of 1.178±0.077 R_{Jup}, and a period of 2.797436±0.000007 d. Additional follow-up observations by Maciejewski et al. (2016) confirmed these planetary parameters.

We observed two transits of HAT-P-37b on 2015 July 1 with the Harris B and R filters (Fig. 4.1). We derive an R_p/R_* for each filter that differ by 1.7σ, with a larger radius in the R band (Fig 4.6). The B-band R_p/R_* is smaller by 2.85σ from the near-IR R_p/R_* (Bakos et al. 2012). Our derived R-band R_p/R_* value agrees within 1σ of the Sloan i band value obtained by Bakos et al. (2012). Near-UV observations are needed to determine if the slope between the B and R filters is real or an unknown systematic in the data. Our other derived physical parameters agree with previous literature to within 1σ (Tables 4.4 and 4.5). We also calculate a refined period with a factor of 6 decrease in error.

4.5.6 WASP-2b

WASP-2b is a short-period hot Jupiter discovered by the WASP survey and confirmed by radial-velocity measurements taken with the SOPHIE spectrograph (Collier Cameron et al. 2007). Extensive photometry and radial velocity measurements have been performed on WASP-2b, further refining its system parameters (Charbonneau et al. 2007a; Daemgen et al. 2009; Southworth et al. 2010; Triaud et al. 2010; Albrecht et al. 2011; Zhang et al. 2011; Husnoo et al. 2012; Sada et al. 2012; Becker et al. 2013).

We observed WASP-2b on 2014 June 14 with the Harris B filter (Fig. 4.2). Our derived physical parameters and transit depth agree with previous literature to within 1σ and we calculate a period with a factor of 2 decrease in error (Tables 4.4 and 4.5).

4.5.7 WASP-24b

WASP-24b is a hot Jupiter detected by WASP and confirmed by radial velocity measurements and additional photometric observations (Street et al. 2010). Further photometric

studies calculated improved system parameters (Southworth et al. 2014) and radial velocity measurements were used to determine that the planet exhibits a symmetrical Rossiter-McLaughlin effect, indicating a prograde, well-aligned orbit (Simpson et al. 2011).

Our observations of WASP-24b took place on 2012 March 23 and 2012 April 6 (Fig. 4.2). We obtained two transits with the Harris R filter and each transit was modeled separately. The R_p/R_* of both dates overlap each other within 1σ. We then found the weighted average of the light curve parameters before deriving the physical parameters. Our weighted average R_p/R_* disagrees with previous R-band observations (Southworth et al. 2014) by 4σ (Fig 4.6). The cause of this difference is unknown but future observations can put better constraints on transit depth and solve this discrepancy. Our other derived parameters generally agree with previous results except for our planetary radius and equilibrium temperature, which differ from Southworth et al. (2014) by 1.4σ and 1.9σ, respectively (Tables 4.4 and 4.5). We calculate a new period with a factor of 2.6 decrease in error (Table 4.5).

4.5.8 WASP-60b

WASP-60b was identified by WASP-North and was confirmed by radial-velocity measurements and follow-up photometry (Hébrard et al. 2013). WASP-60b is an unexpectedly compact planet orbiting a metal-poor star.

We observed a transit of WASP-60b with the Harris B filter on 2012 December 1 (Fig. 4.2). This observation is the first follow-up light curve of WASP-60b. During observations, the automatic guider briefly failed, resulting in a gap in the transit light curve. Despite this, we are able to derive parameters that agree with previous literature to within 1σ (Tables 4.4 and 4.5). We find a B-band R_p/R_* value 1.3σ greater than the discovery R_p/R_*.

4.5.9 WASP-80b

WASP-80b is a warm Saturn/hot Jupiter ($M_p = 0.55 \pm 0.04 M_{jup}$) with one of the largest transit depths (0.17126±0.00031) discovered so far (Triaud et al. 2013). Multiple photometric studies have been done at various wavelengths to refine WASP-80b's planetary parameters (Fukui et al. 2014; Mancini et al. 2014; Triaud et al. 2015; Salz et al. 2015;

Sedaghati et al. 2017). The planet has a transmission spectrum consistent with thick clouds and atmospheric haze (Fukui et al. 2014).

We observed WASP-80b on 2014 June 16 with the Bessell U filter, obtaining one transit (Fig. 4.2). Inclement weather conditions caused our guider to briefly fail, resulting in a gap in the transit light curve. We derive physical parameters that closely agree with previous literature and also calculate a slightly a refined period with a factor of 2 decrease in error (Tables 4.4 and 4.5). Our observations possibly detect a TTV compared to previous work by 3.7σ (Section 4.4.1), however, further observations of WASP-80b are needed in order to confirm this result.

4.5.10 WASP-103b

WASP-103b is a hot Jupiter detected by the WASP survey with a mass of 1.49±0.09 M_{jup}, short period planet (P_p = 0.925542 ± 0.000019 d), and has an orbital radius only 20% larger than the star's Roche radius (Gillon et al. 2014). It was found that there is a faint, cool, and nearby (with a sky-projected separation of 0.242±0.016 arcsec) companion star of WASP-103 (Wöllert & Brandner 2015; Ngo et al. 2016). Further photometric observations were made to refine WASP-103b's planetary parameters and ephemeris (Southworth et al. 2015; Southworth & Evans 2016; Lendl et al. 2017). A comparison of observed planetary radius at different wavelengths found a larger radius at bluer optical wavelengths, but Southworth & Evans (2016) state that Rayleigh scattering cannot be the main cause even when including the contamination of the nearby companion star.

We observed WASP-103b on 2015 June 3 with the Bessell U filter (Fig. 4.2). We derive a dilution-corrected near-UV $\left(R_p/R_*\right)_{cor}$ that differs from the discovery value by 2.1σ. Our other calculated parameters agree with previous literature to within 1σ and our calculated period closely agrees with the period found by Southworth et al. (2015) (Tables 4.4 and 4.6). A variation in R_p/R_* is found from the ultraviolet to the near-infrared wavelengths (Fig 4.7) consistent with that found by Southworth & Evans (2016).

We correct for the dilution due to the companion star being in our aperture using the procedure described below (this procedure is similar to that done by Southworth & Evans 2016). (1) The light curve is modeled with EXOMOP and we find an uncorrected transit

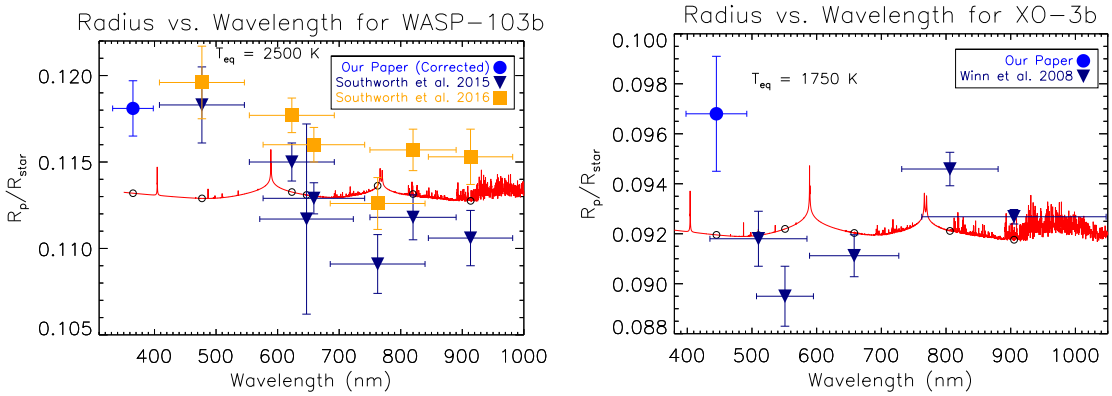

Figure 4.7: Plot of Rp/R_* against wavelength for WASP-103b and XO-3b from this paper and previous literature. Both WASP-103b and XO-3b show variations with wavelength. Other comments are the same as Fig. 4.6

depth of $\left(R_p/R_*\right)_{uncor}$ = 0.1174±0.0016. (2) Theoretical spectra of both stars is produced using ATLAS9-ODFNEW (Castelli & Kurucz 2004). For WASP-103 we use $T_{\rm eff}$ = 6110 K and M_{star} = 1.22 $M_\odot$ (Gillon et al. 2014) and for the companion star we use $T_{\rm eff}$ = 4405 K (Southworth & Evans 2016) and M_{star} = 0.721 $M_\odot$ (Ngo et al. 2016). Additionally, in order to scale the spectrum correctly we use the mass-lumnosity relation $L = L_\odot\,(M/M_\odot)^4$ for stars between 0.5 and 2 $M_\odot$. (3) The ATLAS9-ODFNEW model spectra is convolved with the bandpass of the Bessell U filter (Bessell 1979). (4) The corrected transit depth, $\left(R_p/R_*\right)_{cor}$, is found using the equation (Ciardi et al. 2015)

$$\left(\frac{R_p}{R_*}\right)_{cor} = \left(\frac{R_p}{R_*}\right)_{uncor} \sqrt{\frac{F_{tot}}{F_2}}, \tag{4.4}$$

where F_{tot} is the total flux of both stars and F_2 is the flux from the companion star. In Southworth & Evans (2016) the error of the photometric light curve dominated the error calculation of their corrected transit depth and therefore we also use our photometric error bars for the error in the $(R_p/R_*)_{cor}$. Using this procedure we find a $(R_p/R_*)_{cor}$ = 0.1181 ± 0.0016.

4.5.11 XO-3b

XO-3b is a massive planet (11.79±0.59 M_{Jup}) with a large eccentricity (0.26± 0.017) detected by the XO survey (Johns-Krull et al. 2008). Further photometric observations have refined the system's parameters (Winn et al. 2008a; Hirano et al. 2011; Machalek et al. 2010; Wong et al. 2014) and Hébrard et al. (2008) found that XO-3's spin axis is misaligned with XO-3b's rotation axis.

We observed a transit of XO-3b on 2012 November 30 with the Harris B filter (Fig. 4.3). We derive physical parameters that are in agreement with previous literature (Tables 4.4 and 4.6). Our calculated R_p/R_* is 2σ larger than the V-band R_p/R_* found by Winn et al. (2008a). We calculate a refined period with an error decreased by a factor of 13 from the value found by Winn et al. (2008a). A non-flat spectrum for R_p/R_* is found for XO-3b (Fig 4.7).

4.6 Discussion

4.6.1 Wavelength dependence on the transit depth

We find a constant transit depth across optical wavelengths for the TEPs HAT-P-5b, HAT-P-12b, WASP-2b, WASP-24b, and WASP-80b (Fig 4.6). A lack of variation in radius with wavelength could suggest these planets (HAT-P-5b, HAT-P-12b, WASP-2b, WASP-80b) have clouds/hazes in their upper atmospheres (e.g. Seager & Sasselov 2000; Brown 2001; Gibson et al. 2013b; Marley et al. 2013; Kreidberg et al. 2014) or they have an isothermal pressure-temperature profile (Fortney et al. 2006). Mancini et al. (2014) also do not detect a significant variation in WASP-80b's transit depth with wavelength, and Southworth et al. (2012b) finds a relatively flat spectrum of planetary radii for HAT-P-5b with the exception of their observed radius in the U-band (which they suspect is caused by systematic error in their U-band photometry). A flat spectrum for WASP-24b is also found with the exception of one value. Our R-band R_p/R_* found for WASP-24b differs by 4σ from the previously calculated R_p/R_* (Southworth et al. 2014) for that same band. The cause of this is unclear and future observations are needed to investigate. Our results are consistent with other transiting exoplanet observations having a flat spectrum in optical wavelengths

(i.e. TrES-3b, Turner et al. 2013; GJ 1214b, Bean et al. 2011; Kreidberg et al. 2014; WASP-29b, Gibson et al. 2013a; Gibson et al. 2013b; HAT-P-19b, Mallonn et al. 2015b; HAT-P-1b, HAT-P-13b, HAT-P-16b, HAT-P-22b, TrES-2b, WASP-33b, WASP-44b, WASP-48b, WASP-77Ab, Turner et al. 2016b).

We find variations in the transit depth with wavelength for CoRoT-12b, HAT-P-33b, HAT-P-37b, WASP-103b, and XO-3b (Fig 4.6-4.7), which could indicate scattering (i.e. due to aerosols or Rayleigh scattering) or absorption in their atmospheres (e.g. Benneke & Seager 2012; Griffith 2014). Our observation of HAT-P-37b exhibits a smaller transit depth in B-band than the red/near-IR value. Such a variation has only been seen in a recent paper by Evans et al. (2016) where they observe a smaller B-band transit depth than optical in WASP-121b. Evans et al. (2016) believe a possible cause of such a variation is TiO/VO absorption and this may also be the cause of the transit depth variations seen in HAT-P-37b. However, more theoretical modeling is needed to confirm that TiO/VO is in fact the opacity source. Additionally, a smaller near-UV radius was recently observed in the hot Jupiter WASP-1b (Turner et al. 2016b), however, these observations did not observe in the B-band. Future near-UV and blue-band observations are needed for WASP-103b and XO-3b to determine whether the scattering in their atmospheres is due to Rayleigh scattering (Lecavelier Des Etangs et al. 2008; Tinetti et al. 2010; de Wit & Seager 2013; Griffith 2014) since these bands are the only optical wavelengths not affected by strong spectral features. The radius variations in WASP-103b show a consistently larger transit depth in the near-UV and blue than the rest of the optical (this varation is still present when corrected for dilution due the companion star). Such a radius variation may indicate a change in particle size at different altitudes of the planetary atmosphere (e.g. Wakeford & Sing 2015). We find a larger R-band transit depth in HAT-P-33b and CoRoT-12b than their discovery transit depths. Since the R-filter encompasses the $H\alpha$ line (656.281 nm), our observation could be an indication of atmospheric escape such as that observed in the atmospheres of HD 189733b (Jensen et al. 2012; Cauley et al. 2015; Barnes et al. 2016; Cauley et al. 2017b; Cauley et al. 2017a) and HD 209458b (Astudillo-Defru & Rojo 2013) and predicted (e.g. Christie et al. 2013; Turner et al. 2016a). Follow-up photometry and high-resolution spectroscopy observations are encouraged to confirm all the transit depth variations. These results also agree with observations of other exoplanets not having a

flat spectrum (i.e. HD 209458b, Sing et al. 2008; HAT-P-5b, Southworth et al. 2012b; GJ 3470b, Nascimbeni et al. 2013; Qatar-2, Mancini et al. 2014; WASP-17b, WASP-39b, HAT-P-1b, WASP-31b, HAT-P-12b, HD189733b, WASP-6b, Sing et al. 2016; CoRoT-1b, TrES-4b, WASP-1b, WASP-12b, WASP-36b, Turner et al. 2016b).

For illustration, the observed R_p/R_* differences with wavelength for each target are compared to theoretical predictions (Fortney & Nettelmann 2010) for a model planetary atmosphere (Figure 4.6–4.7). The models used are calculated for planets with a 1 M_{Jup}, $g_p = 25ms^{-1}$ or $g_p = 10ms^{-1}$, base radius of 1.25 R_{Jup} at 10 bar, T_{eq} closest to the measured value for each exoplanet (with model choices of 500, 750, 1000, 1250, 1500, 1750, 2000, 2500 K), and solar metallicity. To provide a best fit to the spectral changes a vertical offset is added to the model. This comparison is helpful as it illustrates the size of observed variation compared to what the theoretical models predict. However, radiative transfer models calculated for each exoplanet individually are needed to fully understand their transmission spectra.

Finally, no signs of asymmetric transits are seen in the near-UV light curves of HAT-P-5b, WASP-80b, and WASP-103b. This result is consistent with ground-based near-UV observations of 19 other transiting exoplanets (Southworth et al. 2012b; Pearson et al. 2014; Turner et al. 2013; Bento et al. 2014; Copperwheat et al. 2013; Zellem et al. 2015; Turner et al. 2016b) that show no evidence of asymmetric transits. Additionally, theoretical modeling by Turner et al. (2016a) using the `CLOUDY` plasma simulation code showed that asymmetric transits cannot be detected in the broad-band near-UV band regardless of the assumed physical phenomena that could cause absorption (e.g. Vidotto et al. 2010a; Lai et al. 2010; Ben-Jaffel & Ballester 2014; Matsakos et al. 2015; Kislyakova et al. 2016).

Variability in the host stars

One of the major assumptions in our interpretation that the planetary atmosphere is the cause of the transit depth variations is that the brightness of the host stars have minimal variability due to stellar activity. The presence of star spots and stellar activity can produce variations in the observed transit depth (e.g. Czesla et al. 2009; Oshagh et al. 2013; Oshagh et al. 2014; Zellem et al. 2015; Zellem et al. 2017). This effect is stronger in the near-

UV and blue and can mimic a Rayleigh scattering signature (e.g. Oshagh et al. 2014; McCullough et al. 2014). No obvious star spot crossing is seen in our data (Figs. 4.1-4.3) with the possible exception of HAT-P-37b (see below).

We estimate how much the transit depth may change due to unocculted spots using the formalization presented by Sing et al. (2011). This method assumes that the spots can be treated as a stellar spectrum but with a lower effective temperature, no surface brightness variation outside the spots, and no plage are present. The effect of these assumptions are a dimming of the star and therefore an increase in the transit depth. Sing et al. (2011) find for HD 189733b that the change in transit depth due to unocculted spots, $\Delta\left(R_p/R_*\right) = 2.08 \times 10^{-3}/2\left(R_p/R_*\right)$ between 375–400 nm. Therefore, unocculted spots have minimal influence (assuming our host stars have unocculted spots similar to HD 189733b) on the observed transit depth variations since our final error bars (Table 4.4) are at least 10 times larger than the influence of these spots (e.g. the influence of unocculted spots would be $\Delta\left[R_p/R_*\right] = 0.00014$ for HAT-P-37b). Qualitatively, this result is consistent with the study by Llama & Shkolnik (2015) that find that stellar activity similar to the Sun has very little effect on the transit depth measured in near-UV to optical wavelengths. Nonetheless, we highly encourage follow-up observations and host star monitoring of all our targets to assess the effect of stellar activity on the observed transit depth variations.

Next, we investigate what effect a star-spot crossing in the light curve of HAT-P-37 would have on its calculated transit depth. In the B-band light curve of HAT-P-37b (Figure 4.1) there may be a star-spot crossing at a phase range of 0.004–0.008. However, the detected signal is very close to the scatter in the light curve. If we model the light curve without the possible star-spot crossing we find a $\left(R_p/R_*\right) = 0.1278 \pm 0.0048$, within 1σ of the transit depth of the entire light curve (0.1253±0.0021). McCullough et al. (2014) present a procedure to estimate the effects of unocculted spots on the transit depth. Their procedure can also be used to estimate the effect of star spot crossings on the transit depth, where instead of unocculted spots increasing the transit depth occulted spots should decrease it. McCullough et al. (2014) find that the change in transit depth due to spots, $\Delta(R_p^2/R_*^2)$, is

$$\Delta\left(\frac{R_p^2}{R_*^2}\right) = \left(\frac{R_p}{R_*}\right)^2 \delta \frac{T_{spot}}{T_{\rm eff}}, \tag{4.5}$$

where R_p/R_* is the unperturbed transit depth, δ is the fractional area of star spots, and T_{spot} is the temperature of the spot. If we set $\Delta(R_p^2/R_*^2)$ = 3100 ppm (the approximate difference between our B-band and the Sloan-i transit depth; Hartman et al. 2011), then we can estimate T_{spot} and δ. For spot temperatures between 2000–5000 K, we find that δ would be between 20 - 50 %. Typical values of δ for solar-like stars is around several % (e.g. Pont et al. 2008; Sing et al. 2011; McCullough et al. 2014), so our estimated δ range is extremely high. Due to both these tests, it seems unlikely that the smaller B-band transit depth of HAT-P-37b is due to an occulted star-spot.

4.7 Conclusions

We observed 11 transiting hot Jupiters (CoRoT-12b, HAT-P-5b, HAT-P-12b, HAT-P-33b, HAT-P-37b, WASP-2b, WASP-24b, WASP-60b, WASP-80b, WASP-103b, XO-3b) from the ground using near-UV and optical filters in order to update their system parameters and constrain their atmospheres. Our observations of CoRoT-12b, HAT-P-37b and WASP-60b are the first follow-up observations of these planets since their discovery and we also obtain the first near-UV light curves of WASP-80b and WASP-103b. We find that HAT-P-5b, HAT-P-12b, WASP-2b, WASP-24b, and WASP-80b exhibit a flat spectrum across the optical wavelengths, suggestive of clouds in their atmospheres. Variation in the transit depths is observed for WASP-103b and XO-3b and may indicate scattering in their atmospheres. Additionally, we observe a smaller B-band transit depth compared to near-IR in HAT-P-37b. Such a variation may be caused by TiO/VO absorption (Evans et al. 2016). We find a larger R-band (which encompasses the Hα line) transit depths in HAT-P-33b and CoRoT-12b and this result may indicate possible atmospheric escape. Follow-up photometry and high-resolution spectroscopy observations are encouraged to confirm all the observed transit depth variations since they are only significant at 2-4.6σ. Our calculated physical parameters agree with previous studies within 1σ with a few exceptions (Tables 4.5–4.6). For the exoplanets HAT-P-12b, HAT-P-37b, WASP-2b, WASP-24b, WASP-80b, and XO-3b we are able to refine their orbital periods from previous work (Tables 4.5–4.6).

Acknowledgments

J. Turner, R. Leiter, and R. Johnson were partially supported by the NASA's Planetary Atmospheres program. J. Turner and R. Leiter were also supported by the The Double Hoo Research Grant. J. Turner was also partially funded by the National Science Foundation Graduate Research Fellowship under Grant No. DGE-1315231.

We would like thank Robert T. Zellem for his help with observations. This research has made use of the Exoplanet Orbit Database (Wright et al. 2011), Exoplanet Data Explorer at exoplanets.org, Exoplanet Transit Database, Extrasolar Planet Transit Finder, NASA's Astrophysics Data System Bibliographic Services, and the International Variable Star Index (VSX) database, operated at AAVSO, Cambridge, Massachusetts, USA. This research has also made use of the NASA Exoplanet Archive, which is operated by the California Institute of Technology, under contract with the National Aeronautics and Space Administration under the Exoplanet Exploration Program.

Chapter 5

The search for radio emission from exoplanets using LOFAR low-frequency beam-formed observations: Data pipeline and preliminary results for the 55 Cnc system

"The cosmos is within us. We are made of star-stuff. We are a way for the cosmos to know itself." Carl Sagan

The text in this chapter is reproduced primarily from Turner J.D., Griessmeier J.-M., Zarka P., Vasylieva I. 2017. The search for radio emission from exoplanets using LOFAR low-frequency beam-formed observations: Data pipeline and preliminary results for the 55 Cnc system. Planetary Radio Emissions VIII. 301–313. arXiv:1710.04997.

5.1 Introduction

One of the most elusive goals in exoplanet science today is the detection of exoplanetary magnetic fields. Observations of an exoplanet magnetosphere would allow to pose con-

straints on planetary properties difficult to study such as their magnetic field strength and structure, rotation period, interior structure, atmospheric dynamics and escape, the presence of extrasolar moons, and the physics of star-planet interactions (Hess & Zarka 2011). The question of whether intrinsic magnetic fields, like those at Jupiter and Saturn, are present on gas giant exoplanets is critical because it greatly affects our understanding of their origins and evolution. Additionally, the deflection of stellar wind particles and cosmic rays due to Earth's magnetic field contribute to its habitability and this may also be the case for exoplanets (e.g. Grießmeier et al. 2015).

The most promising method to detect exoplanet magnetic fields is cyclotron radio emission observations because this method is not susceptible to false positives (Grießmeier et al. 2015, and references therein). However, many studies conducted to find exoplanet radio emission have resulted in non-detections (Zarka et al. 2015; Grießmeier et al. 2015; Grießmeier 2017 and references therein). A few studies find potential emission (Lecavelier des Etangs et al. 2013; Sirothia et al. 2014) but they remain unconfirmed. In this study, we will use for the first time the Low-Frequency Array (LOFAR) Low Band Antenna (LBA) in beam-formed mode to search for radio emission from exoplanets.

5.1.1 Predictions for radio emission from 55 Cnc e

A large amount of theoretical work has been done on predicting radio emission fluxes and maximum frequencies for exoplanets (Zarka et al. 2015; Grießmeier et al. 2015, and references therein). 55 Cnc was determined to be one of the best targets for radio observations due to advantages of a small orbital distance for 55 Cnc e (the inner-most planet), proximity, and planetary multiplicity (Grießmeier et al. 2007) and it shows hints of radio variability in UTR-2 data (V. Ryabov, personal communication). Theoretical predictions suggest the existence of decameter emission up to a few tens of MHz for 55 Cnc e and corresponding flux densities up to hundreds of mJy (Grießmeier et al. 2007; Nichols & Milan 2016). Additionally, 55 Cnc e is a transiting planet which will allow for the possibility of observing a planetary occultation in the radio domain (as done in Lecavelier des Etangs et al. 2013).

5.2 LOFAR Observations

We observed for 18 hours with LOFAR LBA (van Haarlem et al. 2013) in the frequency range 26-73 MHz with full-polarization in beam-formed mode. The observational setup can be found in Table 5.1. And example of a raw LOFAR dynamic spectrum can be found in Figure 5.1. The observations were performed during night/dawn time hours in order to avoid strong contamination by radio frequency interference (RFI). During the observations four digital core beams (FWHM: 7 arcmins at 60 MHz) within the station beam (FWHM: 10 degrees at 60 MHz) were recorded simultaneously on (1) 55 Cnc, (2) a patch of nearby empty sky, (3) the nearby pulsar B0823+26, and (4) a bright radio source (0858.1+2750; 30 Jy at 60 MHz). The extra beams make this setup unique since they can be used for control of instrumental effects, verify that a detection in the exoplanet beam is not a false positive detection (e.g. ionospheric fluctuations), and check the reliability of the data-reduction pipeline. Additionally, cyclotron radio emission observations are expected to be strongly circularly polarized and therefore the polarization information can be also used to verify a real signal. The theoretical sensitivity of the LOFAR observations is ∼16 mJy using the entire bandwidth and a 2-minute integration[1].

Table 5.1: Setup of LOFAR observations of 55 Cnc

Starting Frequency (MHz)	26
Ending Frequency (MHz)	73
Frequency Resolution (kHz)	3.05
Number of Subbands	244
Channels per Subband	64
Time Resolution (msec)	10.5
Total Observing Time (hours)	4.38
Number of LOFAR stations	24 (core)
Beams	target, pulsar, sky, bright source
Polarizations	IQUV

[1]The sensitivity (ΔS) was calculated using the sensitivity equation $\Delta S = S_{sys}\alpha/\sqrt{N(N-1)n_{pol}b\tau}$ where S_{sys} is the system equivalent flux density (SEFD) of an LBA core station (40 kJy, obtained from LOFAR calibration data; van Haarlem et al. 2013), N is the number of stations used, n_{pol} is the number of polarizations (2), b is the bandwidth, τ is the total time of observation, and α is a factor (equal to 1 for the calculated value) taking into account incoherent addition and flagging of data (see Section 5.5).

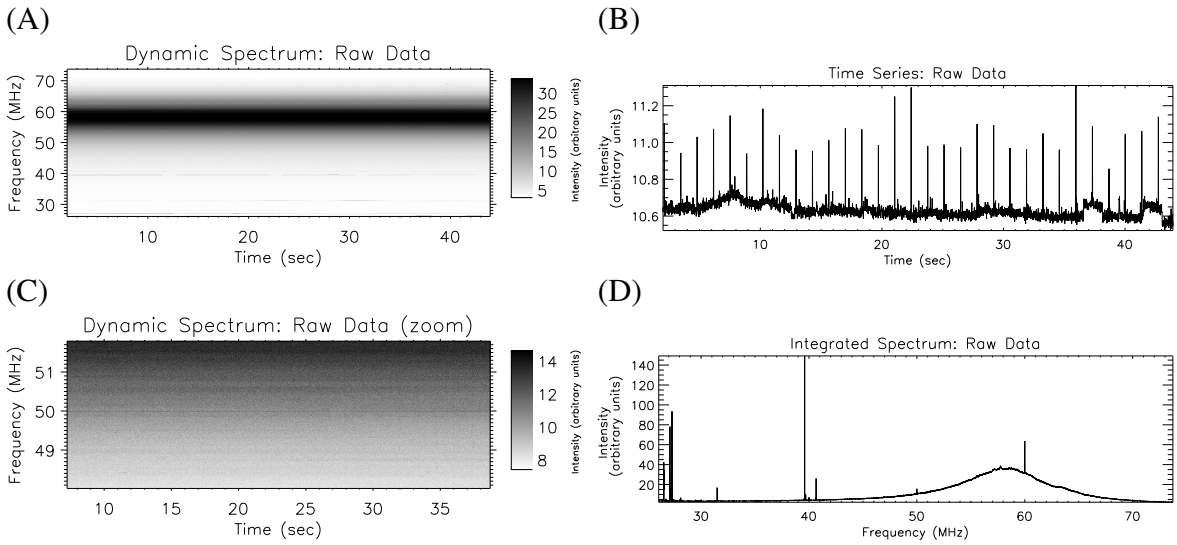

Figure 5.1: **(A)** Example dynamic spectrum of raw Obs #1 LOFAR data. **(C)** Zoomed in dynamic spectrum of panel A. Time series (**B**) and integrated spectrum (**D**) of the raw Obs #1 LOFAR data. The pronounced peak of the frequency response function at 58 MHz is easily seen in the dynamic spectrum and the integrated spectrum. RFI is also easily identifiable as bright spikes in all plots.

5.3 Data Pipeline for LOFAR Observations

We created a pipeline that automatically corrects the data for instrumental effects and finds and masks RFI. This pipeline was adapted from the one created by Vasylieva (2015) to search for radio emission from exoplanets using the radio telescope UTR-2. A flow chart of the pipeline can be found in Figure 5.2. The pipeline consists of three main parts: RFI mitigation, finding the time-frequency telescope response, and applying the corrections found in the first two steps to the data. We will describe each part of the pipeline in greater detail below.

5.3.1 RFI Mitigation

RFI mitigation is the most crucial step in the pipeline since RFI dominates the signal in the low-frequency data and hinders detection of faint astrophysical signals. The RFI mitigation pipeline consists of the following steps: (1) divide the raw data into slices of 42 seconds (4000 spectra), (2) find the frequency response function and divide the data by this function,

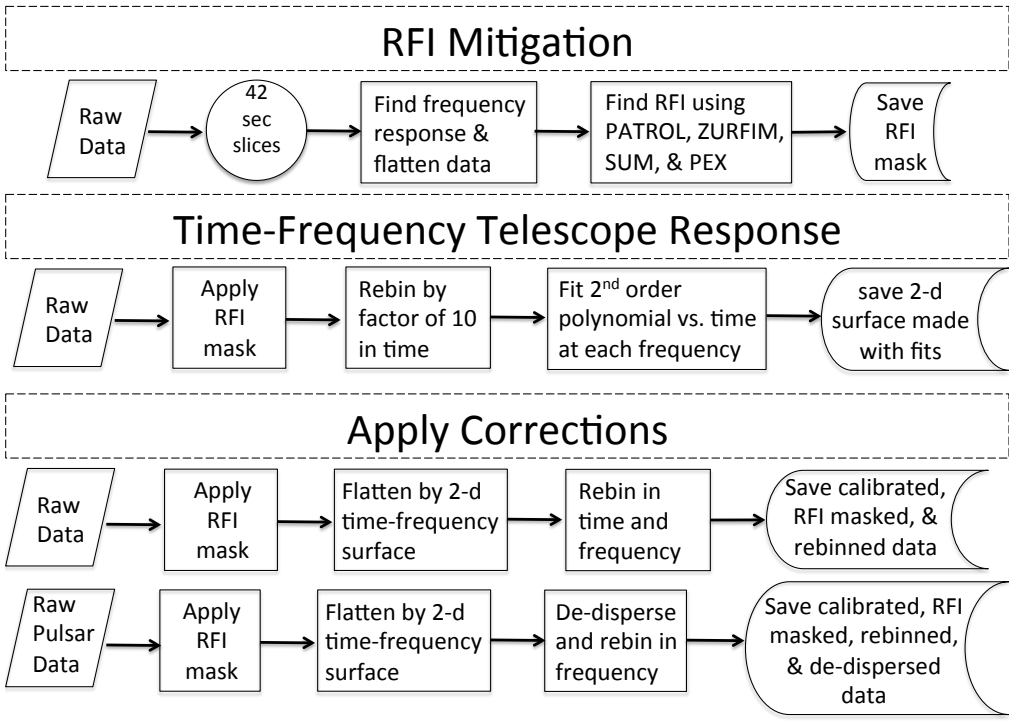

Figure 5.2: Flow chart of the main parts of the pipeline: RFI mitigation, finding the time-frequency telescope response, and applying these corrections to the data.

(3) find RFI, and (4) save the location of the RFI into a mask, an array the same dimensions as the data with a value of 0 (polluted pixels) and 1 (clean pixels) weight. An example of the RFI mitigation can be found in panel A of Figure 5.3. It can be seen that the pipeline is very efficient at finding and masking the brightest RFI. Examining the dynamic spectrum, the integrated spectrum, the time-series (panel C of Figure 5.3), and the fast Fourier transform (FFT) of the pulsar (Section 5.4; panel B of Figure 5.3) after RFI mitigation shows that minimal RFI is left-over in the data. In total, we mask out ~3% of the data. The standard deviation of the data after RFI mitigation decreases by a factor of ~100.

Step (1) and step (2) are required because the dynamic spectrum should not contain any large-scale variations in time and frequency in order to correctly apply step (3). Using only 42 second slices (4000 spectra) in step (1) guarantees that any changes in time are small. Step (2) allows for both the correct identification of RFI located on the outer edges of the response function and not introducing false-positive detections of RFI near the peak

response of the telescope. The frequency response function in step (2) is created using the 10% quantile of the distribution of intensities at each frequency because the 10% quantile is relatively robust against RFI.

Step (3) consists of 4 RFI mitigation techniques (Offringa et al. 2010; Offringa 2012; Zakharenko et al. 2013; Vasylieva 2015, and references therein) combined together for optimal efficiency and processing time: PATROL (Pulsars And TRansients Overall Lookup), ZURFIM (Ze Ultimate RFI Mitigator), SUM (SumThreshold), and Polluted pixel EXpansion (PEX). Each of these techniques uses sigma thresholding (above which the samples are flagged) in the time-frequency domain. After each RFI method is ran, the code updates the mask, and then only runs the next RFI method on the remaining good data. The 4 RFI techniques are described in greater detail below. The first two methods PATROL and ZURFIM both flag whole bad frequency channels and time intervals in the dynamic spectrum (Zakharenko et al. 2013; Vasylieva 2015). These techniques are useful for finding RFI caused by broadcasting radio stations either local or reflected from the ionosphere which results in contaminated frequencies for the entire time interval. Additionally, they can also find short wide-band RFI spikes at all frequencies caused by telescope equipment, vehicles, lightning, or other natural sources. These programs identify RFI using values of the mean (μ) and standard deviation (σ) of each channel. PATROL uses the spectrum integrated over all time to flag bad frequencies and the time-series integrated over all frequencies to flag bad channels, whereas ZURFIM uses the spectrum for each time channel and the time-series for each frequency channel and loops through all times and frequencies. Any frequency channel or time interval with a σ above the sigma thresholding value is flagged (PATROL and ZURFIM do not necessarily have the same thresholding value). The process is iterative until there are no more peaks to exclude.

The third method SUM (Offringa et al. 2010, it is also used as the default RFI mitigation pipeline for LOFAR visibilities) is designed to only flag small patches in the time or frequency direction. A combination of n samples is entirely flagged if its average exceeds the threshold T_n (in units of σ). T_n is equal to $T_n = T_1/a^{\log_2 n}$, where T_1 is the threshold for a single pixels ($T_1 = 10$ for default), a is an empirical coefficient ($a = 1.5$), and n is the size of the sliding window (in powers of 2). The program runs multiple times depending on how many values of n are supplied. The time and frequency directions are run independently

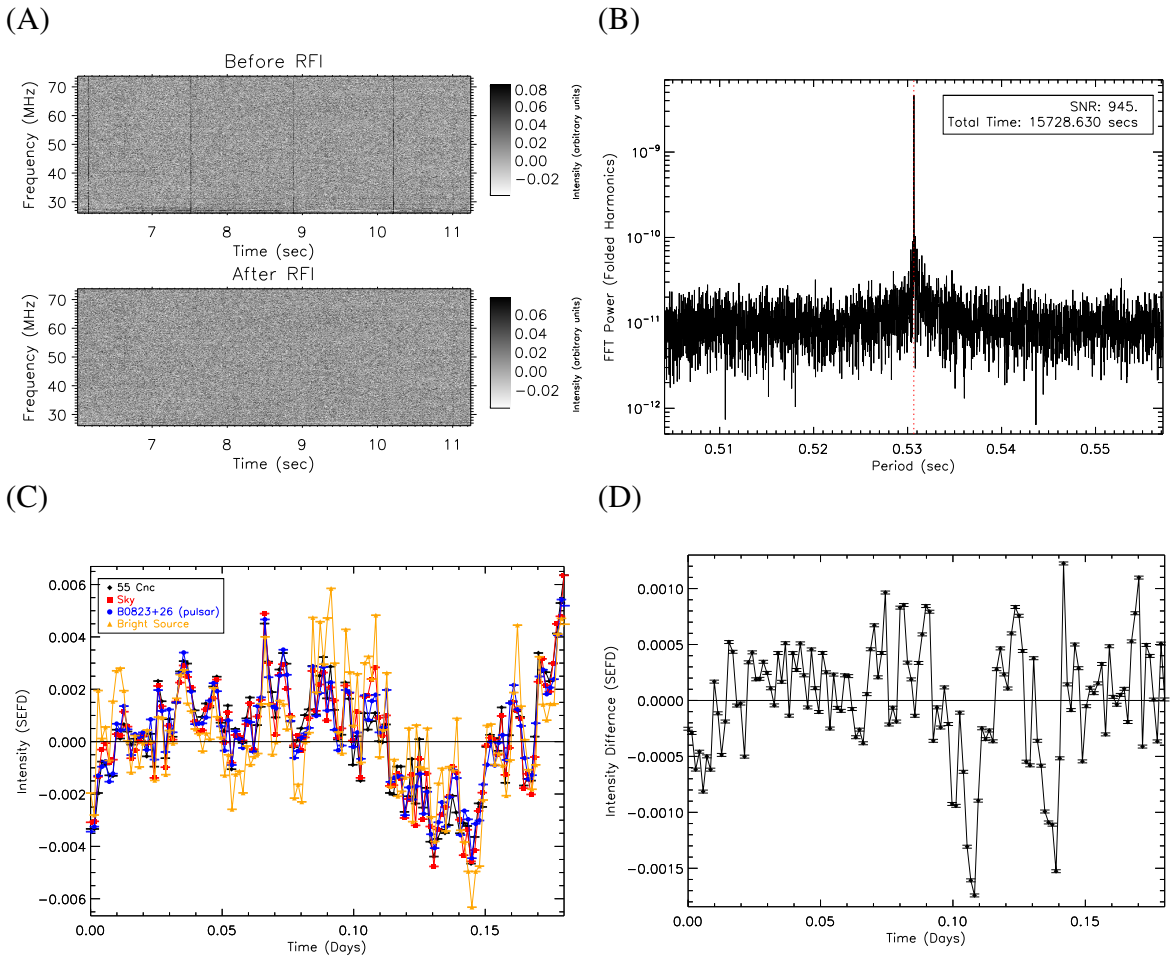

Figure 5.3: Results of the pipeline for Obs #1. **(A)** An example of the normalized dynamic spectrum before and after RFI mitigation. The RFI has been masked and set to the median of the data not containing RFI. **(B)** FFT of the pulsar B0823+26. The known period of the pulsar is marked as a dashed red line and we recover the known period with a signal-to-noise ratio of ~945. **(C)** Time-series of the intensity of all the beams. The intensity was found by integrating over the entire bandwidth (47 MHz) and rebinning to 2 minute intervals. The beams are 55 Cnc (black), sky (red), B0823+26 (blue), and bright source (orange). All curves have been subtracted by one. All beams are similar but we observe scintillation in the bright source. **(D)** Time-series of the intensity difference of the 55 Cnc and sky beam. These two beams are similar and oscillations due to the ionosphere are visible. No bursty radio emission from 55 Cnc is seen.

and then the masks are multiplied together at the end.

The fourth RFI method PEX is very simple. The method just expands the polluted

pixels in the mask by a certain number of pixels in both the time and frequency direction. The program also has the option to only expand patches of interconnected bad pixels of a certain size. This method is useful because strong RFI may contain weaker edges that might be missed by the other methods. PEX is very similar to the Scale Invariant Rank technique (SIR; Offringa 2012) but is simpler and thus computationally much faster.

5.3.2 Time-Frequency Telescope Response

The next part of the pipeline is designed to find the time-frequency response of the telescope. During the development of the pipeline, we found that the frequency response of the telescope changes with time and is different for every beam. These variations are caused by the shape of the beams changing while tracking the different sources. In the pipeline we (1) apply the RFI mask from Section 5.3.1 to the raw data, (2) rebin each slice in the time dimension by a factor of 10, (3) find a second order polynomial fit at each frequency over the entire rebinned and RFI masked data, and (4) create and save the 2-d time-frequency response surface made from these polynomial fits. Step (2) is used to avoid biasing the polynomial fit with any short-term variability and to reduce computational memory. One of the limitations of the above procedure is that any constant or slowly varying signal will change the 2-d time-frequency response function, and thus get removed when we normalize by this function. However, this is not a problem for bursty signals such as the one we expect from an exoplanet.

5.3.3 Apply Corrections

The last part of the pipeline applies the corrections to the data. For every beam except the pulsar beam we (1) apply the RFI mask from Section 5.3.1 to the raw data, (2) flatten the RFI masked data by dividing by the 2-d time-frequency response surface from Section 5.3.2 (now the data are in units of the SEFD), (3) rebin the calibrated and RFI masked data in time and frequency, and (4) save the calibrated, RFI masked, and rebinned data. For the pulsar beam, we perform step (1) and (2) above, (3) de-disperse the data using the pulsar's known dispersion measure and rebin in frequency, and (4) save the calibrated, RFI masked, de-dispersed, and rebinned data. For all the beams excluding the pulsar beam we rebin to a

spectral and time resolution of 45 kHz and 1 second, respectively. For the pulsar beam, the data is rebinned to a spectral resolution of 1 MHz and kept at a time resolution of 10 msec.

5.4 Results

With the calibrated and RFI masked data we can now search for bursty astrophysical signals. The main signals in our data are the pulsar, scintillation of the bright source, ionospheric variations in the sky beam, and any emission from the exoplanet. Each of these signals is described below.

The pulsar (B0823+26[2]) beam is useful because the signal is faint, astrophysical in nature, and can be used to test the reliability of the pipeline. In order to detect B0823+26 we (1) perform an FFT on the calibrated, RFI masked, de-dispersed, and rebinned data and (2) add together the 6 first harmonics in the power spectrum. The FFT was computed using data from 35-49 MHz. If we perform an FFT on the de-dispersed data without masking the RFI, the pulsar is not detected. Thus RFI mitigation is a necessary step in the analysis. We use the pulsar beam to test different tunable parameters in the pipeline such as the thresholding values for the RFI mitigation. The pipeline RFI-mitigation parameters that maximized the FFT power were used for all the beams. An example of an FFT performed on Obs #1 can be found in panel B of Figure 5.3. The pulsar is detected at its known period with a very high signal-to-noise ratio (SNR_{FFT}) of ~945.

Next, we can search for astrophysical signals in our data by plotting the time series of the dynamic spectrum integrated over all frequencies. The time-series of all the beams for Obs #1 can be found in panel C of Figure 5.3. Each beam's intensity was found by integrating over the entire bandwidth (47 MHz) and rebinning to 2 minute intervals. The intensity is in units of the SEFD and to emphasize the variations we also subtract 1 from the data. The SEFD at 30 MHz is approximately equal to the sky background but at 70 MHz it is ~2x the sky. Scintillation of the bright source is seen in the time-series (orange curve in panel C of Figure 5.3). We can only see fluctuations in the bright source's flux and not its average flux due to the way we constructed the time-frequency normalization curve (see Section 5.3.2). The target and sky beams behave roughly the same suggesting similar

[2]All physical information for B0823+26 was taken from the ATNF Pulsar Catalogue (Manchester2005).

but not identical ionospheric conditions. Panel D of Figure 5.3 shows the time-series of the difference between the black (target beam) and red (sky beam) curves of panel C. The variations in the 55 Cnc and sky beam are due to changes in the ionosphere. There are no positives peaks above 2σ, therefore, we do not detect any emission from the exoplanet. However, there are negative peaks above 2σ. This result suggests that we need to have 2 OFF sky beams in future observations to verify that a detection is not a false-positive.

5.5 Discussion

Even though we do not detect any radio emission from the 55 Cnc system, we can still place upper limits on its radio emission. This can be done independently using both the FFT of B0823+26 (panel B of Figure 5.3) and the time-series intensity difference of 55 Cnc to the sky beam (panel D of Figure 5.3).

The upper limit using the pulsar is obtained using the following procedure. The sensitivity of the observations ($\sigma \sim S_{pulsar}/SNR$) can be estimated using the SNR of the pulsar in the time domain and its intrinsic flux measured at the wavelengths observed (S_{pulsar}). However, the SNR_{FFT} in the Fourier domain is not the same as the SNR in the time domain. Therefore, we need to determine a conversion factor between the two. We run simulated pulsar data (random Gaussian noise + pulse, same time and frequency resolution of our data, same time interval) and adjust the pulse/noise ratio to reproduce the SNR_{FFT} of the FFT. We find that a pulse/noise ratio of 0.15 (pulse amplitude = 0.15σ) corresponds to the observed SNR_{FFT} ~945 in the FFT ($SNR_{FFT} \sim 6330\ SNR$). Therefore, the sensitivity of the observations over any time scale (τ) is

$$\sigma(\tau) \approx 6330 \frac{S_{pulsar}}{SNR_{FFT}} \left(\frac{0.0105 \text{ sec}}{\tau} \right)^{1/2} . \tag{5.1}$$

In order to obtain the flux of B0823+26 (S_{pulsar}), we have taken a series of observations using the LOFAR station FR606 in stand-alone mode. The observations were taken in the LBA band (we used data from 50-90 MHz) and flux-calibrated using the method described in Kondratiev et al. (2016); however, we used the beam model 'Hamaker-Carozzi' instead of the 'Hamaker' beam model. With this, the median flux of B0823+26 over 13 observa-

tions was measured as 1210±150 mJy. Using equation (5.1), we find a 3-sigma upper limit of 230 mJy for 55 Cnc for an integration time of 2 minutes and over the entire bandwidth. The advantage of using the FFT for the noise calculation is that any effects (ionosphere, left over instrumental systematics, low-level RFI) not periodic with the pulsar's period do not affect the outcome of the FFT. The 1-sigma sensitivity estimated with the pulsar (~76 mJy) is a factor of ~5 higher than the theoretical sensitivity of LOFAR (16 mJy; Section 5.2) and this factor likely arises from imperfect coherent addition of the station signals and the RFI flagging of data (LOFAR Astronomer's website on Beam Formed Mode[3]).

Next, we can estimate the upper limit using the time-series of the intensity difference between the target and sky beam. The standard deviation in this time-series is ~0.0005 of the SEFD (panel D of Figure 5.3; Figure 5.4). The SEFD from 30-70 MHz for 24 LOFAR stations is 1.7 kJy (the SEFD from one station is 40 kJy; van Haarlem et al. 2013). Therefore, the 1-sigma and 3-sigma sensitivity from these observations would be ~850 mJy and 2.6 Jy, respectively. This 1-sigma limit is ~11 times greater than the sensitivity limit derived using the pulsar (~76 mJy) and ~50 times greater than the thermal noise (~16 mJy; Section 5.2). From this factor of 11, a factor ~ $\sqrt{2}$ comes from the fact that Figure 5.3D is a difference between the fluctuations of the target and sky beams. Part of the factor of $11/\sqrt{2} \sim 8$ may be caused by observing close to the Galactic plane, which is brighter than the high Galactic latitudes. Although 55 Cnc is not in a very bright region of the Galactic plane (see LFmap model from Polisensky 2007). We believe that a large part of this factor of ~8 is due to the different fluctuations of the ionosphere between the two beams. This suggests that the ionosphere substantially varies at an angular scale of a few degrees. Rebinning to different times does improve the standard deviation but only slightly and not with a $t^{-1/2}$ white noise dependence (Figure 5.4). Using the time-averaging method (e.g. Pont et al. 2006, Turner et al. 2016b), we find that there is a substantial amount of red noise (RMS of red noise ~ 0.5 RMS of white noise) in the time-series. Therefore, this indicates that non-Gaussian ionospheric variations are present in the data over many timescales (at least between 1 and a 1000 seconds). The 3-sigma upper limit is also 25 times larger than the theoretically predicted flux density of ~100 mJy for 55 Cnc e (Grießmeier

[3]http://www.astron.nl/radio-observatory/observing-capabilities/depth-technical-information/major-observing-modes/beam-form

et al. 2007; Nichols & Milan 2016; Grießmeier 2017). Hence, with this upper limit it is not yet possible to put strong constraints on the theoretical emission models.

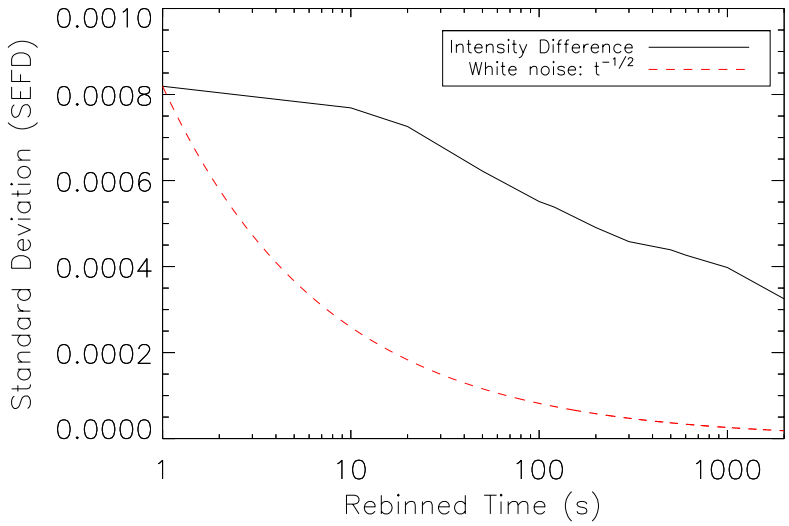

Figure 5.4: Standard deviation of the intensity difference between the target and sky beam for different rebin times (starting at 1 sec). The red dashed curve shows the theoretical white noise curve assuming the noise decreases by $t^{-1/2}$ (the curve starts at the measured standard deviation for a 1 sec rebin time).

Our results suggest that LOFAR LBA beam-formed observations may not be sensitive enough to detect exoplanetary radio emission due to many effects (large SEFD, non-coherent summation, differential ionospheric variations) with the current setup. The large ionospheric variations severely limit the detection capability using only 2 beams. Therefore, three beams (ON and 2 OFF) may be necessary to verify any possible detections against false-positives. Future exoplanet beam-formed observations with LOFAR will be performed with this new setup. Finally, we will more accurately quantify the sensitivity that LOFAR LBA beam-formed observations can reach in an upcoming study using LOFAR observations of Jupiter scaled such that it simulates exoplanetary radio emission (Turner et al. in prep).

5.6 Conclusion

In this paper we present LOFAR Low Band Antenna beam-formed observations of the exoplanetary system 55 Cnc at 26-73 MHz. This is the first published paper on the search for exoplanet radio emissions using beam-formed observations from LOFAR. We created an automatic pipeline to flatten the LOFAR data by the time-frequency response of the telescope, find and mask RFI, and to search for astrophysical signals in our data. During the observations four beams were recorded simultaneously on 55 Cnc, a patch of nearby "empty" sky, the nearby pulsar B0823+26, and a bright constant radio source. The extra beams are used to monitor the time-frequency response of the telescope and ionospheric variability, and to verify the reliability of the pipeline. The pipeline was extensively tested and we found the data to be stable and sensitive enough to detect astrophysical signals from the pulsar and scintillation from the bright source.

Initial analysis of 4 hours of LOFAR data do not show an exoplanet signal. We find a 3-sigma upper limit for the 55 Cnc system of 230 mJy using analysis of the pulsar to estimate the sensitivity and 2.6 Jy using the difference between the integrated time-series of the target and sky beam. These upper limits are a factor of ~5 and ~50 greater than the theoretical sensitivity. The factor of 5 for the pulsar is likely due to imperfect coherent addition of station signals (that also applies to the target-sky beam) and possibly residual RFI. The additional factor of ~11 that affects the target-sky beam is attributed for a large part to large-scale differential variations of the ionosphere between the two beams. This result suggests that the ionosphere substantially varies at an angular scale of a few degrees. Therefore, in all future exoplanet beam-formed observations with LOFAR we will observe with three beams (one ON beam and two OFF beams) to decrease the detection of false-positives. Additionally, 55 Cnc is located on the Galatic plane which likely contributes an additional factor to the sensitivity calculation.

The findings in this study suggest that LOFAR LBA beam-formed observations may not be sensitive enough to detect exoplanetary radio emission or place strong constraints on model predictions. In the future, we will use our pipeline to analyze the full data set of the 55 Cnc observations, more accurately determine the sensitivity LOFAR can reach using Jupiter as a proxy for exoplanetary radio emission, and search for radio emission from

other exoplanets predicted to have detectable radio emission. Finally, the techniques in this paper can be used to analyze beamformed data from future ground-based low-frequency radio telescopes (NenuFAR, LOFAR 2.0, SKA) or reconstructed dynamic spectra from the visibilities of imaging data (Loh et al. in prep).

Acknowledgements

J. Turner was funded by the National Science Foundation Graduate Research Fellowship under Grant No. DGE-1315231. We also thank PNP and PNST for their support. This research has made use of the Exoplanet Orbit Database, Exoplanet Data Explorer at exoplanets.org (Han et al. 2014), Extrasolar Planet Encyclopaedia (exoplanet.eu) maintained by J. Schneider (Schneider et al. 2011), NASA's Astrophysics Data System Bibliographic Services, and the ATNF Pulsar Catalogue (Manchester et al. 2005) located at http://www.atnf.csiro.au/research/pulsar/psrcat. We thank Louis Bondonneau for help with the flux calibration of B0823+26. Finally, we thank the referees, whose comments helped to improve this paper.

Chapter 6

The search for radio emission from exoplanets using LOFAR beam-formed observations: Jupiter as an exoplanet

"We are part of this universe; we are in this universe, but perhaps more important than both of those facts, is that the universe is in us." Neil deGrasse Tyson

The text in this chapter is reproduced primarily from Turner J.D., Griessmeier J.-M., Zarka P., Vasylieva I. 2018. The search for radio emission from exoplanets using LOFAR beam-formed observations: Jupiter as an exoplanet. A&A (submitted). arXiv:1802.07316

6.1 Introduction

The detection and characterization of exoplanetary radio emission would constitute a new and important field of exoplanet science. For example, the detection of planetary auoral radio emission is probably the only method to unambiguously detect exoplanetary magnetic fields (Grießmeier 2015). To date, no confirmed radio detection has been achieved, even though a certain number of observations have been conducted over the past few decades (e.g. Winglee et al. 1986; Bastian et al. 2000; Ryabov et al. 2004; George & Stevens 2007; Lazio & Farrell 2007; Smith et al. 2009; Lecavelier Des Etangs et al. 2009, 2011;

Lazio et al. 2010; Stroe et al. 2012; Hallinan et al. 2013; Lecavelier des Etangs et al. 2013; Sirothia et al. 2014; Murphy et al. 2015; Lynch et al. 2017; Turner et al. 2017a). A summary of all the observational campaigns can be found in Grießmeier (2017, Table 2). In parallel to observational studies, a number of theoretical work has been published (e.g. Zarka et al. 1997; Farrell et al. 1999, 2004; Zarka et al. 2001; Lazio et al. 2004; Stevens 2005; Grießmeier et al. 2005; Grießmeier et al. 2007; Jardine & Collier Cameron 2008; Vidotto et al. 2010b, 2015; Vidotto & Donati 2017; Hess & Zarka 2011; Nichols 2011, 2012; See et al. 2015; Nichols & Milan 2016); an overview is given, e.g., in recent review articles such as Zarka (2011); Zarka et al. (2015); Grießmeier (2015, 2017).

Starting with Zarka et al. (1997) and Farrell et al. (1999), a number of articles have attempted to estimate the radio flux density that can be expected for different types of exoplanets. Of course, such estimates have to be taken carefully. For example, Grießmeier et al. (2007) give uncertainties of approximately one order of magnitude for the flux density and an uncertainty of a factor of 2-3 for the maximum emission frequency for the planet Tau Boötis b. The uncertainties are even larger when different models are compared. Still, such numbers can be used to determine whether the detection of exoplanetary auroral radio emission seems realistic with a given radio telescope and observational setup. Indeed, according to most recent estimates, emission frequencies are compatible with the frequencies at which some radio telescopes of latest generation operate, and estimated flux densities are close to the sensitivity of these instruments. In particular, Grießmeier (2017) find that the flux densities of 15 exoplanets are above the theoretical detection limit of LOFAR as given by Turner et al. (2017a).

With such encouraging radio predictions, radio observations of exoplanets are undertaken by most low-frequency radio telescopes. For these observations, different observing modes and strategies can be used. In the following, we will differentiate between (a) imaging observations and (b) beam-formed observations. Many recent observations (e.g. Hallinan et al. 2013; Sirothia et al. 2014; Lynch et al. 2017) have been recorded in the form of interferometric images using an array of distributed antennas or dishes (e.g. GMRT, LOFAR). Interferometric observations have the advantage of a higher robustness against localized (i.e. site-specific) Radio Frequency Interference (RFI), and are equally sensitive to continuous and moderately bursty signals (i.e. longer than the shortest time constant

in imaging pipelines, typically a few seconds; e.g. Offringa et al. 2014). They are computationally expensive, but offer the possibility to exclude a bad antenna or dish from the analysis even during offline processing. Beam-formed observations have the advantage of a higher time resolution, which can be used to localize and excise short and sporadic RFI more precisely. They cannot reliably detect continuous or slowly varying emission, but excel at the detection of short bursty signals. Compared to imaging observations, only a handful of pixels have to be analyzed, which reduces the computational cost: Typical observations use 1 ON-beam and 1 to 3 OFF-beams, see e.g. Zarka et al. (1997) or Turner et al. (2017a).

For both imaging and beam-formed observations, the determination of a minimum detectable flux density is not straightforward in the case of a bursty signal. The reason for this is that the upper limit depends on the detection method. In this work, we present a detection tool that integrates the processing steps described in Turner et al. 2017a (RFI-mitigation, normalization by the time-frequency (t-f) response function, t-f integration) and a series of sensitive observables based on the work of Vasylieva (2015). In order to test, validate, and quantify the sensitivity reached with this tool, we apply it to a LOFAR observation of Jupiter's magnetospheric radio emission in which the signal from Jupiter is attenuated. The idea is simple: we observe Jupiter, divide its signal by a fixed factor before adding it to an observation of "sky background", thereby creating an artificial dataset best described as "Jupiter as an exoplanet". We then run our pipeline and check whether the (attenuated) radio signal from Jupiter is detected. The maximum factor by which we can divide Jupiter's signal and still achieve a detection gives the sensitivity of our setup (i.e. the combination of the telescope and the processing chain). This method is mainly designed for use with beam-formed data, but an extension to radio imaging observations is under preparation and will be described elsewhere (Loh et al. in prep).

Finally, the instantaneous flux density of Jupiter was obtained from a well-calibrated observation using the Nancay Decameter Array (NDA; Boischot et al. 1980; Lamy et al. 2017) simultaneous to our LOFAR observation of Jupiter. The NDA observation is used to convert the sensitivity of our setup into physical units.

6.2 Observations

For this study, we use four different sets of Low-Frequency Array (LOFAR; van Haarlem et al. 2013) Low Band Antenna (LBA) beam-formed observations in the frequency range 15–62 MHz. The detailed setup and the summary of all observations (date, time, and beam directions) can be found in Table 6.1 and 6.2, respectively. Although full-polarization information was obtained, we only focus on the Stokes-I component in this paper. Analysis of the polarization data will be presented in a follow-up paper as an extension of the present study and will be applied to all exoplanet radio observations. All observations were intentionally scheduled during night time hours to mitigate strong contamination by RFI. The first observation (hereafter Obs #1) was taken on February 11, 2017 from 02:30 to 5:30 UT and the ON-beam was pointed at Jupiter. The dynamic spectrum of this beam can be found in Fig. 6.1a. The structure of the Jupiter emission is very complex and the analysis of this structure (e.g. Burke & Franklin 1955; Carr et al. 1983; Zarka 1998; Kaiser 1993; Imai et al. 2015) is beyond the scope of this study. As expected, Jupiter's emission is only seen below 40 MHz in the observation (Marques et al. 2017).

Due to its anisotropic beaming, Jupiter's emission is visible from Earth only ~10% of the time. It does not, however, occur randomly, but depends on the geometrical position of the Earth, Jupiter, and Jupiter's satellite Io, as expressed by Io's orbital phase and the CML (Central Meridian Longitude = the observer's Jovicentric longitude). Statistical studies have identified times when the probability of detecting Jupiter's decametric emission from Earth is > 50%, (Marques et al. 2017), and for a specific geometry (so-called Io-B emission), the occurrence rate reaches 94% (i.e. nearly permanent emission) (Zarka et al. 2017). To determine a good time window for Obs #1, we made use of the Io-phase/CML diagrams provided by Nançay Radio observatory[1].

Two OFF-beams were obtained simultaneously with the ON-beam, however, the OFF-beams show strong contamination by emission from Jupiter despite being located ~ 2 degrees away from Jupiter. Therefore, a second observation to obtain "clean" OFF-beams was taken on February 18, 2017 from 01:12 to 4:12 UT (hereafter Obs #2). Obs #2 will be used as the "sky background" to which we will add the attenuated Jupiter signal. Two

[1] https://realtime.obs-nancay.fr/dam/data_dam_affiche/data_dam_affiche.php?init=1&lang=en&planete=jupiter

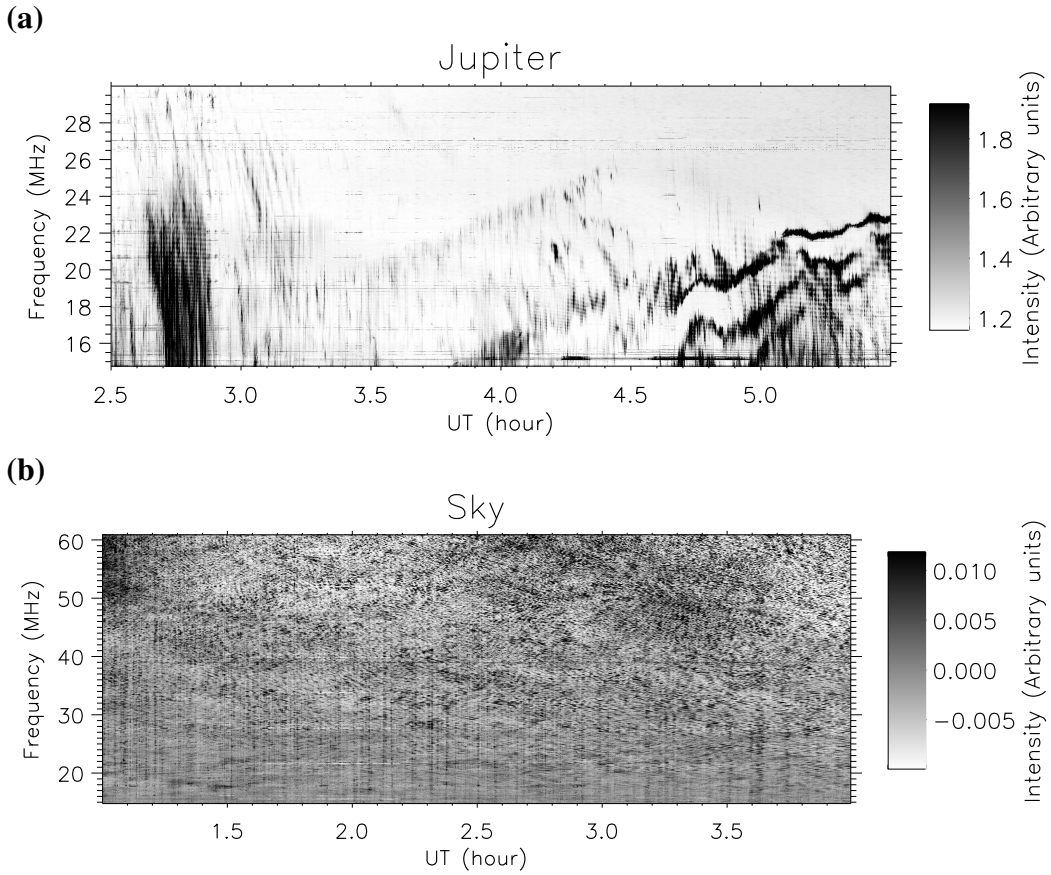

Figure 6.1: Dynamic spectrum with LOFAR LBA of Jupiter in Obs #1 (**a**) from 15 to 30 MHz and of the OFF-beam 1 in Obs #2 (**b**). These observations are normalized by an average value of the background at each frequency. In Obs #1, there was no emission of Jupiter occuring above 30 MHz.

OFF-beams were obtained and the beams' positions were chosen such that no point sources were located within the beam. For this we used the TGSS survey (Intema et al. 2017) at 150 MHz. The dynamic spectrum of one of the OFF-beams can be found in Fig. 6.1b.

While most of the analysis was done using Obs #2 for the "sky background", we also used two other dates of observations with two OFF-beams to verify our results. The third dataset was taken on February 26, 2017 from 01:16 to 04:16 UT (hereafter Obs #3) and was pointed at the same OFF-beam positions as Obs #2. This date had far worse RFI conditions than Obs #2 and also had noticeable large-scale scintillation due to a disturbed ionosphere. The fourth dataset was taken on September 28, 2016 from 23:00 to 04:00 UT

Table 6.1: Setup of the LOFAR LBA beam-formed observations used in this work

Parameter	Value	Units
Array Setup	Core	
# of Stations	24	
Lower Frequency	14.7	MHz
Upper Frequency	62.4	MHz
Channel Bandwidth (b)	3.05	kHz
# of Subbands	244	
Channels per Subband	64	
Time Resolution (τ_r)	10.5	msec
Angular Resolution at 45 MHz	9.2	arcmin
Raw Sensitivity[a] (ΔS)	208	Jy
Polarizations	IQUV	

[a] The theoretical (thermal noise) sensitivity (ΔS) was calculated using the sensitivity equation $\Delta S = S_{sys}/(N\sqrt{n_{pol}\tau_r b})$, where S_{sys} is the system equivalent flux density (SEFD) and equal to 40 kJy (obtained from LOFAR calibration data; van Haarlem et al. 2013), N is the number of stations used, n_{pol} is the number of polarizations (2), b is the channel bandwidth, and τ_r is the time resolution.

(hereafter Obs #4; Table 6.2). Obs #4 was comparable in quality to as Obs #2 (no large scale scintillation patterns) and RFI conditions but was pointed at a different part of the sky.

6.3 "Jupiter as an exoplanet"

6.3.1 Scaling Jupiter's signal

We add the Jupiter signal, multiplied by a factor α ($<< 1$), to the sky (+instrument) background of a typical exoplanet observation, and then try to detect it with our two-step processing pipeline (Sect. 6.4). As we will test below the post-processing in 10 MHz bands, we use the Jupiter signal of Fig. 6.1a detected in the band 15–25 MHz. In order to test our pipeline across the entire LOFAR-LBA range, we need to be able to add the attenuated

Table 6.2: Summary of LOFAR LBA beam-formed observations

Parameter	Obs #1	Obs #2	Obs #3	Obs #4
LOFAR OBS ID	L568467	L570725	L569123	L547645
Date (UT)	February 11, 2017	February 18, 2017	February 26, 2017	September 28, 2016
Time (UT)	02:30-05:30	01:12-04:12	01:16–04:16	23:00–04:00
Target	Jupiter	Tau Boötis	Tau Boötis	Upsilon Andromedae
ON-beam RA (2000)	13:27:49.42	13:47:15.74	13:47:15.74	01:36:47.84
ON-beam DEC (2000)	-07:39:01.70	+17:27:24.90	+17:27:24.90	+41:24:19.60
OFF-beam 1 RA (2000)	13:25:51.27	13:54:44.95	13:54:44.95	01:40:00
OFF-beam 1 DEC (2000)	-09:35:11.94	+16:49:29.20	+16:49:29.20	+38:00:00
OFF-beam 2 RA (2000)	13:35:55.97	13:58:10.366	13:58:10.366	01:30:00
OFF-beam 2 DEC (2000)	-09:05:16.10	+19:00:01.37	+19:00:01.37	+48:00:00

Jupiter signal to any 10 MHz band in the range 10-90 MHz. Having no absolute calibration available in the LOFAR-LBA range, we proceed in two steps: (i) the Jupiter signal detected by LOFAR in Obs #1 ($I_{J,1}$) is expressed in terms of the sky background in the band of observation 15–25 MHz ($I_{S,1}$), i.e. the ratio ($I_{J,1}/I_{S,1}$) is computed as in the following section (Sect. 6.3.2), and it is then transferred to an arbitrary 10 MHz band in the sky background in Obs #2 ($I_{s,2}$); (ii) the flux density of the Jupiter emission is computed from simultaneous calibrated observations performed at the NDA. These two steps are detailed below.

For step (i), we add the dynamic spectrum of the Jupiter observation in the range 15–25 MHz to the dynamic spectrum of the sky background in an arbitrary 10 MHz band of an exoplanet observation (with the same observational setup; Table 6.1) to get a test dynamic spectrum I_{new} following

$$I_{new} = I_{s,2} + \alpha I_{J,2}, \tag{6.1}$$

$$= I_{s,2}\left(1 + \alpha \frac{I_{J,1}}{I_{S,1}} \frac{S_{\text{SEFD},1}}{S_{\text{SEFD},2}}\right), \tag{6.2}$$

where $I_{J,1}/I_{S,1}$ and $I_{s,2}$ are derived from the observational data, α (<<1) is the variable down-scaling parameter, and the ratio $S_{\text{SEFD},1}/S_{\text{SEFD},2}$ can be computed as the ratio of the SEFD in the band 15–25 MHz and in the test frequency band. The full derivation of equation (6.2) can be found in Appendix A.1. From the LOFAR calibration data (van Haarlem et al. 2013), we approximate that the SEFD on an LBA station is 40 kJy in the range 30-70 MHz and that it increases approximately as λ^2 below 30 MHz (mainly due to the steep increase of the sky background). Thus, when transferring the Jupiter signal from the range 15–25 MHz ($\lambda = 11.5 - 18.7$ m) to a test frequency band, equation (6.2) can be simply rewritten

$$I_{new} = I_{S,2}\left(1 + \alpha \frac{I_{J,1}}{I_{S,1}} \left[\frac{max(\lambda_{J,1}, 10m)}{max(\lambda_{S,2}, 10m)}\right]^2 \frac{N_{S,2}}{N_{J,1}}\right), \tag{6.3}$$

$$\tag{6.4}$$

with $N_{S,2}$ and $N_{J,1}$ the number of LBA stations involved in each observation.

Note that equation (6.2) can be used to add the signal (of Jupiter or other) observed with

one telescope in a given frequency range to the background recorded with another telescope in another frequency range, as long as the SEFD of the two telescopes in their respective spectral ranges is known. Equation (6.4) is its application for the considered LOFAR-LBA observations. The Jupiter signal thus transferred retains its absolute intensity (e.g. in Jy).

For step (ii) we use an observation of Jupiter simultaneously taken to the LOFAR one, carried out at the NDA. For this observation, the NDA observes simultaneously in right-hand (RH) and left-hand (LH) circular polarizations from 10 to 40 MHz in 400 spectral channels at a time resolution of 1 second. Hourly calibration sequences on noise sources of known flux density are embedded in the data and allow us to calibrate the observations in absolute flux density (Jy), with an accuracy $\sim 20\%$. From NDA data, we know that the first Jupiter burst about 02:45 UT is RH elliptically polarized, whereas the drifting emission bands starting about 04:00 UT are LH elliptically polarized. However, for this study we did not use the polarization information and summed the RH and LH signals to obtain the total intensity. We removed the main fixed-frequency RFI and the main broadband spikes (recognized as non-Jupiter signal by integration over the 26-40 MHz range). After subtraction of a background (computed in each frequency channel) the cleaned calibrated dynamic spectrum was averaged over the 15–25 MHz range to obtain the time series displayed in Fig. 6.2a (black '+' symbols) together with a running average over 10 seconds (red line). Fig. 6.2b displays the high-pass filtered flux densities obtained by subtracting the 10 second average from 1 second measurements. The bursty spikes in this high-pass filtered time-series will be used for comparison to the results of our processing below (Sect. 6.6). The cumulative distribution function of the values of Fig. 6.2b is displayed in Fig. 6.2c. From that Fig., we see for example that ~100 of high-pass filtered flux density measurements exceed 3×10^4 Jy. By comparing this curve to the actual number of data points of emission detected we can determine the sensitivity of our observations and processing (Sect. 6.6).

6.3.2 Extraction Jupiter's signal

To obtain both the Jupiter signal (I_J) and the sky background in the Jupiter observation $I_{S,1}$ we first need a RFI mask. Since Jupiter is as bright as the RFI, we used a modified version

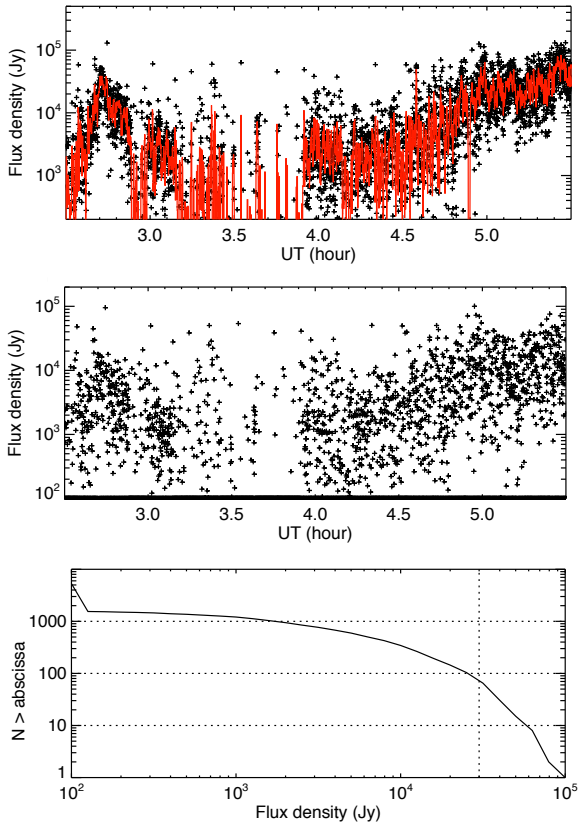

Figure 6.2: **(a)** Calibrated flux density of the Jupiter emission detected on 2017/02/11 between 02:30 and 05:30 UT with the NDA, averaged over the range of 15–25 MHz after background subtraction. Black '+' symbols are the measurements at 1 sec time resolution, whereas the red line is a running average over 10 sec. **(b)** High-pass filtered flux densities obtained by subtracting the 10 sec average from 1 sec measurements. Only values ≥100 Jy are displayed. **(c)** Cumulative distribution function of the values of panel **(b)**.

of the RFI mitigation pipeline presented in Turner et al. (2017a). The following steps are performed: (1) find RFI on the ON-beam above 30 MHz (where no Jupiter emission is present) using the algorithm PATROL (Zakharenko et al. 2013, Vasylieva 2015) to flag entire time steps, (2) find RFI in the OFF-beam using only PATROL to flag entire time steps and frequency channels, and (3) combine the RFI masks from step (1) and (2) together to obtain a final RFI mask. This mask is then applied to Obs #1 and this dataset is used as the Jupiter signal (I_J).

Next, we find $I_{S,1}$ for Obs #1 using the least Jupiter-contaminated OFF-beam (beam 2) and during a time interval (3740 - 3830 seconds after the start of the observation) where

Jupiter's emission was minimal. To find the SEFD we apply the RFI mask from step (3) to the raw data. Then at each frequency we compute the 10% quantile of the distribution of intensities (using this quantile allows for minimal influence from any Jupiter emission or remaining RFI). The level of the 10% quantile is lower than the mean, therefore, SEFD_{orig} has to be corrected. Quantitatively, the 10% quantile (μ_{10}) for a Gaussian distribution with moments (μ, σ_g) is

$$\mu_{10} \sim \mu - 1.3\sigma_g, \tag{6.5}$$

$$\frac{\mu_{10}}{\mu} \sim 1 - \frac{1.3}{\sqrt{n_{pol}\, b\, \tau_r}}, \tag{6.6}$$

where n_{pol} is the number of polarizations (2), b is the frequency resolution (b = 3.05 kHz), and τ_r is the time resolution (τ_r = 10.5 msec). The factor of 1.3 in equation (6.5) and (6.6) was determined using a standard Gaussian distribution. Therefore, the term SEFD_{orig} used in the analysis is obtained from the measured value (μ_{10}) using

$$I_{S,1} = \mu = \mu_{10}\left(1 - \frac{1.3}{\sqrt{n_{pol}\, b\, \tau_r}}\right)^{-1}. \tag{6.7}$$

6.4 Signal processing and observables

6.4.1 Processing pipeline

The data of Observation #2 with (I_{new}) and without the added Jupiter signal were run through the data reduction pipeline described in Turner et al. (2017a). This pipeline performs RFI mitigation, finds the time-frequency (t-f) response function of the telescope and normalizes the data by this function, and rebins the data in broader t-f bins. For RFI mitigation we use four different techniques (Offringa et al. 2010; Offringa 2012; Offringa et al. 2012; Zakharenko et al. 2013; Vasylieva 2015, and references therein) that are combined together for optimal efficiency and processing time. The result of the RFI mititation is an array (mask) of the same dimensions as the data with a value of either 0 (polluted pixels) or 1 (clean pixels). Subsequently, the data is rebinned to a time and frequency resolution of 1 second and 45 kHz. This rebinned data is the input into the post-processing pipeline

(Sect. 6.4.2). The original method used in Turner et al. (2017a) to find the time-frequency response function of the telescope (hereafter, method 1) is biased if some astrophysical emission or left-over RFI is present in the raw dynamic spectrum since the mean of the data is used to create the function. The raw sensitivity of the LOFAR observations is 208 Jy (Table 6.1) where the expected flux from most exoplanets is less than 100 mJy (Grießmeier et al. 2007; Grießmeier 2017). Therefore, for exoplanets we do not expect that the emission will be bright enough to be seen in the raw dynamic spectrum. However, when we test large Jupiter scaling factors (e.g. $\alpha = 10^{-2}$) this is no longer the case.

Therefore, we introduce a new method (hereafter, method 2) to find the time-frequency response function that is less biased towards bright emission in the raw dynamic spectrum. In the pipeline we (1) divide the raw data into sections of 4000 spectra (42 seconds), (2) apply the RFI mask to the raw data, (3) create an integrated spectrum from the 10% quantile of the distribution of intensities at each frequency, (4) correct the average of the 10% quantile such that it is close to the mean using equation (6.6), then (5) find a second order polynomial fit at each frequency over all time sections, and (6) create and save the 2-d time-frequency response surface made from the polynomial fits. As expected, method 1 and method 2 obtain the same results when α is very small (e.g. below $\alpha = 10^{-5}$). When α is large, method 2 is more robust. In addition, method 2 is computationally faster than method 1; therefore method 2 is the preferred method for finding the time-frequency function and will be used in the analysis of this paper.

6.4.2 Post-processing pipeline: Observables of the exoplanet signal

In the following section, we present the post-processing pipeline. After processing the data we compute several observable quantities that we named Q1 to Q4 for the ON- and OFF-beam and examine their behavior over time or frequency. The input dynamic spectrum for the observables is the RFI-mitigated, normalized, and rebinned data (Sect. 6.4.1; Fig. 6.3a). The observable quantities fall into two general categories: extended emission (Q1) or burst emission (Q2 - Q4). Below is the list of observables we defined (similar to the methods in Zarka et al. 1997 and Vasylieva 2015):

- Q1: Extended emission observables

  - Q1a (Time-series): Total power of the dynamic spectrum integrated over all frequencies and rebinned in time to a specified time interval (TI; 2 minutes for the default pipeline) (Fig. 6.3b)
  - Q1b (Integrated spectrum): Total power of the dynamic spectrum integrated over all time and rebinned in frequency to a specified frequency interval (FI; 0.5 MHz for the default pipeline) (Fig. 6.3c)

- Q2 (Normalized high-pass filtered time-series): The normalized high-pass filtered time-series (y)

$$y = \frac{(x - x_s) - \overline{(x - x_s)}}{\sigma_{(x-x_s)}}, \tag{6.8}$$

where x is the time-series of the dynamic spectrum integrated over all frequencies but not rebinned in time and x_s is the low-pass filtered data (low-frequency component) created by running a sliding window of w seconds over x (in the default pipeline $w = 10$ time bins). We subtract by the mean $\overline{(x - x_s)}$ to center y around 0. Finally, the time-series is normalized by its standard deviation in order to unify the thresholds. An example of y can be found in Fig. 6.4a.

We further examine Q2 by creating a scatter plot of the ON-beam values versus the corresponding OFF-beam values (Fig. 6.4b). In this plot, peaks only in the ON-beam would be visible on the right edge of the cloud of points. An example for Q2 of simulated data is given in Fig. 6.5a. Due to residual low-level RFI or ionospheric fluctuations, high values of Q2 frequently occur simultaneously in the ON- and OFF-beam (points close to the main diagonal in Fig. 6.5a). For this reason, we implemented an elliptical correction, as described in Appendix B.1. After the elliptical correction, the Q2 distribution of the sky noise datapoints is much closer to circular, which makes the signal datapoints more apparent. This is demonstrated in Fig. 6.5b. The analysis of real data (Sect. 6.5) will show that this elliptical correction does indeed facilitate the detection of astrophysical signals in the target beam and gives a better sensitivity (i.e. allows the detection of fainter signals).

Next, the observables Q3 and Q4 are defined to systematically and statistically

explore the parameter space of Q2 (y).

- Q3: Time-series of broadband burst emission from Q2 for one threshold τ (in units of sigma)
  - Q3a (Number of Peaks): Number of peaks per TI where $y \geq \tau$ (Fig. 6.6)
  - Q3b (Power of Peaks): Sum of the power of peaks per TI where $y \geq \tau$
  - Q3c (Peak Asymmetry): Number of peaks per TI where $y \geq \tau$ subtracted by number of peaks where $y \leq -\tau$
  - Q3d (Power Asymmetry): Sum of the power of peaks per TI where $y \geq \tau$ subtracted by the sum of |power| of peaks where $y \leq -\tau$
  - Q3e (Peak Offset): Number of peaks per TI where $y \geq \tau$ for the ON (OFF) beam and exceeding the corresponding OFF (ON) values by a factor ≥ 2
  - Q3f (Power Offset): Sum of the power of peaks per TI where $y \geq \tau$ for the ON (OFF) beam and exceeding the corresponding OFF (ON) values by a factor ≥ 2
- Q4a to Q4f: Each observable in Q3 is summed over all times and plotted versus the threshold value τ (Figs. 6.4c–i)

When examining Q3 and Q4, the ON- and OFF-beam are always compared to each other and plotted against a reference curve with the same number of elements. This reference curve is created by taking the mean of the derived Q values from 10000 different Gaussian distributions of random values. When we subtract the ON- and OFF-beam Q value, then the reference curve is the standard deviation of the difference between all the Q values derived from two different Gaussian distributions (each run 10000 times). By default, Q4 is calculated from $\tau = 1...6\sigma$ with a step size of 0.1σ. Q4 is more effective at finding excess faint emission than Q3 since it is summed over all times. Once a detection is found in Q4, then Q3 can be used to localize the emission in time (e.g. Fig 6.6a). The reason for evaluating Q3a and Q4a are to determine if the ON-beam has more positive peaks than the OFF-beam thus indicative of burst emission. The power of the peaks (Q3b and Q4b) highlights more clearly any potential excess. The peak (Q3c and Q4c) and power asymmetry (Q3d and Q3d) are useful at determining whether there is an asymmetry in the

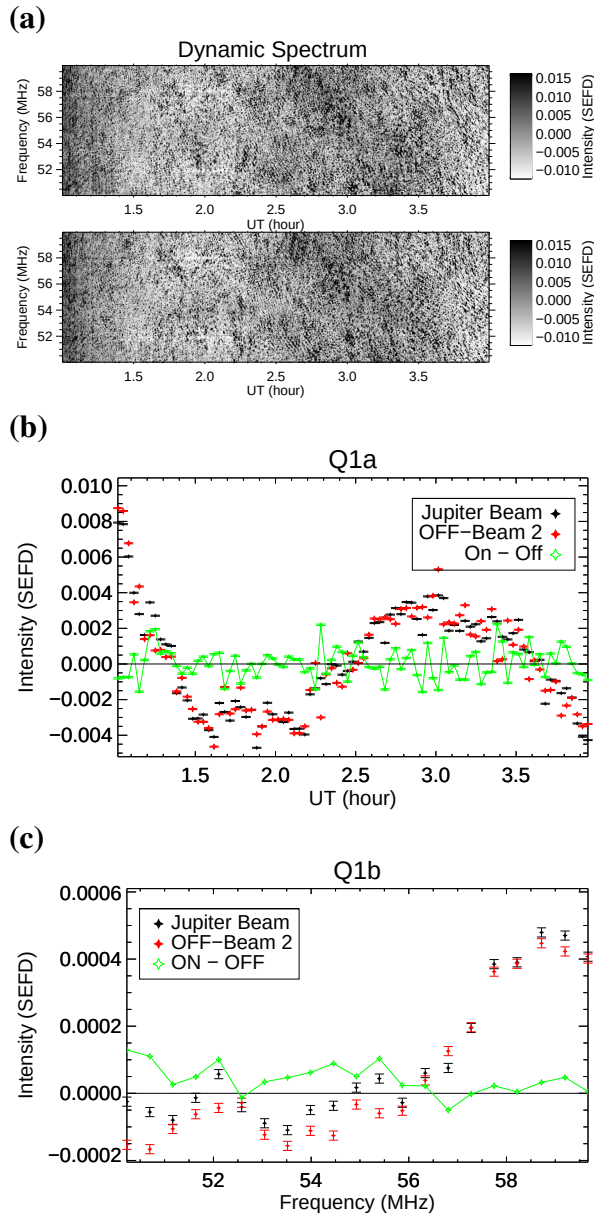

Figure 6.3: Dynamic spectra and extended emission observable Q1 for a scaling value of $\alpha = 10^{-3}$. **(a)** Dynamic spectra for the ON-beam (top) and the OFF-beam (bottom). **(b)** Q1a (time-series integrated over all frequencies). **(c)** Q1b (integrated spectrum summed over all times). See Sect. 6.4.2 for a detailed description of each observable. For all plots the black-points are the ON-beam, the red-points are the OFF-beam, and the green lines are the ON-beam minus the OFF-beam.

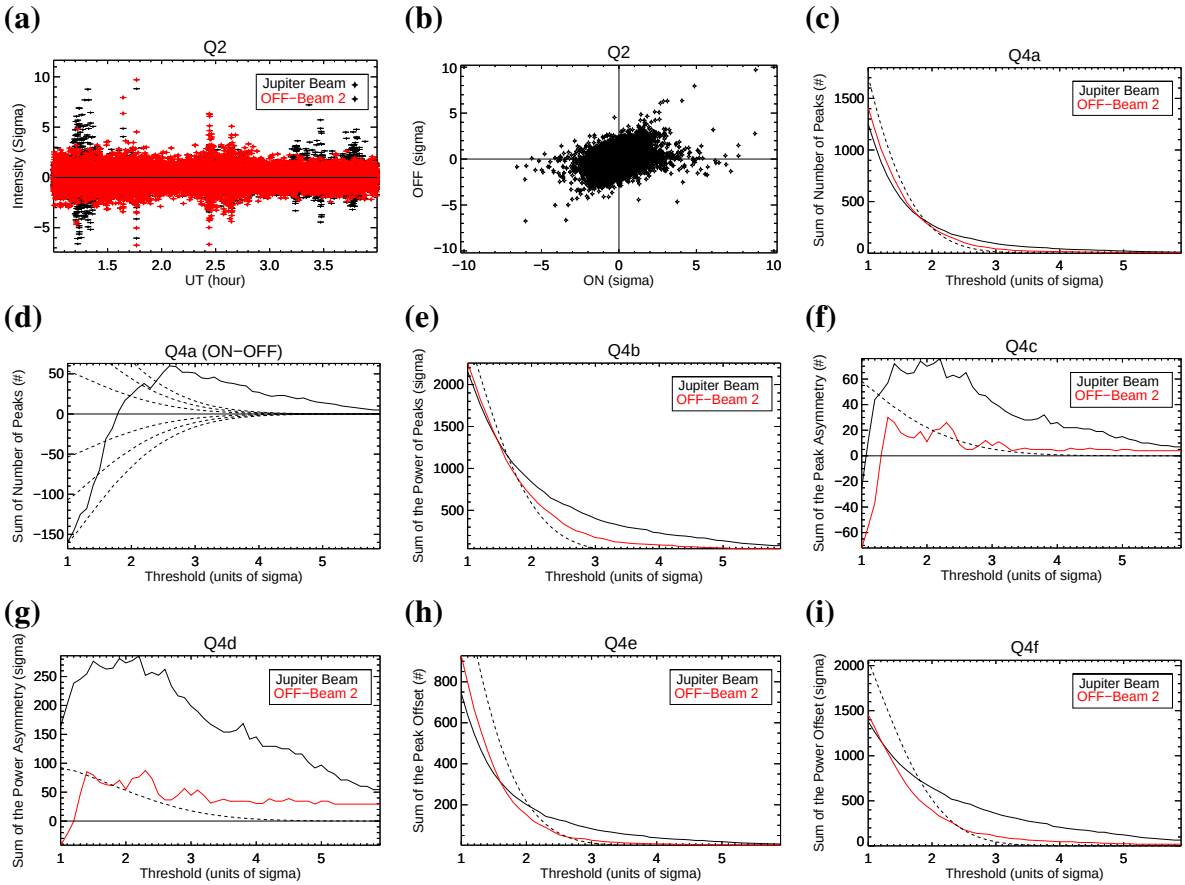

Figure 6.4: Observable quantities (Q2 and Q4) for a scaling value of $\alpha = 10^{-3}$. **(a)** Q2 (high-passed filtered intensities) vs time. **(b)** Q2 scatter plot for the ON- and OFF-beam. **(c)** Q4a (number of peaks). **(d)** Difference of ON - OFF for Q4a. **(e)** Q4b (power of the peaks). **(f)** Q4c (peak asymmetry). **(g)** Q4d (power asymmetry). **(h)** Q4e (peak offset). **(i)** Q4f (power offset). See Sect. 6.4.2 for a detailed description of each observable. For all plots the black lines are the ON-beam and the red lines are the OFF-beam. The dashed line for panels **(c)**, **(e)**, **(f)**, **(g)**, **(h)**, and **(i)** is the mean of the derived Q values from 10000 different Gaussian distributions with the same length as Q2. The dashed lines for panel **(d)** are the 1, 2, 3σ statistical limits of the difference between all the Q values derived from two different Gaussian distributions (each run 10000 times).

signal distribution. These observables are similar to the skewness but are more adopted to a small numbers of outliers. An excess of positive peaks over negative ones could be evidence of bursts. Finally, the peak (Q3e and Q4e) and power offset (Q3f and Q4f) are the best discrimination of real burst emission because they directly correlate any detection

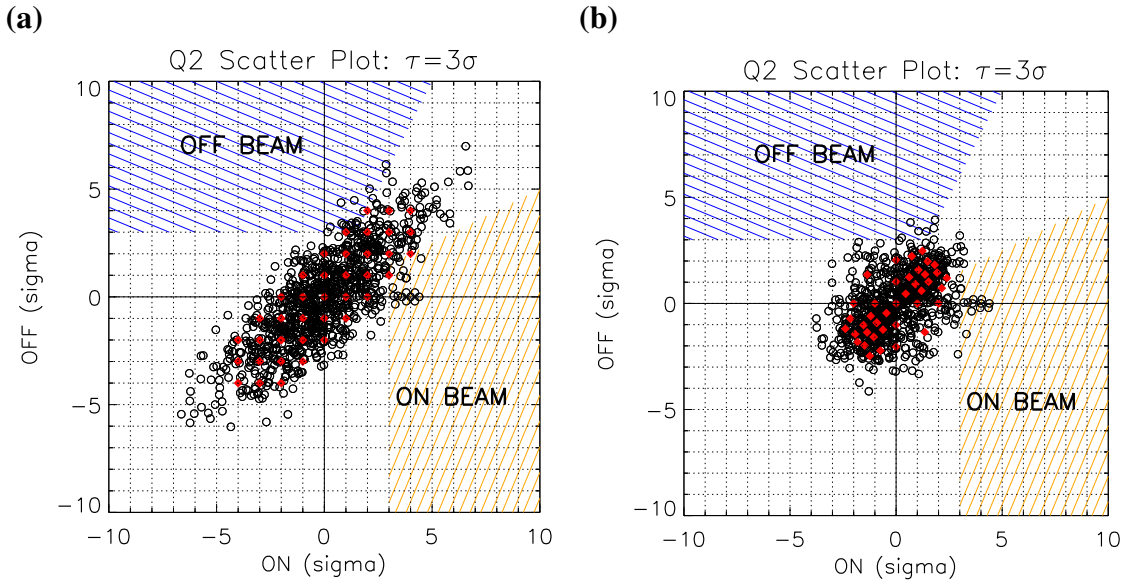

Figure 6.5: Simulated data-points (black) and test-points (red) to demonstrate the observable quantity Q2 and the effect of the elliptical correction. **(a)** Q2 before the elliptical correction. **(b)** Q2 after the elliptical correction. X-axis: Q2 (normalized high-pass filtered intensities) for the ON-beam. Y-axis: same for the OFF-beam. Points with high values in the ON- and OFF-beam (i.e. close to the main diagonal) are due to either residual RFI or ionospheric fluctuations. One of the main detection criteria is based on the number of points with high values only in the ON-beam or only in the OFF-beam. For this, the regions used in Q3e and Q4e are hatched (orange for the ON-beam, and blue for the OFF-beam; see text for the precise definition) for the case of $\tau = 3\sigma$ (i.e. a threshold of 3σ). This figure also illustrates the effect of the elliptical correction described in Appendix B.1. The red test data-points allow for the visualization of the displacement of individual points that leads to the circularization of the cloud. Using these red data-points, it can be seen that the x- and y-axis are unaffected by this procedure; data-points close to the main diagonal are most strongly affected. The black points represent what we expect from an observation, namely sky noise plus a few signal datapoints (injected at ON~4.0 and OFF~0.0 in this example). After elliptical correction, there are clearly more points in the orange than in the blue hatched region.

against the other beam. Additionally, ionospheric effects and any remaining low-level RFI will be concentrated on the diagonal; the peak and power offset mitigate these effects. See Fig. 6.5 for an illustration of where these observables lie in the parameter space of the scatter plot of Q2.

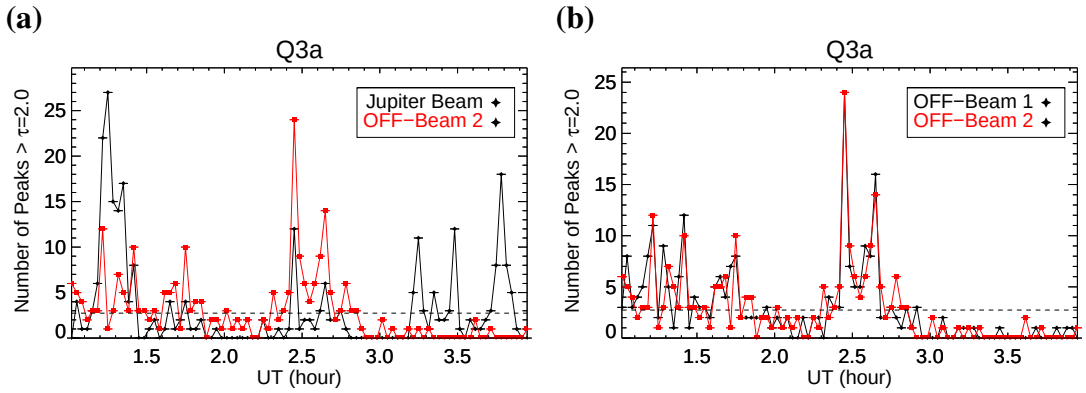

Figure 6.6: Comparison of the observable quantity Q3a between the ON-beam (Jupiter) and OFF-beam 2 **(a)** and the 2 OFF-beams **(b)** for a scaling value $\alpha = 10^{-3}$ and threshold $\tau = 2\sigma$. See Sect. 6.4.2 for a detailed description of Q3a. For all plots the black lines and the red lines correspond to two different beams. The dashed line is the mean of the derived Q values from 10000 different Gaussian distributions with the same length as the time interval (TI). Jupiter's emission is mainly localized between 1.2–1.4 UT and 3.2–3.9 UT, whereas the bright emission between 2.3–2.8 UT can be seen in both OFF beams.

6.5 Data Analysis and Results

In this study, the analysis is performed using 11 different scaling factors (α; equation 6.2) between 10^{-2} to 10^{-7} in steps of $10^{+0.5}$. We use Jupiter emission from 15–25 MHz added to Obs #2 in 4 frequency ranges (20–30, 30–40, 40–50, 50–60 MHz). The comparison of the two OFF-beams in Obs #2 with each other is used as a benchmark for what could be considered a detection. This test proved to be highly important as the OFF-beams contain non-Gaussian noise and there is unknown systematic noise (e.g. low-level RFI, non-corrected instrumental effects, ionospheric differences) in the data (e.g., see Turner et al. 2017a, Figure 4).

A summary of the parameters used in the post-processing can be found in Table 6.3. The rebin time of the processed data (δt) is a very important parameter because this defines the timescale over which we search for excess peaks in Q2. The frequency ($\Delta\nu$) and time range (ΔT) over which we calculate these observables is 10 MHz and 3 hours, respectively. Additionally, we include a threshold cut on the rebinned RFI mask. The rebinned mask no longer consists only of values of 0 (polluted pixels) and 1 (clean pixels) since it was

rebinned and clean pixels were mixed with polluted pixels. The mask threshold we use in our analysis is 90%, meaning a pixel will not be used in the analysis if $\geq$ 10% of the original pixels were contaminated. We use a time interval (TI) of 2 minutes and a frequency interval (FI) of 0.5 MHz for Q1b.

Table 6.3: Nominal parameters for the post-processing setup

Parameter	Value	Units
Width of frequency range ($\Delta\nu$)	10	MHz
Time Range (ΔT)	3	hours
Rebin time of processed data ($\delta\tau$)	1	secs
Mask threshold	90	%
Time interval (TI)	2	minutes
Frequency interval (FI)	0.5	MHz
Low-pass filter smoothing window (w)	10	secs
Threshold (τ) range	1 - 6	sigma

Figs. 6.3, 6.4, and 6.6 show the observable quantities Q1, Q2, Q3a, and Q4 for $\alpha = 10^{-3}$. This test case is very useful to demonstrate how each observable behaves. In this case the ON-beam can be seen to have additional flux in all the Q values except the dynamic spectrum (Fig. 6.3a) and Q1a (Fig 6.3b). For Q3a, it can be seen that Jupiter's emission is mainly localized between 1.2–1.4 UT and 3.2–3.9 UT (Fig. 6.6a) where the emission around 2.3–2.8 UT can be seen in both OFF beams (Fig. 6.6b). This is a good example demonstrating that two OFF beams are required to confirm a detection.

The extended emission observables Q1a and Q1b are only useful when the simulated exoplanet emission is very bright ($\alpha = 10^{-2} - 10^{-3}$) and can be seen by eye in the processed dynamic spectrum. The dominant source of variations in Q1a and Q1b are changes in the ionosphere. Ionospheric variations are the limiting factor in distinguishing real emission from background variations. Therefore, for faint exoplanet emission we would not expect the extended emission observables to be useful for detection.

The observables Q2 - Q4 are more effective at detecting fainter burst emission. The best observables to detect the faintest emission are Q4e and Q4f (Peak/Power Offset). We can reliably detect emission from Jupiter down to a value of $\alpha = 10^{-3.5}$ with the elliptical correction when adding Jupiter to the range 50 - 60 MHz. Fig. 6.7 shows Q4e and Q4f for a value of $\alpha = 10^{-3.5}$ for both the ON- vs. OFF-beam and OFF-beam 1 vs OFF-beam 2. The

main criteria we use to confirm a detection are (1) it is distinctly different than the OFF-beam 1 vs. OFF-beam 2 comparison plot (Fig. 6.7e), (2) it shows an excess $\geq 2\sigma$ statistical significance (dashed lines in Fig. 6.7), and (3) the detection curve is always positive for thresholds $\geq 2\sigma$. Our detection limit for all other frequencies (40 - 50 MHz, 30 - 40 MHz, and 20 - 30 MHz) are half an order of magnitude less sensitive than for the range 50 - 60 MHz. This is expected since the frequency-response curve of LOFAR sharply peaks at 58 MHz (e.g. Figure 1 in Turner et al. 2017a). The detection limits for each frequency range are summarized in Table 6.4.

Next, we test the robustness of the detection limits by varying the parameters of the post-processing from those in Table 6.3. We vary the rebin time of processed data ($\delta\tau$), smoothing window (w), value of the slope for the Peak/Power Offset, frequency range, and the time range. Our detection limit did not significantly change when we varied these parameters. Therefore, our detection limit is robust against the exact parameters used in the analysis. The signal from Jupiter is detected until the data is binned to a $\delta\tau$=30 seconds. Therefore, assuming that an exoplanet broad-band burst radio emission is similar to Jupiter's, a short integration time is essential for a detection. This result also shows that our method of analysis for beam-formed data can be applied to various setups of beam-formed observations and dynamic spectra extracted from the visibilities of imaging pipelines.

Finally, we tested whether the date of observation or the position on the sky has a noticeable effect in our detection limits. For Obs #3, we find detection limits that are half an order of magnitude less sensitive from those found using Obs #2. Finally, performing the analysis on Obs #4 we find detection limits that are similar to Obs #2. Therefore, our detection limits (Table 6.4) are also insensitive to where in the sky we are pointed at, provided that the observations were taken under good conditions.

6.6 Discussion

We demonstrated that we can detect the Jupiter signal down-scaled by a factor $\alpha = 10^{-3.5}$ with the observable Fig. 6.7f. Our detection in Q4f consists of ~100 data-points in the NDA calibration data exceeding 3×10^4 Jy with a threshold $\geq 2\sigma$ (Fig 6.7d). Therefore, this limit corresponds to a flux density of $\sim \alpha \times 3 \times 10^4$ Jy = 9.5 Jy using the value of Jupiter's

Table 6.4: Summary of the scaling factor upper limits found in the analysis

Frequency Range (MHz)	α
Obs #2	
50 - 60	$10^{-3.5}$
40 - 50	10^{-3}
30 - 40	10^{-3}
20 - 30	10^{-3}
Obs #3	
50 - 60	10^{-3}
40 - 50	$10^{-2.5}$
30 - 40	$10^{-2.5}$
20 - 30	$10^{-2.5}$
Obs #4	
50 - 60	$10^{-3.5}$
40 - 50	10^{-3}
30 - 40	10^{-3}
20 - 30	10^{-3}

absolute flux density corresponding to 100 data-points from Fig. 6.2c. This flux density is ~4 times higher than the sensitivity expected for LOFAR beam-formed observations using the 24 core LBA stations:

$$\sigma_{LOFAR} = \frac{SEFD \times 4}{\sqrt{N(N-1) \times 1sec \times 10MHz}} \simeq 2.2Jy \tag{6.9}$$

with a SEFD of 40 kJy (van Haarlem et al. 2013). The factor of 4 in the numerator takes into account the imperfect coherent addition of the station signals and the flagging of RFI in the data[2]. No factor $\sqrt{2}$ is included in the denominator because we have used total intensity data but the Jupiter signal (as well as the expected exoplanetary signal) is ~100% polarized. The factor of 4 difference between the sensitivity calculation (equation 6.9) and the 9.5 Jy deduced from the α value is mostly due to ionospheric variations that were not mitigated during the post-processing and partly due to the fact that our criteria for a burst detection is a statistical significance $\geq 2\sigma$ (Section 6.5; Fig. 6.7f). These ionospheric variations can be seen in Figs. 6.4c to 6.4i since the OFF-beam does not follow a Gaussian-distribution.

[2]LOFAR Astronomer's website on the beam-formed mode located at https://www.astron.nl/radio-observatory/observing-capabilities/depth-technical-information/major-observing-modes/beam-form

One may wonder why bothering with the complex observables to achieve the sensitivity expected for beam-formed observations. The answer is that they allow us to detect confidently a signal and distinguish it from false positives at a 1.5–2σ level, whereas simple detection of a spike in beam-formed data requires generally a $\sim 10\sigma$ level to be considered as reliable. Thus we actually gain a factor > 5 in effective sensitivity (detection capability) with our method. Also, they allow for the detection of relatively sparse and short bursts that would be washed out by averaging over long integrations.

The α value found in our analysis can be decomposed into three separate physical factors (distance, strength of emission compared to Jupiter, and relative Jupiter flux levels):

$$\alpha = \alpha_J \left(\frac{S_J[\mathrm{ref}]}{S_J[\mathrm{obs}]}\right)\left(\frac{5\ AU}{d}\right)^2 = \alpha_J \left(\frac{S_J[\mathrm{ref}]}{S_J[\mathrm{obs}]}\right)\left(\frac{2.4\times 10^{-5}\ pc}{d}\right)^2 \tag{6.10}$$

where α_J is the scaling factor of the emission compared to Jupiter, d is the distance, S_J(obs) is the flux density of the observed Jupiter signal in Obs #1 calibrated using NDA, and S_J(ref) is a reference flux density value of Jupiter to which the putative exoplanet signal is compared. The Jupiter signal (S_J[obs]) of $\sim 3\times 10^4$ Jy is more than a factor 100 below the peak value reached by Jupiter's decametric emission (up to 5×10^6 Jy; Queinnec & Zarka 2001) observed from the Earth, at 5 AU range. To find S_J(ref), we use Jupiter's radio emission levels and occurrence rates given in Zarka et al. (2004, Figure 7). Jupiter does emit continuous decameter emission but the most energetic emission can be found in bursts. During a fairly active emission event, the median flux density of Jupiter's decametric bursts at 5 AU is $\sim 4\times 10^5$ Jy. This flux density is exceeded by $\sim 1\%$ of all detected Jupiter bursts, whereas the level $\sim 4\times 10^4$ Jy is exceeded by $\geq 50\%$ of Jupiter bursts.

We find that we can detect an exoplanetary signal intrinsically 10^6 times stronger than Jupiter's emission strength from a distance of 5 pc using equation (6.10) and taking the mean level of Jupiter's decametric bursts as the reference flux ($S_J[\mathrm{ref}] = 4\times 10^5$ Jy) that would occur for a few minutes within an observation of a few hours. A stronger signal may be detected more often, a weaker one more rarely. In Table 6.5, we show the α_J detection limits for several tests cases with different reference fluxes and distances.

Such signals are indeed expected to exist. According to most models, the strongest emission is expected for close-in planets, especially massive hot Jupiters (Zarka et al.

Table 6.5: Detection limit of LOFAR LBA beam-formed observations found by observing "Jupiter as an exoplanet"

S_J(ref) [Jy at 5 AU]	Distance [pc]	α_J
4×10^4 (a)	5	1×10^7
"	10	4×10^7
"	20	2×10^8
4×10^5 (b)	5	1×10^6
"	10	4×10^6
"	20	2×10^7
6×10^6 (c)	5	6×10^4
"	10	3×10^5
"	20	1×10^6

Notes. — All calculations were done with equation (6.10) where the scaling factor $\alpha = 10^{-3.5}$ and $S_J(obs) = 3\times10^4$ Jy (Sect. 6.3.1, Figure 6.2). **(a)** The level of Jupiter's burst emission exceeded in ≥50% of Jupiter bursts (Zarka et al. 2004, Figure 7), **(b)** The mean level of Jupiter's burst emission exceeded in $\sim$ 1% of Jupiter bursts, **(c)** Maximum peak of Jupiter's S-burst emission (Queinnec & Zarka 2001)

2001; Zarka 2007; Grießmeier et al. 2007; Grießmeier et al. 2011). However, rapidly rotating planets with strong internal plasma sources have also been suggested to produce radio emission at detectable levels at orbital distances of several AU from their host star (Nichols 2011, 2012). Furthermore, the expected radio flux is a function of the age of the exoplanetary host star, with stronger radio signals are expected for planets around young stars (Stevens 2005; Grießmeier et al. 2005, 2007; Grießmeier et al. 2007), and for planets around stars with frequent and powerful coronal mass ejections (Grießmeier et al. 2006, 2007; Grießmeier et al. 2007).

Sources beyond 10-20 pc would need to be extremely intense ($\geq 10^7\times$ Jupiter's), and may be beyond the reach of LOFAR. If the structure of the emission is different from that of Jupiter bursts (e.g. longer bursts of several minutes), the above sensitivity may be improved by an order of magnitude or more.

Finally, let us mention that detection of a radio signal from an exoplanetary system will only constitute the first step. Even though the planetary emission is expected to be much stronger than the stellar emission (see e.g. Grießmeier et al. 2005), one would have to confirm the signal is indeed produced by the exoplanet rather than its host star. The most direct indication would be the detection of radio emission from a transiting planet, with the planetary emission disappearing during secondary eclipses. Secondly, stellar and planetary radio emission have different polarization properties (Zarka 1998), making polarization a very powerful tool even beyond signal detection. Thirdly, one would have to search for a periodicity in the detected signal, and compare its period to the stellar rotation period (or, more precisely, the beat period between the stellar rotation and the planetary orbit, see e.g. Fares et al. 2010), and (if known) the planetary rotation period.

Ancillary data which would help with the interpretation of a radio signal include: stellar lightcurves (correlation with stellar flares), stellar magnetic field maps (e.g. obtained by Zeeman-Doppler-Imaging), the stellar rotation rate, data on the stellar wind (e.g. obtained by astrospheric absorption) or at least a good estimation of the stellar age, the exoplanet's orbital inclination (see Hess & Zarka 2011) and the planetary rotation rate.

6.7 Conclusions and perspectives

Our analysis shows that our pipeline for beam-formed LOFAR data can detect signals of $10^{-3.5}$ times the intensity of Jupiter's emission. This corresponds to either a Jupiter-like planet at a distance of 1300 AU, or an exoplanet with 10^6 times Jupiter's mean radio flux for strong burst emission (4×10^5 Jy; Zarka et al. 2004) at a distance of 5 pc (Table 6.5). According to frequently employed scaling laws (e.g. Zarka et al. 2001; Zarka 2007; Grießmeier et al. 2007), one can expect exoplanetary radio emission up to 10^6 times Jupiter's flux. Our pipeline could potentially detect radio emission from the exoplanets 55 Cnc (12 pc), Tau Boötis (16 pc), and Upsilon Andromedae (13 pc) if their emission can reach 10^6 times the peak flux value reached by Jupiter's decametric burst emission ($\sim 6 \times 10^6$ Jy; Queinnec & Zarka 2001). We have observed all these planets using LOFAR; the analysis using this pipeline is currently on-going, and will be the subject of a follow-up article.

In this study, we present the post-processing extension of our beam-formed reduction

pipeline (Turner et al. 2017a). With this improvement our pipeline can now be applied to various setups of beam-formed data from different telescopes (e.g. LOFAR, UTR-2) and dynamic spectra extracted from radio imaging observations (Loh et al. in prep).

As a subsequent step, the data analysis pipeline will undergo important improvements. The analysis of the polarization information (especially Stokes-V) should allow us to reach a better sensitivity and allow to discriminate planetary emission which is expected to be strongly circularly polarized (e.g. Zarka 1998; Grießmeier et al. 2005) from non-planetary emission.

On a slightly longer timescale, NenuFAR (Zarka et al. 2012; Zarka et al. 2014) will allow more sensitive observations, with an improvement in sensitivity by a significant factor compared to LOFAR's core below 35 MHz. This is precisely the frequency range where we believe most exoplanetary systems will emit.

The Square Kilometer Array (SKA) will be even more sensitive (with an improvement in sensitivity by a factor ~30 compared to LOFAR; Zarka et al. 2015). It will only observe at frequencies above 50 MHz, but there are cases where exoplanetary radio emission is expected to extend to frequencies of a few 100 MHz. This is the case for young and massive planets (Grießmeier 2018) as well as in the case of a unipolar induction mechanism between a hot Jupiter and its parent star (Zarka 2007), making the SKA a promising instrument for exoplanet radio studies (Zarka et al. 2015; Grießmeier 2018).

Besides improvements in telescope sensitivity, many more nearby exoplanets with short orbital periods are likely to be discovered by the upcoming Transiting Exoplanet Survey Satellite mission (TESS; Ricker et al. 2015) and ground-based transit surveys such as the Next-Generation Transit Survey (NGTS; Wheatley et al. 2018) and the Kilodegree Extremely Little Telescope (KELT; Pepper et al. 2007). For example, TESS is predicted to find hundreds of planets within 50 pc and a dozen exoplanets within 10 pc (Sullivan et al. 2015). These new exoplanets may be good candidates for the exoplanetary radio emission search because our detection capability is strongly dependent on distance (Equation 6.10; Table 6.5).

Acknowledgements

J. Turner was funded by the National Science Foundation Graduate Research Fellowship under Grant No. DGE-1315231. We also thank PNP and PNST for their support.

This research has made use of the Exoplanet Orbit Database (Wright et al. 2011), Exoplanet Data Explorer at exoplanets.org (Han et al. 2014), Extrasolar Planet Encyclopaedia (exoplanet.eu) maintained by J. Schneider (Schneider et al. 2011), and NASA's Astrophysics Data System Bibliographic Services.

This paper is based (mostly) on data obtained with the International LOFAR Telescope (ILT) under project codes LC2_018, LC5_DDT_002, LC6_010, and LC7_013. LOFAR (van Haarlem et al. 2013) is the Low Frequency Array designed and constructed by ASTRON. It has observing, data processing, and data storage facilities in several countries, that are owned by various parties (each with their own funding sources), and that are collectively operated by the ILT foundation under a joint scientific policy. The ILT resources have benefitted from the following recent major funding sources: CNRS-INSU, Observatoire de Paris and Université d'Orléans, France; BMBF, MIWF-NRW, MPG, Germany; Science Foundation Ireland (SFI), Department of Business, Enterprise and Innovation (DBEI), Ireland; NWO, The Netherlands; The Science and Technology Facilities Council, UK. We use the TGSS survey (Intema et al. 2017) in our study when determining the locations of the OFF-beams and we thank the staff of the GMRT that made these this survey possible. GMRT is run by the National Centre for Radio Astrophysics of the Tata Institute of Fundamental Research. NDA Jupiter observations were used for the flux calibration in our analysis. The NDA is hosted by the Nançay Radio Observatory/ Unité Scientique de Nançay of the Observatoire de Paris (USR 704-CNRS, supported by Université d'Orléans, OSUC, and Region Centre in France).

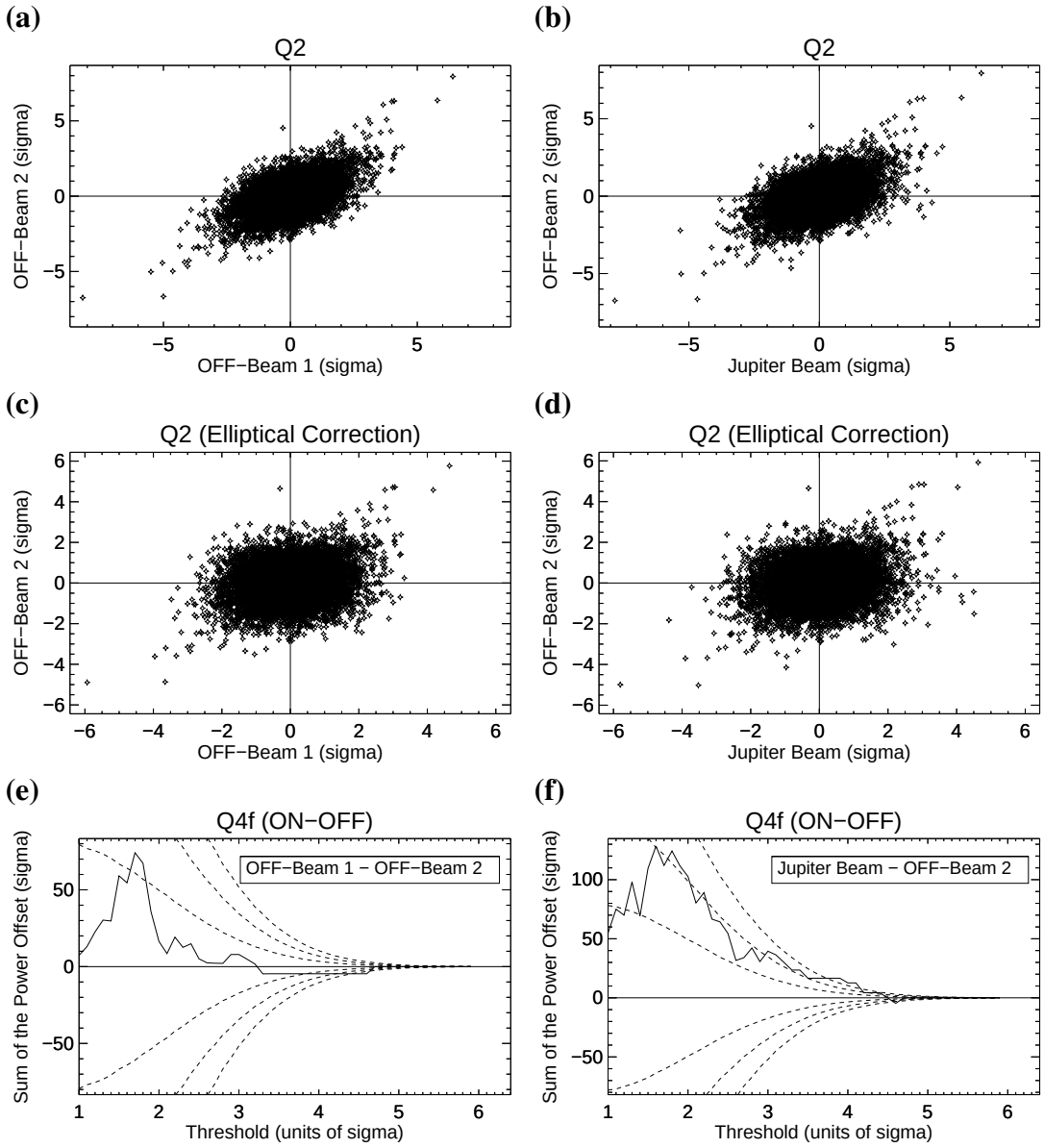

Figure 6.7: Plots of Q2 and Q4f (Power Offset) showing the detection limit ($\alpha = 10^{-3.5}$) for the frequency range 50–60 MHz. **(a)** and **(b)** Q2 before elliptical correction. **(c)** and **(d)** Q2 after elliptical correction. **(e)** and **(f)** Q4f difference of the two beams. The comparison of the two OFF-beams from Obs #2 can be found in the left column (panels **a**, **c**, **e**) and the comparison of ON-beam (Jupiter) vs OFF-beam 2 can be found in the right column (panels **b**, **d**, **f**). The dashed lines for panel **(e)** and **(f)** are the 1, 2, 3 σ statistical limits of the difference between all the Q values derived from two different Gaussian distributions (each run 10000 times). Panel **(f)** shows an excess of ON vs OFF points at $\geq$ 2 σ statistical significance for signals up to a threshold of 4σ. For comparison, in panel **(e)** almost all the excess points are below the 1σ statistical significance level.

Chapter 7

Summary

"Study as if you were to live forever. Live as if you were going to die tomorrow." Isidore of Seville

In this thesis, I have presented research investigating the atmospheres and magnetic fields of exoplanets. A summary of each chapter and future work can be found below.

7.1 Chapter 2

In this chapter, I observed the primary transits of 15 exoplanets (CoRoT-1b, GJ436b, HAT-P-1b, HAT-P-13b, HAT-P-16b, HAT-P-22b, TrES- 2b, TrES-4b, WASP-1b, WASP-12b, WASP-33b, WASP-36b, WASP-44b, WASP-48b, and WASP-77Ab) in the near-UV and several optical photometric bands to search for a wavelength dependence in their transit depths to constrain their atmospheres and determine whether asymmetries are visible in their light curves. Here, I present the first ground-based near-UV light curves for 12 of the targets (CoRoT- 1b, GJ436b, HAT-P-1b, HAT-P-13b, HAT-P-22b, TrES-2b, TrES-4b, WASP-1b, WASP-33b, WASP-36b, WASP-48b, and WASP-77Ab). I find that none of the near-UV transits exhibit any asymmetries, and this result is consistent with recent theoretical predictions by Ben-Jaffel & Ballester (2014) and Turner et al. (2016a). The multiwavelength photometry indicates a constant transit depth from near-UV to optical wavelengths in 10 targets (suggestive of clouds), and a varying transit depth with wavelength in 5 targets (hinting at Rayleigh or aerosol scattering in their atmospheres). I also present the first

detection of a smaller near-UV transit depth than that measured in the optical for WASP-1b; a possible opacity source might be TiO absorption. WASP-36b also exhibits a smaller near-UV transit depth a 2.6σ.

7.2 Chapter 3

In the first part of Chapter 3, I use the CLOUDY plasma simulation code to model the absorption from X-ray to radio wavelengths by 1D slabs of gas in coronal equilibrium with varying densities (10^4–10^8 cm^{-3}) and temperatures (2000–10^6 K) illuminated by a solar spectrum. For slabs at coronal temperatures (10^6 K) and densities even orders of magnitude larger than expected for the compressed stellar wind ($10^4 - -10^5 cm^{-3}$), I find optical depths orders of magnitude too small ($\sim$ 3$\times$ 10^{-7}) to explain the $\sim$3 per cent UV transit depths seen with Hubble (Fossati et al. 2010; Ben-Jaffel & Ballester 2013). Using this result and our model of slabs with lower temperatures (2000–10^4 K), the conclusion is that the UV transits of WASP-12b and HD 189733b are likely due to atoms originating in the planet, as the stellar wind is too highly ionized. A corollary of this result is that transport of neutral atoms from the denser planetary atmosphere outward must be a primary consideration when constructing physical models. In the second part of this chapter, additional calculations using CLOUDY are carried out to model a slab of planetary gas in radiative and thermal equilibrium with the stellar radiation field. Promising sources of opacity from the X-ray to radio wavelengths are discussed, some of which have not yet been observed.

7.3 Chapter 4

In Chapter 4 I present new photometric data of 11 hot Jupiter transiting exoplanets (CoRoT-12b, HAT-P-5b, HAT-P-12b, HAT-P-33b, HAT-P-37b, WASP-2b, WASP-24b, WASP-60b, WASP-80b, WASP-103b, XO-3b) in order to update their planetary parameters and to constrain information about their atmospheres. These observations of CoRoT-12b, HAT-P-37b and WASP-60b are the first follow-up data since their discovery. Additionally, the first near-UV transits of WASP-80b and WASP-103b are presented. I compare the results of our analysis with previous work to search for transit timing variations (TTVs) and a wave-

length dependence in the transit depth. TTVs may be evidence of a third body in the system and variations in planetary radius with wavelength can help constrain the properties of the exoplanets atmosphere. For WASP-103b and XO-3b, I find a possible variation in the transit depths that may be evidence of scattering in their atmospheres. The B-band transit depth of HAT-P-37b is found to be smaller than its near-IR transit depth and such a variation may indicate TiO/VO absorption. These variations are detected from 2-4.6σ, so follow-up observations are needed to confirm these results. Additionally, a flat spectrum across optical wavelengths is found for 5 of the planets (HAT-P-5b, HAT-P-12b, WASP-2b, WASP-24b, WASP-80b), suggestive that clouds may be present in their atmospheres. I calculate a refined orbital period and ephemeris for all the targets, which will help with future observations. No TTVs are seen in our analysis with the exception of WASP-80b and follow-up observations are needed to confirm this possible detection.

7.4 Chapter 5

In this chapter, I search for non-thermal radio emission from the 55 Cnc system which has 5 known exoplanets. According to theoretical predictions 55 Cnc e, the innermost planet, is among the best targets for this search. I observed for 18 hours with the Low-Frequency Array (LOFAR) Low Band Antenna in the frequency range 26–73 MHz with full-polarization and covered 85% of the orbital phase of 55 Cnc e. During the observations four digital beams within the station beam were recorded simultaneously on 55 Cnc, nearby empty sky, a bright radio source, and a pulsar. A pipeline was created to automatically find and mask radio frequency interference, calibrate the time-frequency response of the telescope, and to search for bursty planetary radio signals in our data. Extensive tests and verifications were carried out on the pipeline. Analysis of the first 4 hours of these observations does not detect any exoplanet signal from 55 Cnc but I can confirm that our setup is adequate to detect faint astrophysical signals. I find a 3-sigma upper limit for 55 Cnc of 230 mJy using the pulsar to estimate the sensitivity of the observations and 2.6 Jy using the time-series difference between the target and sky beam. The techniques in this chapter can be used to analyze beamformed data from future ground-based low-frequency radio telescopes (NenuFAR, LOFAR 2.0, SKA) or reconstructed dynamic spectra from the

visibilities of imaging data.

7.5 Chapter 6

In Chapter 6, I investigate the radio emission from Jupiter, scaled such that it mimics emission coming from an exoplanet, observed with low-frequency beam-formed observations using LOFAR. The goals are to define a set of observables that can be used as a guideline in the search for exoplanetary radio emission and to measure effectively the sensitivity limit for LOFAR beam-formed observations. I observe "Jupiter as an exoplanet" by dividing a LOFAR observation of Jupiter by a down-scaling factor and adding this observation to beam-formed data of the "sky background". Then we run this artificial dataset through our processing and post-processing pipeline and determine up to which down-scaling factor Jupiter is still detected in the dataset. I find that exoplanetary radio bursts can be detected at 5 pc if the flux is 10^6 times stronger than the typical level of Jupiters radio bursts during active emission events ($\sim 4 \times 10^5$ Jy). Equivalently, radio bursts up to 20 pc (encompassing the known exoplanets 55 Cnc, Tau Bootis, and Upsilon Andromedae) can be detected assuming the level of emission is 10^6 times stronger than the peak flux of Jupiters decametric burst emission. Analysis of the polarized signal of Jupiter should improve these upper limits by an order of magnitude.

7.6 Future Work

In the future, the LOFAR beam-formed data analysis pipeline presented in Chapters 5 and 6 will undergo important improvements. The analysis of the polarization information (especially Stoked V) should allow us to reach a better sensitivity and allow to discriminate planetary emission which is expected to be strongly circularly polarized (e.g. Zarka 1998; Grießmeier et al. 2005) from non-planetary emission. I expect the sensitivity in Stokes-V to be closer to the thermal noise unlike Stokes-I as shown in Chapters 5 and 6. Therefore, applying the updated Stokes-V pipeline to our exoplanetary LOFAR data should allow for a high chance of detection or significant upper limits that can constrain the theoretical predictions.

Appendix A

"We support astronomy for the same reason we support a symphony orchestra, or an opera, or a poet. Because it distinguishes us as human." Bart Bok

A.1 Jupiter Scaling Derivation

When observing the sky with a radio telescope, we measure, for a signal of antenna temperature T_A, a specific intensity I proportional to the received power

$$I = \frac{2k}{\lambda^2} T_A, \tag{A.1}$$

where λ is the wavelength of interest. The *unpolarized* flux density S for an unresolved source is

$$S = \frac{2kT_A}{A_e}, \tag{A.2}$$

where A_e is the effective area of the telescope used $A_e = \lambda^2/\Omega$ and Ω is the solid angle of the telescope beam in the approximation where the main beam largely dominates. The flux density measured is independent of the radio telescope performing the measurement.

When observing the Galaxy (sky background) with a radio telescope the intensity I_S would be

$$I_S = \frac{2k}{\lambda^2} T_{SG}, \tag{A.3}$$

where T_{SG} is system noise temperature for an observation of the Galaxy. T_{SG} is the sum of the noise contributions in the beam

$$T_{SG} = T_G + T_i, \tag{A.4}$$

where T_G is the antenna temperature measured for the Galaxy, i.e. $T_G = 60K\lambda^{2.55}$, and T_i is the instrumental noise. By definition the System Equivalent Flux Density (S_S) would be

$$S_S = \frac{2kT_{SG}}{A_e} = \frac{2k\left(T_G + T_i\right)}{A_e}. \tag{A.5}$$

The units of S_S are in Jy. Then, the background intensity of the sky I_S measured in the data would be

$$I_S = \frac{2k}{\lambda^2}\left(T_G + T_i\right). \tag{A.6}$$

If we compare two different sky observations (i.e. I_{S1} and I_{S2}) with different instruments and at different wavelengths we have

$$\frac{I_{S1}}{I_{S2}} = \left(\frac{\lambda_2}{\lambda_1}\right)^2 \left(\frac{T_{G1} + T_{i1}}{T_{G2} + T_{i2}}\right). \tag{A.7}$$

When observing Jupiter with a radio telescope, the flux density S_J would be

$$S_J = \frac{2kT_{SJ}}{A_e}, \tag{A.8}$$

where T_{SJ} is the system noise temperature of an observation of Jupiter. The system noise temperature T_{SJ} now includes contributions from Jupiter, the Galaxy, and the instrument

$$T_{SJ} = T_{AJ} + T_G + T_i, \tag{A.9}$$

where T_{AJ} is the observed antenna temperature for Jupiter. T_{AJ} is >> than both T_i and T_G,

therefore, the flux density S_J becomes

$$S_J = \frac{2kT_{AJ}}{A_e}. \tag{A.10}$$

Hence, the intensity of Jupiter observed by a radio telescope would be

$$I_J = \frac{S_J A_e}{\lambda^2}. \tag{A.11}$$

If we compare the intensities of two observations of Jupiter (i.e. I_{J1} and I_{J2}) using different instruments and at different wavelengths we have

$$\frac{I_{J1}}{I_{J2}} = \left(\frac{\lambda_2}{\lambda_1}\right)^2 \left(\frac{A_{e1}}{A_{e2}}\right). \tag{A.12}$$

We consider an observation of Jupiter (Obs #1) with instrument 1 (I_{J1}) in a given frequency range (e.g. 16-26 MHz) and an observation of the sky background (Obs #2) with instrument 2 (I_{S2}) in an arbitrary frequency range (e.g. 50-60 MHz). The instruments and frequency ranges in these observations do not have to be the same. The goal is to synthesize a signal (I_{sim}) with the sky background (I_{S2}) from Obs #2 plus the Jupiter signal as it would have been observed with instrument 2 (I_{J2}) and attenuated by a factor α

$$I_{sim} = I_{S2} + \alpha I_{J2}. \tag{A.13}$$

Therefore, we have

$$I_{sim} = I_{S2}\left[1 + \alpha\left(\frac{I_{J2}}{I_{S2}}\right)\right], \tag{A.14}$$

$$= I_{S2}\left[1 + \alpha\left(\frac{I_{J2}}{I_{J1}}\right)\left(\frac{I_{J1}}{I_{S1}}\right)\left(\frac{I_{S1}}{I_{S2}}\right)\right], \tag{A.15}$$

where I_{S1} is the sky background in Obs #1. I_{S1} has to be measured in an OFF-beam in Obs #1 since the Jupiter emission in the ON-beam is so immense. By using equation (A.7) for the sky background ratio and equation (A.12) for the Jupiter signal ratio, we find that

I_{sim} is equal to

$$I_{sim} = I_{S2}\left[1 + \alpha\left(\frac{I_{J1}}{I_{S1}}\right)\left(\frac{T_{G1} + T_{i1}}{A_{e1}}\right)\left(\frac{A_{e2}}{T_{G2} + T_{i2}}\right)\right], \tag{A.16}$$

$$I_{sim} = I_{S2}\left[1 + \alpha\left(\frac{I_{J1}}{I_{S1}}\right)\left(\frac{S_{S1}}{S_{S2}}\right)\right]. \tag{A.17}$$

Jupiter's intensity I_{J1} and the intensity of the sky I_{S1} in Equation (A.17) can be measured directly from the data in Obs #1 (Section 6.3.2). Equation (A.17) is used as Equation (6.2) in the main text.

Appendix B

"It is the quality of the moment, not the number of days, or events, or of actors, that matters." Ralph Waldo Emerson

B.1 Elliptical correction

Typically, the distribution of points is not 'circular' in the Q2 scatter plot (normalized high-pass filtered intensities, Fig. 6.5a). This is an indication that left-over RFI and/or ionospheric fluctuations affect both the ON- and the OFF-beam simultaneously, leading to points close to the main diagonal. We are interested in signal only identified in the ON-beam (i.e. close to the x-axis), and, to be able to quantify the background of spurious events, the signal identified only in the OFF-beam (i.e. close to the y-axis). In order to be able to detect points close to the x- and y-axis more easily, we circularize the ellipse in the following way:

- We determine the eigenvalues and eigenvectors of the distribution of points.
- The eigenvector gives the angle α of the principal axis of the distribution. It is very close to 45°, showing that there is indeed correlated signal in both beams.
- The eigenvalues give the width of the point distribution along the principal axis and in the direction perpendicular to it.
- We fit an ellipse (tilted at the angle α) to the distribution of points. For each point on the ellipse, we calculate the distance of the point from the origin, $r_{ellipse}(\varphi)$. We normalize $r_{ellipse}(\varphi)$ by $r_{ellipse}(0)$.

- Going back to the initial point distribution, we determine its position in polar coordinates (r_{data}, φ), and scale $r_{data}(\varphi)$ by $r_{ellipse}(\varphi)$.

Figs. 6.5a and 6.5b show a (simulated) point distribution before and after this elliptical correction. The red, filled squares show that data-points on the x- and y-axis are unaffected by this procedure; data-points close to the main diagonal are most strongly affected. Most importantly, this transformation preserves the polar angle φ of each data-point.

The black points in Figs. 6.5a and 6.5b represent what we expect from an observation, namely sky noise plus a few signal datapoints (injected at ON~4.0 and OFF~0.0 in this example). Before elliptical correction, data-points on the x- and y-axis are difficult to pick out by automatic procedures. In particular, the number of points in the hatched orange and blue regions are very close (18 and 20, respectively). This would not be labelled as a detection. After elliptical correction, outliers on the x- and y-axis are much easier to locate. In particular, there are clearly more points in the orange than in the blue hatched region (14 and 5, respectively). In this way, the elliptical correction renders the pipeline more sensitive towards the expected signal.

"If I have seen further than others, it is by standing upon the shoulders of giants." Sir Isaac Newton.

References

Akeson, R. L., Chen, X., Ciardi, D., Crane, M., Good, J., Harbut, M., Jackson, E., Kane, S. R., Laity, A. C., Leifer, S., Lynn, M., McElroy, D. L., Papin, M., Plavchan, P., Ramírez, S. V., Rey, R., von Braun, K., Wittman, M., Abajian, M., Ali, B., Beichman, C., Beekley, A., Berriman, G. B., Berukoff, S., Bryden, G., Chan, B., Groom, S., Lau, C., Payne, A. N., Regelson, M., Saucedo, M., Schmitz, M., Stauffer, J., Wyatt, P., & Zhang, A. 2013, PASP, 125, 989

Albrecht, S., Winn, J. N., Johnson, J. A., Butler, R. P., Crane, J. D., Shectman, S. A., Thompson, I. B., Narita, N., Sato, B., Hirano, T., Enya, K., & Fischer, D. 2011, ApJ, 738, 50

Albrecht, S., Winn, J. N., Johnson, J. A., Howard, A. W., Marcy, G. W., Butler, R. P., Arriagada, P., Crane, J. D., Shectman, S. A., Thompson, I. B., Hirano, T., Bakos, G., & Hartman, J. D. 2012, ApJ, 757, 18

Alexander, R. D., Wynn, G. A., Mohammed, H., Nichols, J. D., & Ercolano, B. 2015, ArXiv e-prints

Alonso, R., Alapini, A., Aigrain, S., Auvergne, M., Baglin, A., Barbieri, M., Barge, P., Bonomo, A. S., Bordé, P., Bouchy, F., Chaintreuil, S., de La Reza, R., Deeg, H. J., Deleuil, M., Dvorak, R., Erikson, A., Fridlund, M., de Oliveira Fialho, F., Gondoin, P., Guillot, T., Hatzes, A., Jorda, L., Lammer, H., Léger, A., Llebaria, A., Magain, P., Mazeh, T., Moutou, C., Ollivier, M., Pätzold, M., Pont, F., Queloz, D., Rauer, H., Rouan, D., Schneider, J., & Wuchterl, G. 2009, A&A, 506, 353

Anderson, D. E. & Cahalan, R. F. 2005, Sol. Phys., 230, 3

Anderson, D. R., Collier Cameron, A., Gillon, M., Hellier, C., Jehin, E., Lendl, M., Maxted, P. F. L., Queloz, D., Smalley, B., Smith, A. M. S., Triaud, A. H. M. J., West, R. G., Pepe, F., Pollacco, D., Ségransan, D., Todd, I., & Udry, S. 2012, MNRAS, 422, 1988

Aschwanden, M. J. 2005, Physics of the Solar Corona. An Introduction with Problems and Solutions (2nd edition)

Astudillo-Defru, N. & Rojo, P. 2013, A&A, 557, A56

Badnell, N. R., O'Mullane, M. G., Summers, H. P., Altun, Z., Bautista, M. A., Colgan, J., Gorczyca, T. W., Mitnik, D. M., Pindzola, M. S., & Zatsarinny, O. 2003, A&A, 406, 1151

Baglin, A. 2003, Advances in Space Research, 31, 345

Bakos, G. Á., Hartman, J., Torres, G., Latham, D. W., Kovács, G., Noyes, R. W., Fischer, D. A., Johnson, J. A., Marcy, G. W., Howard, A. W., Kipping, D., Esquerdo, G. A., Shporer, A., Béky, B., Buchhave, L. A., Perumpilly, G., Everett, M., Sasselov, D. D., Stefanik, R. P., Lázár, J., Papp, I., & Sári, P. 2011, ApJ, 742, 116

Bakos, G. Á., Hartman, J. D., Torres, G., Béky, B., Latham, D. W., Buchhave, L. A., Csubry, Z., Kovács, G., Bieryla, A., Quinn, S., Szklenár, T., Esquerdo, G. A., Shporer, A., Noyes, R. W., Fischer, D. A., Johnson, J. A., Howard, A. W., Marcy, G. W., Sato, B., Penev, K., Everett, M., Sasselov, D. D., Fűrész, G., Stefanik, R. P., Lázár, J., Papp, I., & Sári, P. 2012, AJ, 144, 19

Bakos, G. Á., Howard, A. W., Noyes, R. W., Hartman, J., Torres, G., Kovács, G., Fischer, D. A., Latham, D. W., Johnson, J. A., Marcy, G. W., Sasselov, D. D., Stefanik, R. P., Sipőcz, B., Kovács, G., Esquerdo, G. A., Pál, A., Lázár, J., Papp, I., & Sári, P. 2009, ApJ, 707, 446

Bakos, G. Á., Lázár, J., Papp, I., Sári, P., & Green, E. M. 2002, PASP, 114, 974

Bakos, G. Á., Noyes, R. W., Kovács, G., Latham, D. W., Sasselov, D. D., Torres, G., Fischer, D. A., Stefanik, R. P., Sato, B., Johnson, J. A., Pál, A., Marcy, G. W., Butler,

R. P., Esquerdo, G. A., Stanek, K. Z., Lázár, J., Papp, I., Sári, P., & Sipőcz, B. 2007, ApJ, 656, 552

Ballard, S., Charbonneau, D., Deming, D., Knutson, H. A., Christiansen, J. L., Holman, M. J., Fabrycky, D., Seager, S., & A'Hearn, M. F. 2010, PASP, 122, 1341

Ballerini, P., Micela, G., Lanza, A. F., & Pagano, I. 2012, A&A, 539, A140

Barclay, T., Huber, D., Rowe, J. F., Fortney, J. J., Morley, C. V., Quintana, E. V., Fabrycky, D. C., Barentsen, G., Bloemen, S., Christiansen, J. L., Demory, B.-O., Fulton, B. J., Jenkins, J. M., Mullally, F., Ragozzine, D., Seader, S. E., Shporer, A., Tenenbaum, P., & Thompson, S. E. 2012, ApJ, 761, 53

Barge, P., Baglin, A., Auvergne, M., Rauer, H., Léger, A., Schneider, J., Pont, F., Aigrain, S., Almenara, J.-M., Alonso, R., Barbieri, M., Bordé, P., Bouchy, F., Deeg, H. J., La Reza, D., Deleuil, M., Dvorak, R., Erikson, A., Fridlund, M., Gillon, M., Gondoin, P., Guillot, T., Hatzes, A., Hebrard, G., Jorda, L., Kabath, P., Lammer, H., Llebaria, A., Loeillet, B., Magain, P., Mazeh, T., Moutou, C., Ollivier, M., Pätzold, M., Queloz, D., Rouan, D., Shporer, A., & Wuchterl, G. 2008, A&A, 482, L17

Barnes, J. R., Haswell, C. A., Staab, D., & Anglada-Escudé, G. 2016, MNRAS, 462, 1012

Barnes, J. W., van Eyken, J. C., Jackson, B. K., Ciardi, D. R., & Fortney, J. J. 2013, ApJ, 774, 53

Bastian, T. S., Dulk, G. A., & Leblanc, Y. 2000, ApJ, 545, 1058

Batalha, N. M. 2014, Proceedings of the National Academy of Science, 111, 12647

Bean, J. L. 2009, A&A, 506, 369

Bean, J. L., Benedict, G. F., Charbonneau, D., Homeier, D., Taylor, D. C., McArthur, B., Seifahrt, A., Dreizler, S., & Reiners, A. 2008, A&A, 486, 1039

Bean, J. L., Benedict, G. F., & Endl, M. 2006, ApJL, 653, L65

Bean, J. L., Désert, J.-M., Kabath, P., Stalder, B., Seager, S., Miller-Ricci Kempton, E., Berta, Z. K., Homeier, D., Walsh, S., & Seifahrt, A. 2011, ApJ, 743, 92

Bechter, E. B., Crepp, J. R., Ngo, H., Knutson, H. A., Batygin, K., Hinkley, S., Muirhead, P. S., Johnson, J. A., Howard, A. W., Montet, B. T., Matthews, C. T., & Morton, T. D. 2014, ApJ, 788, 2

Becker, A. C., Kundurthy, P., Agol, E., Barnes, R., Williams, B. F., & Rose, A. E. 2013, ApJL, 764, L17

Béky, B., Holman, M. J., Gilliland, R. L., Bakos, G. Á., Winn, J. N., Noyes, R. W., & Sasselov, D. D. 2013, AJ, 145, 166

Ben-Jaffel, L. 2007, ApJL, 671, L61

—. 2008, ApJ, 688, 1352

Ben-Jaffel, L. & Ballester, G. E. 2013, A&A, 553, A52

—. 2014, ApJL, 785, L30

Benneke, B. & Seager, S. 2012, ApJ, 753, 100

—. 2013, ApJ, 778, 153

Bento, J., Wheatley, P. J., Copperwheat, C. M., Fortney, J. J., Dhillon, V. S., Hickman, R., Littlefair, S. P., Marsh, T. R., Parsons, S. G., & Southworth, J. 2014, MNRAS, 437, 1511

Bergfors, C., Brandner, W., Daemgen, S., Biller, B., Hippler, S., Janson, M., Kudryavtseva, N., Geißler, K., Henning, T., & Köhler, R. 2013, MNRAS, 428, 182

Bessell, M. S. 1979, PASP, 91, 589

Biddle, L. I., Pearson, K. A., Crossfield, I. J. M., Fulton, B. J., Ciceri, S., Eastman, J., Barman, T., Mann, A. W., Henry, G. W., Howard, A. W., Williamson, M. H., Sinukoff, E., Dragomir, D., Vican, L., Mancini, L., Southworth, J., Greenberg, A., Turner, J. D., Thompson, R., Taylor, B. W., Levine, S. E., & Webber, M. W. 2014, MNRAS, 443, 1810

Bisikalo, D., Kaygorodov, P., Ionov, D., Shematovich, V., Lammer, H., & Fossati, L. 2013a, ApJ, 764, 19

Bisikalo, D. V., Kaigorodov, P. V., Ionov, D. E., & Shematovich, V. I. 2013b, Astronomy Reports, 57, 715

Boischot, A., Rosolen, C., Aubier, M. G., Daigne, G., Genova, F., Leblanc, Y., Lecacheux, A., de La Noe, J., & Moller-Pedersen, B. 1980, Icarus, 43, 399

Bonnarel, F., Fernique, P., Bienaymé, O., Egret, D., Genova, F., Louys, M., Ochsenbein, F., Wenger, M., & Bartlett, J. G. 2000, A&AS, 143, 33

Borucki, W. J., Koch, D., Basri, G., Batalha, N., Brown, T., Caldwell, D., Caldwell, J., Christensen-Dalsgaard, J., Cochran, W. D., DeVore, E., Dunham, E. W., Dupree, A. K., Gautier, T. N., Geary, J. C., Gilliland, R., Gould, A., Howell, S. B., Jenkins, J. M., Kondo, Y., Latham, D. W., Marcy, G. W., Meibom, S., Kjeldsen, H., Lissauer, J. J., Monet, D. G., Morrison, D., Sasselov, D., Tarter, J., Boss, A., Brownlee, D., Owen, T., Buzasi, D., Charbonneau, D., Doyle, L., Fortney, J., Ford, E. B., Holman, M. J., Seager, S., Steffen, J. H., Welsh, W. F., Rowe, J., Anderson, H., Buchhave, L., Ciardi, D., Walkowicz, L., Sherry, W., Horch, E., Isaacson, H., Everett, M. E., Fischer, D., Torres, G., Johnson, J. A., Endl, M., MacQueen, P., Bryson, S. T., Dotson, J., Haas, M., Kolodziejczak, J., Van Cleve, J., Chandrasekaran, H., Twicken, J. D., Quintana, E. V., Clarke, B. D., Allen, C., Li, J., Wu, H., Tenenbaum, P., Verner, E., Bruhweiler, F., Barnes, J., & Prsa, A. 2010, Science, 327, 977

Bourrier, V., Lecavelier des Etangs, A., Dupuy, H., Ehrenreich, D., Vidal-Madjar, A., Hébrard, G., Ballester, G. E., Désert, J.-M., Ferlet, R., Sing, D. K., & Wheatley, P. J. 2013, A&A, 551, A63

Braak, C. 2006, Statistics and Computing, 16, 239

Brown, T. M. 2001, ApJ, 553, 1006

Bruntt, H., Southworth, J., Torres, G., Penny, A. J., Clausen, J. V., & Buzasi, D. L. 2006, A&A, 456, 651

Bryans, P., Badnell, N. R., Gorczyca, T. W., Laming, J. M., Mitthumsiri, W., & Savin, D. W. 2006, ApJS, 167, 343

Buchhave, L. A., Bakos, G. Á., Hartman, J. D., Torres, G., Kovács, G., Latham, D. W., Noyes, R. W., Esquerdo, G. A., Everett, M., Howard, A. W., Marcy, G. W., Fischer, D. A., Johnson, J. A., Andersen, J., Fűrész, G., Perumpilly, G., Sasselov, D. D., Stefanik, R. P., Béky, B., Lázár, J., Papp, I., & Sári, P. 2010, ApJ, 720, 1118

Burke, B. F. & Franklin, K. L. 1955, JGR, 60, 213

Busse, F. H. 1976, PEPI, 12, 350

Butler, R. P., Vogt, S. S., Marcy, G. W., Fischer, D. A., Wright, J. T., Henry, G. W., Laughlin, G., & Lissauer, J. J. 2004, ApJ, 617, 580

Cabrera, J., Csizmadia, S., Montagnier, G., Fridlund, M., Ammler-von Eiff, M., Chaintreuil, S., Damiani, C., Deleuil, M., Ferraz-Mello, S., Ferrigno, A., Gandolfi, D., Guillot, T., Guenther, E. W., Hatzes, A., Hébrard, G., Klagyivik, P., Parviainen, H., Pasternacki, T., Pätzold, M., Sebastian, D., Tadeu dos Santos, M., Wuchterl, G., Aigrain, S., Alonso, R., Almenara, J.-M., Armstrong, J. D., Auvergne, M., Baglin, A., Barge, P., Barros, S. C. C., Bonomo, A. S., Bordé, P., Bouchy, F., Carpano, S., Chaffey, C., Deeg, H. J., Díaz, R. F., Dvorak, R., Erikson, A., Grziwa, S., Korth, J., Lammer, H., Lindsay, C., Mazeh, T., Moutou, C., Ofir, A., Ollivier, M., Pallé, E., Rauer, H., Rouan, D., Samuel, B., Santerne, A., & Schneider, J. 2015, A&A, 579, A36

Carone, L., Gandolfi, D., Cabrera, J., Hatzes, A. P., Deeg, H. J., Csizmadia, S., Pätzold, M., Weingrill, J., Aigrain, S., Alonso, R., Alapini, A., Almenara, J.-M., Auvergne, M., Baglin, A., Barge, P., Bonomo, A. S., Bordé, P., Bouchy, F., Bruntt, H., Carpano, S., Cochran, W. D., Deleuil, M., Díaz, R. F., Dreizler, S., Dvorak, R., Eislöffel, J., Eigmüller, P., Endl, M., Erikson, A., Ferraz-Mello, S., Fridlund, M., Gazzano, J.-C., Gibson, N., Gillon, M., Gondoin, P., Grziwa, S., Günther, E. W., Guillot, T., Hartmann, M., Havel, M., Hébrard, G., Jorda, L., Kabath, P., Léger, A., Llebaria, A., Lammer, H., Lovis, C., MacQueen, P. J., Mayor, M., Mazeh, T., Moutou, C., Nortmann, L., Ofir, A., Ollivier, M., Parviainen, H., Pepe, F., Pont, F., Queloz, D., Rabus, M., Rauer, H., Régulo, C.,

Renner, S., de La Reza, R., Rouan, D., Santerne, A., Samuel, B., Schneider, J., Shporer, A., Stecklum, B., Tal-Or, L., Tingley, B., Udry, S., & Wuchterl, G. 2012, A&A, 538, A112

Carr, T. D., Desch, M. D., & Alexander, J. K. 1983, in Physics of the Jovian Magnetosphere, ed. A. J. Dessler (Cambridge University Press, Cambridge and New York), 226–284

Carter, J. A. & Winn, J. N. 2009, ApJ, 704, 51

Carter, J. A., Yee, J. C., Eastman, J., Gaudi, B. S., & Winn, J. N. 2008, ApJ, 689, 499

Cassan, A., Kubas, D., Beaulieu, J.-P., Dominik, M., Horne, K., Greenhill, J., Wambsganss, J., Menzies, J., Williams, A., Jørgensen, U. G., Udalski, A., Bennett, D. P., Albrow, M. D., Batista, V., Brillant, S., Caldwell, J. A. R., Cole, A., Coutures, C., Cook, K. H., Dieters, S., Dominis Prester, D., Donatowicz, J., Fouqué, P., Hill, K., Kains, N., Kane, S., Marquette, J.-B., Martin, R., Pollard, K. R., Sahu, K. C., Vinter, C., Warren, D., Watson, B., Zub, M., Sumi, T., Szymański, M. K., Kubiak, M., Poleski, R., Soszynski, I., Ulaczyk, K., Pietrzyński, G., & Wyrzykowski, Ł. 2012, Nature, 481, 167

Castelli, F. & Kurucz, R. L. 2004, ArXiv Astrophysics e-prints, astro-ph/0405087

Cauley, P. W., Redfield, S., & Jensen, A. G. 2017a, AJ, 153, 217

—. 2017b, AJ, 153, 185

Cauley, P. W., Redfield, S., Jensen, A. G., Barman, T., Endl, M., & Cochran, W. D. 2015, ApJ, 810, 13

Chan, T., Ingemyr, M., Winn, J. N., Holman, M. J., Sanchis-Ojeda, R., Esquerdo, G., & Everett, M. 2011, AJ, 141, 179

Charbonneau, D., Brown, T. M., Burrows, A., & Laughlin, G. 2007a, Protostars and Planets V, 701

Charbonneau, D., Brown, T. M., Latham, D. W., & Mayor, M. 2000, ApJL, 529, L45

Charbonneau, D., Brown, T. M., Noyes, R. W., & Gilliland, R. L. 2002, ApJ, 568, 377

Charbonneau, D., Winn, J. N., Everett, M. E., Latham, D. W., Holman, M. J., Esquerdo, G. A., & O'Donovan, F. T. 2007b, ApJ, 658, 1322

Cherenkov, A. A., Bisikalo, D. V., & Kaigorodov, P. V. 2014, Astronomy Reports, 58, 679

Christensen, U. R. 2010, Space Sci. Rev., 152, 565

Christensen, U. R. & Aubert, J. 2006, GeoJI, 166, 97

Christiansen, J. L., Ballard, S., Charbonneau, D., Deming, D., Holman, M. J., Madhusudhan, N., Seager, S., Wellnitz, D. D., Barry, R. K., Livengood, T. A., Hewagama, T., Hampton, D. L., Lisse, C. M., & A'Hearn, M. F. 2011, ApJ, 726, 94

Christie, D., Arras, P., & Li, Z.-Y. 2013, ApJ, 772, 144

—. 2016, ApJ, 820, 3

Ciardi, D. R., Beichman, C. A., Horch, E. P., & Howell, S. B. 2015, ApJ, 805, 16

Ciceri, S., Mancini, L., Southworth, J., Bruni, I., Nikolov, N., D'Ago, G., Schröder, T., Bozza, V., Tregloan-Reed, J., & Henning, T. 2015, A&A, 577, A54

Ciceri, S., Mancini, L., Southworth, J., Nikolov, N., Bozza, V., Bruni, I., Calchi Novati, S., D'Ago, G., & Henning, T. 2013, A&A, 557, A30

Claret, A. & Bloemen, S. 2011, A&A, 529, A75

Collier Cameron, A., Bouchy, F., Hébrard, G., Maxted, P., Pollacco, D., Pont, F., Skillen, I., Smalley, B., Street, R. A., West, R. G., Wilson, D. M., Aigrain, S., Christian, D. J., Clarkson, W. I., Enoch, B., Evans, A., Fitzsimmons, A., Fleenor, M., Gillon, M., Haswell, C. A., Hebb, L., Hellier, C., Hodgkin, S. T., Horne, K., Irwin, J., Kane, S. R., Keenan, F. P., Loeillet, B., Lister, T. A., Mayor, M., Moutou, C., Norton, A. J., Osborne, J., Parley, N., Queloz, D., Ryans, R., Triaud, A. H. M. J., Udry, S., & Wheatley, P. J. 2007, MNRAS, 375, 951

Collier Cameron, A., Guenther, E., Smalley, B., McDonald, I., Hebb, L., Andersen, J., Augusteijn, T., Barros, S. C. C., Brown, D. J. A., Cochran, W. D., Endl, M., Fossey, S. J., Hartmann, M., Maxted, P. F. L., Pollacco, D., Skillen, I., Telting, J., Waldmann, I. P., & West, R. G. 2010, MNRAS, 407, 507

Colón, K. D., Ford, E. B., Lee, B., Mahadevan, S., & Blake, C. H. 2010, MNRAS, 408, 1494

Copperwheat, C. M., Wheatley, P. J., Southworth, J., Bento, J., Marsh, T. R., Dhillon, V. S., Fortney, J. J., Littlefair, S. P., & Hickman, R. 2013, MNRAS, 434, 661

Cowley, S. W. H., Bunce, E. J., & Nichols, J. D. 2003, JGR, 108, 8002

Croll, B., Albert, L., Lafreniere, D., Jayawardhana, R., & Fortney, J. J. 2010, ApJ, 717, 1084

Croll, B., Lafreniere, D., Albert, L., Jayawardhana, R., Fortney, J. J., & Murray, N. 2011, AJ, 141, 30

Crossfield, I. J. M., Barman, T., Hansen, B. M. S., & Howard, A. W. 2013, A&A, 559, A33

Crossfield, I. J. M., Hansen, B. M. S., & Barman, T. 2012, ApJ, 746, 46

Csizmadia, S., Renner, S., Barge, P., Agol, E., Aigrain, S., Alonso, R., Almenara, J.-M., Bonomo, A. S., Bordé, P., Bouchy, F., Cabrera, J., Deeg, H. J., de La Reza, R., Deleuil, M., Dvorak, R., Erikson, A., Guenther, E. W., Fridlund, M., Gondoin, P., Guillot, T., Hatzes, A., Jorda, L., Lammer, H., Lázaro, C., Léger, A., Llebaria, A., Magain, P., Moutou, C., Ollivier, M., Pätzold, M., Queloz, D., Rauer, H., Rouan, D., Schneider, J., Wuchterl, G., & Gandolfi, D. 2010, A&A, 510, A94

Curtis, S. A. & Ness, N. F. 1986, JGR, 91, 11003

Czesla, S., Huber, K. F., Wolter, U., Schröter, S., & Schmitt, J. H. M. M. 2009, A&A, 505, 1277

Daemgen, S., Hormuth, F., Brandner, W., Bergfors, C., Janson, M., Hippler, S., & Henning, T. 2009, A&A, 498, 567

de Mooij, E. J. W., Brogi, M., de Kok, R. J., Snellen, I. A. G., Kenworthy, M. A., & Karjalainen, R. 2013, A&A, 550, A54

de Wit, J. & Seager, S. 2013, Science, 342, 1473

Deming, D., Fraine, J. D., Sada, P. V., Madhusudhan, N., Knutson, H. A., Harrington, J., Blecic, J., Nymeyer, S., Smith, A. M. S., & Jackson, B. 2012, ApJ, 754, 106

Deming, D., Harrington, J., Laughlin, G., Seager, S., Navarro, S. B., Bowman, W. C., & Horning, K. 2007, ApJL, 667, L199

Deming, D., Sada, P. V., Jackson, B., Peterson, S. W., Agol, E., Knutson, H. A., Jennings, D. E., Haase, F., & Bays, K. 2011, ApJ, 740, 33

Deming, D. & Seager, S. 2017, ArXiv e-prints, astro-ph/1701.00493

Demory, B.-O., de Wit, J., Lewis, N., Fortney, J., Zsom, A., Seager, S., Knutson, H., Heng, K., Madhusudhan, N., Gillon, M., Barclay, T., Desert, J.-M., Parmentier, V., & Cowan, N. B. 2013, ApJL, 776, L25

Dere, K. P., Landi, E., Mason, H. E., Monsignori Fossi, B. C., & Young, P. R. 1997, A&AS, 125, 149

Dittmann, J. A., Close, L. M., Green, E. M., & Fenwick, M. 2009a, ApJ, 701, 756

Dittmann, J. A., Close, L. M., Green, E. M., Scuderi, L. J., & Males, J. R. 2009b, ApJL, 699, L48

Dittmann, J. A., Close, L. M., Scuderi, L. J., & Morris, M. D. 2010, ApJ, 717, 235

Dittmann, J. A., Close, L. M., Scuderi, L. J., Turner, J., & Stephenson, P. C. 2012, New Astron., 17, 438

Eastman, J., Gaudi, B. S., & Agol, E. 2013, PASP, 125, 83

Eastman, J., Siverd, R., & Gaudi, B. S. 2010, PASP, 122, 935

Ehrenreich, D., Bourrier, V., Bonfils, X., Lecavelier des Etangs, A., Hébrard, G., Sing, D. K., Wheatley, P. J., Vidal-Madjar, A., Delfosse, X., Udry, S., Forveille, T., & Moutou, C. 2012, A&A, 547, A18

Ehrenreich, D., Bourrier, V., Wheatley, P. J., Des Etangs, A. L., Hébrard, G., Udry, S., Bonfils, X., Delfosse, X., Désert, J.-M., Sing, D. K., & Vidal-Madjar, A. 2015, Nature, 522, 459

Enoch, B., Anderson, D. R., Barros, S. C. C., Brown, D. J. A., Collier Cameron, A., Faedi, F., Gillon, M., Hébrard, G., Lister, T. A., Queloz, D., Santerne, A., Smalley, B., Street, R. A., Triaud, A. H. M. J., West, R. G., Bouchy, F., Bento, J., Butters, O., Fossati, L., Haswell, C. A., Hellier, C., Holmes, S., Jehin, E., Lendl, M., Maxted, P. F. L., McCormac, J., Miller, G. R. M., Moulds, V., Moutou, C., Norton, A. J., Parley, N., Pepe, F., Pollacco, D., Segransan, D., Simpson, E., Skillen, I., Smith, A. M. S., Udry, S., & Wheatley, P. J. 2011, AJ, 142, 86

Esteves, L. J., De Mooij, E. J. W., & Jayawardhana, R. 2013, ApJ, 772, 51

Evans, T. M., Sing, D. K., Wakeford, H. R., Nikolov, N., Ballester, G. E., Drummond, B., Kataria, T., Gibson, N. P., Amundsen, D. S., & Spake, J. 2016, ApJL, 822, L4

Fares, R., Donati, J.-F., Moutou, C., Jardine, M. M., Grießmeier, J.-M., Zarka, P., Shkolnik, E. L., an d C. Catala, D. B., & Cameron, A. C. 2010, 406, 409

Farrell, W. M., Desch, M. D., & Zarka, P. 1999, J. Geophys. Res., 104, 14025

Farrell, W. M., Lazio, T. J. W., Zarka, P., Bastian, T. J., Desch, M. D., & Ryabov, B. P. 2004, P&SS, 52, 1469

Ferland, G. J., Korista, K. T., Verner, D. A., Ferguson, J. W., Kingdon, J. B., & Verner, E. M. 1998, PASP, 110, 761

Ferland, G. J., Porter, R. L., van Hoof, P. A. M., Williams, R. J. R., Abel, N. P., Lykins, M. L., Shaw, G., Henney, W. J., & Stancil, P. C. 2013, Rev. Mex. Astron. Astrofis, 49, 137

Ford, E. B. 2006, ApJ, 642, 505

Fortney, J. J., Cooper, C. S., Showman, A. P., Marley, M. S., & Freedman, R. S. 2006, ApJ, 652, 746

Fortney, J. J., Lodders, K., Marley, M. S., & Freedman, R. S. 2008, ApJ, 678, 1419

Fortney, J. J., Marley, M. S., & Barnes, J. W. 2007, ApJ, 659, 1661

Fortney, J. J. & Nettelmann, N. 2010, Space Sci. Rev., 152, 423

Fossati, L., Bourrier, V., Ehrenreich, D., Haswell, C. A., Kislyakova, K. G., Lammer, H., Lecavelier des Etangs, A., Alibert, Y., Ayres, T. R., Ballester, G. E., Barnes, J., Bisikalo, D. V., Collier, A., Cameron, Czesla, S., Desert, J.-M., France, K., Guedel, M., Guenther, E., Helling, C., Heng, K., Homstrom, M., Kaltenegger, L., Koskinen, T., Lanza, A. F., Linsky, J. L., Mordasini, C., Pagano, I., Pollacco, D., Rauer, H., Reiners, A., Salz, M., Schneider, P. C., Shematovich, V. I., Staab, D., Vidotto, A. A., Wheatley, P. J., Wood, B. E., & Yelle, R. V. 2015, ArXiv e-prints

Fossati, L., Haswell, C. A., Froning, C. S., Hebb, L., Holmes, S., Kolb, U., Helling, C., Carter, A., Wheatley, P., Collier Cameron, A., Loeillet, B., Pollacco, D., Street, R., Stempels, H. C., Simpson, E., Udry, S., Joshi, Y. C., West, R. G., Skillen, I., & Wilson, D. 2010, ApJL, 714, L222

Fukui, A., Kawashima, Y., Ikoma, M., Narita, N., Onitsuka, M., Ita, Y., Onozato, H., Nishiyama, S., Baba, H., Ryu, T., Hirano, T., Hori, Y., Kurosaki, K., Kawauchi, K., Takahashi, Y. H., Nagayama, T., Tamura, M., Kawai, N., Kuroda, D., Nagayama, S., Ohta, K., Shimizu, Y., Yanagisawa, K., Yoshida, M., & Izumiura, H. 2014, ApJ, 790, 108

Fulton, B. J., Shporer, A., Winn, J. N., Holman, M. J., Pál, A., & Gazak, J. Z. 2011, AJ, 142, 84

Gazak, J. Z., Johnson, J. A., Tonry, J., Dragomir, D., Eastman, J., Mann, A. W., & Agol, E. 2012, Advances in Astronomy, 2012

Gelman, A. & Rubin, D. B. 1992, Statist.Sci., 7, 457

George, S. J. & Stevens, I. R. 2007, MNRAS, 382, 455

Gibson, N. P., Aigrain, S., Barstow, J. K., Evans, T. M., Fletcher, L. N., & Irwin, P. G. J. 2013a, MNRAS, 428, 3680

—. 2013b, MNRAS, 436, 2974

Gibson, N. P., Aigrain, S., Pollacco, D. L., Barros, S. C. C., Hebb, L., Hrudková, M., Simpson, E. K., Skillen, I., & West, R. 2010, MNRAS, 404, L114

Gilliland, R. L., Jenkins, J. M., Borucki, W. J., Bryson, S. T., Caldwell, D. A., Clarke, B. D., Dotson, J. L., Haas, M. R., Hall, J., Klaus, T., Koch, D., McCauliff, S., Quintana, E. V., Twicken, J. D., & van Cleve, J. E. 2010, ApJL, 713, L160

Gillon, M., Anderson, D. R., Collier-Cameron, A., Delrez, L., Hellier, C., Jehin, E., Lendl, M., Maxted, P. F. L., Pepe, F., Pollacco, D., Queloz, D., Ségransan, D., Smith, A. M. S., Smalley, B., Southworth, J., Triaud, A. H. M. J., Udry, S., Van Grootel, V., & West, R. G. 2014, A&A, 562, L3

Gillon, M., Demory, B.-O., Triaud, A. H. M. J., Barman, T., Hebb, L., Montalbán, J., Maxted, P. F. L., Queloz, D., Deleuil, M., & Magain, P. 2009, A&A, 506, 359

Gillon, M., Hatzes, A., Csizmadia, S., Fridlund, M., Deleuil, M., Aigrain, S., Alonso, R., Auvergne, M., Baglin, A., Barge, P., Barnes, S. I., Bonomo, A. S., Bordé, P., Bouchy, F., Bruntt, H., Cabrera, J., Carone, L., Carpano, S., Cochran, W. D., Deeg, H. J., Dvorak, R., Endl, M., Erikson, A., Ferraz-Mello, S., Gandolfi, D., Gazzano, J. C., Guenther, E., Guillot, T., Havel, M., Hébrard, G., Jorda, L., Léger, A., Llebaria, A., Lammer, H., Lovis, C., Mayor, M., Mazeh, T., Montalbán, J., Moutou, C., Ofir, A., Ollivier, M., Pätzold, M., Pepe, F., Queloz, D., Rauer, H., Rouan, D., Samuel, B., Santerne, A., Schneider, J., Tingley, B., Udry, S., Weingrill, J., & Wuchterl, G. 2010, A&A, 520, A97

Gillon, M., Pont, F., Demory, B.-O., Mallmann, F., Mayor, M., Mazeh, T., Queloz, D., Shporer, A., Udry, S., & Vuissoz, C. 2007, A&A, 472, L13

Granata, V., Nascimbeni, V., Piotto, G., Bedin, L. R., Borsato, L., Cunial, A., Damasso, M., & Malavolta , L. 2014, Astronomische Nachrichten, 335, 797

Grießmeier, J.-M. 2015, in Astrophysics and Space Science Library, Vol. 411, Astrophysics and Space Science Library, ed. H. Lammer & M. Khodachenko, 213

Grießmeier, J.-M. 2017, in Planetary Radio Emissions VIII, ed. M. P. G. Fischer, G. Mann & P. Zarka (Austrian Academy of Sciences Press, Vienna), 285–299

Grießmeier, J.-M. 2018, in Handbook of Exoplanets, ed. H. J. Deeg & J. A. Juan Antonio Belmonte (Springer), 159

Grießmeier, J.-M., Motschmann, U., Khodachenko, M., & Rucker, H. O. 2006, in Planetary Radio Emissions VI, ed. H. O. Rucker, W. S. Kurth, & G. Mann (Austrian Academy of Sciences Press, Vienna), 571–579

Grießmeier, J.-M., Motschmann, U., Mann, G., & Rucker, H. O. 2005, A&A, 437, 717

Grießmeier, J.-M., Preusse, S., Khodachenko, M., tschmann, U. M., Mann, G., & Rucker, H. O. 2007, 55, 618

Grießmeier, J.-M., Stadelmann, A., Grenfell, J. L., Lammer, H., & Motschmann, U. 2009, Icarus, 199, 526

Grießmeier, J.-M., Stadelmann, A., Motschmann, U., Belisheva, N. K., Lammer, H., & Biernat, H. K. 2005, Astrobiology, 5, 587

Grießmeier, J.-M., Tabataba-Vakili, F., Stadelmann, A., Grenfell, J. L., & Atri, D. 2015, A&A, 581, A44

Grießmeier, J.-M., Zarka, P., & Girard, J. N. 2011, 46, RS0F09

Grießmeier, J.-M., Zarka, P., & Spreeuw, H. 2007, A&A, 475, 359

Griffith, C. A. 2014, Royal Society of London Philosophical Transactions Series A, 372, 30086

Hallinan, G., Sirothia, S. K., Antonova, A., Ishwara-Chandra, C. H., Bourke, S., Doyle, J. G., Hartman, J., & Golden, A. 2013, ApJ, 762, 34

Han, E., Wang, S. X., Wright, J. T., Feng, Y. K., Zhao, M., Fakhouri, O., Brown, J. I., & Hancock, C. 2014, PASP, 126, 827

Hansen, B. M. S. & Barman, T. 2007, ApJ, 671, 861

Hardy, L. K., Butterley, T., Dhillon, V. S., Littlefair, S. P., & Wilson, R. W. 2015, MNRAS, 454, 4316

Hartman, J. D., Bakos, G. Á., Torres, G., Kovács, G., Noyes, R. W., Pál, A., Latham, D. W., Sipőcz, B., Fischer, D. A., Johnson, J. A., Marcy, G. W., Butler, R. P., Howard, A. W., Esquerdo, G. A., Sasselov, D. D., Kovács, G., Stefanik, R. P., Fernandez, J. M., Lázár, J., Papp, I., & Sári, P. 2009, ApJ, 706, 785

Hartman, J. D., Bakos, G. Á., Torres, G., Latham, D. W., Kovács, G., Béky, B., Quinn, S. N., Mazeh, T., Shporer, A., Marcy, G. W., Howard, A. W., Fischer, D. A., Johnson, J. A., Esquerdo, G. A., Noyes, R. W., Sasselov, D. D., Stefanik, R. P., Fernandez, J. M., Szklenár, T., Lázár, J., Papp, I., & Sári, P. 2011, ApJ, 742, 59

Haswell, C. A., Fossati, L., Ayres, T., France, K., Froning, C. S., Holmes, S., Kolb, U. C., Busuttil, R., Street, R. A., Hebb, L., Collier Cameron, A., Enoch, B., Burwitz, V., Rodriguez, J., West, R. G., Pollacco, D., Wheatley, P. J., & Carter, A. 2012, ApJ, 760, 79

Haynes, K., Mandell, A. M., Madhusudhan, N., Deming, D., & Knutson, H. 2015, ArXiv e-prints

Hebb, L., Collier-Cameron, A., Loeillet, B., Pollacco, D., Hébrard, G., Street, R. A., Bouchy, F., Stempels, H. C., Moutou, C., Simpson, E., Udry, S., Joshi, Y. C., West, R. G., Skillen, I., Wilson, D. M., McDonald, I., Gibson, N. P., Aigrain, S., Anderson, D. R., Benn, C. R., Christian, D. J., Enoch, B., Haswell, C. A., Hellier, C., Horne, K., Irwin, J., Lister, T. A., Maxted, P., Mayor, M., Norton, A. J., Parley, N., Pont, F., Queloz, D., Smalley, B., & Wheatley, P. J. 2009, ApJ, 693, 1920

Hébrard, G., Bouchy, F., Pont, F., Loeillet, B., Rabus, M., Bonfils, X., Moutou, C., Boisse, I., Delfosse, X., Desort, M., Eggenberger, A., Ehrenreich, D., Forveille, T., Lagrange, A.-M., Lovis, C., Mayor, M., Pepe, F., Perrier, C., Queloz, D., Santos, N. C., Ségransan, D., Udry, S., & Vidal-Madjar, A. 2008, A&A, 488, 763

Hébrard, G., Collier Cameron, A., Brown, D. J. A., Díaz, R. F., Faedi, F., Smalley, B., Anderson, D. R., Armstrong, D., Barros, S. C. C., Bento, J., Bouchy, F., Doyle, A. P., Enoch, B., Gómez Maqueo Chew, Y., Hébrard, É. M., Hellier, C., Lendl, M., Lister, T. A., Maxted, P. F. L., McCormac, J., Moutou, C., Pollacco, D., Queloz, D., Santerne, A., Skillen, I., Southworth, J., Tregloan-Reed, J., Triaud, A. H. M. J., Udry, S., Vanhuysse, M., Watson, C. A., West, R. G., & Wheatley, P. J. 2013, A&A, 549, A134

Henry, G. W., Marcy, G. W., Butler, R. P., & Vogt, S. S. 2000, ApJL, 529, L41

Herrero, E., Morales, J. C., Ribas, I., & Naves, R. 2011, A&A, 526, L10

Hess, S. L. G. & Zarka, P. 2011, A&A, 531, A29

Hirano, T., Narita, N., Sato, B., Winn, J. N., Aoki, W., Tamura, M., Taruya, A., & Suto, Y. 2011, PASJ, 63, L57

Holman, M. J., Fabrycky, D. C., Ragozzine, D., Ford, E. B., Steffen, J. H., Welsh, W. F., Lissauer, J. J., Latham, D. W., Marcy, G. W., Walkowicz, L. M., Batalha, N. M., Jenkins, J. M., Rowe, J. F., Cochran, W. D., Fressin, F., Torres, G., Buchhave, L. A., Sasselov, D. D., Borucki, W. J., Koch, D. G., Basri, G., Brown, T. M., Caldwell, D. A., Charbonneau, D., Dunham, E. W., Gautier, T. N., Geary, J. C., Gilliland, R. L., Haas, M. R., Howell, S. B., Ciardi, D. R., Endl, M., Fischer, D., Fürész, G., Hartman, J. D., Isaacson, H., Johnson, J. A., MacQueen, P. J., Moorhead, A. V., Morehead, R. C., & Orosz, J. A. 2010, Science, 330, 51

Holman, M. J. & Murray, N. W. 2005, Science, 307, 1288

Holman, M. J., Winn, J. N., Latham, D. W., O'Donovan, F. T., Charbonneau, D., Torres, G., Sozzetti, A., Fernandez, J., & Everett, M. E. 2007, ApJ, 664, 1185

Holmström, M., Ekenbäck, A., Selsis, F., Penz, T., Lammer, H., & Wurz, P. 2008, Nature, 451, 970

Howard, A. W., Sanchis-Ojeda, R., Marcy, G. W., Johnson, J. A., Winn, J. N., Isaacson, H., Fischer, D. A., Fulton, B. J., Sinukoff, E., & Fortney, J. J. 2013, Nature, 503, 381

Howell, S. B., Sobeck, C., Haas, M., Still, M., Barclay, T., Mullally, F., Troeltzsch, J., Aigrain, S., Bryson, S. T., Caldwell, D., Chaplin, W. J., Cochran, W. D., Huber, D., Marcy, G. W., Miglio, A., Najita, J. R., Smith, M., Twicken, J. D., & Fortney, J. J. 2014, PASP, 126, 398

Hoyer, S., Rojo, P., & López-Morales, M. 2012, ApJ, 748, 22

Hoyer, S., Rojo, P., López-Morales, M., Díaz, R. F., Chambers, J., & Minniti, D. 2011, ApJ, 733, 53

Hubbard, W. B., Fortney, J. J., Lunine, J. I., Burrows, A., Sudarsky, D., & Pinto, P. 2001, ApJ, 560, 413

Hubeny, I., Burrows, A., & Sudarsky, D. 2003, ApJ, 594, 1011

Husnoo, N., Pont, F., Mazeh, T., Fabrycky, D., Hébrard, G., Bouchy, F., & Shporer, A. 2012, MNRAS, 422, 3151

Imai, M., Lecacheux, A., Moncuquet, M., Bagenal, F., Higgins, C. A., Imai, K., & Thieman, J. R. 2015, JGR, 120, 1888

Intema, H. T., Jagannathan, P., Mooley, K. P., & Frail, D. A. 2017, A&A, 598, A78

Jardine, M. & Collier Cameron, A. 2008, A&A, 490, 843

Jenkins, J. M., Caldwell, D. A., & Borucki, W. J. 2002, ApJ, 564, 495

Jensen, A. G., Redfield, S., Endl, M., Cochran, W. D., Koesterke, L., & Barman, T. 2012, ApJ, 751, 86

Johns-Krull, C. M., McCullough, P. R., Burke, C. J., Valenti, J. A., Janes, K. A., Heasley, J. N., Prato, L., Bissinger, R., Fleenor, M., Foote, C. N., Garcia-Melendo, E., Gary, B. L., Howell, P. J., Mallia, F., Masi, G., & Vanmunster, T. 2008, ApJ, 677, 657

Johnson, J. A., Winn, J. N., Narita, N., Enya, K., Williams, P. K. G., Marcy, G. W., Sato, B., Ohta, Y., Taruya, A., Suto, Y., Turner, E. L., Bakos, G., Butler, R. P., Vogt, S. S., Aoki, W., Tamura, M., Yamada, T., Yoshii, Y., & Hidas, M. 2008, ApJ, 686, 649

Johnson, M. C., Cochran, W. D., Collier Cameron, A., & Bayliss, D. 2015, ApJL, 810, L23

Kaiser, M. L. 1993, JGR, 98, 18

Kasting, J. 2010, How to Find a Habitable Planet (Princeton University Press)

Kipping, D. & Bakos, G. 2011, ApJ, 733, 36

Kipping, D. M., Bakos, G. Á., Hartman, J., Torres, G., Shporer, A., Latham, D. W., Kovács, G., Noyes, R. W., Howard, A. W., Fischer, D. A., Johnson, J. A., Marcy, G. W., Béky, B., Perumpilly, G., Esquerdo, G. A., Sasselov, D. D., Stefanik, R. P., Lázár, J., Papp, I., & Sári, P. 2010, ApJ, 725, 2017

Kipping, D. M. & Spiegel, D. S. 2011, MNRAS, 417, L88

Kislyakova, K. G., Holmström, M., Lammer, H., Odert, P., & Khodachenko, M. L. 2014, Science, 346, 981

Kislyakova, K. G., Pilat-Lohinger, E., Funk, B., Lammer, H., Fossati, L., Eggl, S., Schwarz, R., Boudjada, M. Y., & Erkaev, N. V. 2016, MNRAS, 461, 988

Knutson, H. A., Benneke, B., Deming, D., & Homeier, D. 2014a, Nature, 505, 66

Knutson, H. A., Fulton, B. J., Montet, B. T., Kao, M., Ngo, H., Howard, A. W., Crepp, J. R., Hinkley, S., Bakos, G. Á., Batygin, K., Johnson, J. A., Morton, T. D., & Muirhead, P. S. 2014b, ApJ, 785, 126

Knutson, H. A., Howard, A. W., & Isaacson, H. 2010, ApJ, 720, 1569

Kondratiev, V. I., Verbiest, J. P. W., Hessels, J. W. T., Bilous, A. V., Stappers, B. W., Kramer, M., Keane, E. F., Noutsos, A., Osłowski, S., Breton, R. P., Hassall, T. E., Alexov, A., Cooper, S., Falcke, H., Grießmeier, J.-M., Karastergiou, A., Kuniyoshi, M., Pilia, M., Sobey, C., ter Veen, S., van Leeuwen, J., Weltevrede, P., Bell, M. E., Broderick, J. W., Corbel, S., Eislöffel, J., Markoff, S., Rowlinson, A., Swinbank, J. D., Wijers, R. A. M. J., Wijnands, R., & Zarka, P. 2016, A&A, 585, A128

Koskinen, T. T., Lavvas, P., Harris, M. J., & Yelle, R. V. 2014, Royal Society of London Philosophical Transactions Series A, 372, 30089

Kovács, G., Kovács, T., Hartman, J. D., Bakos, G. Á., Bieryla, A., Latham, D., Noyes, R. W., Regály, Z., & Esquerdo, G. A. 2013, A&A, 553, A44

Kramida, A., Yu. Ralchenko, Reader, J., & and NIST ASD Team. 2014, NIST Atomic Spectra Database (ver. 5.2), Available at: `http://physics.nist.gov/asd`

Kreidberg, L., Bean, J. L., Désert, J.-M., Benneke, B., Deming, D., Stevenson, K. B., Seager, S., Berta-Thompson, Z., Seifahrt, A., & Homeier, D. 2014, Nature, 505, 69

Kreidberg, L., Line, M. R., Bean, J. L., Stevenson, K. B., Désert, J.-M., Madhusudhan, N., Fortney, J. J., Barstow, J. K., Henry, G. W., Williamson, M. H., & Showman, A. P. 2015, ApJ, 814, 66

Kulow, J. R., France, K., Linsky, J., & Loyd, R. O. P. 2014, ApJ, 786, 132

Lai, D., Helling, C., & van den Heuvel, E. P. J. 2010, ApJ, 721, 923

Lammer, H., Bredehöft, J. H., Coustenis, A., Khodachenko, M. L., Kaltenegger, L., Grasset, O., Prieur, D., Raulin, F., Ehrenfreund, P., Yamauchi, M., Wahlund, J.-E., Grießmeier, J.-M., Stangl, G., Cockell, C. S., Kulikov, Y. N., Grenfell, J. L., & Rauer, H. 2009, A&Ar, 17, 181

Lamy, L., Zarka, P., Cecconi, B., Klein, L.-K., Masson, S., Denis, L., Coffre, A., & Viou, C. 2017, ArXiv e-prints, astro-ph/1709.03821

Landi, E., Del Zanna, G., Young, P. R., Dere, K. P., & Mason, H. E. 2012, ApJ, 744, 99

Lanza, A. F. 2009, A&A, 505, 339

Lanza, A. F. 2015, in Cambridge Workshop on Cool Stars, Stellar Systems, and the Sun, Vol. 18, 18th Cambridge Workshop on Cool Stars, Stellar Systems, and the Sun, ed. G. T. van Belle & H. C. Harris, 811–830

Lazio, W., T. J., Farrell, W. M., Dietrick, J., Greenlees, E., Hogan, E., Jones, C., & Hennig, L. A. 2004, ApJ, 612, 511

Lazio, T. J. W., Carmichael, S., Clark, J., Elkins, E., Gudmundsen, P., Mott, Z., Szwajkowski, M., & Hennig, L. A. 2010, AJ, 139, 96

Lazio, T. J. W. & Farrell, W. M. 2007, ApJ, 668, 1182

Lazio, T. J. W., Shkolnik, E., Hallinan, G., & Planetary Habitability Study Team. 2016, Planetary Magnetic Fields: Planetary Interiors and Habitability, Tech. rep.

Lecacheux, A., Konovalenko, A. A., & Rucker, H. O. 2004, Planetary and Space Science, 52, 1357

Lecavelier Des Etangs, A., Pont, F., Vidal-Madjar, A., & Sing, D. 2008, A&A, 481, L83

Lecavelier Des Etangs, A., Sirothia, S. K., Gopal-Krishna, & Zarka, P. 2009, A&A, 500, L51

—. 2011, A&A, 533, A50

Lecavelier des Etangs, A., Sirothia, S. K., Gopal-Krishna, & Zarka, P. 2013, A&A, 552, A65

Lee, J. W., Youn, J.-H., Kim, S.-L., Lee, C.-U., & Hinse, T. C. 2012, AJ, 143, 95

Lendl, M., Cubillos, P. E., Hagelberg, J., Müller, A., Juvan, I., & Fossati, L. 2017, A&A, 606, A18

Line, M. R., Knutson, H., Deming, D., Wilkins, A., & Desert, J.-M. 2013, ApJ, 778, 183

Linsky, J. L., Yang, H., France, K., Froning, C. S., Green, J. C., Stocke, J. T., & Osterman, S. N. 2010, ApJ, 717, 1291

Liu, F., Asplund, M., Ramírez, I., Yong, D., & Meléndez, J. 2014, MNRAS, 442, L51

Llama, J. & Shkolnik, E. L. 2015, ApJ, 802, 41

Llama, J., Vidotto, A. A., Jardine, M., Wood, K., Fares, R., & Gombosi, T. I. 2013, MNRAS, 436, 2179

Llama, J., Wood, K., Jardine, M., Vidotto, A. A., Helling, C., Fossati, L., & Haswell, C. A. 2011, MNRAS, 416, L41

López-Morales, M., Coughlin, J. L., Sing, D. K., Burrows, A., Apai, D., Rogers, J. C., Spiegel, D. S., & Adams, E. R. 2010, ApJL, 716, L36

Lovelace, R. V. E., Romanova, M. M., & Barnard, A. W. 2008, MNRAS, 389, 1233

Lykins, M. L., Ferland, G. J., Kisielius, R., Chatzikos, M., Porter, R. L., van Hoof, P. A. M., Williams, R. J. R., Keenan, F. P., & Stancil, P. C. 2015, ApJ, 807, 118

Lynch, C. R., Murphy, T., Kaplan, D. L., Ireland, M., & Bell, M. E. 2017, MNRAS, 467, 3447

Maceroni, C. & Rucinski, S. M. 1997, PASP, 109, 782

Machalek, P., Greene, T., McCullough, P. R., Burrows, A., Burke, C. J., Hora, J. L., Johns-Krull, C. M., & Deming, D. L. 2010, ApJ, 711, 111

Maciejewski, G., Dimitrov, D., Mancini, L., Southworth, J., Ciceri, S., D'Ago, G., Bruni, I., Raetz, S., Nowak, G., Ohlert, J., Puchalski, D., Saral, G., Derman, E., Petrucci, R., Jofre, E., Seeliger, M., & Henning, T. 2016, AcA, 66, 55

Maciejewski, G., Dimitrov, D., Seeliger, M., Raetz, S., Bukowiecki, Ł., Kitze, M., Errmann, R., Nowak, G., Niedzielski, A., Popov, V., Marka, C., Goździewski, K., Neuhäuser, R., Ohlert, J., Hinse, T. C., Lee, J. W., Lee, C.-U., Yoon, J.-N., Berndt, A., Gilbert, H., Ginski, C., Hohle, M. M., Mugrauer, M., Röll, T., Schmidt, T. O. B.,

Tetzlaff, N., Mancini, L., Southworth, J., Dall'Ora, M., Ciceri, S., Zambelli, R., Corfini, G., Takahashi, H., Tachihara, K., Benkő, J. M., Sárneczky, K., Szabo, G. M., Varga, T. N., Vaňko, M., Joshi, Y. C., & Chen, W. P. 2013, A&A, 551, A108

Maciejewski, G., Errmann, R., Raetz, S., Seeliger, M., Spaleniak, I., & Neuhäuser, R. 2011, A&A, 528, A65

Maciejewski, G., Ohlert, J., Dimitrov, D., Puchalski, D., Nedoroscik, J., Vanko, M., Marka, C., Baar, S., Raetz, S., Seeliger, M., & Neuhauser, R. 2014, Acta Astron., 64, 27

Madhusudhan, N. 2012, ApJ, 758, 36

Madhusudhan, N. & Winn, J. N. 2009, ApJ, 693, 784

Mallonn, M., Nascimbeni, V., Weingrill, J., von Essen, C., Strassmeier, K. G., Piotto, G., Pagano, I., Scandariato, G., Csizmadia, S., Herrero, E., Sada, P. V., Dhillon, V. S., Marsh, T. R., Künstler, A., Bernt, I., & Granzer, T. 2015a, A&A, 583, A138

Mallonn, M., von Essen, C., Weingrill, J., Strassmeier, K. G., Ribas, I., Carroll, T. A., Herrero, E., Granzer, T., Claret, A., & Schwope, A. 2015b, A&A, 580, A60

Manchester, R. N., Hobbs, G. B., Teoh, A., & Hobbs, M. 2005, AJ, 129, 1993

Mancini, L., Nikolov, N., Southworth, J., Chen, G., Fortney, J. J., Tregloan-Reed, J., Ciceri, S., van Boekel, R., & Henning, T. 2013, MNRAS, 430, 2932

Mancini, L., Southworth, J., Ciceri, S., Dominik, M., Henning, T., Jørgensen, U. G., Lanza, A. F., Rabus, M., Snodgrass, C., Vilela, C., Alsubai, K. A., Bozza, V., Bramich, D. M., Calchi Novati, S., D'Ago, G., Figuera Jaimes, R., Galianni, P., Gu, S.-H., Harpsøe, K., Hinse, T., Hundertmark, M., Juncher, D., Kains, N., Korhonen, H., Popovas, A., Rahvar, S., Skottfelt, J., Street, R., Surdej, J., Tsapras, Y., Wang, X.-B., & Wertz, O. 2014, A&A, 562, A126

Mandel, K. & Agol, E. 2002, ApJL, 580, L171

Mandushev, G., O'Donovan, F. T., Charbonneau, D., Torres, G., Latham, D. W., Bakos, G. Á., Dunham, E. W., Sozzetti, A., Fernández, J. M., Esquerdo, G. A., Everett, M. E., Brown, T. M., Rabus, M., Belmonte, J. A., & Hillenbrand, L. A. 2007, ApJL, 667, L195

Maness, H. L., Marcy, G. W., Ford, E. B., Hauschildt, P. H., Shreve, A. T., Basri, G. B., Butler, R. P., & Vogt, S. S. 2007, PASP, 119, 90

Markwardt, C. B. 2009, in Astronomical Society of the Pacific Conference Series, Vol. 411, Astronomical Data Analysis Software and Systems XVIII, ed. D. A. Bohlender, D. Durand, & P. Dowler, 251

Marley, M. S., Ackerman, A. S., Cuzzi, J. N., & Kitzmann, D. Clouds and Hazes in Exoplanet Atmospheres, ed. S. J. Mackwell, A. A. Simon-Miller, J. W. Harder, & M. A. Bullock, 367–391

Marques, M. S., Zarka, P., Echer, E., Ryabov, V. B., Alves, M. V., Denis, L., , & Coffre, A. 2017, A&A, 604, A17

Matsakos, T., Uribe, A., & Königl, A. 2015, A&A, 578, A6

Maxted, P. F. L., Anderson, D. R., Collier Cameron, A., Doyle, A. P., Fumel, A., Gillon, M., Hellier, C., Jehin, E., Lendl, M., Pepe, F., Pollacco, D. L., Queloz, D., Ségransan, D., Smalley, B., Southworth, K., Smith, A. M. S., Triaud, A. H. M. J., Udry, S., & West, R. G. 2013, PASP, 125, 48

Mayor, M. & Queloz, D. 1995, Nature, 378, 355

McCullough, P. R., Crouzet, N., Deming, D., & Madhusudhan, N. 2014, ApJ, 791, 55

McKenzie, J. F., Axford, W. I., & Banaszkiewicz, M. 1997, Geophys. Res. Lett., 24, 2877

McLaughlin, D. B. 1924, ApJ, 60, 22

Miralda-Escudé, J. 2002, ApJ, 564, 1019

Mislis, D., Schröter, S., Schmitt, J. H. M. M., Cordes, O., & Reif, K. 2010, A&A, 510, A107

Mizutani, H., Yamamoto, T., & Fujimura, A. 1992, AdSpR, 12, 265

Mordasini, C., Alibert, Y., Klahr, H., & Henning, T. 2012, A&A, 547, A111

Morisset, C. 2013, pyCloudy: Tools to manage astronomical Cloudy photoionization code, Astrophysics Source Code Library

Morton, D. C. 1991, ApJs, 77, 119

—. 2000, ApJs, 130, 403

Moses, J. I., Line, M. R., Visscher, C., Richardson, M. R., Nettelmann, N., Fortney, J. J., Barman, T. S., Stevenson, K. B., & Madhusudhan, N. 2013, ApJ, 777, 34

Moutou, C., Deleuil, M., Guillot, T., Baglin, A., Bordé, P., Bouchy, F., Cabrera, J., Csizmadia, S., & Deeg, H. J. 2013, Icarus, 226, 1625

Moutou, C., Díaz, R. F., Udry, S., Hébrard, G., Bouchy, F., Santerne, A., Ehrenreich, D., Arnold, L., Boisse, I., Bonfils, X., Delfosse, X., Eggenberger, A., Forveille, T., Lagrange, A.-M., Lovis, C., Martinez, P., Pepe, F., Perrier, C., Queloz, D., Santos, N. C., Ségransan, D., Toublanc, D., Troncin, J. P., Vanhuysse, M., & Vidal-Madjar, A. 2011, A&A, 533, A113

Moya, A., Bouy, H., Marchis, F., Vicente, B., & Barrado, D. 2011, A&A, 535, A110

Murgas, F., Pallé, E., Zapatero Osorio, M. R., Nortmann, L., Hoyer, S., & Cabrera-Lavers, A. 2014, A&A, 563, A41

Murphy, T., Bell, M. E., Kaplan, D. L., Gaensler, B. M., Offringa, A. R., Lenc, E., Hurley-Walker, N., Bernardi, G., Bowman, J. D., Briggs, F., Cappallo, R. J., Corey, B. E., Deshpande, A. A., Emrich, D., Goeke, R., Greenhill, L. J., Hazelton, B. J., Hewitt, J. N., Johnston-Hollitt, M., Kasper, J. C., Kratzenberg, E., Lonsdale, C. J., Lynch, M. J., McWhirter, S. R., Mitchell, D. A., Morales, M. F., Morgan, E., Oberoi, D., Ord, S. M., Prabu, T., Rogers, A. E. E., Roshi, D. A., Shankar, N. U., Srivani, K. S., Subrahmanyan, R., Tingay, S. J., Waterson, M., Wayth, R. B., Webster, R. L., Whitney, A. R., Williams, A., & Williams, C. L. 2015, MNRAS, 446, 2560

Murray-Clay, R. A., Chiang, E. I., & Murray, N. 2009, ApJ, 693, 23

Narita, N., Sato, B., Hirano, T., Winn, J. N., Aoki, W., & Tamura, M. 2010, PASJ, 62, 653

Nascimbeni, V., Piotto, G., Bedin, L. R., Damasso, M., Malavolta, L., & Borsato, L. 2011, A&A, 532, A24

Nascimbeni, V., Piotto, G., Pagano, I., Scandariato, G., Sani, E., & Fumana, M. 2013, A&A, 559, A32

Nelder, J. A. & Mead, R. 1965, The Computer Journal, 7, 308

Nelson, B. & Davis, W. D. 1972, ApJ, 174, 617

Ngo, H., Knutson, H. A., Hinkley, S., Bryan, M., Crepp, J. R., Batygin, K., Crossfield, I., Hansen, B., Howard, A. W., Johnson, J. A., Mawet, D., Morton, T. D., Muirhead, P. S., & Wang, J. 2016, ApJ, 827, 8

Nichols, J. D. 2011, MNRAS, 414, 2125

—. 2012, MNRAS, 427, L75

Nichols, J. D. & Milan, S. E. 2016, MNRAS, 461, 2353

Nichols, J. D., Wynn, G. A., Goad, M., Alexander, R. D., Casewell, S. L., Cowley, S. W. H., Burleigh, M. R., Clarke, J. T., & Bisikalo, D. 2015, ApJ, 803, 9

Nikolov, N., Sing, D. K., Pont, F., Burrows, A. S., Fortney, J. J., Ballester, G. E., Evans, T. M., Huitson, C. M., Wakeford, H. R., Wilson, P. A., Aigrain, S., Deming, D., Gibson, N. P., Henry, G. W., Knutson, H., Lecavelier des Etangs, A., Showman, A. P., Vidal-Madjar, A., & Zahnle, K. 2014, MNRAS, 437, 46

Noyes, R. W., Hartmann, L. W., Baliunas, S. L., Duncan, D. K., & Vaughan, A. H. 1984, ApJ, 279, 763

O'Donovan, F. T., Charbonneau, D., Harrington, J., Madhusudhan, N., Seager, S., Deming, D., & Knutson, H. A. 2010, ApJ, 710, 1551

O'Donovan, F. T., Charbonneau, D., Mandushev, G., Dunham, E. W., Latham, D. W., Torres, G., Sozzetti, A., Brown, T. M., Trauger, J. T., Belmonte, J. A., Rabus, M., Almenara, J. M., Alonso, R., Deeg, H. J., Esquerdo, G. A., Falco, E. E., Hillenbrand, L. A., Roussanova, A., Stefanik, R. P., & Winn, J. N. 2006, ApJL, 651, L61

Offringa, A. R. 2012, PhD thesis, University of Groningen, http://hdl.handle.net/11370/b427903c-bf23-4bd5-b641-a58993f54291

Offringa, A. R., de Bruyn, A. G., Biehl, M., Zaroubi, S., Bernardi, G., & Pandey, V. N. 2010, MNRAS, 405, 155

Offringa, A. R., McKinley, B., Hurley-Walker, N., Briggs, F. H., Wayth, R. B., Kaplan, D. L., Bell, M. E., Feng, L., Neben, A. R., Hughes, J. D., Rhee, J., Murphy, T., Bhat, N. D. R., Bernardi, G., Bowman, J. D., Cappallo, R. J., Corey, B. E., Deshpande, A. A., Emrich, D., Ewall-Wice, A., Gaensler, B. M., Goeke, R., Greenhill, L. J., Hazelton, B. J., Hindson, L., Johnston-Hollitt, M., Jacobs, D. C., Kasper, J. C., Kratzenberg, E., Lenc, E., Lonsdale, C. J., Lynch, M. J., McWhirter, S. R., Mitchell, D. A., Morales, M. F., Morgan, E., Kudryavtseva, N., Oberoi, D., Ord, S. M., Pindor, B., Procopio, P., Prabu, T., Riding, J., Roshi, D. A., Shankar, N. U., Srivani, K. S., Subrahmanyan, R., Tingay, S. J., Waterson, M., Webster, R. L., Whitney, A. R., Williams, A., & Williams, C. L. 2014, MNRAS, 444, 606

Offringa, A. R., van de Gronde, J. J., & Roerdink, J. B. T. M. 2012, A&A, 539, A95

O'Rourke, J. G., Knutson, H. A., Zhao, M., Fortney, J. J., Burrows, A., Agol, E., Deming, D., Désert, J.-M., Howard, A. W., Lewis, N. K., Showman, A. P., & Todorov, K. O. 2014, ApJ, 781, 109

Oshagh, M., Santos, N. C., Boisse, I., Boué, G., Montalto, M., Dumusque, X., & Haghighipour, N. 2013, A&A, 556, A19

Oshagh, M., Santos, N. C., Ehrenreich, D., Haghighipour, N., Figueira, P., Santerne, A., & Montalto, M. 2014, A&A, 568, A99

Pál, A., Sárneczky, K., Szabó, G. M., Szing, A., Kiss, L. L., Mező, G., & Regály, Z. 2011, MNRAS, 413, L43

Pearson, K. A., Turner, J. D., & Sagan, T. G. 2014, New Astron., 27, 102

Pepper, J., Pogge, R. W., DePoy, D. L., Marshall, J. L., Stanek, K. Z., Stutz, A. M., Poindexter, S., Siverd, R., O'Brien, T. P., Trueblood, M., & Trueblood, P. 2007, PASP, 119, 923

Perna, R., Menou, K., & Rauscher, E. 2010a, ApJ, 719, 1421

—. 2010b, ApJ, 724, 313

Polisensky, E. 2007, Long Wavelength Array Memo Series, 111

Pollacco, D. L., Skillen, I., Collier Cameron, A., Christian, D. J., Hellier, C., Irwin, J., Lister, T. A., Street, R. A., West, R. G., Anderson, D. R., Clarkson, W. I., Deeg, H., Enoch, B., Evans, A., Fitzsimmons, A., Haswell, C. A., Hodgkin, S., Horne, K., Kane, S. R., Keenan, F. P., Maxted, P. F. L., Norton, A. J., Osborne, J., Parley, N. R., Ryans, R. S. I., Smalley, B., Wheatley, P. J., & Wilson, D. M. 2006, PASP, 118, 1407

Pont, F., Endl, M., Cochran, W. D., Barnes, S. I., Sneden, C., MacQueen, P. J., Moutou, C., Aigrain, S., Alonso, R., Baglin, A., Bouchy, F., Deleuil, M., Fridlund, M., Hébrard, G., Hatzes, A., Mazeh, T., & Shporer, A. 2010, MNRAS, 402, L1

Pont, F., Knutson, H., Gilliland, R. L., Moutou, C., & Charbonneau, D. 2008, MNRAS, 385, 109

Pont, F., Zucker, S., & Queloz, D. 2006, MNRAS, 373, 231

Poppenhaeger, K., Schmitt, J. H. M. M., & Wolk, S. J. 2013, ApJ, 773, 62

Popper, D. M. 1984, AJ, 89, 132

Popper, D. M. & Etzel, P. B. 1981, AJ, 86, 102

Press, W. H., Teukolsky, S. A., Vetterling, W. T., & Flannery, B. P. 1992, Numerical recipes in FORTRAN. The art of scientific computing

Queinnec, J. & Zarka, P. 2001, P&SS, 49, 365

Ranjan, S., Charbonneau, D., Désert, J.-M., Madhusudhan, N., Deming, D., Wilkins, A., & Mandell, A. M. 2014, ApJ, 785, 148

Rappaport, S., Barclay, T., DeVore, J., Rowe, J., Sanchis-Ojeda, R., & Still, M. 2014, ApJ, 784, 40

Rappaport, S., Levine, A., Chiang, E., El Mellah, I., Jenkins, J., Kalomeni, B., Kite, E. S., Kotson, M., Nelson, L., Rousseau-Nepton, L., & Tran, K. 2012, ApJ, 752, 1

Rauer, H., Erikson, A., Kabath, P., Hedelt, P., Boer, M., Carone, L., Csizmadia, S., Eigmüller, P., Paris, P. v., Renner, S., Tournois, G., Titz, R., & Voss, H. 2010, AJ, 139, 53

Reiners, A. & Christensen, U. R. 2010, A&A, 522, A13

Ribas, I., Font-Ribera, A., & Beaulieu, J.-P. 2008, ApJL, 677, L59

Ricci, D., Ramón-Fox, F. G., Ayala-Loera, C., Michel, R., Navarro-Meza, S., Fox-Machado, L., Reyes-Ruiz, M., Sevilla, S. B., & Curiel, S. 2015, PASP, 127, 143

Ricker, G. R., Winn, J. N., Vanderspek, R., Latham, D. W., Bakos, G. Á., Bean, J. L., Berta-Thompson, Z. K., Brown, T. M., Buchhave, L., Butler, N. R., Butler, R. P., Chaplin, W. J., Charbonneau, D., Christensen-Dalsgaard, J., Clampin, M., Deming, D., Doty, J., De Lee, N., Dressing, C., Dunham, E. W., Endl, M., Fressin, F., Ge, J., Henning, T., Holman, M. J., Howard, A. W., Ida, S., Jenkins, J. M., Jernigan, G., Johnson, J. A., Kaltenegger, L., Kawai, N., Kjeldsen, H., Laughlin, G., Levine, A. M., Lin, D., Lissauer, J. J., MacQueen, P., Marcy, G., McCullough, P. R., Morton, T. D., Narita, N., Paegert, M., Palle, E., Pepe, F., Pepper, J., Quirrenbach, A., Rinehart, S. A., Sasselov, D., Sato, B., Seager, S., Sozzetti, A., Stassun, K. G., Sullivan, P., Szentgyorgyi, A., Torres, G., Udry, S., & Villasenor, J. 2015, Journal of Astronomical Telescopes, Instruments, and Systems, 1, 014003

Rogers, J., López-Morales, M., Apai, D., & Adams, E. 2013, ApJ, 767, 64

Rogers, J. C., Apai, D., López-Morales, M., Sing, D. K., & Burrows, A. 2009, ApJ, 707, 1707

Rossiter, R. A. 1924, ApJ, 60, 15

Russell, C. T. 1978, Nature, 272, 147

Russell, C. T. & Dougherty, M. K. 2010, Space Sci. Rev., 152, 251

Ryabov, V. B., Zarka, P., & Ryabov, B. P. 2004, Planet. Space Sci., 52, 1479

Saar, S. H., Butler, R. P., & Marcy, G. W. 1998, ApJL, 498, L153

Sada, P. V., Deming, D., Jennings, D. E., Jackson, B. K., Hamilton, C. M., Fraine, J., Peterson, S. W., Haase, F., Bays, K., Lunsford, A., & O'Gorman, E. 2012, PASP, 124, 212

Sada, P. V. & Ramón-Fox, F. G. 2016, PASP, 128, 024402

Safronov, V. S. 1972, in Evolution of the protoplanetary cloud and formation of the earth and planets., by Safronov, V. S.. Translated from Russian. Jerusalem (Israel): Israel Program for Scientific Translations, Keter Publishing House, 212 p.

Salz, M., Banerjee, R., Mignone, A., Schneider, P. C., Czesla, S., & Schmitt, J. H. M. M. 2015, A&A, 576, A21

Salz, M., Czesla, S., Schneider, P. C., & Schmitt, J. H. M. M. 2016, A&A, 586, A75

Sánchez-Lavega, A. 2004, ApJL, 609, L87

Sano, Y. 1993, JGG, 45, 65

Sansonetti, J. E. 2005, Journal of Physical and Chemical Reference Data, 34, 1559

Saur, J., Grambusch, T., Duling, S., Neubauer, F. M., & Simon, S. 2013, A&A, 552, A119

Schlawin, E., Zhao, M., Teske, J. K., & Herter, T. 2014, ApJ, 783, 5

Schneider, J., Dedieu, C., Le Sidaner, P., Savalle, R., & Zolotukhin, I. 2011, A&A, 532, A79

Schöier, F. L., van der Tak, F. F. S., van Dishoeck, E. F., & Black, J. H. 2005, A&A, 432, 369

Schröter, S., Schmitt, J. H. M. M., & Müller, H. M. 2012, A&A, 539, A97

Schwarz, G. 1978, The Annals of Statistics, 6, 461

Scuderi, L. J., Dittmann, J. A., Males, J. R., Green, E. M., & Close, L. M. 2010, ApJ, 714, 462

Seager, S. 2011, in Exoplanets, edited by S. Seager. Tucson, AZ: University of Arizona Press, 2011, 526 pp. ISBN 978-0-8165-2945-2.

Seager, S. & Sasselov, D. D. 2000, ApJ, 537, 916

Sedaghati, E., Boffin, H. M. J., Delrez, L., Gillon, M., Csizmadia, S., Smith, A. M. S., & Rauer, H. 2017, MNRAS, 468, 3123

See, V., Jardine, M., Fares, R., Donati, J.-F., & Moutou, C. 2015, Monthly Notices of the Royal Astronomical Society, 450, 4323

Selhorst, C. L., Barbosa, C. L., & Válio, A. 2013, ApJL, 777, L34

Shporer, A., Tamuz, O., Zucker, S., & Mazeh, T. 2007, MNRAS, 376, 1296

Simpson, E. K., Pollacco, D., Cameron, A. C., Hébrard, G., Anderson, D. R., Barros, S. C. C., Boisse, I., Bouchy, F., Faedi, F., Gillon, M., Hebb, L., Keenan, F. P., Miller, G. R. M., Moutou, C., Queloz, D., Skillen, I., Sorensen, P., Stempels, H. C., Triaud, A., Watson, C. A., & Wilson, P. A. 2011, MNRAS, 414, 3023

Sing, D. K., Fortney, J. J., Nikolov, N., Wakeford, H. R., Kataria, T., Evans, T. M., Aigrain, S., Ballester, G. E., Burrows, A. S., Deming, D., Désert, J.-M., Gibson, N. P., Henry, G. W., Huitson, C. M., Knutson, H. A., Lecavelier Des Etangs, A., Pont, F., Showman, A. P., Vidal-Madjar, A., Williamson, M. H., & Wilson, P. A. 2016, Natur, 529, 59

Sing, D. K., Lecavelier des Etangs, A., Fortney, J. J., Burrows, A. S., Pont, F., Wakeford, H. R., Ballester, G. E., Nikolov, N., Henry, G. W., Aigrain, S., Deming, D., Evans, T. M., Gibson, N. P., Huitson, C. M., Knutson, H., Showman, A. P., Vidal-Madjar, A., Wilson, P. A., Williamson, M. H., & Zahnle, K. 2013, MNRAS, 436, 2956

Sing, D. K., Pont, F., Aigrain, S., Charbonneau, D., Désert, J.-M., Gibson, N., Gilliland, R., Hayek, W., Henry, G., Knutson, H., Lecavelier Des Etangs, A., Mazeh, T., & Shporer, A. 2011, MNRAS, 416, 1443

Sing, D. K., Vidal-Madjar, A., Désert, J.-M., Lecavelier des Etangs, A., & Ballester, G. 2008, ApJ, 686, 658

Sing, D. K., Wakeford, H. R., Showman, A. P., Nikolov, N., Fortney, J. J., Burrows, A. S., Ballester, G. E., Deming, D., Aigrain, S., Désert, J.-M., Gibson, N. P., Henry, G. W., Knutson, H., Lecavelier des Etangs, A., Pont, F., Vidal-Madjar, A., Williamson, M. W., & Wilson, P. A. 2015, MNRAS, 446, 2428

Sirothia, S. K., Lecavelier des Etangs, A., Gopal-Krishna, Kantharia, N. G., & Ishwar-Chandra, C. H. 2014, A&A, 562, A108

Smith, A. M. S., Anderson, D. R., Collier Cameron, A., Gillon, M., Hellier, C., Lendl, M., Maxted, P. F. L., Queloz, D., Smalley, B., Triaud, A. H. M. J., West, R. G., Barros, S. C. C., Jehin, E., Pepe, F., Pollacco, D., Segransan, D., Southworth, J., Street, R. A., & Udry, S. 2012, AJ, 143, 81

Smith, A. M. S., Anderson, D. R., Skillen, I., Collier Cameron, A., & Smalley, B. 2011, MNRAS, 416, 2096

Smith, A. M. S., Collier Cameron, A., Greaves, J., Jardine, M., Langston, G., & Backer, D. 2009, MNRAS, 395, 335

Snellen, I. A. G., de Mooij, E. J. W., & Albrecht, S. 2009, Nature, 459, 543

Sokov, E. N., Vereshchagina, I. A., Gnedin, Y. N., Devyatkin, A. V., Gorshanov, D. L., Slesarenko, V. Y., Ivanov, A. V., Naumov, K. N., Zinov'ev, S. V., Bekhteva, A. S.,

Romas, E. S., Karashevich, S. V., & Kupriyanov, V. V. 2012, Astronomy Letters, 38, 180

Southworth, J. 2008, MNRAS, 386, 1644

—. 2010, MNRAS, 408, 1689

—. 2011, MNRAS, 417, 2166

—. 2012, MNRAS, 426, 1291

Southworth, J., Bruni, I., Mancini, L., & Gregorio, J. 2012a, MNRAS, 420, 2580

Southworth, J., Bruntt, H., & Buzasi, D. L. 2007a, A&A, 467, 1215

Southworth, J. & Evans, D. F. 2016, MNRAS, 463, 37

Southworth, J., Hinse, T. C., Burgdorf, M., Calchi Novati, S., Dominik, M., Galianni, P., Gerner, T., Giannini, E., Gu, S.-H., Hundertmark, M., Jørgensen, U. G., Juncher, D., Kerins, E., Mancini, L., Rabus, M., Ricci, D., Schäfer, S., Skottfelt, J., Tregloan-Reed, J., Wang, X.-B., Wertz, O., Alsubai, K. A., Andersen, J. M., Bozza, V., Bramich, D. M., Browne, P., Ciceri, S., D'Ago, G., Damerdji, Y., Diehl, C., Dodds, P., Elyiv, A., Fang, X.-S., Finet, F., Figuera Jaimes, R., Hardis, S., Harpsøe, K., Jessen-Hansen, J., Kains, N., Kjeldsen, H., Korhonen, H., Liebig, C., Lund, M. N., Lundkvist, M., Mathiasen, M., Penny, M. T., Popovas, A., Prof., S., Rahvar, S., Sahu, K., Scarpetta, G., Schmidt, R. W., Schönebeck, F., Snodgrass, C., Street, R. A., Surdej, J., Tsapras, Y., & Vilela, C. 2014, MNRAS, 444, 776

Southworth, J., Mancini, L., Ciceri, S., Budaj, J., Dominik, M., Figuera Jaimes, R., Haugbølle, T., Jørgensen, U. G., Popovas, A., Rabus, M., Rahvar, S., von Essen, C., Schmidt, R. W., Wertz, O., Alsubai, K. A., Bozza, V., Bramich, D. M., Calchi Novati, S., D'Ago, G., Hinse, T. C., Henning, T., Hundertmark, M., Juncher, D., Korhonen, H., Skottfelt, J., Snodgrass, C., Starkey, D., & Surdej, J. 2015, MNRAS, 447, 711

Southworth, J., Mancini, L., Maxted, P. F. L., Bruni, I., Tregloan-Reed, J., Barbieri, M., Ruocco, N., & Wheatley, P. J. 2012b, MNRAS, 422, 3099

Southworth, J., Mancini, L., Novati, S. C., Dominik, M., Glitrup, M., Hinse, T. C., Jørgensen, U. G., Mathiasen, M., Ricci, D., Maier, G., Zimmer, F., Bozza, V., Browne, P., Bruni, I., Burgdorf, M., Dall'Ora, M., Finet, F., Harpsøe, K., Hundertmark, M., Liebig, C., Rahvar, S., Scarpetta, G., Skottfelt, J., Smalley, B., Snodgrass, C., & Surdej, J. 2010, MNRAS, 408, 1680

Southworth, J., Maxted, P. F. L., & Smalley, B. 2004a, MNRAS, 349, 547

—. 2004b, MNRAS, 351, 1277

Southworth, J., Wheatley, P. J., & Sams, G. 2007b, MNRAS, 379, L11

Sozzetti, A., Bonomo, A. S., Biazzo, K., Mancini, L., Damasso, M., Desidera, S., Gratton, R., Lanza, A. F., Poretti, E., Rainer, M., Malavolta, L., Affer, L., Barbieri, M., Bedin, L. R., Boccato, C., Bonavita, M., Borsa, F., Ciceri, S., Claudi, R. U., Gandolfi, D., Giacobbe, P., Henning, T., Knapic, C., Latham, D. W., Lodato, G., Maggio, A., Maldonado, J., Marzari, F., Martinez Fiorenzano, A. F., Micela, G., Molinari, E., Mordasini, C., Nascimbeni, V., Pagano, I., Pedani, M., Pepe, F., Piotto, G., Santos, N., Scandariato, G., Shkolnik, E., & Southworth, J. 2015, A&A, 575, L15

Sozzetti, A., Torres, G., Charbonneau, D., Winn, J. N., Korzennik, S. G., Holman, M. J., Latham, D. W., Laird, J. B., Fernandez, J., O'Donovan, F. T., Mandushev, G., Dunham, E., Everett, M. E., Esquerdo, G. A., Rabus, M., Belmonte, J. A., Deeg, H. J., Brown, T. N., Hidas, M. G., & Baliber, N. 2009, ApJ, 691, 1145

Starchenko, S. V. & Jones, C. A. 2002, Icarus, 157, 426

Stempels, H. C., Collier Cameron, A., Hebb, L., Smalley, B., & Frandsen, S. 2007, MNRAS, 379, 773

Stevens, I. R. 2005, MNRAS, 356, 1053

Stevenson, D. J. 1979, GApFD, 12, 139

—. 1984, AN, 305, 257

Stevenson, K. B., Bean, J. L., Madhusudhan, N., & Harrington, J. 2014a, ApJ, 791, 36

Stevenson, K. B., Bean, J. L., Seifahrt, A., Désert, J.-M., Madhusudhan, N., Bergmann, M., Kreidberg, L., & Homeier, D. 2014b, AJ, 147, 161

Stevenson, K. B., Harrington, J., Lust, N. B., Lewis, N. K., Montagnier, G., Moses, J. I., Visscher, C., Blecic, J., Hardy, R. A., Cubillos, P., & Campo, C. J. 2012, ApJ, 755, 9

Street, R. A., Simpson, E., Barros, S. C. C., Pollacco, D., Joshi, Y., Todd, I., Collier Cameron, A., Enoch, B., Parley, N., Stempels, E., Hebb, L., Triaud, A. H. M. J., Queloz, D., Segransan, D., Pepe, F., Udry, S., Lister, T. A., Depagne, É., West, R. G., Norton, A. J., Smalley, B., Hellier, C., Anderson, D. R., Maxted, P. F. L., Bentley, S. J., Skillen, I., Gillon, M., Wheatley, P., Bento, J., Cathaway-Kjontvedt, P., & Christian, D. J. 2010, ApJ, 720, 337

Stroe, A., Snellen, I. A. G., & Röttgering, H. J. A. 2012, A&A, 546, A116

Sullivan, P. W., Winn, J. N., Berta-Thompson, Z. K., Charbonneau, D., Deming, D., Dressing, C. D., Latham, D. W., Levine, A. M., McCullough, P. R., Morton, T., Ricker, G. R., Vanderspek, R., & Woods, D. 2015, ApJ, 809, 77

Sutherland, R. S. & Dopita, M. A. 1993, ApJs, 88, 253

Swain, M., Deroo, P., Tinetti, G., Hollis, M., Tessenyi, M., Line, M., Kawahara, H., Fujii, Y., Showman, A. P., & Yurchenko, S. N. 2013, Icarus, 225, 432

Szabó, G. M., Kiss, L. L., Benkő, J. M., Mező, G., Nuspl, J., Regály, Z., Sárneczky, K., Simon, A. E., Leto, G., Zanmar Sanchez, R., Ngeow, C.-C., Kővári, Z., & Szabó, R. 2010, A&A, 523, A84

Teske, J. K., Cunha, K., Smith, V. V., Schuler, S. C., & Griffith, C. A. 2014, ArXiv e-prints

Teske, J. K., Turner, J. D., Mueller, M., & Griffith, C. A. 2013, MNRAS, 431, 1669

Tinetti, G., Deroo, P., Swain, M. R., Griffith, C. A., Vasisht, G., Brown, L. R., Burke, C., & McCullough, P. 2010, ApJ, 712, L139

Todorov, K., Deming, D., Harrington, J., Stevenson, K. B., Bowman, W. C., Nymeyer, S., Fortney, J. J., & Bakos, G. A. 2010, ApJ, 708, 498

Todorov, K. O., Deming, D., Knutson, H. A., Burrows, A., Sada, P. V., Cowan, N. B., Agol, E., Desert, J.-M., Fortney, J. J., Charbonneau, D., Laughlin, G., Langton, J., Showman, A. P., & Lewis, N. K. 2012, ApJ, 746, 111

Torres, G. 2007, ApJL, 671, L65

Torres, G., Winn, J. N., & Holman, M. J. 2008, ApJ, 677, 1324

Trammell, G. B., Arras, P., & Li, Z.-Y. 2011, ApJ, 728, 152

Trammell, G. B., Li, Z.-Y., & Arras, P. 2014, ApJ, 788, 161

Tremblin, P. & Chiang, E. 2013, MNRAS, 428, 2565

Triaud, A. H. M. J., Anderson, D. R., Collier Cameron, A., Doyle, A. P., Fumel, A., Gillon, M., Hellier, C., Jehin, E., Lendl, M., Lovis, C., Maxted, P. F. L., Pepe, F., Pollacco, D., Queloz, D., Ségransan, D., Smalley, B., Smith, A. M. S., Udry, S., West, R. G., & Wheatley, P. J. 2013, A&A, 551, A80

Triaud, A. H. M. J., Collier Cameron, A., Queloz, D., Anderson, D. R., Gillon, M., Hebb, L., Hellier, C., Loeillet, B., Maxted, P. F. L., Mayor, M., Pepe, F., Pollacco, D., Ségransan, D., Smalley, B., Udry, S., West, R. G., & Wheatley, P. J. 2010, A&A, 524, A25

Triaud, A. H. M. J., Gillon, M., Ehrenreich, D., Herrero, E., Lendl, M., Anderson, D. R., Collier Cameron, A., Delrez, L., Demory, B.-O., Hellier, C., Heng, K., Jehin, E., Maxted, P. F. L., Pollacco, D., Queloz, D., Ribas, I., Smalley, B., Smith, A. M. S., & Udry, S. 2015, MNRAS, 450, 2279

Turner, J. D., Christie, D., Arras, P., Johnson, R. E., & Schmidt, C. 2016a, MNRAS, 458, 3880

Turner, J. D., Grießmeier, J.-M., Zarka, P., & Vasylieva, I. 2017a, in Planetary Radio Emissions VIII, ed. M. P. G. Fischer, G. Mann & P. Zarka (Austrian Academy of Sciences Press, Vienna), 301–313

Turner, J. D., Grießmeier, J.-M., Zarka, P., & Vasylieva, I. 2018, ArXiv e-prints, astro-ph/1802.07316

Turner, J. D., Leiter, R. M., Biddle, L. I., Pearson, K. A., Hardegree-Ullman, K. K., Thompson, R. M., Teske, J. K., Cates, I. T., Cook, K. L., Berube, M. P., Nieberding, M. N., Jones, C. K., Raphael, B., Wallace, S., Watson, Z. T., & Johnson, R. E. 2017b, MNRAS, 472, 3871

Turner, J. D., Pearson, K. A., Biddle, L. I., Smart, B. M., Zellem, R. T., Teske, J. K., Hardegree-Ullman, K. K., Griffith, C. C., Leiter, R. M., Cates, I. T., Nieberding, M. N., Smith, C.-T. W., Thompson, R. M., Hofmann, R., Berube, M. P., Nguyen, C. H., Small, L. C., Guvenen, B. C., Richardson, L., McGraw, A., Raphael, B., Crawford, B. E., Robertson, A. N., Tombleson, R., Carleton, T. M., Towner, A. P. M., Walker-LaFollette, A. M., Hume, J. R., Watson, Z. T., Jones, C. K., Lichtenberger, M. J., Hoglund, S. R., Cook, K. L., Crossen, C. A., Jorgensen, C. R., Romine, J. M., Thompson, A. R., Villegas, C. F., Wilson, A. A., Sanford, B., Taylor, J. M., & Henz, T. N. 2016b, , 459, 789

Turner, J. D., Smart, B. M., Hardegree-Ullman, K. K., Carleton, T. M., Walker-LaFollette, A. M., Crawford, B. E., Smith, C.-T. W., McGraw, A. M., Small, L. C., Rocchetto, M., Cunningham, K. I., Towner, A. P. M., Zellem, R., Robertson, A. N., Guvenen, B. C., Schwarz, K. R., Hardegree-Ullman, E. E., Collura, D., Henz, T. N., Lejoly, C., Richardson, L. L., Weinand, M. A., Taylor, J. M., Daugherty, M. J., Wilson, A. A., & Austin, C. L. 2013, MNRAS, 428, 678

Vaiana, G. S., Cassinelli, J. P., Fabbiano, G., Giacconi, R., Golub, L., Gorenstein, P., Haisch, B. M., Harnden, Jr., F. R., Johnson, H. M., Linsky, J. L., Maxson, C. W., Mewe, R., Rosner, R., Seward, F., Topka, K., & Zwaan, C. 1981, ApJ, 245, 163

van Haarlem, M. P., Wise, M. W., Gunst, A. W., Heald, G., McKean, J. P., Hessels, J. W. T., de Bruyn, A. G., Nijboer, R., Swinbank, J., Fallows, R., Brentjens, M., Nelles, A., Beck, R., Falcke, H., Fender, R., Hörandel, J., Koopmans, L. V. E., Mann, G., Miley, G., Röttgering, H., Stappers, B. W., Wijers, R. A. M. J., Zaroubi, S., van den Akker, M., Alexov, A., Anderson, J., Anderson, K., van Ardenne, A., Arts, M., Asgekar, A., Avruch,

I. M., Batejat, F., Bähren, L., Bell, M. E., Bell, M. R., van Bemmel, I., Bennema, P., Bentum, M. J., Bernardi, G., Best, P., Bîrzan, L., Bonafede, A., Boonstra, A.-J., Braun, R., Bregman, J., Breitling, F., van de Brink, R. H., Broderick, J., Broekema, P. C., Brouw, W. N., Brüggen, M., Butcher, H. R., van Cappellen, W., Ciardi, B., Coenen, T., Conway, J., Coolen, A., Corstanje, A., Damstra, S., Davies, O., Deller, A. T., Dettmar, R.-J., van Diepen, G., Dijkstra, K., Donker, P., Doorduin, A., Dromer, J., Drost, M., van Duin, A., Eislöffel, J., van Enst, J., Ferrari, C., Frieswijk, W., Gankema, H., Garrett, M. A., de Gasperin, F., Gerbers, M., de Geus, E., Grießmeier, J.-M., Grit, T., Gruppen, P., Hamaker, J. P., Hassall, T., Hoeft, M., Holties, H. A., Horneffer, A., van der Horst, A., van Houwelingen, A., Huijgen, A., Iacobelli, M., Intema, H., Jackson, N., Jelic, V., de Jong, A., Juette, E., Kant, D., Karastergiou, A., Koers, A., Kollen, H., Kondratiev, V. I., Kooistra, E., Koopman, Y., Koster, A., Kuniyoshi, M., Kramer, M., Kuper, G., Lambropoulos, P., Law, C., van Leeuwen, J., Lemaitre, J., Loose, M., Maat, P., Macario, G., Markoff, S., Masters, J., McFadden, R. A., McKay-Bukowski, D., Meijering, H., Meulman, H., Mevius, M., Middelberg, E., Millenaar, R., Miller-Jones, J. C. A., Mohan, R. N., Mol, J. D., Morawietz, J., Morganti, R., Mulcahy, D. D., Mulder, E., Munk, H., Nieuwenhuis, L., van Nieuwpoort, R., Noordam, J. E., Norden, M., Noutsos, A., Offringa, A. R., Olofsson, H., Omar, A., Orrú, E., Overeem, R., Paas, H., Pandey-Pommier, M., Pandey, V. N., Pizzo, R., Polatidis, A., Rafferty, D., Rawlings, S., Reich, W., de Reijer, J.-P., Reitsma, J., Renting, G. A., Riemers, P., Rol, E., Romein, J. W., Roosjen, J., Ruiter, M., Scaife, A., van der Schaaf, K., Scheers, B., Schellart, P., Schoenmakers, A., Schoonderbeek, G., Serylak, M., Shulevski, A., Sluman, J., Smirnov, O., Sobey, C., Spreeuw, H., Steinmetz, M., Sterks, C. G. M., Stiepel, H.-J., Stuurwold, K., Tagger, M., Tang, Y., Tasse, C., Thomas, I., Thoudam, S., Toribio, M. C., van der Tol, B., Usov, O., van Veelen, M., van der Veen, A.-J., ter Veen, S., Verbiest, J. P. W., Vermeulen, R., Vermaas, N., Vocks, C., Vogt, C., de Vos, M., van der Wal, E., van Weeren, R., Weggemans, H., Weltevrede, P., White, S., Wijnholds, S. J., Wilhelmsson, T., Wucknitz, O., Yatawatta, S., Zarka, P., Zensus, A., & van Zwieten, J. 2013, A&A, 556, A2

van Werkhoven, T. I. M., Brogi, M., Snellen, I. A. G., & Keller, C. U. 2014, A&A, 561, A3

Vasylieva, I. 2015, Theses, Paris Observatory

Vidal-Madjar, A., Désert, J.-M., Lecavelier des Etangs, A., Hébrard, G., Ballester, G. E., Ehrenreich, D., Ferlet, R., McConnell, J. C., Mayor, M., & Parkinson, C. D. 2004, ApJL, 604, L69

Vidal-Madjar, A., Huitson, C. M., Bourrier, V., Désert, J.-M., Ballester, G., Lecavelier des Etangs, A., Sing, D. K., Ehrenreich, D., Ferlet, R., Hébrard, G., & McConnell, J. C. 2013, A&A, 560, A54

Vidal-Madjar, A., Lecavelier des Etangs, A., Désert, J.-M., Ballester, G. E., Ferlet, R., Hébrard, G., & Mayor, M. 2003, Nature, 422, 143

—. 2008, ApJL, 676, L57

Vidotto, A. A. & Donati, J.-F. 2017, A&A, 602, A39

Vidotto, A. A., Fares, R., Jardine, M., Moutou, C., & Donati, J.-F. 2015, MNRAS, 449, 4117

Vidotto, A. A., Jardine, M., & Helling, C. 2010a, ApJL, 722, L168

—. 2011a, MNRAS, 411, L46

—. 2011b, MNRAS, 414, 1573

Vidotto, A. A., Llama, J., Jardine, M., Helling, C., & Wood, K. 2011c, Astronomische Nachrichten, 332, 1055

Vidotto, A. A., Opher, M., Jatenco-Pereira, V., & Gombosi, T. I. 2010b, ApJ, 720, 1262

von Essen, C., Czesla, S., Wolter, U., Breger, M., Herrero, E., Mallonn, M., Ribas, I., Strassmeier, K. G., & Morales, J. C. 2014, A&A, 561, A48

von Essen, C., Mallonn, M., Albrecht, S., Antoci, V., Smith, A. M. S., Dreizler, S., & Strassmeier, K. G. 2015, A&A, 584, A75

Wakeford, H. R. & Sing, D. K. 2015, A&A, 573, A122

Wang, Y.-H., Wang, S., Liu, H.-G., Hinse, T. C., Laughlin, G., Wu, D.-H., Zhang, X., Zhou, X., Wu, Z., Zhou, J.-L., Wittenmyer, R. A., Eastman, J., Zhang, H., Hori, Y., Narita, N., Chen, Y., Ma, J., Peng, X., Zhang, T.-M., Zou, H., Nie, J.-D., & Zhou, Z.-M. 2017, AJ, 154, 49

Wheatley, P. J., Collier Cameron, A., Harrington, J., Fortney, J. J., Simpson, J. M., Anderson, D. R., Smith, A. M. S., Aigrain, S., Clarkson, W. I., Gillon, M., Haswell, C. A., Hebb, L., Hébrard, G., Hellier, C., Hodgkin, S. T., Horne, K. D., Kane, S. R., Maxted, P. F. L., Norton, A. J., Pollacco, D. L., Pont, F., Skillen, I., Smalley, B., Street, R. A., Udry, S., West, R. G., & Wilson, D. M. 2010, ArXiv e-prints

Wheatley, P. J., West, R. G., Goad, M. R., Jenkins, J. S., Pollacco, D. L., Queloz, D., Rauer, H., Udry, S., Watson, C. A., Chazelas, B., Eigmüller, P., Lambert, G., Genolet, L., McCormac, J., Walker, S., Armstrong, D. J., Bayliss, D., Bento, J., Bouchy, F., Burleigh, M. R., Cabrera, J., Casewell, S. L., Chaushev, A., Chote, P., Csizmadia, S., Erikson, A., Faedi, F., Foxell, E., Gänsicke, B. T., Gillen, E., Grange, A., Günther, M. N., Hodgkin, S. T., Jackman, J., Jordán, A., Louden, T., Metrailler, L., Moyano, M., Nielsen, L. D., Osborn, H. P., Poppenhaeger, K., Raddi, R., Raynard, L., Smith, A. M. S., Soto, M., & Titz-Weider, R. 2018, MNRAS, 475, 4476

Wilson, P. A., Sing, D. K., Nikolov, N., Lecavelier des Etangs, A., Pont, F., Fortney, J. J., Ballester, G. E., López-Morales, M., Désert, J.-M., & Vidal-Madjar, A. 2015, MNRAS, 450, 192

Winglee, R. M., Dulk, G. A., & Bastian, T. S. 1986, ApJL, 309, L59

Winn, J. N. 2010, ArXiv e-prints, astro-ph/1001.2010

Winn, J. N. 2011, in IAU Symposium, Vol. 276, IAU Symposium, ed. A. Sozzetti, M. G. Lattanzi, & A. P. Boss, 230–237

Winn, J. N., Holman, M. J., Bakos, G. Á., Pál, A., Johnson, J. A., Williams, P. K. G., Shporer, A., Mazeh, T., Fernandez, J., Latham, D. W., & Gillon, M. 2007, AJ, 134, 1707

Winn, J. N., Holman, M. J., Torres, G., McCullough, P., Johns-Krull, C., Latham, D. W., Shporer, A., Mazeh, T., Garcia-Melendo, E., Foote, C., Esquerdo, G., & Everett, M. 2008a, ApJ, 683, 1076

Winn, J. N., Johnson, J. A., Howard, A. W., Marcy, G. W., Bakos, G. Á., Hartman, J., Torres, G., Albrecht, S., & Narita, N. 2010, ApJ, 718, 575

Winn, J. N., Johnson, J. A., Narita, N., Suto, Y., Turner, E. L., Fischer, D. A., Butler, R. P., Vogt, S. S., O'Donovan, F. T., & Gaudi, B. S. 2008b, ApJ, 682, 1283

Withbroe, G. L. 1988, ApJ, 325, 442

Wöllert, M. & Brandner, W. 2015, A&A, 579, A129

Wolszczan, A. & Frail, D. A. 1992, Nature, 355, 145

Wong, I., Knutson, H. A., Cowan, N. B., Lewis, N. K., Agol, E., Burrows, A., Deming, D., Fortney, J. J., Fulton, B. J., Langton, J., Laughlin, G., & Showman, A. P. 2014, ApJ, 794, 134

Woods, T., Bailey, S., Eparvier, F., Lawrence, G., Lean, J., McClintock, B., Roble, R., Rottman, G., Solomon, S., Tobiska, W., & White, O. 2000, Physics and Chemistry of the Earth, Part C: Solar, Terrestrial Planetary Science, 25, 393

Wright, J. T., Fakhouri, O., Marcy, G. W., Han, E., Feng, Y., Johnson, J. A., Howard, A. W., Fischer, D. A., Valenti, J. A., Anderson, J., & Piskunov, N. 2011, PASP, 123, 412

Wright, J. T., Marcy, G. W., Fischer, D. A., Butler, R. P., Vogt, S. S., Tinney, C. G., Jones, H. R. A., Carter, B. D., Johnson, J. A., McCarthy, C., & Apps, K. 2007, ApJ, 657, 533

Yantis, W. F., Sullivan, III, W. T., & Erickson, W. C. 1977, in Bulletin of the American Astronomical Society, Vol. 9, Bulletin of the American Astronomical Society, 453

Yelle, R. V. 2004, Icarus, 170, 167

Zakharenko, V. V., Vasylieva, I. Y., Konovalenko, A. A., Ulyanov, O. M., Serylak, M., Zarka, P., Grießmeier, J.-M., Cognard, I., & Nikolaenko, V. S. 2013, MNRAS, 431, 3624

Zarka, P. 1998, JGR, 103, 20159

—. 2007, P&SS, 55, 598

Zarka, P. 2011, in Planetary Radio Emissions VII, ed. H. O. Rucker, W. S. Kurth, P. Louarn, & G. Fischer (Austrian Academy of Sciences Press, Vienna), 287–301

Zarka, P., Cecconi, B., & Kurth, W. S. 2004, JGR, 109, A09S15

Zarka, P., Girard, J. N., Tagger, M., & Denis, L. 2012, in SF2A-2012: Proceedings of the Annual meeting of the French Society of Astronomy and Astrophysics, ed. S. Boissier, P. de Laverny, N. Nardetto, R. Samadi, D. Valls-Gabaud, & H. Wozniak, 687–694

Zarka, P., Lazio, J., & Hallinan, G. 2015, Advancing Astrophysics with the Square Kilometre Array (AASKA14), 120

Zarka, P., Marques, M. S., Louis, C., Ryabov, V. B., Lamy, L., Echer, E., & Cecconi, B. 2017, in Planetary Radio Emissions VIII, ed. M. P. G. Fischer, G. Mann & P. Zarka (Austrian Academy of Sciences Press, Vienna), 45–58

Zarka, P., Queinnec, J., Ryabov, B. P., Ryabov, V. B., Shevchenka, V. A., Arkhipov, A. V., Rucker, H. O., Denis, L., Gerbault, A., Dierich, P., & Rosolen, C. 1997, in Planetary Radio Emission IV, ed. H. O. Rucker, S. J. Bauer, & A. Lecacheux, 101

Zarka, P., Tagger, M., et al. 2014, NenuFAR: instrument description and science case, Tech. rep., *www.researchgate.net/publication/*308806477*_NenUFAR_Instrument_description_and_science$_c$ase*

Zarka, P., Treumann, R. A., Ryabov, B. P., & Ryabov, V. B. 2001, Astrophys. Space. Sci., 277, 293

Zellem, R. T., Griffith, C. A., Pearson, K. A., Turner, J. D., Henry, G. W., Williamson, M. H., Ryleigh Fitzpatrick, M., Teske, J. K., & Biddle, L. I. 2015, ApJ, 810, 11

Zellem, R. T., Lewis, N. K., Knutson, H. A., Griffith, C. A., Showman, A. P., Fortney, J. J., Cowan, N. B., Agol, E., Burrows, A., Charbonneau, D., Deming, D., Laughlin, G., & Langton, J. 2014, ApJ, 790, 53

Zellem, R. T., Swain, M. R., Roudier, G., Shkolnik, E. L., Creech-Eakman, M. J., Ciardi, D. R., Line, M. R., Iyer, A. R., Bryden, G., Llama, J., & Fahy, K. A. 2017, ApJ, 844, 27

Zhang, J.-C., Cao, C., Song, N., Wang, F.-G., & Zhang, X.-T. 2011, Chin. Astron. Astrophys., 35, 409

Zhao, M., Monnier, J. D., Swain, M. R., Barman, T., & Hinkley, S. 2012, ApJ, 744, 122

Zuluaga, J. I., Bustamante, S., Cuartas, P. A., & Hoyos, J. H. 2013, ApJ, 770, 23

"Its the not the Destination, It's the journey." Ralph Waldo Emerson